EFFECTS OF PRECIPITATION, RECOVERY AND RECRYSTALLIZATION ON THE MICROSTRUCTURAL EVOLUTION OF MICROALLOYED AUSTENITE

BY

HATEM S. ZUROB, B. ENG.

A Thesis

Submitted to the School of Graduate Studies
in Partial Fulfilment of the Requirements
for the Degree
Doctor of Philosophy

McMaster University

THE MICROSTRUCTURAL EVOLUTION OF MICROALLOYED AUSTENITE

Doctor of Philosophy (2003)
(Engineering)

McMaster University
Hamilton, Ontario

TITLE: Effects of Precipitation, Recovery and Recrystallization on the Microstructural Evolution of Microalloyed Austenite.

AUTHOR: Hatem Zurob, B. Eng. (McMaster University)

SUPERVISOR: Professor G. R. Purdy and Professor G. C. Weatherly.

NUMBER OF PAGES: xxi, 208

ABSTRACT

The deformation of metals and alloys increases the energy of the system through the storage of dislocations. This stored-energy is the driving force for the processes of recovery and recrystallization. In microalloyed steels, the dislocations provide the necessary nucleation sites for the precipitation of fine dispersions of carbonitrides. Thus, the deformation of microalloyed austenite is followed by three simultaneous processes, namely, recovery, recrystallization and precipitation. The processes are closely coupled and the progress of each is strongly influence by the evolution of the other processes.

In this contribution, existing models of recovery, recrystallization and precipitation have been coupled to produce a physically-based model of the evolution of microalloyed austenite following deformation. The model's predictions are in excellent quantitative agreement with the existing experimental observations in the literature.

A series of fully-austenitic model alloys was developed to examine the underlying assumptions of the above model. The model alloys are based on the Ni-Fe-Nb-C system and were designed to match the stacking-fault-energy of low carbon steels. In this way, it was possible to observe the evolution of microstructure directly in an alloy that closely resembled C-Mn steels. Precipitation in the model alloys was studied extensively, using the

techniques of small angle neutron scattering and electron microscopy. In addition, mechanical testing was used to study the variation of the yield stress in deformed and annealed samples.

The predictions of the model are shown to be in good agreement with the experimental observations. Both point to a strong interaction between precipitation and recovery in microalloyed steels. This interaction dominates the microstructural evolution of these steels at low rolling-temperatures.

PREFACE

The present study was motivated by research into the grain refinement of microalloyed steels. Industrially, fine-grained structures are achieved using very sophisticated thermomechanical treatments. In general, these involve a high-temperature solution treatment followed by two rounds of deformation. The first round takes place at high-temperatures and results in repeated grain refinement by recrystallization. The second rolling step is carried out at low temperatures with the aim of accumulating strain to promote the nucleation of ferrite on cooling. In recent years, the problem of strain-accumulation received increasing attention, because of the possibility of accumulating enough strain to initiate dynamic recrystallization. This would make it possible to produce ultra fine-grained steels.

In this contribution, we examined the fundamental problem of microstructural evolution following the deformation of a supersaturated alloy. The deformation of microalloyed austenite at low temperatures, sets the stage for the simultaneous processes of precipitation, recovery and recrystallization. The above processes are reviewed in detail in chapter (1). In chapter (2), a quantitative physically-based model is developed to describe the above processes as well as their interactions. In order to verify the model, a series of austenitic model alloys were developed. The processes of precipitation and recovery were

studied extensively in these alloys. The results are reported in chapter (3). Detailed discussion of the model and the experimental results is presented in chapter (4) where we demonstrate the merit of the model.

Various parts of this work were developed in collaboration with other researchers. I would like to acknowledge the contributions of Drs. C. R. Hutchinson, Y. Brechet and G. Purdy in the development of the present model. Many of the ideas presented here, emerged during our various discussions. I was able to develop these ideas into a quantitative model thanks to a very productive collaboration with Dr. Hutchinson. Two papers emerged from the above collaborations and these are appended at the end of this work.

In addition, I would like to acknowledge the very important experimental contributions of Dr. Y. J. Wang in the area of small angle-neutron scattering. The scattering measurements, and their initial analysis, were carried out by Dr. Wang. I was responsible for the transmission electron microscopy. The results of our collaboration were published in "Applied Physics A"; the full text appears at the end of this thesis.

ACKNOWLEDGEMENTS:

I am indebted to my supervisors, Dr. Purdy and Dr. Weatherly for their guidance and encouragement. I can't begin to describe my gratitude for the many learning opportunities that they provided me with. I am also grateful to Dr. Metzger for serving on my supervisory committee.

A sincere note of gratitude is extended to Dr. Y. Brechet, Dr. D. Embury and Dr. C. Hutchinson for the valuable ideas that they contributed to this work. I am very grateful to Dr. Subramanian for introducing me to the topic of microalloying. I wish to note, with gratitude, that the model alloys were prepared and hot-rolled at IRSID (Metz, France) under the supervision of Dr. D. Quidort.

I wish to thank the staff of the department of Materials Science and Engineering as well as the staff of the Brockhouse Institute for their assistance in the course of this work. I am particularly grateful to Mr. Jim Garrett; I will always remember with gratitude the many times when Jim stayed late or worked over the weekend to get the samples done on time.

The financial support of the Natural Science and Engineering Research Council and

McMaster University is gratefully acknowledged. I also wish to acknowledge the support of GKSS (Geesthacht, Germany), for the neutron scattering work.

I am also grateful for the support and encouragement of my parents and my brother, Rafik. Above all, "*Praise be to God, who has guided us to this. Never could we have found guidance, had it not been for the guidance of God*"

TABLE OF CONTENTS

Chapter (2): Physically-Based Model of the Microstructural Evolution of Hot-Worked Austenite

Chapter (3): Experimental Work on the Model Alloy

LIST OF FIGURES:

LIST OF TABLES:

SYMBOLS AND ABBREVIATIONS:

α_n	*Constant in equation (2.16) ~ 1.05.*
α_T	*Constant in equation (2.8) ~ 0.15.*
β^*	*Rate at which the atoms are being added to the critical nucleus.*
γ	*Interphase energy.*
γ_{gb}	*Grain boundary energy.*
δ	*Grain boundary thickness.*
ΔG^*	*Nucleation barrier.*
ΔG_v	*Chemical driving force for precipitation.*
ϵ	*Strain.*
η	*Number of dislocations in Eq. (4.4).*
λ	*Spacing of precipitate particles on a dislocation.*
μ	*Shear modulus.*
ρ	*Dislocation density.*
ρ_m, ρ_p	*Neutron scattering length density of the matrix and precipitate.*
σ	*Stress.*
$\Sigma(q)$	*Fourier transform of the form factor.*
τ	*Shear stress for a single crystal.*
ψ	*Probability of development function.*
a	*Lattice parameter of austenite.*
b	*Magnitude of the Burgers vector.*
C	*Solute Concentration.*
D	*Diffusion coefficient.*
D_γ	*Diameter of austenite grains.*
D_b	*Grain boundary diffusion coefficient.*
D_{bulk}	*Bulk diffusion coefficient.*
D_c	*Diameter of the critical recrystallization nucleus.*
D_{pipe}	*Diffusion coefficient along dislocation pipes.*
$dS/d\Omega$	*Differential scattering cross-section.*
E_b	*Binding energy of solute to the boundary.*
EDX	*Energy dispersive X-ray analysis.*
F	*Nucleation constant. Adjustable parameter in Eq. (2.14).*
F	*Scattering factor (eq. 3.1).*
F.P.P.	*Frank partial precipitation.*
F(r)	*Obstacle strength for a precipitate of size r.*
f(r)	*Statistical distribution function of particle size.*

f_v	*Precipitate volume fraction.*
G	*Driving force: G(t) is the driving force for recrystallization, G_{rec} is the driving force for recovery.*
I	*Scattering Intensity.*
J	*Diffusion flux.*
JMAK	*Johnson-Mehl-Avrami-Kolmogorov Model.*
k	*Recrystallization constant: adjustable parameter in Eq (2.5).*
k_b	*Boltzmann's constant.*
k_S	*Particle-strength constant; adjustable parameter in Eq. (2.30).*
l	*Spacing of pinning centres on a dislocation (Eq. 1.10).*
l	*Length scale over which recovery takes place (Eq. 2.7).*
M	*Grain boundary mobility in austenite.*
M_i	*Intrinsic grain boundary mobility in austenite.*
n	*Number density of precipitate.*
n_c	*Minimum number (density) of precipitates needed for complete pinning of recovery.*
n_{total}	*Number of available precipitate nucleation sites per unit volume.*
N_{rex}	*Number of recrystallization nuclei.*
N_v	*Number of atoms per unit volume.*
P(x)	*Distribution function defining the statistical distribution of atoms.*
Q	*Activation energy of diffusion.*
q	*Scattering vector (neutron).*
R	*Softened fraction.*
R	*Austenite Grain radius.*
R_{core}	*Radius of the dislocation pipe.*
R_d	*Mesh size of the dislocation network.*
R_g	*Gas constant.*
r	*Average radius of precipitate particles.*
r_i	*Radius of a specific precipitate particle.*
r_n	*Critical radius for nucleation of precipitate particles.*
SANS	*Small angle neutron scattering.*
SFE	*Stacking fault energy.*
S_v	*Surface area per unit volume.*
T	*Temperature.*
T_{sol}	*Precipitate dissolution temperature.*
t	*Time.*
$t_{x\%}$	*Time needed for a given process to go to x% completion.*
U_a	*Activation energy for recovery.*
V	*Volume.*
V_a	*Activation volume of recovery.*
V_m	*Molar volume.*
v	*Speed of the recrystallization front.*

v	*Volume of a precipitate particle.*
v_d	*Debye Frequency.*
X	*Recrystallized Volume Fraction.*
X_{ext}	*Extended recrystallized volume fraction.*
Z	*Zeldovich non-equilibrium factor.*
Z	*Zener-Holloman Parameter.*
Z	*Zener pressure.*

Chapter 1:

Literature Review

Microalloyed steels constitute 10% of the world's steel production. The attractive properties of these steels are largely attributed to the presence of small additions (0.01-0.1%) of one or more of the elements Nb, Ti and V. These elements combine with C and N to form various precipitates of the type MX, where M is the microalloying element and X is carbon and/or nitrogen. The precipitates are formed almost exclusively on defects in the material, e.g. dislocations and grain-boundaries. The term strain-induced precipitation refers to the formation of large numbers of extremely fine precipitates on the defects (dislocations) created during deformation. In addition to strengthening the steel, these fine precipitates provide a unique opportunity for manipulating the microstructure of the steel.

In general, the deformation of a supersaturated microalloyed steel sets the stage for the simultaneous processes of recrystallization, recovery and (strain-induced) precipitation. The three processes are strongly coupled because they all influence, and are influenced by, the dislocation density. As a result, the individual processes and, to a lesser extent, their interactions have been studied extensively over the past 30 years. Very sophisticated rolling

schedules are now used to produce steels of very fine grain-size. In this chapter, the individual processes of precipitation, recrystallization and recovery are reviewed in sections (1.1-1.3). In sections (1.4-1.6), the literature on the interaction between these processes is examined. The chapter ends with a critical discussion of the existing literature (1.7). The aim of the discussion is to highlight areas where improvement is most needed and to identify the most promising ways of proceeding.

1.1 Precipitation

The precipitation of MX carbonitrides in austenite was the subject of numerous investigations. Most of these studies had one of three objectives: i) determination of the composition and solubility of the precipitates, ii) modelling the time-temperature curves and, to a much lesser extent, iii) determining the nature of the iron/MX interface. Each of these areas will be considered next.

1.1.1 Composition and Solubility:

The microalloying elements precipitate in the form of simple NaCl carbides (MC) and nitrides (MN). These compounds are frequently carbon or nitrogen deficient. The various carbides and nitrides are mutually soluble leading to simple carbonitrides, like

Nb(C,N) or complex carbonitrides, like (Nb,Ti)(C, N). In all cases the nitrides are less soluble than the carbides. NbN is 10 times less soluble than NbC while TiN is 1000 times less soluble than TiC. The solubility difference reflects the fact that the nitrides are more stable than the carbides. Consequently, the nitrogen to carbon ratio in the carbonitride is always higher than that in the bulk. The composition of the carbonitride tends towards that of the nitride in alloys with high nitrogen and low microalloying contents. A quick survey of 10 different Nb-microalloyed steels indicates that the C:N ratio is typically between 4:3 and 1:1. In other words, the Nb precipitates that form in industrial steels will very rarely consist of simple carbides [1].

Most investigations have focussed on determining the solubility constant of the pure carbides and to a lesser extent the pure nitrides. Fewer investigations dealt with the solubility of either the simple or complex carbonitrides. Two approximations are made when deriving the solubility constant [2, 3]. The first is that the Henrian activity coefficient of Nb is unity. In other words, the interaction between solutes is being ignored. The second approximation is related to the stoichiometry of the precipitate: A constant stoichiometry is usually used despite the fact that the composition of the precipitate may vary as it grows. More importantly, the stoichiometry will vary from one steel to another. As a result of these approximations, the solubility constant is only valid for the compositions over which it was derived. This partly explains the large spread (> 100°C) in the predictions of the various solubility constants. Several authors have carried out detailed thermodynamic treatments that avoided the above approximations [2-4]. The results of these models are very accurate

but can't be represented as a simple solubility constant.

To a lesser extent, experimental uncertainties are also responsible for the large spread in the predictions of the solubility limit. The most reliable techniques for determining the solubility are *precipitate extraction* and *gaseous equilibrium* [1,5]. In the first technique the matrix is chemically dissolved. The precipitates are collected and weighed. This information along with the initial composition of the alloy makes it possible to determine the amount of the microalloying elements in solution. The second method involves equilibrating a series of Fe-Nb alloys with a carbon (or nitrogen) atmosphere of a given activity. The carbon (or nitrogen) content of the alloys is then determined. This information is sufficient to extract the solubility limit under the carbon activity being used. The process is repeated in order to determine the whole solubility curve [6]. Admittedly, both techniques have their limitations. The first technique tends to miss the smallest precipitates. In addition, neither technique takes account of the effect of particle size on solubility. Palmiere et al, claim to have overcome the latter problem by using atom probe measurements [5].

1.1.2 Precipitation Kinetics:

Carbonitrides precipitate heterogeneously as a consequence of the large misfit between the precipitates and the matrix. This misfit ranges from ~ 15% in the case of VN to ~ 25% in the case of NbC [7]. The most prominent nucleation sites are dislocations and

grain-boundaries [8]. Several investigations concluded that dislocations are by far the most important nucleation sites, especially in coarse grained materials. For a grain size of 50μm, boundary precipitation accounts for less than 1% of the total precipitates formed [9]. In fact, the works of [10, 11] indicate that grain-boundary precipitation is itself dominated by precipitation on extrinsic dislocations.

The earliest efforts to quantitatively describe the precipitations of carbonitrides in microalloyed steels date back to the late 1980's. Dutta and Sellars [9] as well as Liu and Jonas [12] modelled the nucleation stage. The results were expressed in terms of the time needed for the precipitation of 5% of the equilibrium precipitate fraction. This approach led to expressions that are inversely proportional to the classical steady-state nucleation rate. For example, equation (1.1) below is widely quoted in the literature:

$$t_{5\%} = F(\rho)C_M^{-1}D_M \exp\left(B\Delta G^* / R_g T\right) \qquad (1.1)$$

In this equation B is a correction factor that accounts for the smaller nucleation barrier when precipitation takes place on dislocations. $F(\rho)$ is the number of available nucleation sites. Dutta and Sellars [9] used $F(\rho) = A\varepsilon^1 Z^{0.5}$ while Liu and Jonas used $A'\alpha^3/\rho$ [12]. In both relations, A and B were calculated to fit the experimental data.

The next generation of models appeared in the early 1990's and it took into account the evolution of precipitation as a function of time. Park et al [13] expanded the initial model of Liu and Jonas [12] to include the growth of precipitates under both isothermal and continuous cooling conditions. Around the same time, Dutta et al [14] examined,

qualitatively, the effects of growth and coarsening on the evolution of precipitation-hardening. The new models offered significant improvement over the earliest attempts. However, the temperature-dependence of the precipitation kinetics continued to be poorly represented by the available models [15, 16]. In general, the predicted precipitation times increased very quickly above the nose of the precipitation-time-temperature (PTT) curves. Several authors attributed the above discrepancy to non-equilibrium segregation [16, 17, 18]. It is argued that non-equilibrium segregation takes place due to the strong interaction between the microalloying elements and vacancies. The result is an increased local supersaturation which results in enhanced precipitation. The most detailed treatment of this kind is due to Liu [16] and it results in a much improved agreement for the case considered by the author. Unfortunately, the usefulness of the model is limited because of its complexity and because of the large number of unknown/adjustable parameters involved.

Most recently, Fujita and Bhadeshia [19] and Dutta et al [20] presented more detailed models that take into account the nucleation, growth and coarsening of the precipitates. The new models allowed for simultaneous nucleation and growth as well as a smooth transition from growth to coarsening kinetics. In particular, the second model appears to accurately describe the observed precipitation kinetics for a wide range of temperatures and compositions.

1.1.3 Precipitate-Matrix Interphase:

The preferred orientation relationship between an NaCl-type precipitate and a face-centred cubic (FCC) matrix depends on the lattice misfit [21]. A cube-on-cube orientation relationship is expected when the misfit is less than ~ 25% as is the case for most carbonitrides in steel. This prediction has been confirmed experimentally for V, Ti and Nb in low-carbon steels, stainless steels and Ni alloys [21-25].

The only HRTEM observations of the interface between MX precipitates and austenite are due to Furuhara et al [21] and Sugita [26]. These observations involved, respectively, VC in a 12%Mn steel and TiC in SUS321 stainless steel. In both cases, arrays of misfit dislocations were observed in the matrix. The spacing of the dislocations corresponded to that which would provide complete accommodation of the misfit. This observation is in agreement with the simple thermodynamic model of Liu and Jonas [27] which indicates that more than 95% of the elastic strain is relieved by misfit dislocations.

The orientation dependence of the interfacial energy continues to be poorly understood. In the experiments of Furuhara et al [21] the precipitates were octahedral with facets of the {111} type. The facets were persistent and did not change with time. Kisternich [7] used the technique of moiré fringes to study the precipitation of TiC in stainless steels. According to Kisternich [7], many particles were faceted with the facet planes being predominantly {111}. However, only few particles revealed an octahedral shape. Kisternich [7] attributed the irregular particle shapes to nucleation on irregular dislocation networks. It is worth pointing out the Furuhara et al [21] carried out their

experiments on non-deformed samples. As such, there is no disagreement between their results and those of Kisternich [7]. The predominance of facets of the {111}-type could be interpreted in terms of these planes having the lowest interfacial energy. This interpretation would be consistent with the results of atomistic simulations of binary FCC-FCC systems with large lattice misfits [28, 29]. One can't, however, rule out the possibility that the {111} facets are dominant because of the low stacking fault energy of the steels considered [21].

Yang and Enomoto [30, 31] used a broken-bond method to calculate the chemical energy of the γ-Fe / MX interface. The model predicted that the {001} and {111} planes should have, respectively, the lowest and highest energies. This result is largely due to the exceptional high strength of the M-X bonds. Consequently, the energy of the interface is minimized by those planes with the smallest number of broken M-X bonds. The same authors expanded the model to incorporate a structural energy contribution [32], but the results were unchanged. According to Yang and Enomoto [32], the equilibrium particle shape is a cube with {001} facets. This conclusion is at odds with the above observations on stainless steels and Mn steels. On the other hand, cubic particles are frequently observed in low carbon steels [33, 34].

Estimates of the magnitude of the interfacial energy vary from 0.3 J/m^2 to more than 1.5 J/m^2 [1, 14, 35, 36]. Unfortunately, none of these estimates is based on accurate data or rigorous calculations. In view of this lack of information, Sellars [14] suggested a value of 0.5 J/m^2, which is typical of incoherent interphase boundaries. Gladman [1] advocated

values in the range 0.6-1.0 J/m^2 as being more representative of ferrous interphase boundaries. One should keep in mind that the interfacial energy may be a function of temperature and composition. The Cahn-Hilliard treatment [37] indicates that the energy of a continuous interphase is a function of both temperature and composition. While this model is not applicable to the case of MX carbides in austenite, it is a reminder of the fact that temperature and composition may play a role.

1.2 Recrystallization:

The process of recrystallization involves the nucleation and subsequent growth of strain-free regions in the deformed material. High angle boundaries separate the recrystallized grains from the deformed material. As these boundaries move, the deformed material is replaced by strain-free grains and the energy of the system is reduced [38].

Three types of recrystallization can be distinguished: static recrystallization, metadynamic recrystallization and dynamic recrystallization [38]. A minimum strain (deformation) is needed to initiate static recrystallization. This deformation must be sufficient to create the recrystallizing nuclei and to sustain their growth. Increasing the deformation reduces the incubation period and increases the rate of recrystallization. Eventually a critical strain is reached above which recrystallization starts before the end of

deformation. Metadynamic recrystallization refers to the case in which, the nuclei are formed during deformation and consequently no incubation period is observed. In the case of dynamic recrystallization, repeated nucleation and growth occur during deformation.

Only static recrystallization is considered in this investigation. Throughout this paper the term "recrystallization" will refer to static recrystallization. The following section will deal with the experimental techniques used to study recrystallization. In section (1.2.2), the JMAK model of recrystallization is described. This is followed by a discussion of the effect of solutes on recrystallization (solute drag effect).

1.2.1 Recrystallization Measurements

In the microalloying literature two techniques are commonly used to characterize recrystallization: quantitative optical microscopy and flow stress restoration. Optical microscopy has the potential to provide information on the recrystallized fraction, grain size, growth rate and to some extent the rate of nucleation [39]. The main difficulty is that the austenite structure is not retained at room temperature. Some measurements can be made if the steel transforms to martensite on quenching. In ultra-low carbon steels, ferrite is formed on quenching and optical work is very difficult. Flow stress restoration measurements are carried out in the austenite range. These measurements allow the estimation of the recrystallized fraction as a function of time. Both techniques are discussed in more detail next.

1.2.1.1 Optical Metallography:

Orsetti Rossi and Sellars [39] reviewed the potential applications of quantitative metallography to recrystallization. The results of this survey are summarized in table (1.1) below. The main difficulty is being able to etch the martensite effectively to reveal the former austenite grain boundaries. Even in cases where the austenite phase is retained, it is difficult to manually distinguish between the recrystallized and deformed grains. As a result, the technique found very limited use in the microalloying literature [40].

Quantity	Method of Measurement
X_v (Recrystallized volume fraction) *- results are accurate for $0.1<X<0.9$* *- n_r is the number of point falling in recrystallized grains*	Point counting.
d (Equivalent diameter before or after recrystallization.) *- $d_{(1)}$, $d_{(2)}$, $d_{(3)}$ refer to the diameters calculated using lines parallel to the rolling, transverse and thickness directions.* *- N is the number of boundaries intersected by the line.*	Mean linear intercept $d_{(i)} = L / N_{(i)}$ $d = [d_{(1)}\, d_{(2)}\, d_{(3)}]^{1/3}$
d (Equivalent diameter during recrys.) *-d^d refers to the diameter of a deformed grain.* *-d^r refers to the diameter of a recrystallized grain.*	Mean linear intercept $d^{\,r}_{(i)} = X_v / N^r_{(i)}$ $d^{\,d}_{(i)} = (1-X_v)/N^d_{(i)}$ $d = [d_{(1)}\, d_{(2)}\, d_{(3)}]^{1/3}$
S^{mig} (migrating boundary area) *- assuming equiaxed grains.* *- N^{rd} is the number of boundaries between deformed and recrystallized grains.*	Mean linear intercept $S^{mig} \sim 2\, N^{rd} / L$
$\bar{G}$ (average growth rate)	$\overline{G} = \frac{1}{S^{mig}} \cdot \frac{dX}{dt}$
$\tilde{N}$ (nucleation rate) - accurate estimates are possible by serial analysis which is very time consuming. - less accurate estimates are possible using a single section.	

Table (1.1): *A summary of the recrystallization parameters that could be estimated using quantitative metallography.*

1.2.1.2 Flow Stress Restoration:

Flow stress restoration provides an efficient method of following the softening kinetics of austenite. Each data point requires two successive deformations. The first deformation provides the driving force for recrystallization. The specimen's response to the second deformation is used to determine the amount of softening that took place between the two deformations. If no softening took place the second flow curve should follow the extension of the first. At the other extreme, if complete softening took place, the second flow curve would be identical to the first [41]. For cases between the two extremes a law of mixture is used: $R = (\sigma_W - \sigma_P) / (\sigma_W - \sigma_R)$. In this equation, R refers to the softened fraction, σ_P, σ_W and σ_R refer to the flow stresses of the partially-restored, work-hardened and completely-restored materials, respectively. The processes of recovery, recrystallization, precipitation and grain-growth, all contribute to the value of R. As a result, the softening fraction is, in general, very different from the recrystallized fraction. In simple systems where recovery and recrystallization are the only processes taking place, the recrystallized fraction can be estimated from the softening data by carefully defining the values of σ_P, σ_W and σ_R. At least six different methods exist for this purpose [41-45]. These methods were reviewed by Fernandez et al [42] and a brief summary is provided in appendix (A1). Under the best of circumstances, the calculated recrystallized fraction is found to be within ± 5 - 10% of the value measured optically. Kang et al [46] demonstrated that the above methods of estimating the recrystallized fraction become completely inaccurate when significant precipitation hardening takes place. Unfortunately, the derivation of recrystallized fractions from softening data continues to be a common practice in the microalloying literature.

1.2.2 JMAK Model

The simplest model of recrystallization is that due to Kolmogorov, Johnson and Mehl and Avrami. We will refer to this approach as the JMAK model. The model is based on the key concept of the extended recrystallized volume fraction [38]:

$$X_{ext} = \int_0^t V(t)\,\dot{N}\,dt \tag{1.2}$$

In this equation, $\dot{N}$ is the nucleation rate (assumed constant) and $V(t)$ is the volume of a single recrystallized grain. The extended fraction does not take into account the fact that new nuclei may not form in areas that have already recrystallized. In addition, the effect of impingement is not taken into account. For a random distribution of nuclei, the actual recrystallized fraction is obtained from the extended fraction using the relation:

$$X = 1 - \exp\left(-X_{ext}\right) \tag{1.3}$$

Combining the above equations and replacing the volume by $4\pi\,(v\,t)^3 / 3$ one obtains:

$$X = 1 - \exp\left(\tfrac{4\pi}{3}\int_0^t \dot{N} v^3 t^3 dt\right) \tag{1.4}$$

Assuming the growth rate, v, is constant and equal to MG_r, where M is the mobility and G_r is the driving force for recrystallization, one obtains:

$$X = 1 - \exp\left(\frac{\pi}{3}\dot{N}\,M^3 G_r^3 t^4\right) \tag{1.5}$$

This is the standard JMAK equation for the case of constant nucleation and growth rates. More generally, the equation may be written as:

$$X = 1 - \exp(-Bt^m) \tag{1.6}$$

where m is the Avrami or the JMAK exponent.

It is also possible to consider the case in which the (local) nucleation rate is a decreasing function of time. In the limiting case of site-saturation the nucleation rate decreases very rapidly. As a result, one may assume that all of the nuclei were formed at the start of recrystallization. This assumption leads to a JMAK exponent of 3. The JMAK exponent would lie between 3 and 4 if the nucleation rate decreased at a finite rate [38, 47].

The experimentally determined JMAK exponents are usually less than or equal to 2. This discrepancy is attributed to the fact that in reality, the growth rate is not constant [38, 47]. Temporal and spatial variations of the driving force could reduce the JMAK exponent to values similar to those observed experimentally [38, 47]. This led to the development of relaxed JMAK models, in which the growth rate is a decreasing function of time [38, 47, 48].

The validity of the extended volume approach was called into question by a number of authors (see review by [48]). Recently, Cahn [49] demonstrated that the JMAK approach is accurate provided that the nuclei are randomly distributed. The requirement of a random distribution of nuclei is, therefore, the most serious limitation of the JMAK approach [38, 47].

1.2.3 Solute Drag Effect:

It is well established that small solute additions can reduce the rate of recrystallization through the solute-drag effect [38, 50, 51]. This phenomenon was modelled extensively by Cahn [52], Lücke and Stüwe [53] and Hillert and Sundman [54]. In the case of microalloyed steels, a number of authors [15, 55-58] presented strong evidence for the retardation of recrystallization by the microalloying elements in solution. The bulk of the evidence comes from experiments on decarburized/denitrided steels as well as experiments above the carbonitride dissolution temperature. In these experiments the possibility of precipitation is ruled out and the observed retardation is solely due to solute drag [15, 55]. It appears that solute drag can increase the recrystallization time by 1 to 2 orders of magnitude. Niobium and vanadium have, respectively, the strongest and the weakest retardation effect [57].

Cahn's treatment of solute-drag [52] is easily incorporated within the JMAK framework. The interface mobility, in the presence of strong-solute drag conditions, is given by:

$$M = \left(1/M_i + \alpha C_o\right)^{-1} \tag{1.7}$$

In this equation, M_i is the interface mobility in the absence of solute-drag (intrinsic mobility) and C_o is the bulk solute concentration. The constant, α, is a function of both the solute-boundary binding energy and the cross-boundary solute diffusion coefficient. Simielli et al [59] used this approach to interpret observations on the recrystallization of microalloyed ferrite and austenite.

1.3 Recovery:

Recovery refers to the gradual decrease in the energy of the system through the annihilation and rearrangement of dislocations [38]. Once again, we will distinguish between dynamic and static recovery; only the latter is reviewed here. A number of processes take place during recovery; These include, dislocation glide, cross-slip and climb. Depending on the material, the applied deformation and the annealing temperature, one of the above processes would control the over-all rate of recovery [38, 60]. In alloys, recovery is also influenced by the solute-drag effect, which can limit the rates of dislocation glide and climb [60]. Experimental measurements of the recovery kinetics in microalloyed steels are reviewed in section (1.3.1). This is followed by a brief discussion on the modelling of recovery (1.3.2) and the effect of solutes on the rate of recovery (1.3.3).

1.3.1 Experimental Measurements in Microalloyed Steels:

In general, recovery is observed indirectly through its effect on bulk material properties. For example, measurements of electrical resistivity and hardness are commonly used to follow the progress of recovery [38]. In the microalloying literature, recovery is usually studied using the double-deformation method and the technique of stress-relaxation [15]. A brief review of the experimental observations follows:

1.3.1.1 Double-deformation Method:

The double-deformation method was described in section (1.2.2.2). In general, recovery, recrystallization and precipitation will all contribute to the measured softening fraction [46]. For this reason, it is important to choose conditions under which recovery is the only process taking place. The work of Yamamoto et al [15] is perhaps the most comprehensive investigation of this type. In this work a number of microalloyed steels were decarburized to eliminate the effect of precipitation. In addition, metallographic measurements on the above steels indicated that the initial softening (up to about R= 20%) was solely due to recovery. Three important observations emerged from the work of Yamamoto et al [15]:

a) The microalloying elements (Nb, Ti and V) significantly retard the kinetics of recovery. The retardation increases in the order V < Ti < Nb. The same trends were reported by Andrade et al [58] and Muruyama et al [61].

b) The retardation effect depends on the solute concentration. This effect is clearly demonstrated in figure (1.1). In this figure, $t_{20\%}$ is the time needed to achieve 20% softening (recovery). The concentration dependence of $t_{20\%}$ differs from one solute to another, in agreement with the first observation.

c) The effect of concentration on recovery changes as a function of temperature. This effect is also seen in figure (1.1) where the slope of the $t_{20\%}$ vs. C curve changes as a function of temperature.

The above observations received surprisingly little attention in the literature. We'll try to shed some light on these observations in sections (1.3.2), (1.3.3) and Appendix (A2).

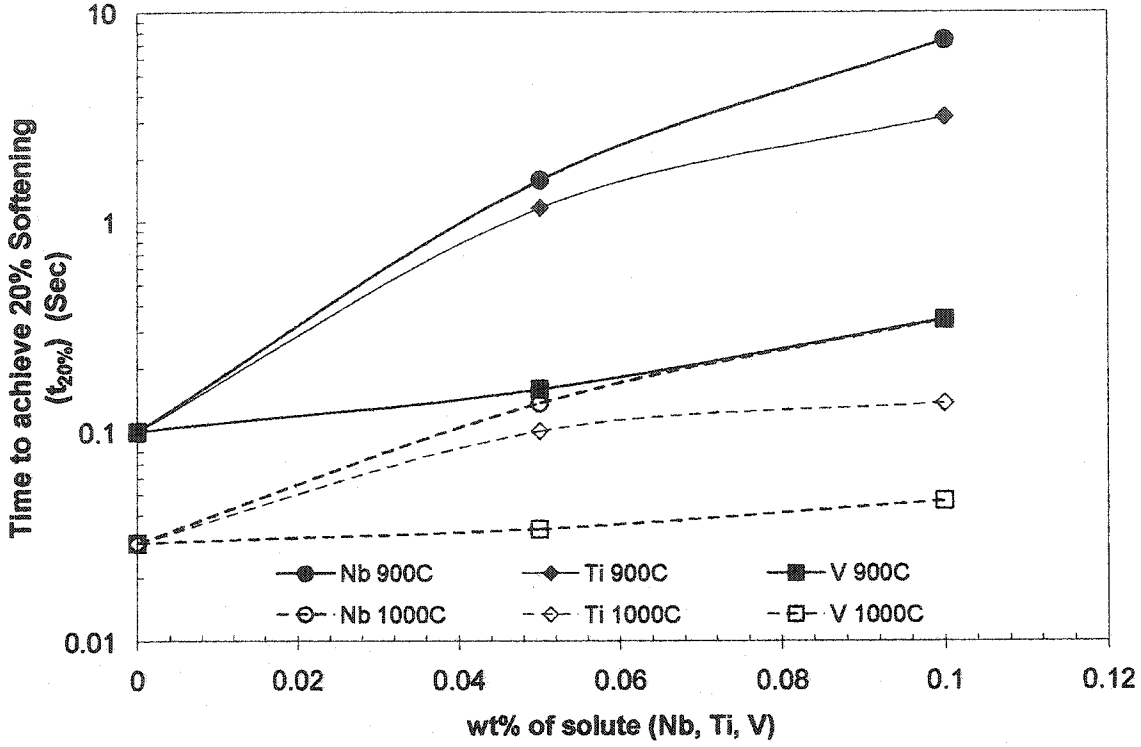

Figure (1.1): *The results of Yamamoto et al [15] on the effect of temperature and solute-concentration on the kinetics of recovery.*

1.3.1.2 Stress-Relaxation Method:

In the microalloying literature the stress-relaxation method is commonly used to detect the onset of precipitation or to estimate the recrystallized fraction [41, 62, 63]. Ironically, stress-relaxation has been overlooked as a method of studying the kinetics of recovery. The investigation by Arieta and Sellars [64] represents the only attempt to study the effect of microalloying on the kinetics of recovery. In this investigation, the activation energy for recovery was measured as a function of the Nb content. Unfortunately, the measured values, which fell between 400 and 800 kJ/mole, cannot be reconciled with any physical mechanism (see section 1.3.2). In addition, the activation energy showed strong

temperature dependence. This along with the large scatter of the experimental data has led us to avoid discussing these results in detail. The important point, however, is that the recovery of microalloyed steels follows a logarithmic rate law over a wide range of temperatures and compositions (see section 1.3.2).

1.3.2 Modeling of Recovery in Microalloyed Steels:

The decay of the flow-stress is generally found to follow either logarithmic or power-law kinetics [38]:

$$\sigma = c_1 - c_2 \ln(t) \tag{1.7}$$

$$\sigma = c_3 - c_4 (t)^{-m} \tag{1.8}$$

Logarithmic kinetics are commonly observed in microalloyed steels at intermediate annealing temperatures ($T_m/2$) [62-65]. The logarithmic kinetics could be attributed to glide control or solute-drag control [60]. In both cases, the evolution of the flow stress is given by a rate law of the form [60, 66]:

$$\frac{d\sigma}{dt} = -c_5 \sigma^2 \exp\left(-\frac{U_a}{R_g T}\right) \sinh\left(\frac{\sigma V_a}{k_b T}\right) \tag{1.9}$$

In this equation U_a is the activation energy for the recovery process. The value of the activation energy ranges from that of pipe-diffusion to the activation energy for the self (or solute) bulk diffusion [60]. The activation volume, V_a, is related to the spacing of the pinning centres. These centres may be jogs on a screw dislocation, as in the case of glide, or solute atoms as in the general case of solute-drag [60]. In deriving equation (1.9) it is assumed that

the flow stress is a function of only the dislocation density (single-state variable approach). This treatment becomes inaccurate when the microstructure is made up of subgrains with a relatively low internal dislocation density.

1.3.3 Effect of Solutes on Recovery:

In order to apply equation (1.9) to microalloyed steels, it is important to identify the effect of the microalloying elements (solute) on the activation energy and the activation volume. This is the subject of sections (1.3.3.1) and (1.3.3.2).

1.3.3.1 Activation Energy.

In the absence of reliable data on microalloyed steels, experimental measurements on other systems are considered. Monzen et al [67] studied the effect of solutes on the activation energy for recovery in Cu. The experiments involved the careful observation of the recovery (by climb) of Orowan loops around α-Fe particles in Cu. A total of 5 solutes were considered, namely, Ni, Co, Ag, Bi and P. In each case, the solute content was varied between 0 and 0.1%. The authors report that in all cases, the activation energy changed from that of self-diffusion to the activation energy of the solute in Cu. Phosphorus was the only solute that did not follow the above trend: The addition of phosphorus did not change the activation energy. The above observations were explained in terms of the relative values of Q_{self} and Q_{solute}. In general, the larger of the two is expected to be rate limiting. In the case of P, Q_{solute} is less than Q_{self}. Consequently, the addition of P does not change the activation

energy. This is an important observation, because the activation energies for the diffusion of Nb, Ti and V are smaller than the self-diffusion energy in austenite [68, 69]. As such, microalloying is not expected to change the activation energy. The effect of microalloying should, therefore, enter through the activation volume.

1.3.3.2 Activation Volume.

The activation volume was defined as $b\,a^{*}\,l$, where l is the obstacle spacing and a^{*} is the activation distance. In the case of a jogged screw dislocation, l is equal to the jog spacing. Estimation of the jog spacing is a very difficult problem. A crude estimate could be obtained if the jogs are assumed to form, primarily, as a result of the intersection of dislocations. Under these circumstances the number of jogs is related to the dislocation density [60]:

$$l_{jog} = c_6 / \sqrt{\rho} \qquad (1.10)$$

The constant, c_6, is close to unity in materials with high stacking fault energy.

When solute-drag is the rate-controlling process, the spacing of the pinning centers is expected to be proportional to $1/C^{n}$. The value of the exponent, n, ranges from 1 in the case of small bow-outs to ½ in the case of strong bow-outs [60]. In the most general case, the effective obstacle spacing will include contributions from both solute-atoms and forest-type jogs. This idea will be developed further in appendix (A2) where it will be shown that the results of Yamamoto et al [15] can be satisfactorily explained.

1.4 Interactions between Precipitation and Recrystallization:

The evolution of recrystallization is significantly complicated by the occurrence of precipitation. Fine precipitate dispersions have the potential to slow down and, in some cases, halt recrystallization [1, 9]. On the other hand, coarse precipitates may enhance recrystallization by reducing solute drag [38]. The importance of these effects placed precipitation-kinetics and Zener-drag at the centre of the microalloying literature. Interestingly, the effect of recrystallization on precipitation has been frequently overlooked. Recrystallization may hinder the precipitation of MX by eliminating the precipitate nucleation sites. In addition, the passage of a moving boundary through a dispersion of particles may lead to particle dissolution and re-precipitation as well as accelerated particle coarsening [70-72].

The present review is limited to the pinning effect that a dispersion of precipitates exerts on a moving boundary. This problem was first analysed by Zener [73] who argued that the energy of the system is lowered when the boundary makes contact with the precipitates. For the boundary to continue moving, enough energy must be supplied to recreate the boundary and this leads to Zener drag. The complete derivation leads to the expression [1, 73]:

$$Z = \frac{3}{2}\left(\frac{f_v \gamma_b}{r}\right) \tag{1.11}$$

In the case of coherent particles, the Zener drag is larger because the passage of the boundary leaves behind an incoherent precipitate with a higher interphase energy. The Zener drag caused by a coherent particle is therefore larger (~ 2×) than that caused by an incoherent particle of the same size [74]. A similar argument can be applied to the microalloying carbonitrides [75]. Although these precipitates are incoherent, they do possess an orientation relationship with the matrix. The passage of the boundary will destroy this orientation relationship, leading to an increase in the interphase energy. As a result, the Zener drag caused by the microalloying carbonitrides is expected to be larger than that given by equation (1.11). Other improvements of the Zener estimate involved the incorporation of particle shape [76-78], size distribution [77] and the statistics arising from the finite flexibility of the boundary [79]. Hazzeldine [78] reviewed the above effects and concluded that the Zener estimate was within a factor of 4 from the new estimates. Finally, it is important to keep in mind that the Zener equation is derived for a planar boundary. For this condition to apply, the grain size should be much larger than the interparticle spacing. If this is not the case, the Zener expression needs to be modified as discussed by [38].

In the microalloying literature, the effect of Zener pinning on recrystallization is discussed qualitatively in terms of the *recrystallization-precipitation-time-temperature* (RPTT) diagram [15, 40, 80, 81]. A typical RPTT diagram is shown in figure (1.2). The diagram is interpreted in terms of the competition between precipitation and recrystallization. At high temperatures, recrystallization is the faster process and is expected to proceed to completion with little or no delay due to precipitation. As the temperature

decreases, precipitation becomes the faster process and recrystallization is slowed down significantly. The progress of recrystallization in the presence of precipitation is then described by the blue curve in figure (1.2).

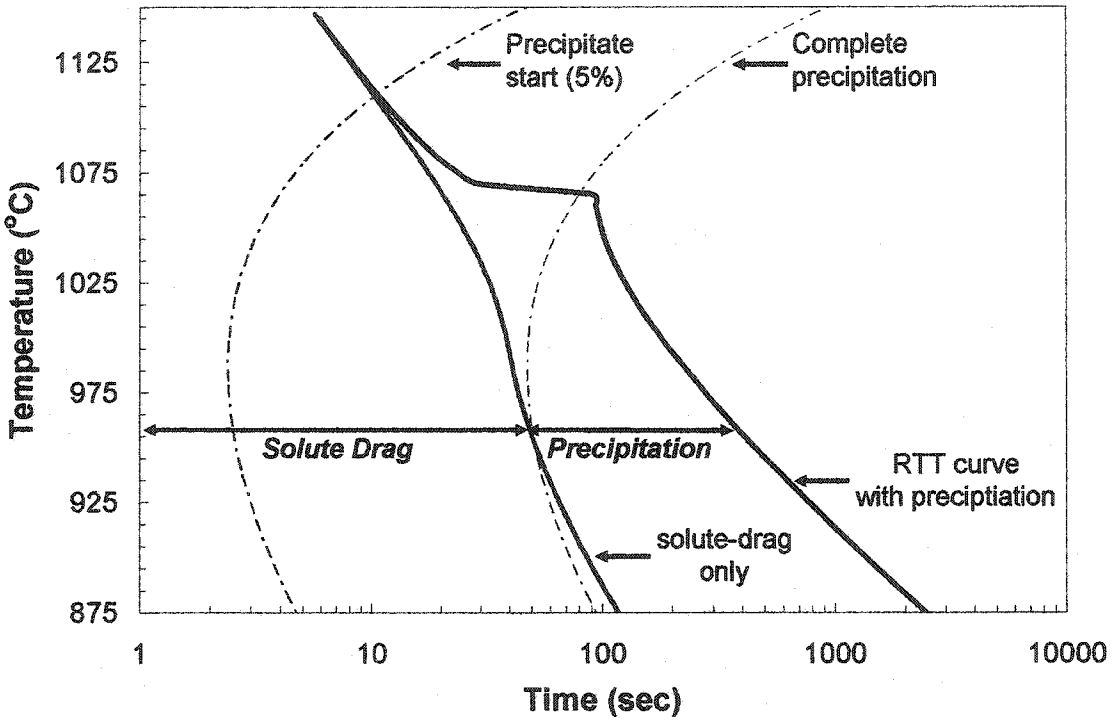

Figure (1.2): *Schematic recrystallization-precipitation-time-temperature (RPTT) diagram for a typical microalloyed steel. The recrystallization curves shown are for X = 50%*

Semi-quantitative models have been developed around the concept of the RPTT diagram [9, 82]. For example, Dutta and Sellars [9] introduced the concept of the *recrystallization-stop-temperature*, RST. This is defined as the (highest) temperature for which, no recrystallization can take place between passes. The RST was estimated by equating the curve for 5% recrystallization with that for 5% precipitation. In this and similar models, the processes of precipitation and recrystallization are coupled *after the fact*. In

addition, the treatment does not take into account the effect of particle size and volume fraction (i.e. Zener drag). A more appropriate treatment would involve replacing the driving force in equation (1.5) with $(G_r - Z)$ [38, 47]. Quantitative treatments of this type have been used, successfully, to model grain-growth [38, 83]. In the case of recrystallization, a number of authors [38, 40] pointed out that the Zener term is insufficient to halt recrystallization under most practical conditions. This lead Hansen et al [40] to develop a modified expression for the pinning force. In the new treatment, precipitation is assumed to take place, exclusively, on the sub-boundaries. As a result, enhanced pinning is expected in the vicinity of the recrystallization nuclei and boundaries. This enhanced pinning approach is frequently used in the literature [84-87]. Still a number of important questions remain. In particular, the deformed structure needs to be examined as a function of temperature to determine the conditions under which well-developed subgrains are formed. Additionally, the applicability of a Zener-type approach to the pinning of sub-boundaries needs to be examined carefully [88].

1.5 Interaction between Precipitation and Recovery:

The interaction between precipitation and recovery has been largely overlooked in the microalloying literature. Most of the available information came about as a byproduct of works on the effect of precipitation on recrystallization [15, 55]. The above investigations

indicate that the recovered-fraction is reduced by a factor of 3 - 10 in the presence of precipitation. Unfortunately, no effort has been made to investigate or to model the above observations in detail. For this reason, the following discussion is largely based on observations in non-ferrous systems with fine particle dispersions.

Precipitation and recovery interact for two reasons: Firstly, the microalloyed carbonitrides are nucleated heterogeneously on dislocations [14, 20] and secondly, the precipitate particles are able to pin the dislocations [38]. The first of these interactions is easily modelled in terms of the number of available nucleation sites. The progress of recovery, is expected to lower the precipitate number-density by decreasing the number of available nucleation sites. Additional effects could result from a change in the effective diffusion coefficient as a result of a change in the contribution from pipe diffusion. Of much more importance is the pinning effect that particles exert on dislocations. This effect has been discussed extensively in terms of its effect on the flow stress [89, 90]. In contrast, there is little discussion of the effect of pinning on the kinetics of recovery. We will devote the rest of this section to the effect of pinning on the kinetics of recovery. Following Humphreys and Hatherly [38], the discussion is divided into two sections: In section (1.5.1) we examine the case in which the dislocations are randomly distributed. Well-developed sub-structures are examined in section (1.5.2).

1.5.1 Pinning of a Random Array of Dislocations

Significant pinning of a random array of dislocations can only take place when the particle spacing is smaller than or equal to the 'mesh' size of the dislocation network [38]. For most alloy systems this condition is not expected under practical industrial conditions. In microalloyed steels, particle number densities of over 10^{21} /m^3 are possible. This leads to a unique situation in which the precipitate dispersion could significantly retard the recovery of the dislocation network. Humphreys and Hatherly [38] treated the problem in terms of a force balance. The driving force for the recovery of a 3-D dislocation network of mesh size R_d is approximately:

$$G_{rec} = \frac{\mu b^2}{R_d} \tag{1.12}$$

A dispersion with a particle spacing of λ, will exert an opposing force of the order of:

$$G_{dp} = \frac{c_7 \mu b^2}{\lambda} \tag{1.13}$$

The potential for very strong pinning is demonstrated by a simple order of magnitude calculation: Using a typical dislocation density of 5×10^{14} m^{-2} and assuming a cubic network of dislocations, the mesh size is found to be ~ 75 nm. This is compared to an average nearest-neighbor distance of ~ 45 nm in a random dispersion having a number-density of 10^{22} m^{-3}.

In principle, a quantitative recovery model could be based on equations (1.12) and (1.13). Such treatment would need to incorporate a precipitation model that describes the evolution of the precipitate number density. Qualitatively, the pinning force is expected to peak at short times before decreasing gradually as a result of coarsening. In the coarsening

regime, the rate of recovery will be largely controlled by the rate of particle coarsening [38] as described in section (1.5.2). Finally, it should be pointed out that equation (1.13) is based on the Orowan process. There is reasonable evidence to suggest that particle-cutting is the operating mechanism for carbides less than 4 nm in diameter [23, 91-93]. Any pinning equation based on the cutting-mechanism would include a dependence on particle size [90]. As a result, the evolution of particle-size is also necessary for any quantitative treatment of recovery in two-phase alloys.

1.5.2 Pinning of Sub-boundaries

The case of sub-boundary pinning becomes increasingly relevant as the deformation temperature increases. For the most part, the literature treats sub-boundary pinning as a special case of grain-boundary (Zener) pinning [38]. The applicability of the Zener approach to the case of low angle grain-boundaries and sub-boundaries is questionable [88]. These boundaries are made up of individual dislocations and move through the coordinated motion of these dislocations. As a result, the interaction between fine-particle dispersions and sub-boundaries is very complex. In the case of microalloyed steels, there is an additional complication arising from the fact that precipitation will occur preferentially on the sub-boundaries. If this is the case, the classical Zener equation will need to be modified to take into account the non-uniform precipitate distribution [38, 40]. In spite of the above difficulties, the Zener approach appears justified in the absence of alternative models and due to the lack of reliable data on sub-boundary pinning and sub-grain growth [38].

Humphreys and Hatherly [38] used a simple force balance to describe the net driving force for the subgrain growth:

$$P_{net} = \frac{c_8 \gamma_b}{R} - \frac{3 f_v \gamma_b}{2r} \qquad (1.14)$$

The first term is the driving force for subgrain growth and the second is the Zener drag. This treatment indicates that subgrain growth (and hence recovery) would stagnate at a critical subgrain size of $R_c = 4rc_8/(3f_v)$. Additional recovery is possible only as a result of particle coarsening. In other words, the rate of recovery will be controlled by the rate of change of particle size. This condition is, sometimes, referred to as extended recovery. It has been observed in a number of materials including carbon-steels and aluminum alloys [38].

1.6 Interaction between Recovery and Recrystallization:

It is generally accepted that the nucleation of recrystallization involves recovery in the form of subgrain growth or subgrain coalescence [38]. Many of the details of this process are still poorly understood. Experimental observations indicate that recrystallization is, frequently, close to being site-saturated [94, 95]. This is particularly the case when large deformations are used and when the grain size is not excessively large. Under these circumstances, useful models can be developed without considering the nucleation step in detail.

For the remainder of this section, we will treat recovery and recrystallization as competing mechanisms for lowering the stored dislocation-energy. In general, large deformations, low temperatures and high values of the stacking-fault-energy will all favor recovery over recrytallization [38, 96]. The competition between the two processes is readily modeled within the JMAK framework by using a time-dependent growth rate [38, 47, 96]:

$$v = MG_r \approx \tfrac{1}{2} M\mu b^2 \rho(t) \qquad (1.15)$$

Recovery is expected to reduce the dislocation density and to slow down the progress of recrystallization. Furu et al [47] demonstrated this approach for the case in which v varies as $(1+t/\tau)^{-b}$. The main result is a decrease in the rate of recrystallization which can be described in terms of a decreasing JMAK exponent. For the case of site-saturation, the JMAK exponent approached a value of $3(1-b)$. Other authors [47, 96] described similar treatments with similar results.

1.7 Critical Assessment of the Literature:

The microstructural evolution of a hot-worked microalloyed steel is controlled by the interaction between three fundamental processes, namely, precipitation, recrystallization and recovery. Our knowledge of these processes and of their interactions varies widely. On the one hand, the areas of precipitation and particle-boundary interaction have received a great deal of attention. The process of recovery, on the other hand, appears to have been

completely overlooked. On the whole, the microalloying literature is still very qualitative. Quantitative physically-based models are lacking, particularly, in the area of process-interactions. In the few cases where quantitative models are available, it has not been possible to experimentally verify some of the models' assumptions. For example, in the precipitation model of Dutta et al [20], nucleation is assumed to take place, exclusively, on dislocation nodes. The particle number-density is assumed equal to the number of dislocation nodes. These hypotheses cannot be directly verified because of the decomposition of austenite on cooling. For the same reason, it is difficult to obtain reliable information on the deformation sub-structure and the precipitate distribution. With this in mind, two areas of research have been identified as being very important for future progress. The first area is the physically-based modelling of the *interactions* between precipitation, recrystallization and recovery. The second area involves the direct observation of the microstructural evolution on a model austenitic alloy. Both areas are discussed in more detail below.

1.7.1 Physically-based Modelling:

The complex behaviour of industrial alloys can only be described in terms of a model that incorporates all of the relevant elementary processes as well as their interactions. In chapter (2) an effort is made to develop such a model. The proposed model incorporates the processes of precipitation, recrystallization and recovery as well as their interactions. The main objective of the modelling is to explore the various process interactions and their

consequences on the microstructural evolution. This approach allowed us to clarify a number of issues that caused a lot of controversy in the literature. For instance, a number of authors indicated that the Zener drag is insufficient to halt recrystallization (section 1.4). Our integrated model suggests that recovery can lower the driving force of recrystallization to a point where Zener pinning becomes effective. This interpretation is only possible when all three processes are included.

1.7.2 Experimental Work on Model Alloys:

Direct observation of the austenitic microstructure can provide valuable information on the deformed structure, precipitation, recovery and recrystallization. This information is needed to ensure that our understanding of the underlying science is accurate. In recent years, a number of groups have identified the need for model alloy systems. Researchers at the University of Sheffield developed a model alloy system based on the composition Fe-30%Ni [86, 87]. In chapter (3) we will examine the problem of choosing the most useful model alloy. In chapter (4), the results of experiments on the model alloy are used to verify our physically-based model.

Chapter 2:

Physically-Based Model of the Microstructural Evolution of Hot-worked Austenite.

The literature review revealed the need for a physically-based model, that incorporates the processes of precipitation, recrystallization and recovery. Many of the elementary blocks of such a model have already been reviewed in chapter (1). The purpose of this chapter is to integrate the various blocks into a single quantitative model. Most of the emphasis is placed on the way in which the various processes interact.

In the first part of this chapter, quantitative models are developed to describe the individual processes of recrystallization, recovery and precipitation. In section (2.1), a simple recrystallization model is presented. This module takes into account the effects of recovery and Zener pressure on the driving force for recrystallization. In addition, the mobility term is allowed to change in response to changes in the amount of solute in the matrix. Recovery is modelled in section (2.2) with special emphasis on the effect of precipitation. The evolution of precipitation is the subject of section (2.3). The proposed

precipitation model takes into account the processes of nucleation, growth and coarsening and allows for a smooth transition between them. The interactions between the various processes are summarized in section (2.4), which also includes a discussion of the simplifications made in the model.

The rest of the chapter is devoted to the assessment and discussion of the model. In section (2.5), the predictions of the model are compared with existing experimental data, over a wide range of alloy compositions and temperatures. The insights gained from the model are discussed in section (2.6). Finally, the limitations of the model are discussed in section (2.7).

2.1 Recrystallization Module:

The simplest treatment of recrystallization is that involving the JMAK model under the assumption of site-saturation. This simple approach is very attractive, given the lack of information on the nucleation of recrystallization in microalloyed steels. Thus, the recrystallized fraction is given by:

$$X = 1 - \exp\left(- N_{rex} \left(\int_0^t M(t)G(t)dt \right)^3 \right) \qquad (2.1)$$

Three quantities enter into equation (2.1): a) the net driving force for recrystallization, *G(t)*, b) the mobility of grain boundaries *M(t)* and c) the number of recrystallization nuclei per

unit volume, N_{rex}. These quantities are discussed in sections (2.1.1) - (2.1.3). In section (2.1.4), the above equation is modified to include a probability term that reflects the ease with which the nuclei may develop into recrystallized grains.

2.1.1 The Driving Force for Recrystallization, *G(t)*

The driving force for recrystallization is the stored energy of deformation, often expressed as $\frac{1}{2}\rho(t)\mu b^2$ [38]. Following [38, 47], the effect of concurrent precipitation on the driving force for recrystallization is expressed as a stored-energy modified by a retarding Zener-drag term. Under conditions of an evolving precipitate distribution and in the presence of recovery, the net driving force is given by:

$$G(t) = \frac{1}{2}\rho(t)\mu b^2 - \frac{3\gamma_{gb} f_v(t)}{r(t)} \qquad (2.2)$$

In this equation, γ_{gb}, $f_v(t)$ and $r(t)$ denote the austenite grain-boundary energy, precipitate volume-fraction and the mean precipitate radius, respectively. The Zener-drag term in equation (2.2) is twice the classical Zener pressure. This larger value is used for two reasons: Firstly, the strong orientation dependence of the interphase energy is expected to make it more difficult for the boundary to detach from the precipitates (section 1.4). Secondly, by utilizing this upper-limit, we hope to demonstrate more convincingly, that in many cases, the Zener force is of insufficient magnitude to halt the *progress* of recrystallization in the absence of recovery processes.

2.1.2 Grain Boundary Mobility, *M(t)*:

The effect of solute elements on the mobility of grain boundaries has been treated by Cahn [52]. In general, the drag effect reduces the mobility in a non-linear manner depending on the velocity. A simplified mobility which is proportional to the solute content is used in this treatment. For low driving forces, Cahn's solution simplifies to:

$$M(t) = \left(\frac{1}{M_i} + \alpha C_{Nb} \right)^{-1}, \quad \alpha = \frac{\delta N_v (k_b T)^2}{E_b D} \left(\sinh\left(\frac{E_b}{k_b T} \right) - \frac{E_b}{k_b T} \right) \tag{2.3}$$

where δ is the width of the segregation profile, N_v is the number of atoms per unit volume, E_b is the binding energy of solute atoms to grain-boundaries and D is the cross-boundary diffusion coefficient. While no estimates of the cross-boundary coefficient are available in the literature, reasonable values can be inferred from the width of segregation profile. Maruyama et al [97] estimated the segregation profile of Nb in ferrite to be about 1-2 nm on each side of the boundary. Wider profiles are expected in austenite and as a result the value of the cross-boundary coefficient is expected to be similar to that of the bulk diffusion coefficient. In this investigation a value of ten-times the bulk-diffusion coefficient appeared to result in a reasonable concentration dependence of mobility.

Estimation of the intrinsic mobility (M_i) of a pure metal is a difficult problem. The classical treatment of Turnbull [98] is clearly an upper limit as it neglects all possible attachment kinetics. A rough order of magnitude estimate of the real mobility in a pure metal is one-half the Turnbull estimate:

$$M_i = \frac{\delta D_{gb} V_m}{2b^2 R_g T} \tag{2.4}$$

In this equation, D_{gb} is the grain-boundary self-diffusion coefficient and V_m is the molar volume of austenite.

2.1.3 Number of Nucleation Sites, N_{rex}:

The nucleation of recrystallization is assumed to occur at the onset of annealing, at a number of sites proportional to the grain-boundary area per unit volume, S_v. If A_c is the area occupied on the grain-boundary by each nucleus, the number of nuclei per unit volume can be expressed as:

$$N_{rex} = \frac{kS_v}{A_c} \tag{2.5}$$

In our model, S_v is estimated using the analytical equation of Yoshie et al [99]. The area of the critical nucleus is estimated using the Bailey-Hirsch theory [100] for nucleation. The ratio of S_v/A_c represents the maximum number of possible nuclei. The adjustable constant, k, is used to capture the fact that only some of the potential nuclei are formed.

2.1.4 Probability of Developing:

Equation (2.1) assumes that the nuclei are formed at $t = 0$ and that they start to grow immediately. However, in the presence of precipitation the evolution of the substructure is hampered by the presence of strong particle-pinning. This effect is well documented in the

literature [15, 55, 57, 101, 102]. For instance, Yamamoto et al [15] reported that fine carbonitrides are able to delay the onset of recrystallization by an order of magnitude. In order to capture the effect of pinning, we introduced the *probability of development*, Ψ, which represents the ease with which a nucleus is able to develop and grow. The recrystallized fraction is then given by:

$$X = 1 - \exp\left(- N_{rex} \left(\int \Psi(t) M(t) G(t) dt \right)^3 \right) \tag{2.6}$$

We defined Ψ in terms of the length-scale, l, over which recovery takes place, hence:

$$\Psi = \left(\frac{l}{D_c} \right) \tag{2.7}$$

where D_c is the diameter of the critical nucleus. In the absence of precipitation, l is equal to D_c and the probability of development is 1. In the event of precipitation on dislocations, the value of l is dramatically reduced to ρ/n, where n is the number of precipitate particles. The introduction of Ψ allows us to capture the effect of sub-boundary pinning on the onset of recrystallization. Typically, the value of l would drop from ~5μm, prior to precipitation, to ~100 nm at peak hardness. During coarsening, the value of l starts to increase again making recrystallization more viable once again.

2.2 Recovery Module:

It is assumed that the flow stress of the precipitate-free austenite, σ, is related to the total dislocation density, ρ, and the yield stress of the precipitate-free fully-recrystallized

state, σ_y, by a forest-type hardening relation [103]:

$$\sigma = \sigma_y + M\alpha_T \mu b\sqrt{\rho} \tag{2.8}$$

where M is the Taylor factor (~3.1 for FCC) and α_T is a constant of the order of 0.15. Following Verdier et al [66], the rate of change of the internal stress due to the dislocations is expressed as:

$$\frac{d(\sigma-\sigma_y)}{dt} = -\frac{64(\sigma-\sigma_y)^2 v_d}{9M^3\alpha_T^2 E}\exp\left(\frac{-U_a}{k_bT}\right)\sinh\left(\frac{(\sigma-\sigma_y)V_a}{k_bT}\right) \tag{2.9}$$

where U_a and V_a are the activation energy and activation volume of the recovery process. The temperature and composition dependence of U_a and V_a were discussed in section (1.3). In order to minimize the number of unknown parameters, both quantities are assumed independent of temperature and composition. This assumption is revisited in chapter (4).

The effect of precipitation on recovery was, briefly, reviewed in section (1.5.1). In this section, a simple model is developed to take account of the effect of precipitation on recovery. Starting with equations (1.12) and (1.13), the net driving force for the recovery of a 3-D dislocation network can be expressed as:

$$G_R^{Net} = \frac{\mu b^2}{R_d} - \frac{c\mu b^2}{\lambda} \tag{2.10}$$

The ratio of the net-driving force (Eq. 2.10) to the total driving force ($\mu b^2/R_d$) may be thought of as the unpinned fraction of the dislocation network :

$$\Im = \frac{G_R^{Net}}{G_{total}} = 1 - \frac{cR_d}{\lambda} \tag{2.11}$$

For a cubic array of dislocations, the mesh size (R_d) is equal to $(3/\rho)^{½}$. In the case of precipitation on dislocations, the average pinning distance, λ, is approximated as ρ/n, where

n is the number of particles. As a result, equation (2.10) may be rewritten as:

$$\Im = 1 - \left(c\sqrt{\frac{3}{\rho}}\right) \Big/ \left(\frac{\rho}{n}\right) = 1 - \frac{c\sqrt{3}n}{\rho^{1.5}} \approx 1 - \frac{n}{n_c} \tag{2.12}$$

where n_c is the number of dislocation nodes $\propto \rho^{1.5}$. The effect of precipitation on recovery, is then modelled by assuming that a certain fraction of the network (R_d / λ or n/n_c) is not available for recovery. Complete pinning is expected when the number of precipitate particles is equal to the number of dislocation nodes. Therefore, in the presence of precipitation, the rate of recovery is given by:

$$\frac{d(\sigma - \sigma_y)}{dt} = -\frac{64(\sigma - \sigma_y)^2 v_d}{9M^3 \alpha_T^2 E} \exp\left(\frac{-U_a}{k_b T}\right) \sinh\left(\frac{(\sigma - \sigma_y)V_a}{k_b T}\right)\left(1 - \frac{n(t)}{n_c(t)}\right) \qquad n < n_c \tag{2.13a}$$

$$\frac{d(\sigma - \sigma_y)}{dt} = 0 \qquad n > n_c \tag{2.13b}$$

The predictions of equation (2.13) are shown in figure (2.1a). This figure is constructed for the case of a Nb-microalloyed steel that exhibits concurrent recovery and precipitation. Initially, recovery proceeds according to equation (2.9) with little or no interference due to precipitation. However, as the number of precipitate particles increases, the rate of recovery is reduced as described by equation (2.13a). When the number of particles becomes greater than or equal to the total number of dislocation nodes, $n \geq n_c$, recovery is completely halted. This continues to be the case, until the onset of particle coarsening. In the coarsening regime, recovery proceeds at a rate controlled by the rate of particle coarsening. Recovery under these conditions is, sometimes, referred to as *extended*

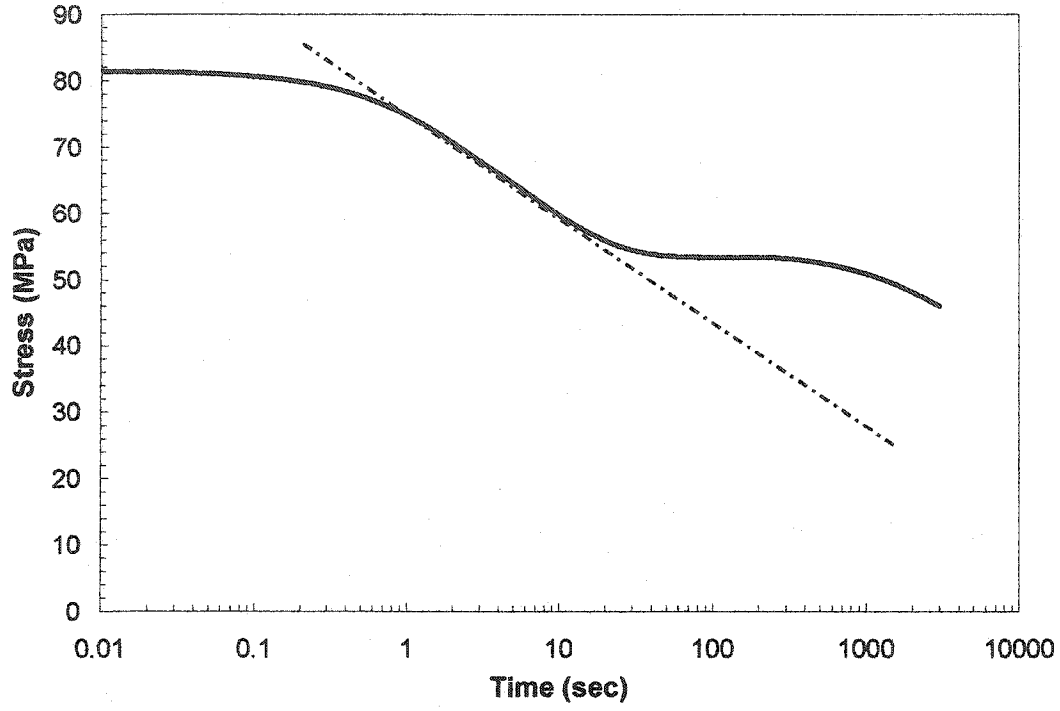

Figure (2.1a): *The effect of precipitation on recovery according to Eq. (2.13). The data is for steel N3 at 950°C (see section 2.6.3 for details).*

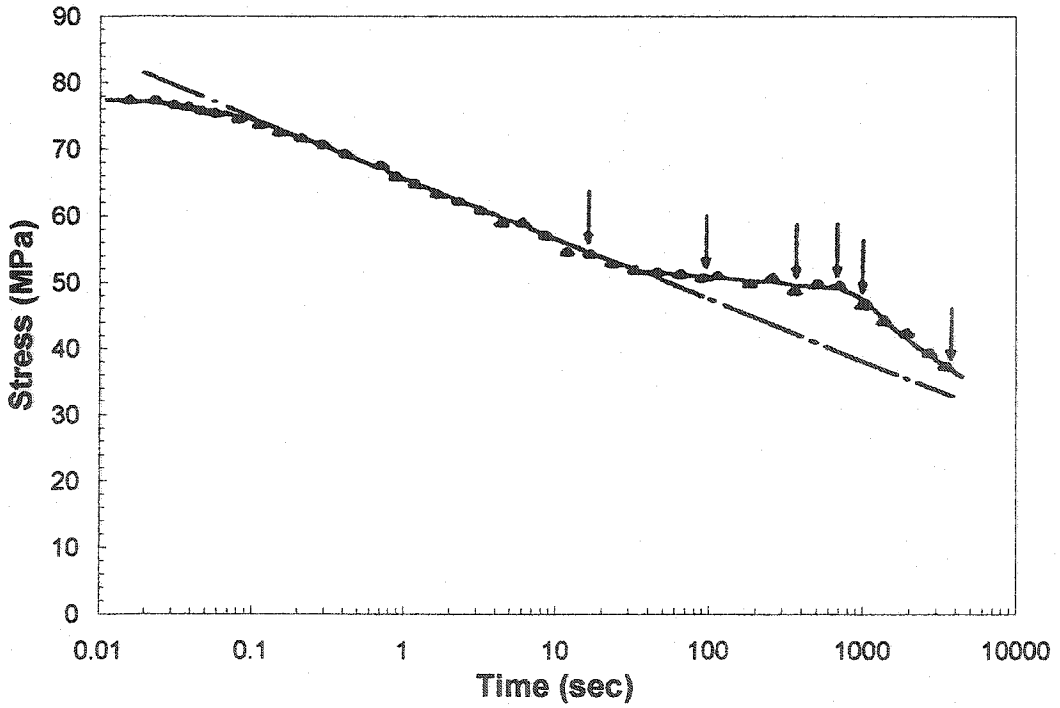

Figure (2.1b): *Experimental stress-relaxation curve measured by Liu and Jonas [62] at 900°C in a steel containing 0.25%Ti and 0.05%C.*

recovery (section 1.5). Figure (2.1b) is the experimental stress-relaxation data of Liu and Jonas [62] for a Ti-microalloyed steel that also exhibits concurrent recovery and precipitation. The model predictions in (2.1a) reproduce the general form of the experimental stress-relaxation curve. This is interpreted as a validation of the general form of equation (2.13).

Before proceeding further, it is necessary to comment on the effect of particle-size on the interaction between precipitates and dislocations. The pinning term in equation (2.10) is based on the Orowan process which is independent of particle-size. The Orowan assumption, of strong non-shearable particles, breaks down when the particle-size is very small [92]. Under these circumstances, a size-dependent pinning term is necessary [90]. In order to capture this effect, we multiplied the number of particles in Eq. (2.13a) by a size-factor that varies linearly from 0 to 1 as the particle radius changes from 0 to 1 nm. The size factor is constant and equal to 1 for all particles that are larger than 1nm (radius). This approach is not rigorous, but it allows us to maintain the simplicity of the model.

2.3 Precipitation Module:

The present treatment is largely based on the precipitation model of Deschamps and Brechet [104]. Precipitation is assumed to occur in two stages: The first stage treats

nucleation and growth as concurrent processes and the second deals with concurrent growth and coarsening. The average precipitate radius and the number density of precipitates are monitored. This approach has, recently, been applied to the precipitation of NbX in austenite [20] and appears to result in reasonable agreement with the experimental data.

2.3.1 Nucleation and Growth:

Nucleation is assumed to occur exclusively on dislocations. Dutta and Sellars [9] demonstrated that this is indeed a reasonable assumption. The steady-state nucleation rate is given by:

$$\frac{dn}{dt} = \left(1 - \frac{n}{n_{total}}\right) Z\beta^* n_{total} \exp\left(\frac{-\Delta G_n}{k_b T}\right) \qquad (2.14)$$

In this equation, Z is the Zeldovich non-equilibrium factor, β^* is the rate at which atoms are added to the critical nucleus, n_{total} is the number of nucleation sites and ΔG_n is the activation barrier for the nucleation process. An Avrami-type term ($1\text{-}n/n_{total}$) has been added to the classical nucleation equation to account for the progressive consumption of available nucleation sites [19]. Following Russell [105], the product $Z\beta^*$ was approximated as $D_{pipe} C_{Nb} / a^2$, where D_{pipe} is the solute diffusion coefficient along the dislocations lines and a is approximately equal to the lattice constant. The density of nucleation sites, n_{total}, was approximated as $F\rho/b$, where F is an adjustable parameter smaller than unity.

Estimation of the critical energy for nucleation on dislocations, ΔG_n, was discussed

by Cahn [106] and Gomez and Pound [107]. In general, it is necessary to solve, simultaneously, for the shape and size of the critical nucleus. The full analysis is complex and is not justified in the present case. Instead, the critical nucleus is (incorrectly) assumed to be spherical and the activation energy is obtained from the following energy balance [20, 108]:

$$\Delta G = V\Delta G_V + A\gamma - \frac{\mu b^2 r \ln(r/b)}{2\pi(1-\nu)} - \mu b^2 r/5 \qquad (2.15)$$

In this equation, V and A are the volume and area of the nucleus, ΔG_V is the free energy change attending nucleation, γ is the interphase energy and ν is Poisson's ratio. The chemical driving force, ΔG_V, and the composition of the carbonitride, were estimated using the method described by Gladman [1] and the solubility constants of Narita [109].

During the nucleation-and-growth stage, the evolution of the average particle radius is given by [20, 102]:

$$\frac{dr}{dt} = \frac{D_{eff}}{r}\frac{C_{Nb} - C^r_{Nb}}{C^P_{Nb} - C^{Eq}_{Nb}} + \frac{1}{n}\frac{dn}{dt}\left(\alpha_n r_n - r\right) \qquad (2.16)$$

The first term in this equation is the standard (parabolic) growth law for a spherical particle. We used C^r_{Nb} to denote the concentration of Nb in equilibrium with a precipitate particle of radius r. The second term in equation (2.16) is the rate of change of the average particle radius as a result of the nucleation of n particles of size $\alpha_n r_n$. The constant, α_n, is taken to be 1.05 and it accounts for the fact that the nucleated particle will grow, only if its radius is larger than the critical radius. Finally, it should be pointed out that the effective diffusion coefficient is used in equation (2.16). This quantity is a weighted average of the bulk and

pipe diffusion coefficients of Nb in austenite [20]:

$$D_{eff} = D_{pipe}\pi R_{core}^2 \rho + D_{bulk}(1 - \pi R_{core}^2 \rho) \quad (2.17)$$

where, R_{core} is the radius of the dislocation core, taken to be equal to the Burgers vector, b.

2.3.2 Growth and Coarsening

The transition from nucleation-and-growth to growth-and-coarsening, takes place when more particles are disappearing, as a result of coarsening, than forming as a result of nucleation. Under conditions of simultaneous growth and coarsening, the average rate of change of particle diameter is given by [104]:

$$\frac{dr}{dt} = (1 - f_{coarse})\left.\frac{dr}{dt}\right|_{growth} + f_{coarse}\left.\frac{dr}{dt}\right|_{coarsening} \quad (2.18a)$$

$$f_{coarse} = 1 - erf\left(4\left(\frac{r}{r_n} - 1\right)\right) \quad (2.18b)$$

In this equation, $dr/dt|_{growth}$ denotes the rate of change of particle size under pure growth conditions. Similarly, $dr/dt|_{coarsening}$ refers to the rate of change under pure coarsening. The two contributions are weighted by the coarsening function, f_{coarse}. This function varies from 0 under growth conditions ($r >> r_n$) to 1 under coarsening conditions ($r = r_n$). Deschamps and Brechet [104] showed that the exact form of the coarsening function is not critical to the overall kinetics.

In the case of pure growth, the rate of change of particle size ($dr/dt|_{growth}$) is given by the standard parabolic growth law (Eq. 2.16). During pure coarsening, the Lifshitz-Slyozov-

Wagner (LSW) approach leads to [110-112]:

$$\left.\frac{dr_i}{dt}\right|_{coarsening} = \frac{D_{eff}}{r_i}\frac{C^{r}_{Nb} - C^{ri}_{Nb}}{C^{P}_{Nb} - C^{Eq}_{Nb}} \qquad (2.19)$$

In keeping with equation (2.16), r is used to denote the *average* precipitate radius. The new variable, r_i, refers to the radius of a specific/individual particle. Precipitates whose radii (r_i) are greater than the average radius (r) will grow and those whose radii are smaller than r, will shrink. Strictly speaking, the rate of change of the *average* radius is obtained by averaging equation (2.19) over the particle-size distribution. An approximate solution [112] is obtained by substituting the value of r which makes the greatest contribution to the average. Following, Deschamps and Brechet [104], r_i is set equal to (27/23) r and the rate of change of particle size is given by[a]:

$$\left.\frac{dr}{dt}\right|_{coarsening} = \frac{D_{eff}}{r_i}\frac{C^{r}_{Nb} - C^{27/23r}_{Nb}}{C^{P}_{Nb} - C^{Eq}_{Nb}} \qquad (2.20)$$

An equation similar to (2.18) is used to calculate the rate of change of the number of nuclei. Under pure growth conditions, the number of nuclei is constant and $dN/dt|_{growth}=0$. In the case of pure coarsening, the rate of change of the number of nuclei is obtained by implicit differentiation of equation (2.21) with respect to time [104]:

$$C\left(1-\frac{4}{3}\pi n R^3\right) = C_o - \frac{4}{3}\pi n R^3 \qquad (2.21)$$

The resulting expression is a function of the rate of change of the average radius (Eq. 2.18) and the rate of change of concentration. Evaluation of the latter quantity is discussed in Appendix (A3), which also describes the manner in which C^{r}_{Nb} is evaluated.

---

[a] Implicit in the treatment of [102] is the assumption of a Gaussian distribution with a standard deviation of r/3. Other treatments utilize r_i/r of 1.5 to 2 [110]. The differences are not very large.

2.4 Summary of the Model:

The main features of our model are shown in figure (2.2). Those terms which provide the coupling between recovery, recrystallization and precipitation are highlighted to emphasize the inter-dependency of the above processes. A number of simplifications have been made in this model. These are discussed in section (2.4.1). This is followed by a discussion of the physical quantities that enter into the model (2.4.2).

2.4.1 Simplifying Assumptions:

Several simplifying assumptions have been made concerning the interactions between recovery, recrystallization and precipitation. These assumptions are, briefly, discussed below:

(a) It is assumed that the progress of recrystallization does not influence the precipitation process. This has two practical implications. Firstly, the reduction in the number of potential precipitate nucleation sites due to recrystallization is not accounted for. Secondly, the model does not capture any differences that may exist between the evolution of particle-size and number-density in the recrystallized and unrecrystallized regions. In other words, we assume that precipitation occurs mainly on dislocations in the unrecrystallized regions and that it is not perturbed by the passage of the recrystallization front.

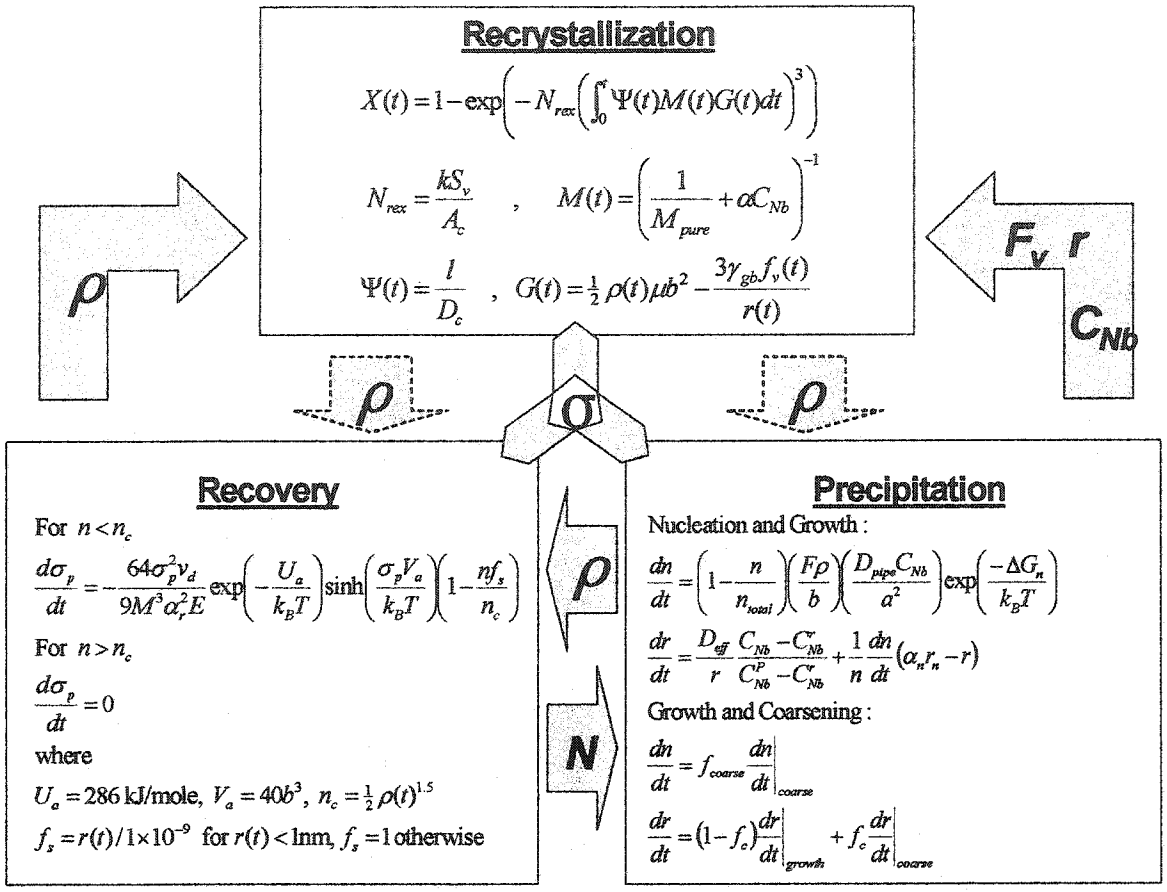

Figure (2.2): *Summary of the recrystallization, recovery and precipitation modules as well as their interactions. The dotted arrows refer to interactions that were not considered here.*

(b) The nucleation of recrystallization is assumed to be site-saturated. The possible role of recovery in facilitating the nucleation of recrystallization is not considered. This hypothesis is reasonable provided that the applied deformation is large and the initial grain-size is not excessively large.

(c) Constant activation enthalpy, U_a, and volume, V_a, are assumed for recovery. The effect of a varying matrix solute content (arising from the progress of precipitation) on the activation energy and volume of recovery are not considered. This

assumption is made for the sake of simplicity and amounts to the consideration of the activation enthalpy and activation volume as average quantities having a small variation with the solute content. Strong effects are expected for low solute concentrations where the relative variation of V_a becomes important.

(d) The plastic flow stress is described by a single state-variable approach (Eq. 2.8). This assumption is very reasonable at low temperatures where the dislocation density is reasonably uniform. As the temperature increases, well-developed cell-structures and subgrain boundaries are expected to form. Under these conditions, a two state variable approach involving the dislocation density and cell size is probably more appropriate [60].

2.4.2 Parameter Identification:

Most of the physical quantities that enter into the present model are known with a reasonable degree of accuracy. The values of some of the key quantities that enter into the model are summarized in table (2.1). Still, a number of important physical quantities are not very well-known. In what follows, reasonable estimates are discussed for: i) the interphase energy, γ, ii) the activation enthalpy, U_a and volume, V_a, for recovery and iii) the binding energy of Nb to grain-boundaries.

Parameter	Value
Shear modulus, μ	81×10^{9} [0.91-(T(K)-300)/1810] Pa [113]
Bulk diffusion coefficient of Nb in austenite, D_{bulk}	$0.83\times10^{-4}\exp(-266500/RT)$ m^2/s [114]
Pipe diffusion coefficient of Nb in austenite, D_{pipe}	$4\times10^{-4}\exp(-172500/RT)$ m^2/s; average based on [115]

Table (2.1): Values of the physical constants used in the present model.

2.4.2.1 Interphase Energy:

Estimates of the austenite-MX interphase energy vary from ~0.3 to more than 1.5 J/m^2 (section 1.1.3). In addition, the interphase energy is expected to depend on the annealing temperature and alloy composition [32]. In order to arrive at a reasonable expression for the interphase energy, the critical nucleation radii were estimated for a wide range of alloys and temperatures. Reasonable radii in the range of 1 to 2 b were obtained using an interfacial energy of:

$$\gamma = 2.5\times10^{-5}(T_{sol}-T)^{1.5}+0.375 \qquad (2.22)$$

The units of γ and T are, respectively, J/m^2 and K. The composition dependence of the interfacial energy enters through T_{sol} which is the temperature at which the precipitate is completely dissolved. The temperature dependence is of the order of 0.5 mJ/K, in general agreement with the measured temperature dependence of grain-boundary energies in metals [112]. The interphase energy is then ~1.2 J/m^2 at 0 K which is in reasonable agreement with the atomistic modeling of Yang and Enomoto [24]. At hot-working temperatures, γ varies between 0.40 and 0.60 J/m^2. For the sake of consistency, the grain-boundary energy, γ_{gb}, is also expressed as a function of temperature, thus:

also expressed as a function of temperature, thus:

$$\gamma_{gb} = 1.3115 - 0.0005T \qquad (2.23)$$

As before, the boundary energy is expressed in units of J/m^2, while the temperature is expressed in K. This expression, leads to reasonable values of 0.5-0.75 J/m^2 within the hot-working regime.

2.4.2.2 Activation Energy and Volume:

The activation energy for the recovery process is expected to lie between 0.6-1 Q_{diff}, where Q_{diff} is the activation energy for self-diffusion or solute-diffusion, depending on the rate controlling process [60]. The activation energy for the self-diffusion of Fe in austenite is ~286 kJ/mol [68] while that of Nb diffusion in austenite is 266 kJ/mol [114]. Therefore, a composition-independent activation enthalpy, U_a, of 286 kJ/mole was chosen (section 1.3). An average activation volume of $40b^3$ was then obtained by fitting the stress-relaxation data of Arieta and Sellars [64] and Silveira et al [65] to Eq. (2.9) with, $U_a = 286$ kJ/mole, $M = 3.1$ and $v_d = 2 \times 10^{12}$ s^{-1}.

2.4.2.3 Binding Energy:

The binding energy of Nb to austenite grain-boundaries is not very well-known. Several estimates are available for the binding energies of the microalloying elements to ferrite grain boundaries [40, 97, 116-119]. In addition, some atomistic simulations are available for metallic systems with a large atomic misfit [120]. The available data is reviewed in Appendix (A4). Based on this review, a value of 0.25 eV is used.

2.5 Comparison with Experimental Data:

The overwhelming majority of available experimental information is in the form of fractional softening plots, evaluated from double-deformation experiments [see Chapter (1)]. The softening-fraction is a good quantitative indicator of the recrystallized volume-fraction when recrystallization is the only process taking place. If simultaneous recovery is occurring, the unrecrystallized regions soften at the same time as the recrystallized regions grow. The overall hardness evolution is then a convoluted combination of these two phenomena. If in addition precipitation occurs, it would contribute to the hardness evolution by decreasing the solid-solution hardening and increasing the precipitation hardening. In our comparison with experimental data, care has been taken to distinguish between the hardness evolution, obtained from the double-deformation test, and the recrystallization kinetics, obtained from optical metallography.

In section (2.5.1), a "virtual" double-deformation test is developed. The purpose of this module is to allow us to compare our results with the experimental data. In section (2.5.2), the predicted softening-fractions are compared to the experimental values for a wide range of temperatures and compositions. Finally, the curve-fitting parameters that enter into the model are discussed in section (2.5.3).

2.5.1 Softening-fraction Calculation:

Several methods have been developed to evaluate the softening fraction from a double-deformation test. These methods were reviewed, briefly, in Appendix (1.1). The softening fraction is typically evaluated as:

$$S = \frac{\sigma_1 - \sigma_2}{\sigma_1 - \sigma_3} \tag{2.24}$$

where, σ_1, σ_2 and σ_3 are, respectively, the flow stresses of the work-hardened, partially-softened and completely-softened material. The various methods of calculating the softening fraction (S) differ in the details of the evaluation of σ_1, σ_2 and σ_3. The 5% total-strain method [53, 55] is used in this derivation. In this method, σ_1 is the flow-stress evaluated by extrapolating the initial loading curve by a strain of 5%. The stress in the recrystallized material, σ_3, is taken to coincide with the (first) loading stress at a strain of 5%. Finally, σ_2 is the flow stress on reloading (after annealing) evaluated at a strain of 5%.

The empirical flow stress relation of Yoshie et al [121] has been used for evaluation of σ_1, σ_2 and σ_3. The values of σ_1 and σ_3 are evaluated directly from equation (2.25) assuming that no dynamic processes (recrystallization or precipitation) occur during loading:

$$\sigma = 22.7\varepsilon^{0.223}\dot{\varepsilon}^{0.048}D_\gamma^{-0.07}\exp\left(\frac{2880}{T}\right)\exp(166C_{Nb}) \tag{2.25}$$

The calculation of σ_2 is complex as it includes contributions from precipitation-hardening, recrystallization and work-hardening. The recrystallized, σ_{Rex}, and unrecrystallized, $\sigma_{Non\text{-}Rex}$, fractions are added using a simple law of mixtures to obtain:

$$\sigma = \sigma_{Rex}X + \sigma_{Non-rex}(1-X) \tag{2.26}$$

The flow stress of the recrystallized material, σ_{Rex}, contains a contribution from precipitation, σ_{ppt}, and another from the dislocation free matrix, $\sigma_{Rex\text{-}Matrix}$:

$$\sigma_{Rex} = \sqrt{\sigma^2_{Rex-Matrix} + \sigma^2_{ppt}} \quad (2.27)$$

Similarly, the flow stress of the unrecrystallized material, $\sigma_{Non\text{-}Rex}$, contains contributions from precipitation, σ_{ppt}, and work-hardening, $\sigma_{NonRex\text{-}Matrix}$:

$$\sigma_{Non-Rex} = \sqrt{\sigma^2_{NonRex-Matrix} + \sigma^2_{ppt}} \quad (2.28)$$

The evaluation of σ_{ppt}, $\sigma_{Rex\text{-}Matrix}$ and $\sigma_{NonRex\text{-}Matrix}$ is described next.

2.5.1.1 Recrystallized Matrix:

In equation (2.27), $\sigma_{Rex\text{-}Matrix}$ is the contribution to the flow-stress resulting from a fully-recrystallized and precipitate free matrix. This contribution is calculated directly from equation (2.25) using a strain of 5%. Equation (2.25) depends on the Nb concentration. As a result, the change in solution-hardening is taken into account by substituting the instantaneous Nb concentration.

2.5.1.2 Partly-recovered Matrix:

Reloading of the partly-recovered matrix will result in a contribution of $\sigma_{NonRex\text{-}Matrix}$. For simplicity, we assume that during recovery, the stress-relaxation retraces the initial loading curve. At any point in time, a strain ,$\varepsilon(t)$, can be identified which is consistent with the current value of the flow stress, $\sigma(t)$. The value of $\sigma_{NonRex\text{-}Matrix}$ is then calculated from equation (2.25) by extrapolating the above strain by 5%.

2.5.1.3 Precipitation Contribution:

The problem of precipitation-hardening has been examined extensively in the

literature [89, 90]. In this contribution, the treatment of Deschamps and Brechet [104] is used:

$$\sigma_p = \frac{M}{bL}\int_0^{\infty} f(r)F(r)dr \qquad (2.29)$$

In this equation, $f(r)$ is the statistical-distribution function of particle-size, while $F(r)$ is the obstacle strength for a precipitate of size r. In the case of particle shearing, $F(r) = k_s\mu br$, where k_s is an adjustable parameter that depends on the mechanism involved. In the case of particle-bypass, the obstacle strength is, simply, $F(r) = 0.8\mu b^2$ [89]. The transition between the two mechanisms occurs when $r = r_c = 0.8b/k_s$. We therefore have:

$$\sigma_p = \frac{M}{bL}\left(\int_0^{r_c} f(r)k_S\mu br dr + 0.8\mu b^2\int_{r_c}^{\infty} f(r)dr\right) \qquad (2.30)$$

In the Deschamps-Brechet [104] model, the particle-size distribution is essentially a Gaussian. We therefore have two additional parameters that need to be identified: i) the obstacle strength constant, k_s and ii) the standard-deviation of the distribution. In section (2.5.2), k_s is used as an adjustable parameter. The standard-deviation was estimated from the experimental particle-size distributions, where available. In the absence of experimental data, a value of $r/2$ was used.

2.5.2 Assessment of the Model:

The present description of the interaction between precipitation, recrystallization and recovery is assessed by examining the experimental data on four Nb-steels [46, 81, 122]. The compositions of these steels are listed in Table (2.2), below:

Alloy [Ref.]	C	Si	Mn	S	Nb	Al	N
N1 [46]	0.076	0.06	1.3	0.003	0.03	--	0.006
N2 [122]	0.2	0.2	1	0.013	0.007	0.006	0.006
N3 [81]	0.21	0.18	1.1	0.014	0.024	0.007	0.006
N4 [81]	0.21	0.19	1.1	0.015	0.058	0.008	0.006

Table (2.2): *Compositions (wt%) of the alloys used to test the validity of the model.*

In the experimental investigation of Kang et al [46], samples of steel (N1) were solution treated at 1200 °C for 10min to dissolve all of the carbonitrides. A compression strain of 0.30 was applied at the deformation temperature using a hot-rolling simulator. Each sample was held at temperature for a time varying from 0.1 and 10000 sec, before applying a second deformation of the order of 1-8%. The double-compression test provided data on the softening fraction as a function of time. Selected samples were quenched immediately following the annealing treatment. These samples were used to measure the recrystallized fraction and the precipitate size using optical metallography and TEM, respectively. The predicted particle-size evolution at 850°C is shown in figure (2.3a). The softening and recrystallized fractions are shown in figure (2.3b).

In order to arrive at figures (2.3a) and (2.3b), three curve-fitting parameters are used. The first of these is the *nucleation parameter*, F, which appears in equation (2.14) in connection with the calculation of the number of nucleation sites. This parameter was

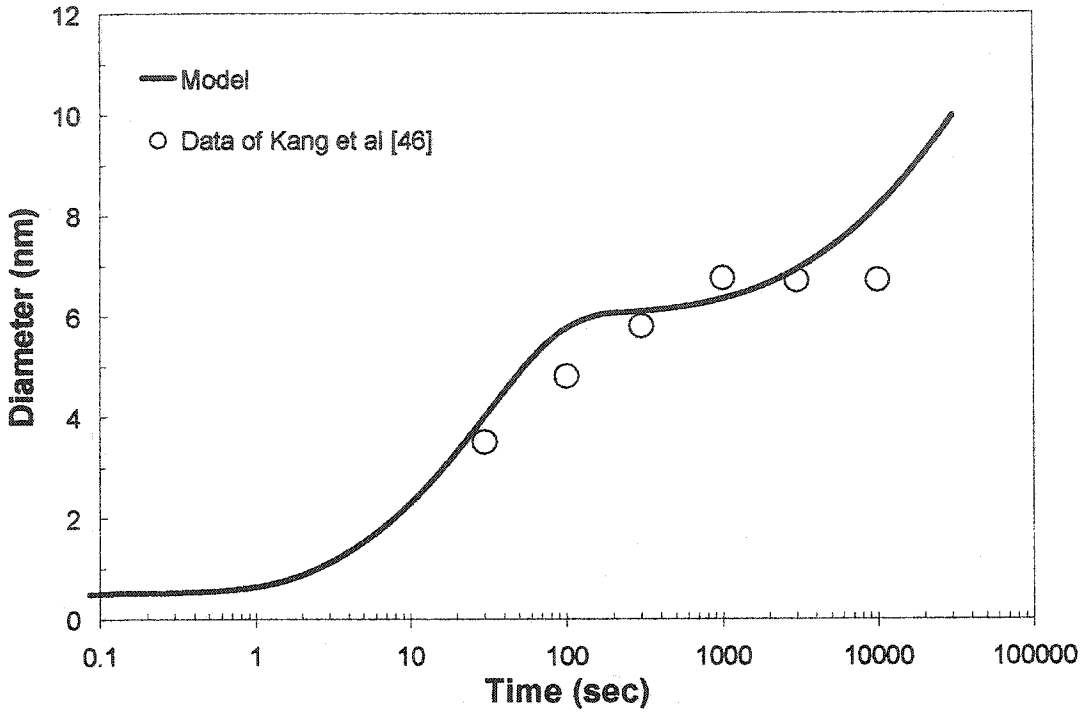

Figure (2.3a): *Comparison of the predicted and measured particle diameter evolution in steel N1 at 850°C.*

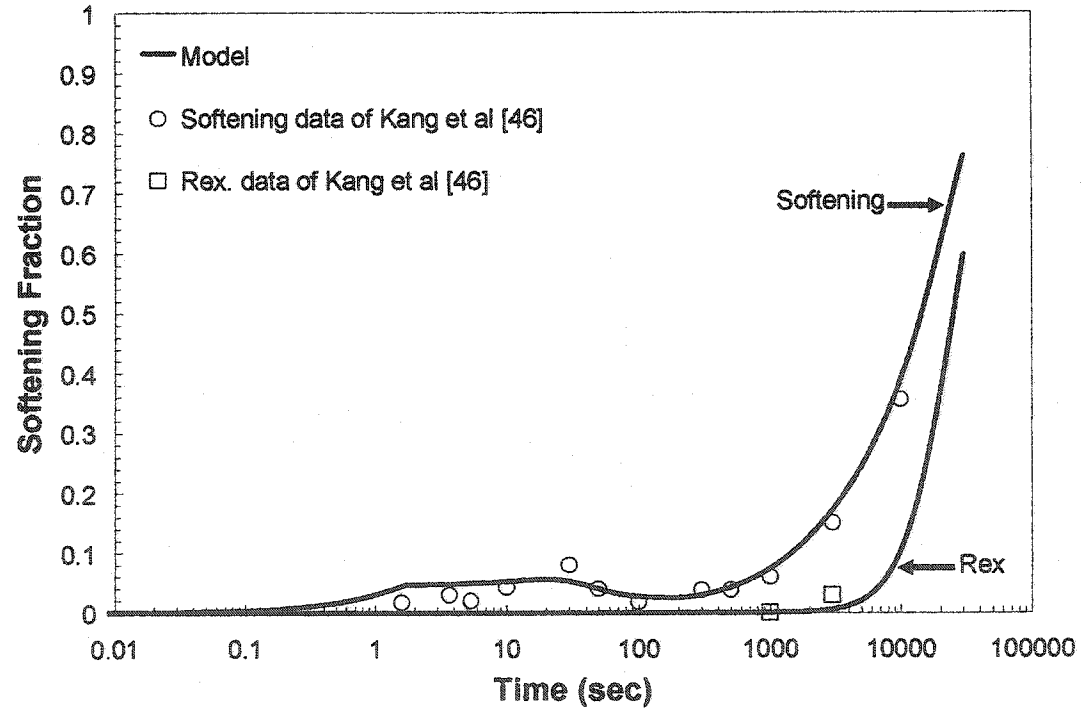

Figure (2.3b): *Comparison of the predicted and measured softening and recrystallized fractions in steel N1 at 850°C.*

estimated from our knowledge of the equilibrium precipitate volume fraction and the precipitate diameter at the onset of coarsening (measured by [46]). At 850°C, F was estimated to be 2.07×10^{-3}. The predicted evolution of particle-diameter in the presence of concurrent recovery and recrystallization is in excellent agreement with the measured particle diameters as shown in figure (2.3a). The second curve-fitting parameter is the constant, k, which enters into the calculation of the number of recrystallization nuclei (Eq. 2.5). The value of this parameter was adjusted to obtain the best fit with the experimental recrystallization data. As shown in figure (2.3b) reasonable agreement is obtained between the modelled and experimental recrystallized fraction. Finally, the obstacle strength, k_s, which appears in equation (2.30) was assumed to be 0.06 for all of the steels in table (2.2). The value of k_s is critical for determining the time at which the transition from particle cutting to particle bypass takes place.

The same procedure was applied to the available experimental data at 900 °C. The predicted time evolution of the particle diameter is again in excellent agreement with the experimental observations of Figure (2.4a). The softening and recrystallization fractions show reasonable agreement with experiment, Figure (2.4b). In this case, the predicted softening fraction is generally larger than the experimentally measured fraction. This indicates that our simple descriptions of recovery and precipitation-hardening do not accurately capture the temperature-dependence of these processes. More will be said on this in section (2.7).

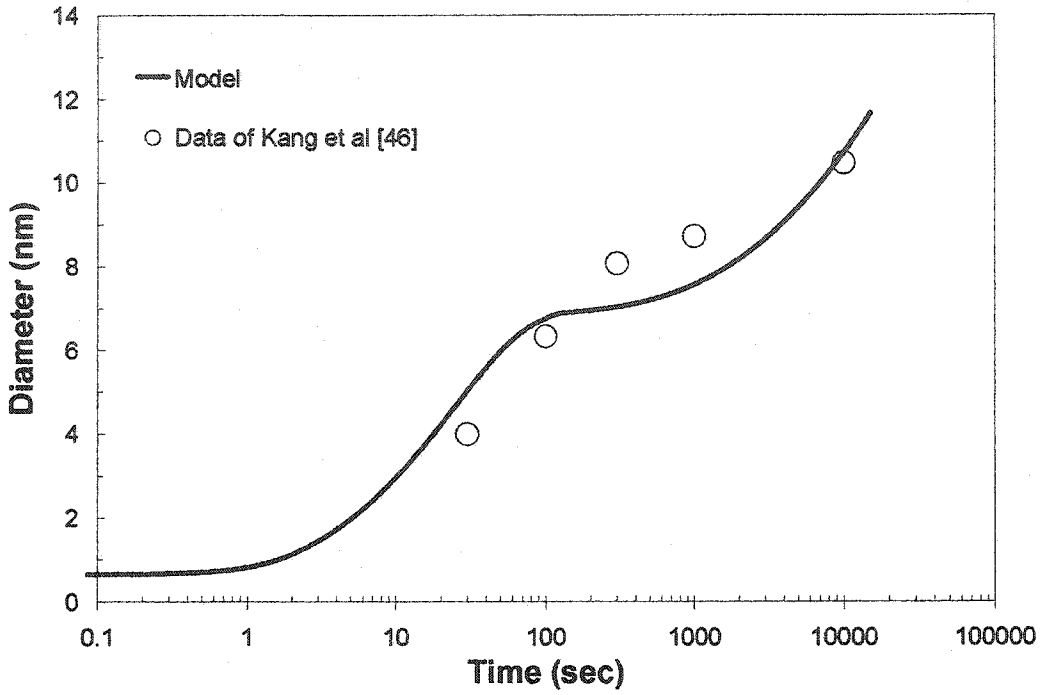

Figure (2.4a): *Comparison of the predicted and measured particle diameter evolution in steel N1 at 900°C.*

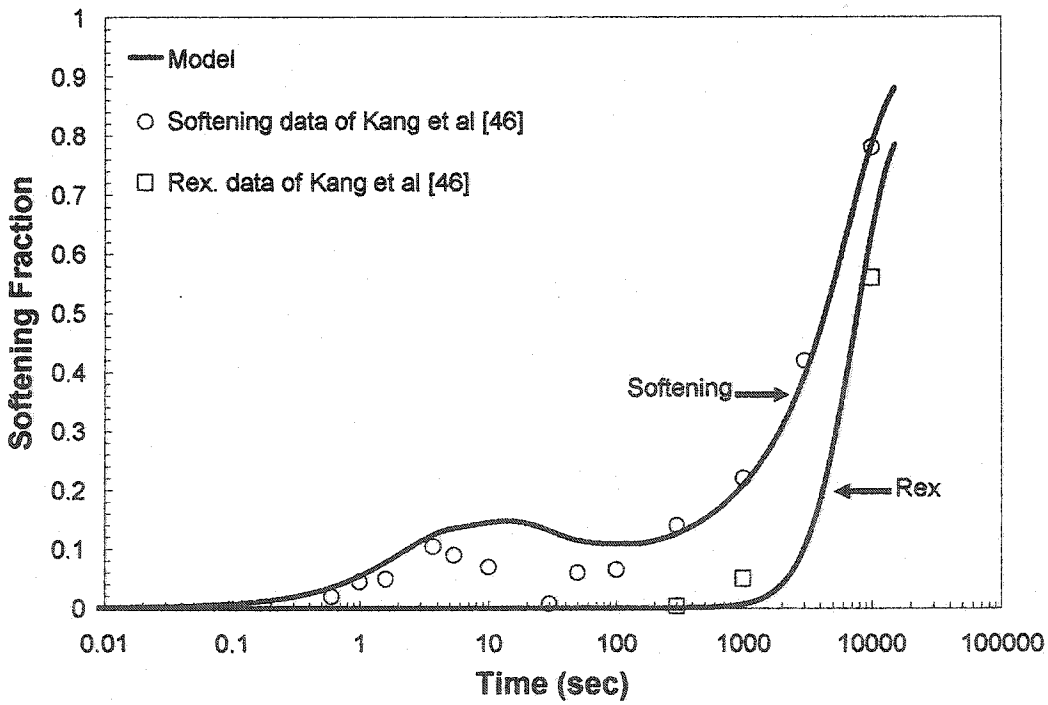

Figure (2.4b): *Comparison of the predicted and measured softening and recrystallized fractions in steel N1 at 900°C.*

The model has also been applied to the experimental data of Gomez et al [122] (Alloy N2) and Medina et al [81] (Alloys N3 and N4) to illustrate its applicability to a range of microalloyed Nb steels. The predicted and experimentally observed softening fractions for alloys N2, N3 and N4 are plotted in Figures (2.5)-(2.7). In each case, the values of the parameters, F and k were chosen to give the best fit of the experimental data, while k_s was kept constant at 0.06. Overall, the predictions of the model are in excellent agreement with the experimental data. It is particularly interesting to note that the plateaus on the softening curve are well reproduced. In figure (2.7), two plateaus are observed in agreement with the experimental data. Finally, it should be mentioned that the peak particle number-density varied from 1×10^{21} - 1×10^{22} /m^3 in agreement with the available experimental results [87, 123].

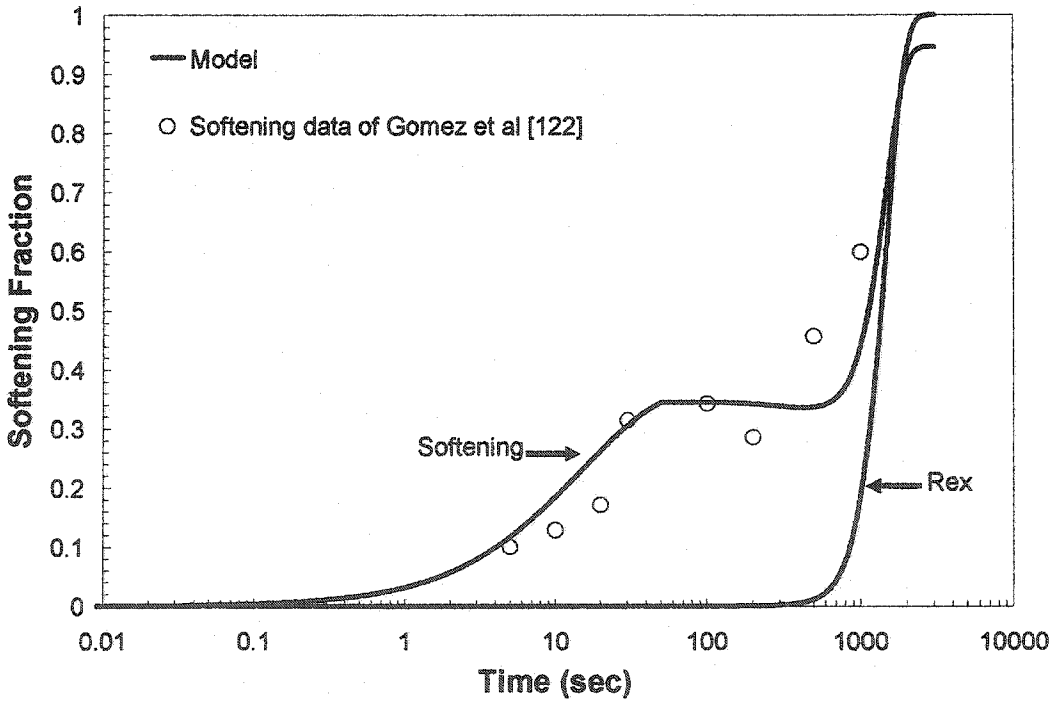

Figure (2.5): *Comparison of the predicted and measured softening and recrystallized fractions in steel N2 at 850°C.*

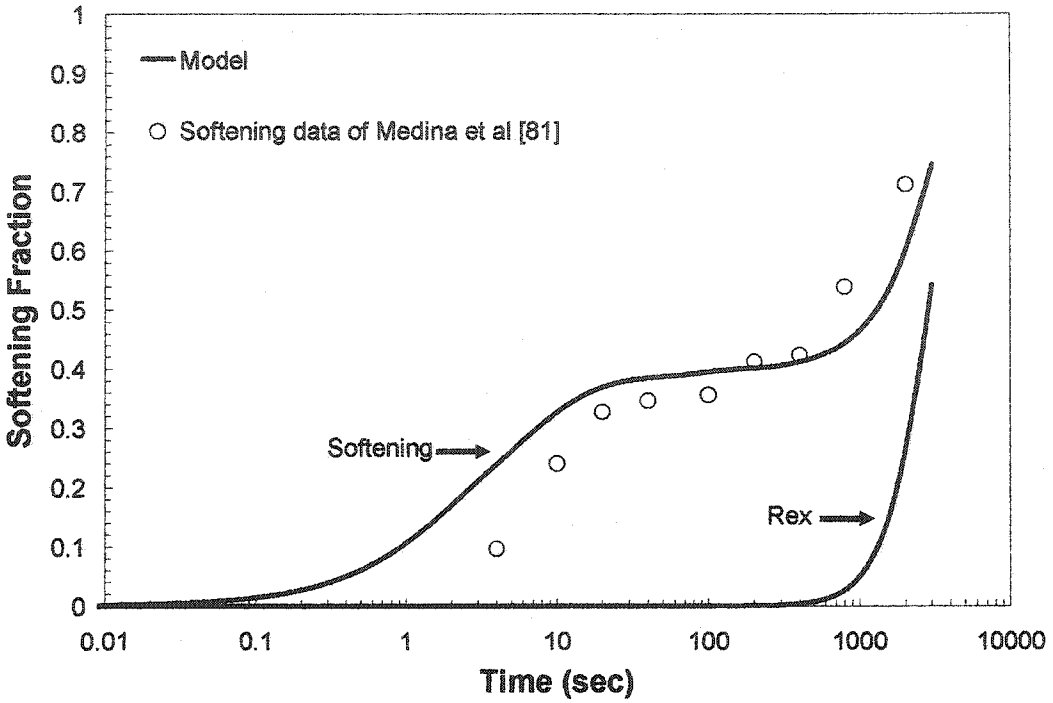

Figure (2.6): *Comparison of the predicted and measured softening and recrystallized fractions in steel N3 at 950°C.*

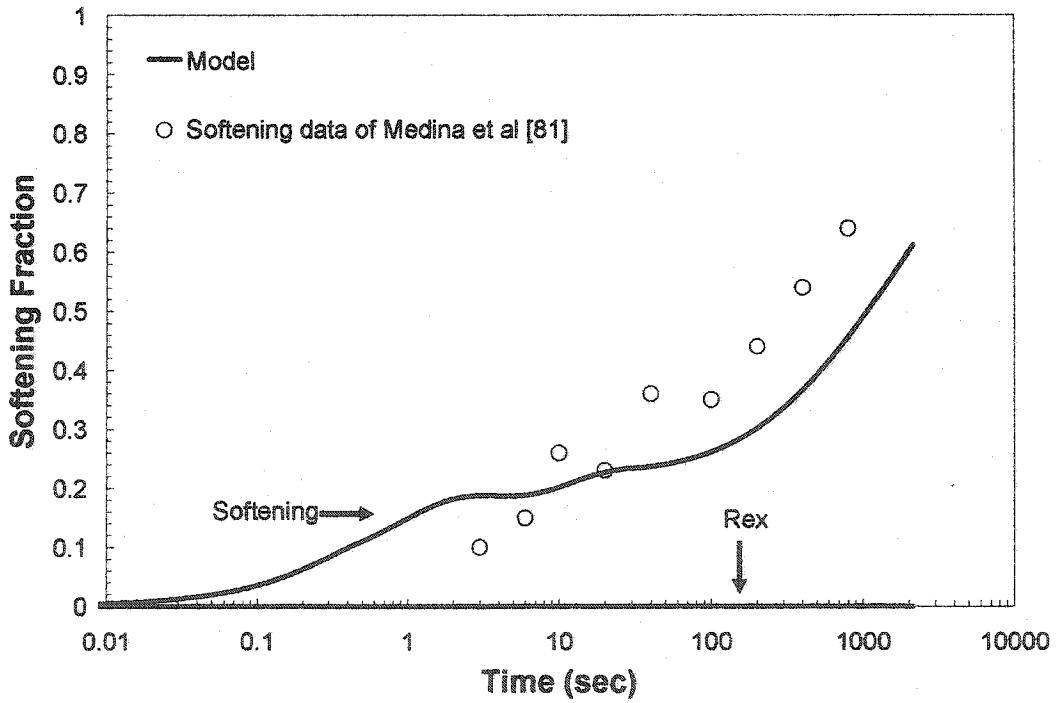

Figure (2.7): *Comparison of the predicted and measured softening and recrystallized fractions in steel N4 at 1000°C.*

2.5.3 Magnitude of the Adjustable Parameters.

We have presented a simple physically-based model for the interaction between precipitation, recovery and recrystallization in microalloyed austenite. The model contains three physically-based adjustable-parameters. The first parameter, F, is related to the average particle-spacing on the dislocation line (d_p):

$$d_p = \frac{b}{F} \tag{2.31}$$

In the present model, the optimum value of F varied between ~1×10^{-3} and 3×10^{-3}. This leads to the very reasonable particle spacing of 100-200 nm [87].

The second adjustable parameter is the geometric factor, k, which appears in Eq. (2.5). The value of k is directly related to the recrystallized austenite grain-size. If we assume that the recrystallized grains are spherical with an average diameter, D_R, then:

$$\frac{kS_v}{A_c} = \left(\frac{4}{3}\pi\left(\frac{D_R}{2}\right)^3\right)^{-1} \tag{2.32}$$

The value of k is then expected to lie between 5×10^{-2} and 5×10^{-5} depending on the initial grain-size and the applied deformation. In the present investigation, the optimum values of k fell between 1×10^{-3} and 3×10^{-6}. These values slightly overestimated the recrystallized grain-size. Improved agreement is possible by incorporating a threshold force of the order of $0.1G(t)$. For simplicity, we continue to use equation (2.6) without the incorporation of any threshold forces.

The remaining adjustable parameter is the obstacle strength, k_s, which appears in equation (2.30). A constant value of 0.06 was used throughout this chapter. This value implies that the transition from particle-shearing to particle bypass occurs at $r = 0.8b/0.06$ ~13b ~3.4 nm. This is approximately twice the values suggested by [91, 93]. The possible origins of this discrepancy are discussed in chapter (4).

2.6 Discussion of the Modelling Results:

Overall, excellent agreement is observed between the experimental results and the predictions of the model. In this section, an effort is made to clarify the manner in which the various processes interact to produce the observed softening curves. The discussion is divided into three sections: In section (2.6.1) we describe the interactions leading to a single plateau on the softening-time curve. The conditions leading to the observation of two softening plateaus are discussed in section (2.6.2). It will be shown that the origin of these plateaus is related to the interaction between precipitation and recovery with no contribution from recrystallization. In section (2.6.3), the possible effects of precipitation and solute-drag on the onset of recrystallization are discussed in detail.

2.6.1 Softening Curve with a Single-Plateau

A single plateau or a hump is frequently observed on the softening curves of microalloyed steels. This feature is occasionally attributed to the temporary stoppage of recrystallization as a result of strong particle pinning [81, 122, 124]. The available metallographic observations [46, 101,102] indicate, however, that the these plateaus occur before the onset of recrystallization. In this section, an effort is made to clarify the contributions of recovery, recrystallization and precipitation to the evolution of the softening-curve.

The softening curve for steel N1 at 850°C is reproduced in figure (2.8). Marked on the new figure are the individual contributions due to recovery, recrystallization, precipitation-hardening and solid-solution-softening. In addition, there is a contribution that arises from the test method used. Each of these contributions is discussed next. It is important to point out that the contributions in figure (2.8) are not to scale. In addition, the contributions are not added linearly. Care should, therefore, be taken in interpreting the magnitudes of the contributions.

Recrystallization Contribution: In figure (2.8), the onset of recrystallization is delayed to very long times of the order of ~1000 sec. This delay is due to a combination of the solute-drag effect and particle pinning. This statement is quantified in section (2.6.3). For the time being, it is sufficient to point out that recrystallization is not responsible for the formation of the plateau in the softening curve.

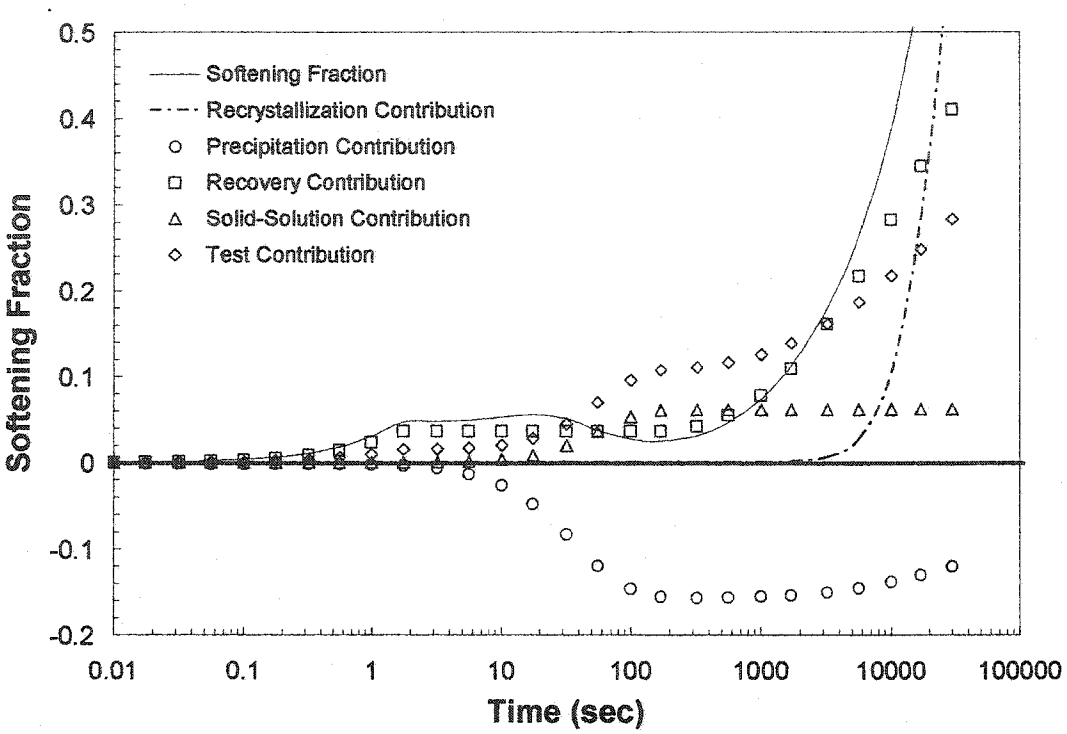

Figure (2.8): *The occurrence of a single plateau is interpreted in terms of the individual process-contributions to the softening curve (N1 at 850°C).*

Recovery Contribution: In the present example, the number of precipitates is initially smaller than the number of dislocation nodes. As a result, limited recovery is possible at the onset of annealing. The precipitate-free nodes will quickly disappear as a result of recovery and complete pinning is achieved after ~2 sec. The state of complete pinning persists until the onset of coarsening at ~300 sec. During coarsening, recovery proceeds at a rate which is controlled by the precipitate-coarsening kinetics (extended recovery). In summary, recovery is the only process contributing to the softening curve at short times of <1 sec. Between 1 and 300 sec, recovery makes no additional contribution to the softening curve. For t > 300 sec, recovery is one of the processes that contribute to the observed softening.

Precipitation Hardening: This contribution is calculated in terms of equation (2.30). The transition from particle-cutting to particle-bypass occurs close to the peak hardness at ~ 100sec. The reduction in precipitation hardening at long times is due to particle coarsening. Precipitation-hardening dominates the softening curve at intermediate times, between 50 and 1000sec. At very long times, the loss of precipitation hardening contributes, along with recovery and recrystallization, to the increased softening.

Solid-Solution Hardening: The presence of Nb in solution contributes to the strength of the steel. During precipitation, Nb is removed from the matrix. This results in the loss of solid-solution strengthening as shown in figure (2.8). The contribution is most important at short to intermediate times as it partially offsets the effect of precipitation-hardening.

Test Contribution: Interestingly, the testing method will contribute to the measured softening fraction. This is primarily due to the variation of the work-hardening rate with strain. The application of 5% strain to a deformation-free material results in more work-hardening than the application of the same strain to a material which has already been deformed by, say, 30%. It is difficult to separate the present contribution from the solid-solution contribution because the Nb content will also change the rate of work-hardening. In a way, the *"test-contribution"* acts to amplify the recovery and solid-solution contributions. This amplification effect is dependent on the technique used to evaluate the softening fraction (e.g 1% vs. 5% method). The contribution shown in figure (2.8) is that arising from the 5% method.

2.6.2 Softening Curve with Two Plateaus:

Occasionally, softening curves with two plateaus are observed in the literature [81, 125]. The model is able to predict these plateaus as shown in figure (2.7). In this section, the various interactions that give rise to the two-plateaus are discussed. The contributions of the individual processes are plotted along with the total softening in figure (2.9). It is clearly seen that the second plateau is associated with the onset of coarsening and the resumption of recovery, much like the plateau of section (2.6.1). The origin of the first plateau is not clear from figure (2.9). In order to clarify the origin of the first plateau, the *differential-softening contributions* (ΔS) are plotted in figure (2.10), where:

$$\Delta S = \frac{dS}{d\log(t)} \tag{2.33}$$

The idea is to identify those contributions which are changing most quickly in the vicinity of the plateau. It appears from figure (2.10) that the first plateau results from a balance between the rates of change of the hardening and softening processes. In a sense, the first plateau is a *dynamic* plateau. In contrast, the second plateau at 20-100 s is static, because all of the processes have come to a stop. Recovery is temporarily halted at 20-100sec and precipitation is largely complete, leading to little or no change in the solid-solution and precipitation-hardening effects.

The next logical question is why two plateaus are observed in some steels but not in others. In general, two-plateaus are observed in steels with exceptionally high Nb and

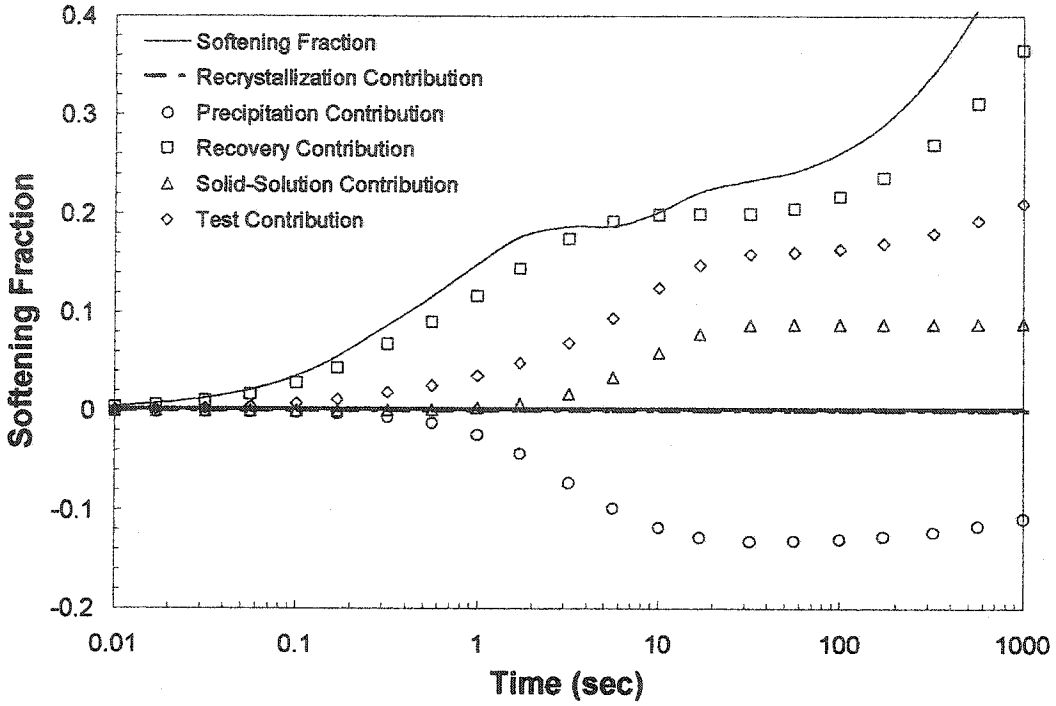

Figure (2.9): *The occurrence of two plateaus is interpreted in terms of the individual process-contributions to the softening curve (N4 at 1000°C).*

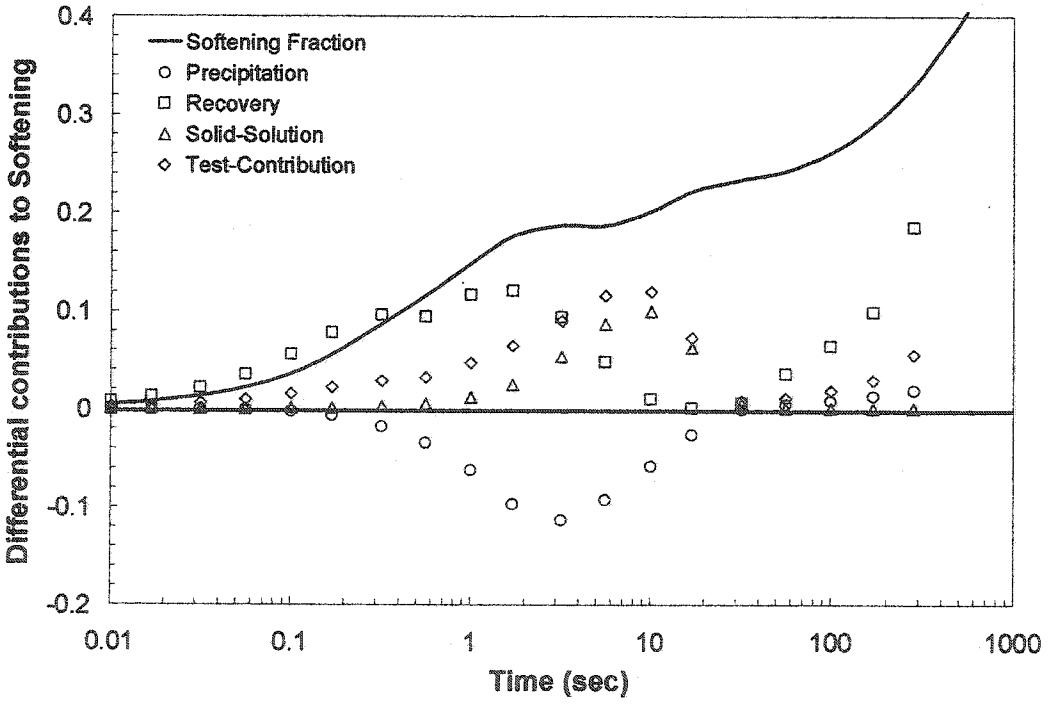

Figure (2.10): *The origin of the two plateaus in steel N4 at 1000°C, is explained in terms of the differential contributions to softening.*

medium to high carbon contents. To date, all of the observations occurred at temperatures in excess of 975°C. Careful comparison of figures (2.8) and (2.9) shows a change in the relative positions of the precipitation and recovery contributions. This shift is attributed to the effect of temperature on precipitation and recovery. The higher temperature of figure (2.9) results in complete precipitation within 10 seconds; this is compared to the 100 seconds needed in figure (2.8). This shift causes the recovery and precipitation contributions to overlap at high-temperatures, resulting in a dynamic plateau where the hardness does not change. The high solute content of the steels with two plateaus results in strong solid-solution-softening and this contributes to softening needed for the transition from one plateau to the other.

2.6.3 Effect of Microalloying on the Onset of Recrystallization:

The strong effect of microalloying on the onset of recrystallization is well-documented [15, 55, 57, 101, 102]. Careful experimental work has shown that the delay in recrystallization is due to a combination of solute-drag [15, 61] and precipitation pinning [101, 102]. For example, Jonas and Akben [57] showed that the presence of Nb in solution would delay the onset of recrystallization by an order of magnitude in comparison with a Nb-free steel. If precipitation takes place, the onset of recrystallization is delayed by two orders of magnitude.

In our model, the effect of solute-drag is taken into account in the mobility term.

The effect of precipitation enters into the model through the Zener pressure term in $G(t)$ and through the probability of development, Ψ. In order to evaluate the contributions of solute-drag and precipitation, we evaluated the time for 1% recrystallization under a number of different conditions. The results are shown in table (2.3), which refers to steel N1 at 850°C. Overall, the calculated contributions are in excellent agreement with the experimental estimates. The time for the onset of recrystallization in the absence of precipitation and solute-drag (condition d) is somewhat overestimated. Typically a value of 1-3 sec is expected.

Condition	**Comments**	$t_{1\%}$ **(s)**
(a) Experimental data	Steel N1: 0.03%Nb, 0.076%C, 0.006%N $T = 850$°C	3000
(b) Present model	$Z(t) = 3\gamma f_v/r$, $\Psi(t) = l/D_c$. $M(t)$: decreasing function due to precipitation.	3700
(c) Model without precipitation	$Z(t) = 0$, $\Psi(t) = 1$ $M(t) = M_o$ (constant value for 0.03%Nb).	105
(d) Model without precipitation or solute drag.	$Z(t) = 0$, $\Psi(t) = 1$ $M(t) = M_i$ (intrinsic mobility).	8

Table (2.3): *Contributions of precipitation and solute-drag to the retardation of the onset of recrystallization.*

In addition, it is possible to evaluate the contributions of the Zener-drag term, $Z(t)$, and the development probability, $\Psi(t)$, to the precipitation effect. Our calculations indicate that the probability term is far more important than the Zener drag; The delay which is brought about by the pinning of the sub-boundaries (i.e. Ψ) is approximately 10 times larger than the effect brought about by the Zener-term. This result is in agreement with the fact

that the Zener-drag is, in general, significantly lower than the driving force for recrystallization. This is clearly shown in figure (2.11). We therefore conclude that the retardation of recrystallization by precipitation is largely due to the pinning of the sub-boundaries. The Zener term is rarely large enough to halt recrystallization.

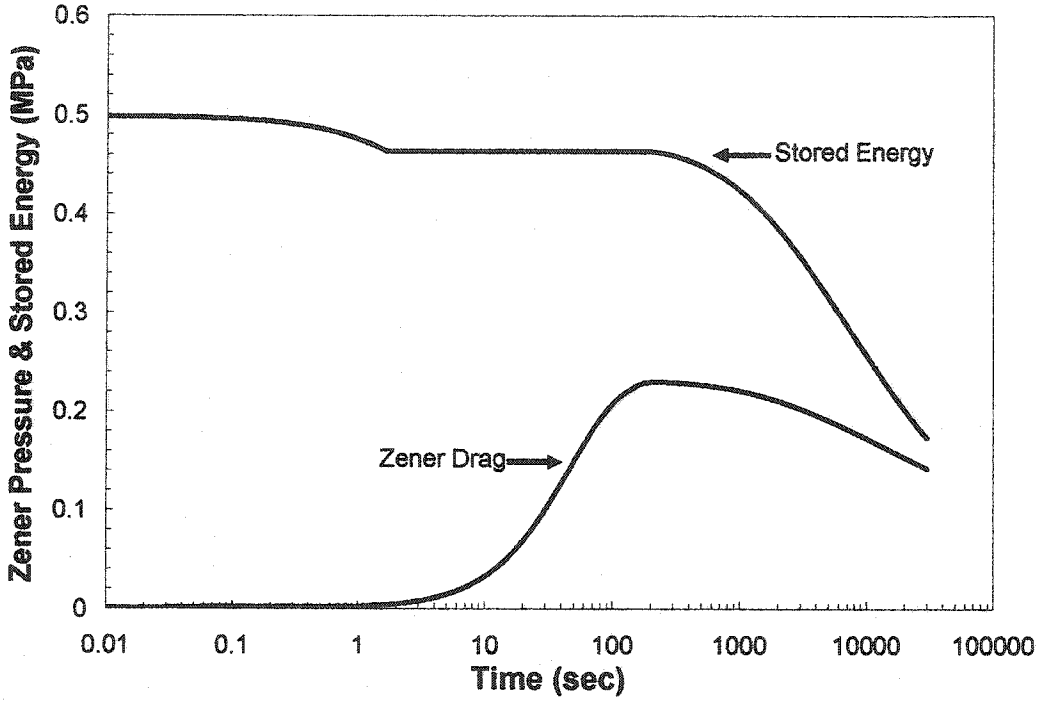

Figure (2.11): ***Comparison between the magnitude of the driving force for recrystallization and the Zener pressure (N1 at 850°C).***

2.7 Limitations of the Model

We have presented a simple physically-based model that takes account of the interactions between precipitation, recovery and recrystallization. In this section, two important limitations of the model are discussed.

2.7.1 Poor Fit at High Temperatures:

The model appears to provide an excellent description of the microstructural evolution at low temperatures and under strong-precipitation conditions. Increasing the temperature, will result in increasingly less satisfactory agreement. This is clearly seen by comparing figures (2.3), (2.4) and (2.12) which correspond to the evolution of steel N1 at 850, 900 and 950°C. In principle, the poor fit at high temperatures could be attributed to two main factors: First, it is possible that the temperature dependancies of precipitation, recovery or recrystallization are not accurately captured in the model. Secondly, it may be that the mechanism of one or more of the above processes changes at high temperatures. These possibilities are examined in sections (2.7.1.1) and (2.7.1.2) below.

2.7.1.1 Temperature Dependence:

In constructing the present model a number of critical assumptions have been made concerning the temperature-dependence of recrystallization, recovery and precipitation. In this section, we will focus on the processes of recovery and precipitation. The temperature-dependence of recrystallization is discussed in section (2.7.2) which deals with the limitations of our recrystallization model.

Starting with the process of recovery, it was assumed that the activation volume and energy are independent of temperature. This assumption is not very reasonable in the case of the activation volume. Based on equation (A2.1), deforming the material at a higher

temperature would result in fewer intersections of dislocations. As a result, a larger activation-volume is expected. This effect would amplify the error in the model and as such is not likely to be responsible for the observed difficulties.

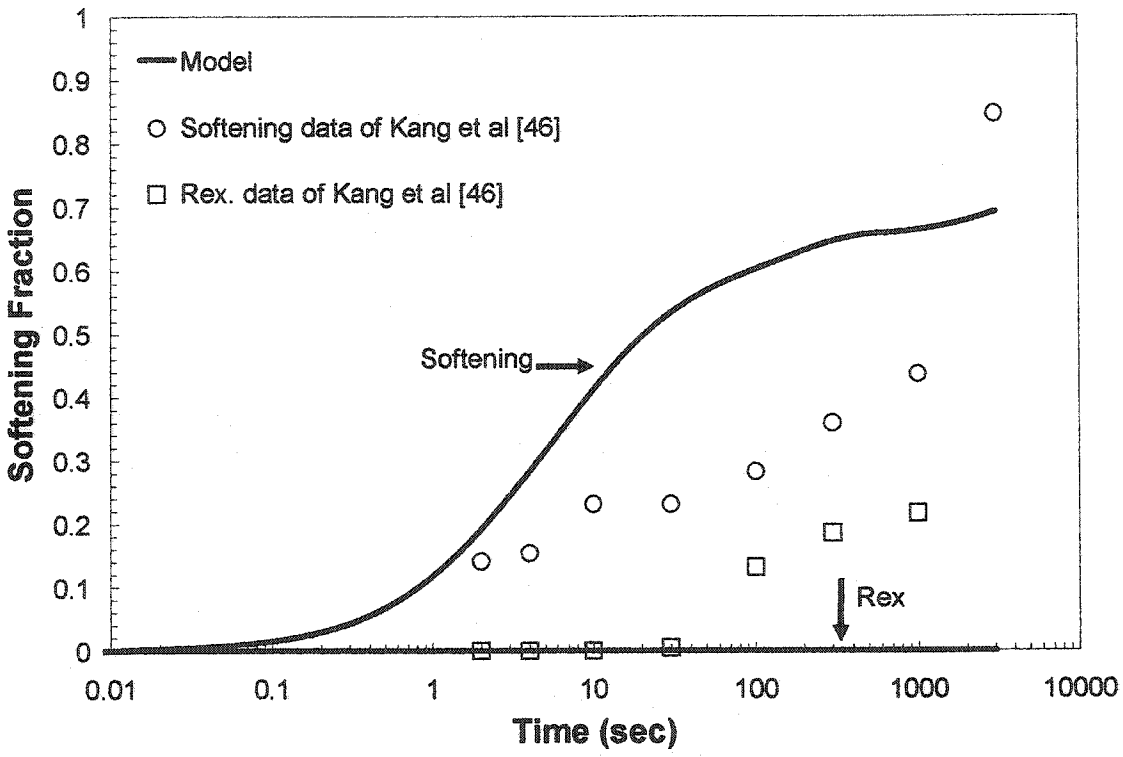

Figure (2.12): *Comparison of the predicted and measured softening and recrystallized fractions in steel N1 at 950°C.*

The temperature dependence of precipitation enters primarily through the diffusion coefficient and the activation energy for nucleation. Estimation of the latter quantity is difficult because it depends on the interphase energy and the chemical driving force for precipitation. In recent years, sophisticated models of the driving force have been constructed. As a result, the model could be improved by replacing the solubility product

approach with a full thermodynamic analysis based on the highly developed databases of ThermoCalc, for example. In contrast, there is still no reliable estimate of the temperature-dependence of the interphase-energy. This appears to be the most serious challenge in modelling the precipitation kinetics. In section (1.1) we pointed out that most of the available precipitation models fail at high temperatures because the critical nucleus becomes excessively large. We managed to reduce this problem by utilizing an interphase energy that decreases with temperature. Still, the problem persists to some extent. Figure (2.12) corresponds to the deformation of steel N1 at a temperature of 950°C, which is about 120 degrees below the solubility limit. In this case, the critical nucleus had a diameter of 0.9 nm! This results in a very small nucleation-rate and small number density of precipitates. The overestimation of the softening fraction in figure (2.12) is then the result of insufficient precipitation.

In the course of developing this model, we investigated the possibility of using a more detailed driving force analysis as well as the possibility of using a smaller interphase energy to capture the high-temperature behaviour. It was found that combinations of the driving-force and interphase energy which led to reasonable agreement at high temperatures, resulted in very small nucleation diameters (< 0.4 nm) at low temperatures. We are therefore led to speculate that one or more of the following changes are happening:

- At low temperatures, the microalloying elements may aggregate to form tiny clusters with the interstitial atoms. These tiny clusters may still exert a pinning force on the

dislocations. The existence of such clusters is suggested in Cahn's treatment of precipitation on dislocations [106]. Experimental evidence for the existence of such clusters and of their effect on recovery has recently been presented by Maruyama and Smith [126].

- Strong non-equilibrium segregation may be taking place at high-temperatures. This argument was developed by Liu [16] and appears to lead to enhanced precipitation at high temperatures.

Given the present status of our knowledge, it is felt that the above arguments could not be convincingly applied in the model.

2.7.1.2 Change in Mechanism:

In the previous section, we discussed the high-temperature limitations of the model in terms of the temperature-dependence of the processes involved. It was implicitly assumed that the mechanism of a given process does not change with temperature. In this section, we examine the possibility that the mechanisms of recovery and precipitation are changed at high-temperatures.

It is well-known that deformation at high-temperatures results in a highly-developed substructure which consists of dislocation cells and sub-boundaries. The stored-energy of this structure can't be described accurately in terms of the single state-variable approach of Eq. (2.6). Consequently, the stress-relaxation equations of section (2.2) are expected to become increasingly less accurate as the temperature increases. Nes [60] argued that under

these conditions, the recovery kinetics are best described in terms of the dislocation density in the cell-walls and the cell size.

In addition, to the change in the governing equation of recovery, we expect a change in the interaction between recovery and precipitation at high-temperatures. In the case of a well-developed substructure, precipitation is expected to occur preferentially at the cell-walls. This results in strong localized pinning of the cell-walls and sub-boundaries. It may well be, that an interaction of this type is responsible for strong pinning which is observed in figure (2.12).

2.7.2 Kinetics of Recrystallization:

Careful examination of the predicted recrystallization curves in figures (2.3)-(2.7) indicates that, once started, recrystallization proceeds very quickly. This has been a consistent criticism of the JMAK approach [38]. Improvements are possible only through the adoption of a more sophisticated model. At this stage, this does not appear to be justified.

Chapter 3:

Experimental Work on the Model Alloy

The interaction between precipitation and recovery plays an important role in the microstructural evolution of hot-worked steel. This interaction has been largely overlooked in the literature. For this reason, most of our experimental work will be devoted to studying the interaction of precipitation and recovery in the *absence of recrystallization.* This corresponds to the important industrial case of finish rolling, in which, the main objective is to accumulate strain in the absence of static-recrystallization.

The experiments were carried out on a series of austenitic model alloys with the same stacking fault energy as C-Mn steels. In this way, it was possible to observe, directly, the precipitation of NbC on whole dislocations. The development and preparation of the model alloys are described in section (3.1). Transmission electron microscopy is used, in section (3.2), to study the precipitation of NbC in the model alloy. The information obtained from this technique includes, the orientation relationship of the precipitates as well as particle-size, shape and distribution. The TEM information is complemented by an extensive study of the precipitation kinetics using the technique of Small Angle Neutron

Scattering (SANS). Using this technique we were able to obtain information on particle size, number and volume fraction as a function of time, section (3.3). Information on the progress of recovery and its interaction with precipitation is obtained using a series of double deformation tests. In section (3.4), the results of the double-deformation tests are presented in the form of softening-fraction diagrams.

In Chapter (4), results of the various experimental techniques are combined to provide a more complete description of the processes taking place. Additional insight is gained by comparing the experimental data and the modelling results.

3.1 Development and Preparation of the Model Alloys:

The decomposition of austenite precludes direct observation of the deformed microstructure. For this reason, there is a need to develop a model alloy, in which the austenite phase is retained at room temperature. The Fe-Ni system is an attractive starting point for the design of such alloy. It is well-known that nickel is an effective austenite stabilizer [127]. In addition, the interaction between nickel and carbon is very weak and repulsive [128]. As a result, the only effect of Ni addition on the precipitation of carbonitrides is to increase the solubility of Nb and C in the steel. In recent years, several model alloys have been proposed based on the Fe-Ni system. Researchers at the University

of Sheffield [86, 87, 129] proposed a number of alloys with the base composition of Fe-30%Ni. This composition corresponds to the minimum amount of Ni needed to retain austenite at room temperature. In contrast, Hurely et al [130, 131] and Adachi et al [132] used a model alloy containing 70% Ni to study the deformed structure of austenite. This alloy has the advantage of having the same stacking-fault energy (SFE) as pure iron at 1100°C [133, 134]. Given the important effect of the SFE on deformation [38], precipitation [135] and recovery [38, 136], we decided to base our model alloys on the Fe-70%Ni system.

3.1.1 Design Considerations:

For a meaningful comparison between precipitation in the model alloys and precipitation in microalloyed steels, two conditions should be met: Firstly, NbX should be the only precipitate formed. Secondly, the precipitates should form on whole dislocations and with a cube-on-cube orientation relationship. In addition, to the above requirements, it is *advantageous* to be able to produce an alloy in which the precipitates are completely dissolved on solution treatment. Each of these criteria is discussed below with the aim of arriving at specific alloy compositions:

3.1.1.1 Phase Stability:

We used the *Fedat* [137] database of *ThermoCalc*™ to investigate the range of compositions over which NbC is the only stable precipitate in Ni-30%Fe. The calculations indicate that graphite is formed when the Nb to C ratio is significantly less than unity.

Large ratios of Nb to C, are expected to result in the precipitation of a Laves phase of the type Fe_2Nb. The useful range of Nb to C ratios is, therefore, limited to ~ 0.8 - 15.

3.1.1.2 Precipitation on Dislocations:

The precipitation of NbC on whole dislocations and Frank partials is well documented in the literature on austenitic stainless-steels [22, 138, 139] and Ni-superalloys [135]. Kotval [135] demonstrated that the mode of precipitation is determined by the stacking fault energy (SFE); Niobium carbide will precipitate, exclusively, on grain boundaries and whole dislocations in alloys with a high SFE ($\geq$ 50 mJ/m^2). Frank-partial precipitation occurs in alloys with intermediate SF energies in the range of 20-50 mJ/m^2. The stacking fault energy of Ni-30%Fe is approximately 75 mJ/m^2 [134]. The available data [134, 140-142] on the concentration dependence of the SFE indicates that the addition of Nb and C is unlikely to reduce the SFE by more than 20 mJ/m^2. As a result, we have concluded that precipitation in the proposed Ni-30%Fe-Nb-C alloys is expected to take place, exclusively, on whole dislocations.

Concerning the orientation-relationship, the available data on the precipitation of MC carbides in Ni-superalloys indicates that a cube-on-cube relationship is usually observed [25, 143. 144]. The most relevant study is by Scarlin and Edington [143] who observed the cube-on-cube O.R. in the case for VC precipitation in Ni-38%Fe. Experimental verification of the cube-on-cube O.R. is presented in section (3.2).

3.1.1.3 Solubility:

The requirement of complete dissolution at high-temperatures places an upper limit on the amounts of Nb and C that could be added to the alloy. For a Nb to C ratio of 1, it is possible to dissolve up to 2% Nb in the matrix [137]. This leads to a precipitate fraction of over 2% at 700°C.

3.1.2 Alloy Preparation:

The above guidelines were used to prepare seven model alloys. The actual compositions of the alloys are listed in table (3.1) below. For each alloy, the dissolution temperature and the precipitate fraction were estimated using the *Fedat* database [137].

ID	Fe*	Nb	C	Nb:C (atomic)	$T_{dissolution}$ (°C)	V_f NbC (700°C)	SFE** (mJ/m^2)
O	29	0	0	N/A	N/A	N/A	75
L	30	0.33	0.027±0.005	1.5	925	0.25%	60
M	30	0.85	0.117±0.010	1	1196	0.98%	50
L1	30	0.33	0.010±0.002	4	835	0.08%	62
M1	30	0.85	0.077±0.003	1.5	1143	0.68%	52
M2	30	0.85	0.040±0.002	3	1066	0.39%	53
M3	30	0.85	0.009±0.003	11	921	0.09%	55

Table (3.1): *Compositions of the model alloys (wt%). * Impurity contents are as follows (wt%): Al 0.007, Cr 0.07, Mn 0.013, N_2 0.0003, P 0.0014, S 0.004, Si 0.024, Ti 0.008. ** Rough estimates based on [134,140,141].*

The alloys were prepared by melting Ni and Fe in the ratio of 70:30 to produce a heat of ~ 45 kg. Niobium and carbon were added in two steps to produce alloys L and M. In order to break down the as-cast structure, the ingots were reheated to 1250°C for 24 hrs. This was followed by six hot-rolling passes that reduced the sample thickness from 60 to 30 mm. An intermediate solution treatment at 1350°C for 30 minutes was applied before a second round of rolling which reduced the thickness to 15 mm. The above treatment is summarized in figure (3.1) below. Alloys L and M were subjected to an additional solution treatment at 1225°C for 16-24 hrs, before being used for any experimental work.

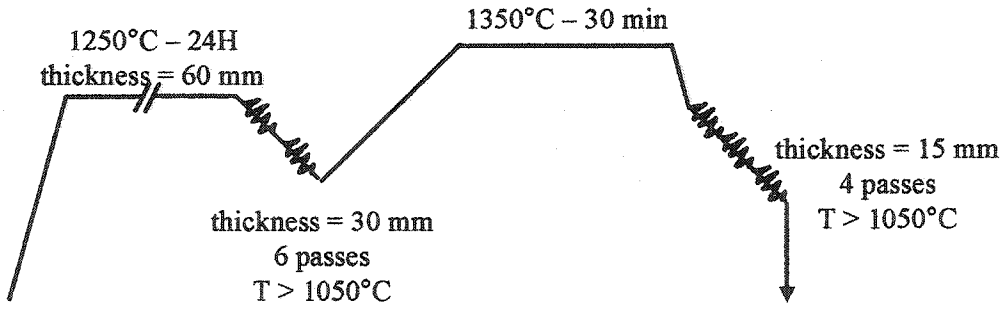

Figure (3.1): *Initial homogenization treatment used to break up the as cast structure.*

The remaining alloys, i.e. M1, M2, M3 and L1, were prepared from alloys M and L via a two-step heat treatment. In the first step, the parent alloys (L or M) were decarburized using wet-hydrogen at 1100-1200°C. This step brought the average carbon concentration down to within the vicinity of the desired value. In the second step, the desired composition was achieved by homogenizing the samples under a CO/CO_2 atmosphere of the desired carbon activity. In addition, the homogenization treatment served to eliminate the carbon concentration gradient that resulted from the decarburisation step. In all cases, the homogenization was carried out above the precipitate dissolution temperature in order to

ensure that all the Nb and C are in solution. Typically, the above heat-treatments combined for a total time of 3 to 7 days, at temperatures of 1100-1250°C. This extended high-temperature exposure should ensure the homogeneity of the structure.

3.1.3 Experimental Approach:

The aim of the present experiments is to study the interactions between precipitation and recovery at a fundamental level and under highly controlled conditions. It is hoped that the following experiments will allow us to further our understanding of the processes taking place and to improve the model of chapter (2). It is *not* our objective, however, to simulate industrial hot-working conditions. With this in mind, we adopted a simple procedure involving the room-temperature deformation and high-temperature annealing of the samples. Admittedly, this approach would not capture the dynamic processes that take place during high-temperature deformation. It does, however, allow us to study precipitation and recovery in a very simple and controlled manner.

Most of the experimental work described below followed the deformation/annealing schedule shown in figure (3.2), below. The applied deformation ranged from 10 to 40%, with 20% being the condition most commonly used. Annealing was carried out between 700 and 945°C. Critical to the present approach is one's ability to heat the samples quickly to the desired annealing temperature. For this reason, short heat-treatments were carried out using a salt-bath with continuous stirring of the samples. For longer heat-treatments, the

samples were sealed in quartz under an argon pressure of 250 mtorr. In this case, a two zone furnace was used in order to achieve the required heating rates. Typically, the desired temperature was achieved within less than 50 sec in the case of the salt-bath and less than 100 sec in the case of the two-zone furnace. In all cases, the samples were quenched in water upon completion of the heat-treatment. The quartz capsules were smashed in order to allow for faster cooling.

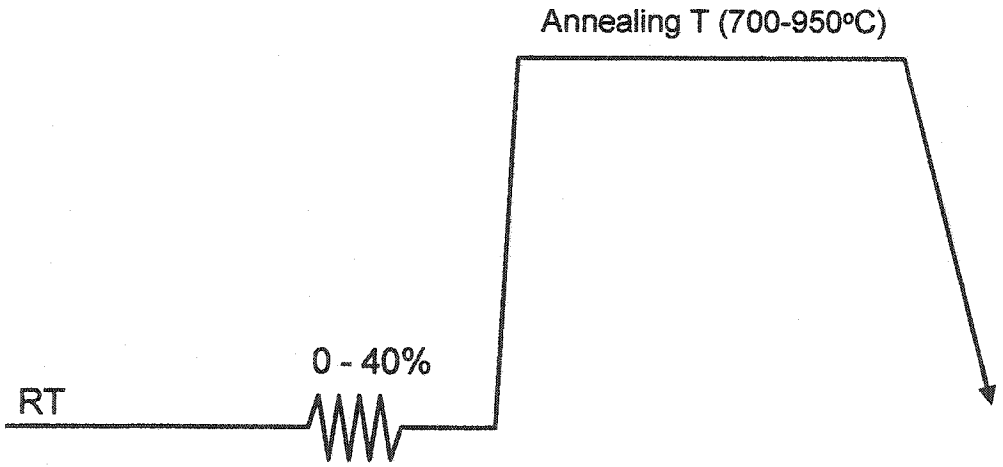

Figure (3.2): *Schematic diagram of the deform-and-anneal treatment used throughout this work.*

In the following sections, the processes of precipitation and recovery are investigated using the techniques of: transmission electron microscopy (3.2), small angle neutron scattering (3.3) and double-deformation tests (3.4). These techniques are used in a complementary manner to provide a more complete picture of the processes taking place. For convenience, the various techniques are discussed separately. The reader should keep in mind, however, that in practice these experiments are related and in many cases involved the same samples.

3.2 Electron Microscopy:

Transmission electron microscopy was used to obtain information on the deformed structure (3.2.1), the precipitate size, shape and distributions (3.2.2) as well as the interaction between precipitation and recovery (3.2.3). Admittedly, the TEM work which is described below is not very detailed and much remains to be done. However, the knowledge gained from the presented observations is sufficient to verify a number of critical assumptions in the model. In addition, the information obtained below complements the results of the SANS and double-deformation tests.

3.2.1 Deformed Structure:

The deformation of austenite sets the stage for the competing processes of recovery and strain-induced precipitation. It is, therefore, important to study the as deformed structure, as well as the evolution of this structure during annealing. Figure (3.3) corresponds to the as-deformed structure of a specimen which has been deformed to a (true) tensile strain of 0.33 at room temperature. As expected, the structure consists of dense tangles of dislocations. In some areas, it appears that dislocation-cells are beginning to form. Overall, however, the structure is very random.

The evolution of the deformed structure is strongly dependent on the annealing

temperature. Figures (3.4) and (3.5) correspond, respectively, to the partly-recovered structures at 700°C and 900°C. In the first case, the dislocation distribution continues to be relatively random even after 200 minutes at temperature (Fig. 3.4). In contrast, deformation bands are quickly formed at 900°C. Figure (3.5) corresponds to a total heating time of 50 sec, of this time less than 5 sec are at 900°C. Clearly, the two situations need to be modelled differently. Once again, we expect our model to produce more satisfactory results at the lower temperatures where the assumption of a random distribution of dislocations is more reasonable.

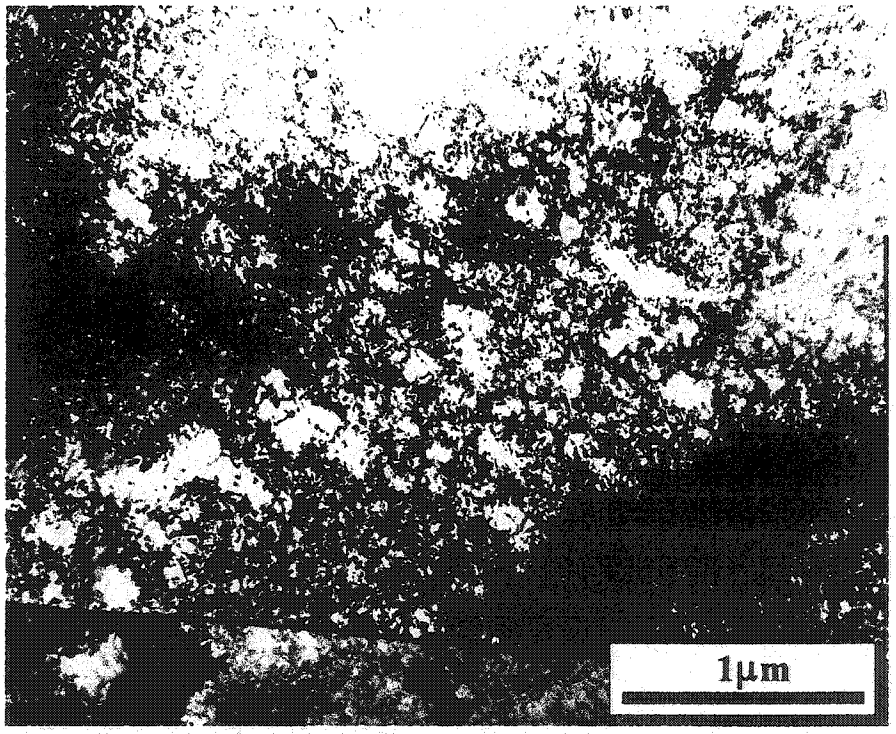

Figure (3.3): *As deformed structure of alloy M deformed 40% in tension. [Courtesy of C. R. Hutchinson].*

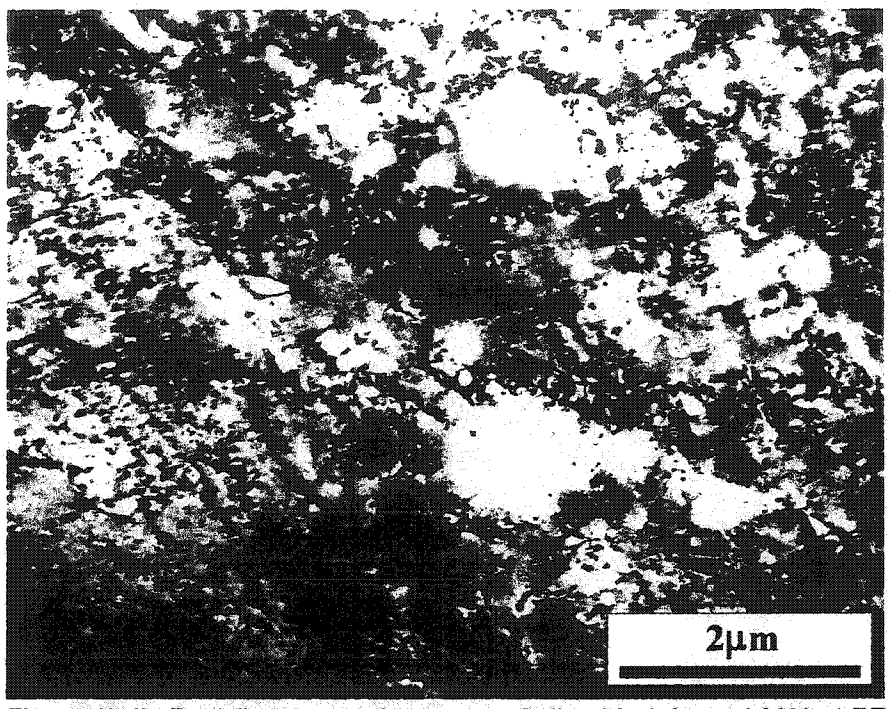

Figure (3.4): *Partially recovered structure of alloy M, deformed 20% at RT and annealed for 200 min at 700°C.*

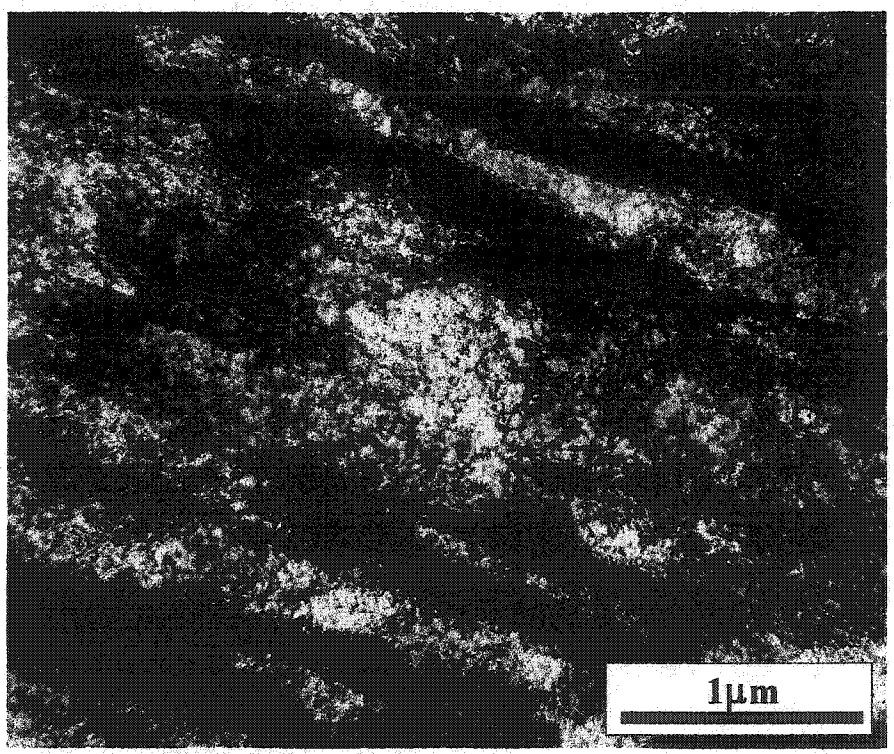

Figure (3.5): *The partially-recovered structure of alloy M, deformed 40% at RT and annealed for ~5 sec at 900°C.*

3.2.2 Precipitation:

The purpose of this section is to investigate the basic aspects of precipitation in the model alloys. In section (3.2.2.1), the morphology of the precipitates is briefly discussed. The precipitate-matrix orientation relationship is determined in section (3.2.2.2). Finally, quantitative measurements of particle-size and size-distribution are presented in section (3.2.2.3).

3.2.2.1 Particle Shape:

Deform-and-anneal treatments of the type shown in figure (3.2) were used to promote precipitation in fully solution-treated samples. In all cases, annealing below the dissolution temperature resulted in a fine precipitate dispersion similar to that shown in figure (3.6). The precipitates appeared in two morphologies; The vast majority had an aspect ratio of ~1 and appeared to be either cubic, spherical or irregularly shaped. Elongated, plate-like precipitates were also observed (Fig. 3.6b) Both precipitate types were shown to consist of Nb and C. In addition, the diffraction patterns of both were found to be consistent with the NaCl structure. As such, both morphologies were identified as NbC. For the rest of this investigation, we will only consider the blocky precipitates. Only these are observed in microalloyed steels. To a first approximation, the long, plate-like particles are ignored. This appears justified, given the low number density of the elongated particles.

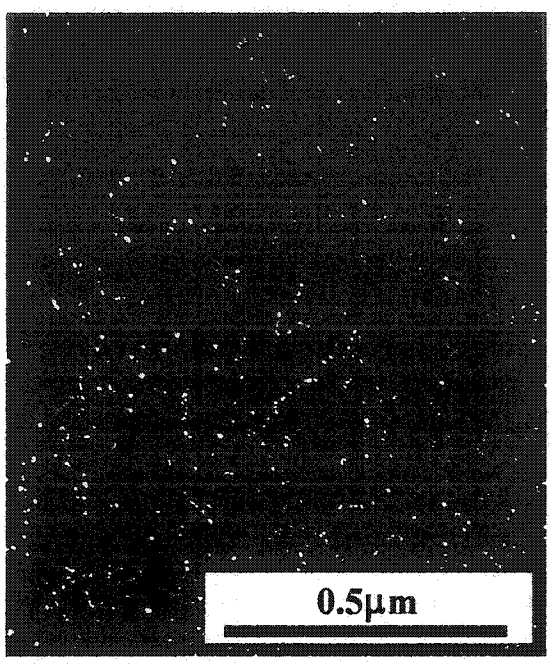

Figure (3.6a): *Dark-field image of NbC particles in alloy M, deformed 20% and annealed for 200 min at 700°C.*

Figure (3.6b): *Extraction-replica of alloy M, deformed 20% and annealed for 200 min at 700°C.*

3.2.2.2 Orientation-Relationship:

The technique of selected-area-diffraction (SAD) was used to determine the orientation-relationship between the precipitates and the matrix. A cube-on-cube orientation is, clearly, seen in the diffraction patterns of figure (3.7). From these patterns, the misfit between NbC and the matrix is estimated to be ~ 25%. Interestingly, the dark-field images which are formed using the precipitate spots (e.g. 3.6a, 3.9b) do not show any of the elongated (plate-like) particles. This suggests that the main difference between the blocky and the elongated precipitates is the orientation-relationship.

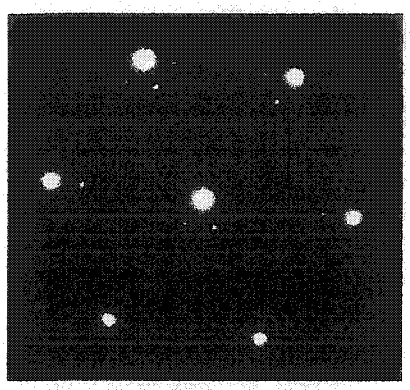

Figure (3.7a): *SAD pattern of a (111) zone. The Precipitate spots as well as double reflections are clearly seen.*

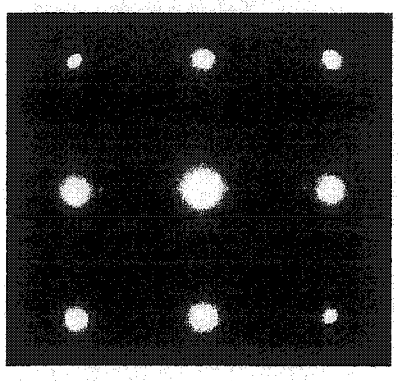

Figure (3.7b): *SAD pattern of a (002) zone axis.*

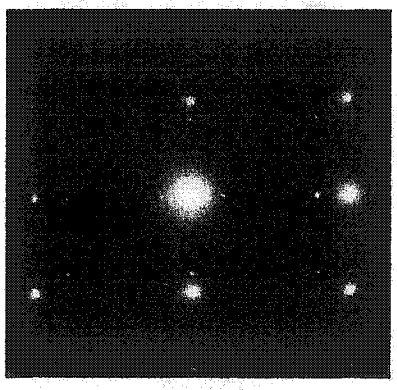

Figure (3.7c): *SAD pattern of a (112) zone axis.*

3.2.2.3 Extraction Replicas:

Extraction replicas were used, extensively, to obtain quantitative data on the average precipitate size as well as the particle-size distribution. The results presented here are meant to complement the neutron-scattering data of the next section.

- *Effect of Super-saturation on Particle Size*: The average particle-size was measured for alloys M, M1, M2, M3, L and L1 under identical conditions. The samples were deformed (at RT) to a *constant flow-stress* of 350 MPa and annealed at 800°C for 12hrs. The results are listed in table (3.2) below. This data is very important for testing the ability of the model to capture the effect of alloy composition on the precipitation kinetics. The results are used in chapter (4). For the time being, it is sufficient to point out that the particle size decreases in the sequence M, M1, M2 because the number of nuclei is essentially constant, while the amount of available solute is decreasing. A large particle-size is obtained in alloy M3 because the supersaturation is very small and few nuclei are formed in spite of the abundance of nucleation sites.

Alloy	Average Particle Size (nm)	Standard Dev. (nm)
M	9	3
M1	7	2
M2	5	2
M3	23	8
L	10	4
L1	15	7

Table (3.2): *Effect of alloy composition on the average particle size after 12hrs at 800°C.*

- *Particle-Size Distribution*: We investigated the effect of annealing time and applied deformation on the particle-size distribution. The evolution of the particle-size distribution in a non-deformed alloy[a] at 700°C is shown in figure (3.8). Included in the same diagram, is the particle-size distribution of a sample which was cold-rolled to a reduction of 30% and annealed for 1 hr. The precipitate volume-fraction (measured by SANS) in this sample is equal to the precipitate fraction in the undeformed sample after 100 hrs. The powerful effect of deformation on the precipitation kinetics and the particle size is immediately clear.

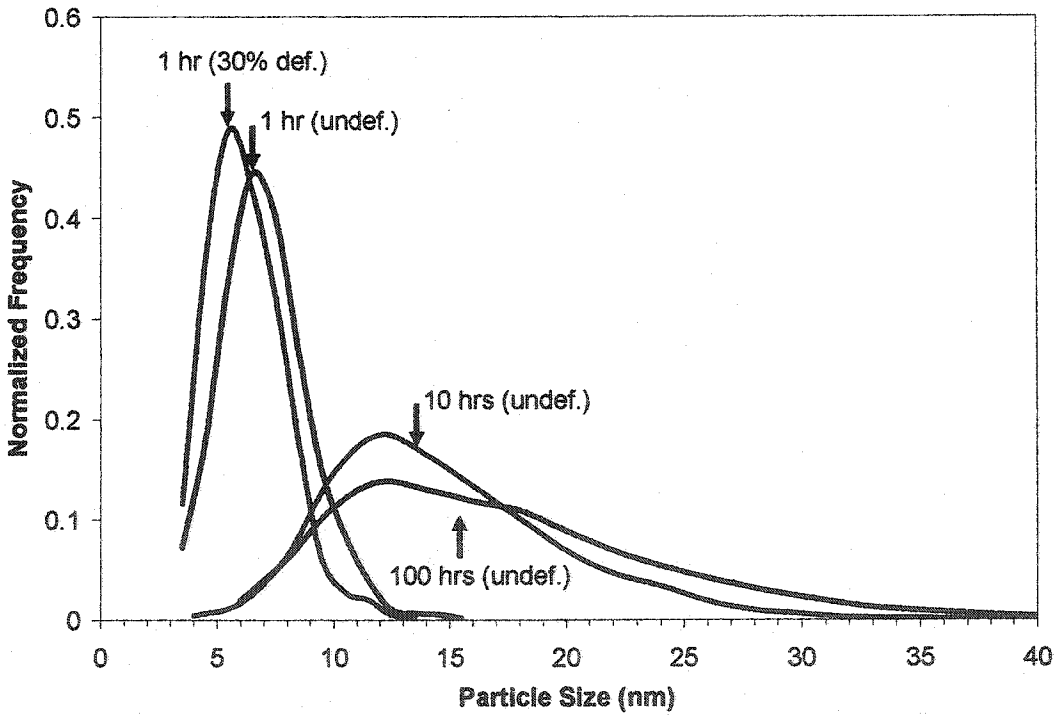

Figure (3.8): *Evolution of the particle size distribution in alloy M. The arrows indicate the average particle size.*

[a] This alloy contained 1.3%Nb and 0.16%C. This composition was used in the early stages of the investigation. It was later abandoned in favour of alloy M.

3.2.3 Interaction between Recovery and Precipitation:

In this section we are primarily concerned with the precipitation of NbC on dislocations and the resulting pinning of recovery. Figures (3.9) and (3.10) are, respectively, the DF images obtained using the matrix spot and the precipitate spot. Comparison of the two figures demonstrates that precipitation of NbC takes place exclusively on dislocations. In the present case, complete pinning of recovery is expected as a result of the large number of precipitate particles per unit length of dislocation. As the number of particles decreases, limited recovery becomes possible.

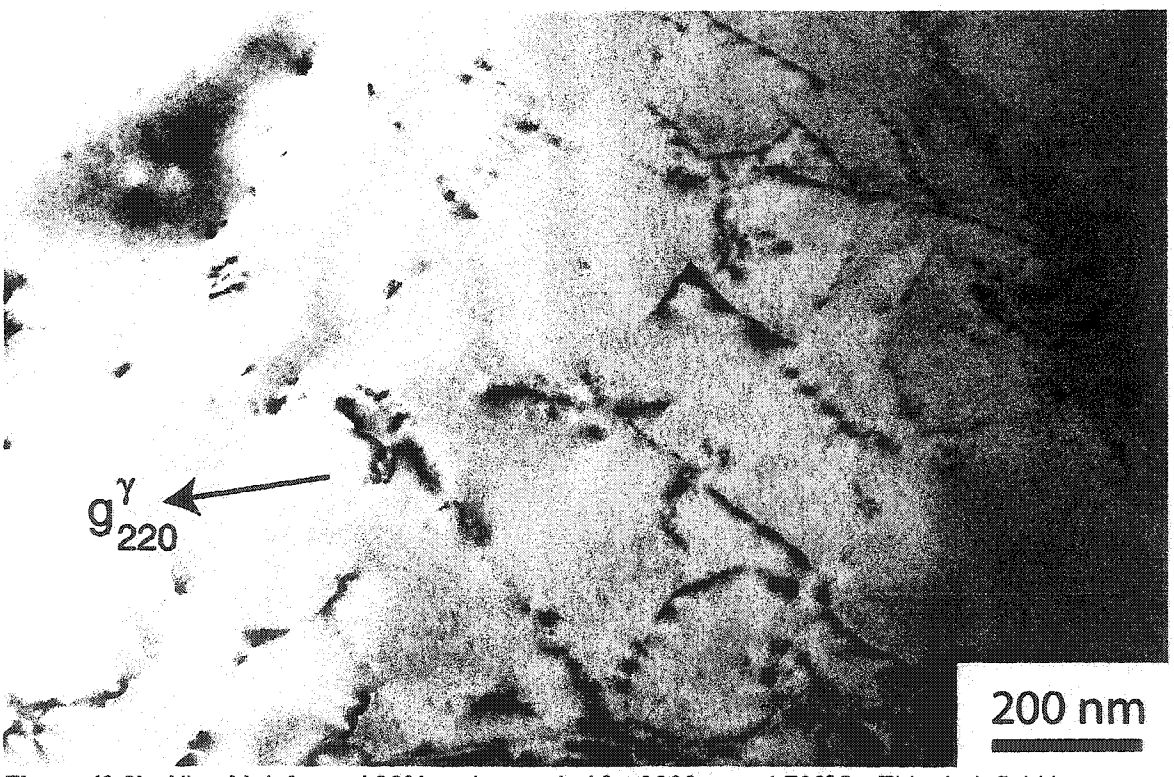

Figure (3.9): *Alloy M deformed 20% and annealed for 2000 sec at 700°C. This dark-field image is formed using the matrix (220) reflection. [courtesy of C. R. Hutchinson].*

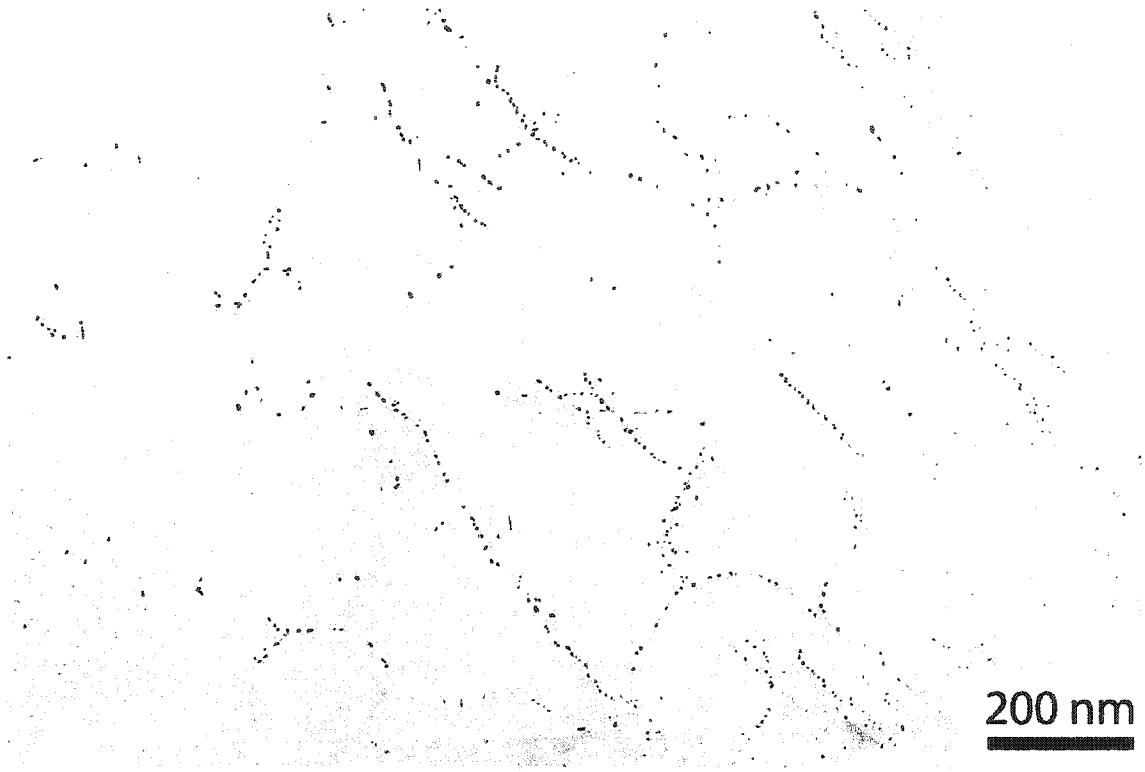

Figure (3.10): *Image of the same region as (3.9), formed using the precipitate (220) reflection. Please note that the negative of the image is shown for clarity. [courtesy of C. R. Hutchinson]*

3.3 Small-Angle Neutron Scattering:

Small-angle neutron scattering is a powerful technique for studying particle dispersions in the range of ~1 - 100 nm. The information obtained includes the particle-size, number density and volume fraction. It is also possible to calculate the surface-area to volume ratio of the particles as well as the particle-size distribution. Section (3.3.1) offers a brief introduction to the technique. In sections (3.3.2) and (3.3.3), our experimental results are presented and discussed.

3.3.1 Introduction to the Technique:

The scattering power is defined as the number of free electrons, which scattering independently, would produce the same intensity as the object considered. For a finite crystal, the scattering power per unit cell is given by the general equation [145]:

$$I = \frac{F_{hkl}^2}{Vv_c} \sum_h \sum_k \sum_l \left| \Sigma(q - r_{hkl}) \right|^2 \qquad (3.1a)$$

Here, F_{hkl} is the structure factor related to the *hkl* node, q is the scattering vector and r_{hkl} is the reciprocal lattice vector which defines the *hkl* node. The function inside the brackets (Σ) is the Fourier transform of the form factor. By definition, the form factor is equal to 1 inside the scattering object and 0 outside. For very small angles in the immediate vicinity of the central peak (i.e. 000 node), equation (3.1) simplifies:

$$I = \frac{F^2}{Vv_c} \left| \Sigma(q) \right|^2 \qquad (3.1b)$$

This expression depends only on the *shape and size* of the scattering body. It contains no information on the crystal structure. As such, small angle neutron scattering is a powerful technique for studying both crystalline and amorphous particles. The main limitation is that the central peak is usually very narrow and can't be distinguished from the transmitted beam. The peak becomes broader as the size of the scattering object decreases. When the scattering object is less than about 100 nm, the central peak is easily distinguished and useful information may be obtained on the scattering object [145].

For the simple case of a dilute system of identical, randomly-distributed particles,

the intensity of the central peak is given by [145-147]:

$$\frac{dS}{d\Omega}(q) = (\rho_p - \rho_m)^2 \left|\Sigma(q)\right|^2 / n \qquad (3.2)$$

The new quantities in this equation are the total number of precipitate particles, n, and the *neutron scattering-length density* of the precipitate, ρ_p, and of the matrix, ρ_m. We also introduced, the *differential scattering cross-section*, $dS/d\Omega$, which has units of $(m^2.Sr^{-1})$. This quantity is directly proportional to the scattering intensity and frequently the two terms are used interchangeably.

The aim of a neutron scattering experiment is to measure the scattering intensity as a function of the scattering vector. An example of the experimentally obtained data is shown in figure (3.11) (see p. 100). Information on particle size, shape and number is obtained by fitting the experimental data to the theoretical expressions of the form factor. The details are described briefly below.

3.3.1.1 Number of Particles:

The function, $\Sigma(q)$, has the important property of being equal to the total scattering volume when the scattering angle is equal to zero. As a result, extrapolation of the experimentally measured intensity to $q = 0$, would provide an estimate of the total precipitate volume. Given the size of an individual particle, one is able to calculate the number of precipitate particles [145].

3.3.1.2 Particle Radius:

If the precipitate particles are spherical, the average value of the form factor is given by [145]:

$$\Sigma(q) = V \exp\left(2\pi^2 q^2 r_G^2\right) \tag{3.3}$$

where r_G is the Guinier radius. For a spherical particle, the Guinier radius, r_G, is related to the particle radius, r, by the equation: $r_G = (3/5)^{1/2} r$. The value of r_G is calculated from the slope of the Guinier plot (log (I) vs. q^2).

3.3.1.3 Volume Fraction:

The precipitate volume fraction is related to the integrated intensity through the relations [146]:

$$\frac{1}{V_s}\int \frac{dS}{d\Omega}(q)d^3q = f_v(1-f_v)(\rho_p - \rho_m) \tag{3.4}$$

In this equation, V_S is the volume of the system and f_v is the precipitate volume fraction. In addition, to the above quantities, it is also possible to obtain information on the precipitate shape and size-distribution [146]. In the present investigation, we used TEM to study the shape and size-distribution of the particles.

3.3.2 Experimental Details:

We used SANS to study the kinetics of NbC precipitation in alloy M. An annealing temperature of 700°C was chosen in order to prevent the onset of recrystallization and to

limit the extent of recovery. In this way, we are able to ensure that the observed changes in the scattering intensity are solely due to precipitation. The samples were solution treated at 1225°C for 20 hrs to ensure the complete dissolution of NbC. The specimen were then deformed to (true) strains of 10%, 18% and -36%. The first two samples were deformed in tension (12.5 mm diameter), the third was cold-rolled. A fourth sample was used in the undeformed condition.

For each of the above samples, the scattering intensity was measured following annealing treatments of 20 to 2×10^6 sec (at 700°C). All of the annealing treatments corresponding to a given deformation were carried out on a *single* sample. Thus, the sample would be annealed for a given time increment, before being quenched and studied by SANS. Upon completion of the scattering measurement, the sample is annealed again for an additional increment of time and the scattering intensity is re-measured. This approach eliminates sample-to-sample variations and allows us to calculate the precipitate and number fraction more accurately. An important disadvantage of this approach is the large uncertainty associated with the magnitude of the shortest annealing times. In addition, we are not certain as to the effect of quenched-in vacancies on the precipitation kinetics. Finally, it is worth pointing out that for the first 3600 seconds, the samples were aged in a salt-bath. Further ageing was carried out in a conventional furnace, with the sample sealed under vacuum.

The neutron scattering measurements were carried out using the conventional

small-angle neutron scattering facility (SANS-2) at the GKSS Institute in Geesthacht, Germany. The neutron wavelength was 0.53 nm. A 2-dimensional detector was positioned at distances between 1 and 20m from the sample. This provided a scattering vector interval ranging from 0.02 nm^{-1} to 2.5 nm^{-1}. Because of the ferromagnetic nature of the alloy at room-temperature, a horizontal magnetic field was applied perpendicular to the incoming neutron beam in order to fully align the magnetic moment of the sample. We determined that an applied field of 2 Tesla is sufficient to achieve full alignment under the present conditions. The application of the magnetic field meant that only nuclear scattering occurred in the horizontal plane, while both nuclear and magnetic scattering occurred in the vertical plane. We are thus able to isolate the nuclear scattering component.

We also investigated the effect of sample orientation on the scattering measurements. To that end, some of the samples were measured twice, once with the deformation direction parallel to the magnetic field and once with the deformation direction perpendicular to the field. The scattering spectra were identical in both cases.

Finally, selected aging conditions were examined using transmission electron microscopy. The TEM measurements were used to complement and verify the present SANS work.

3.3.3 Results and Discussion:

The scattering data was processed using the standard methods described by Kostroz [147] and Bacon [148]. For each sample, the differential scattering cross-section was extracted from the measured horizontal scattering intensity. Figure (3.11) is a plot of the difference between the differential scattering cross-sections in the solution-treated and annealed states vs. the scattering vector. The evolution of the curve is attributed to the progress of NbC precipitation.

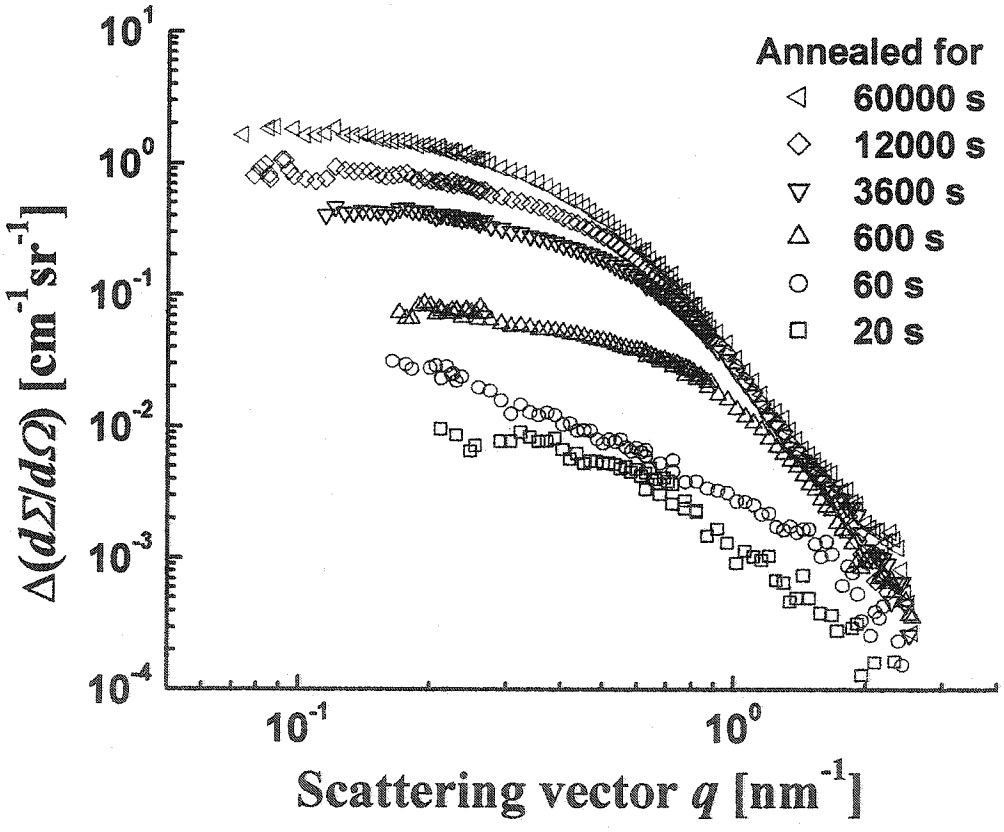

Figure (3.11): *The difference between the differential scattering cross-sections of the annealed and solution-treated samples is plotted as a function of the scattering vector. Note that the scattering cross section is expressed per unit volume (hence the units).*

The precipitate volume fraction, f_v, was estimated from equation (3.4). The integrated intensity was calculated from the data presented in figure (3.11) using a q^{-4} extrapolation for values of q outside the measured range. This extrapolation leads to a high uncertainty at the shortest aging times. The time-evolution of the precipitate fraction is shown in figure (3.12). The effect of deformation on the precipitation kinetics is clearly evident; It takes 10^4 sec for complete precipitation to take place in the most highly deformed sample, compared to10^6 s in the undeformed sample. The results for the 10% sample should be interpreted with caution. This sample was accidentally decarburized during the initial solution-treatment. The carbon content of the sample is ~0.09wt%.

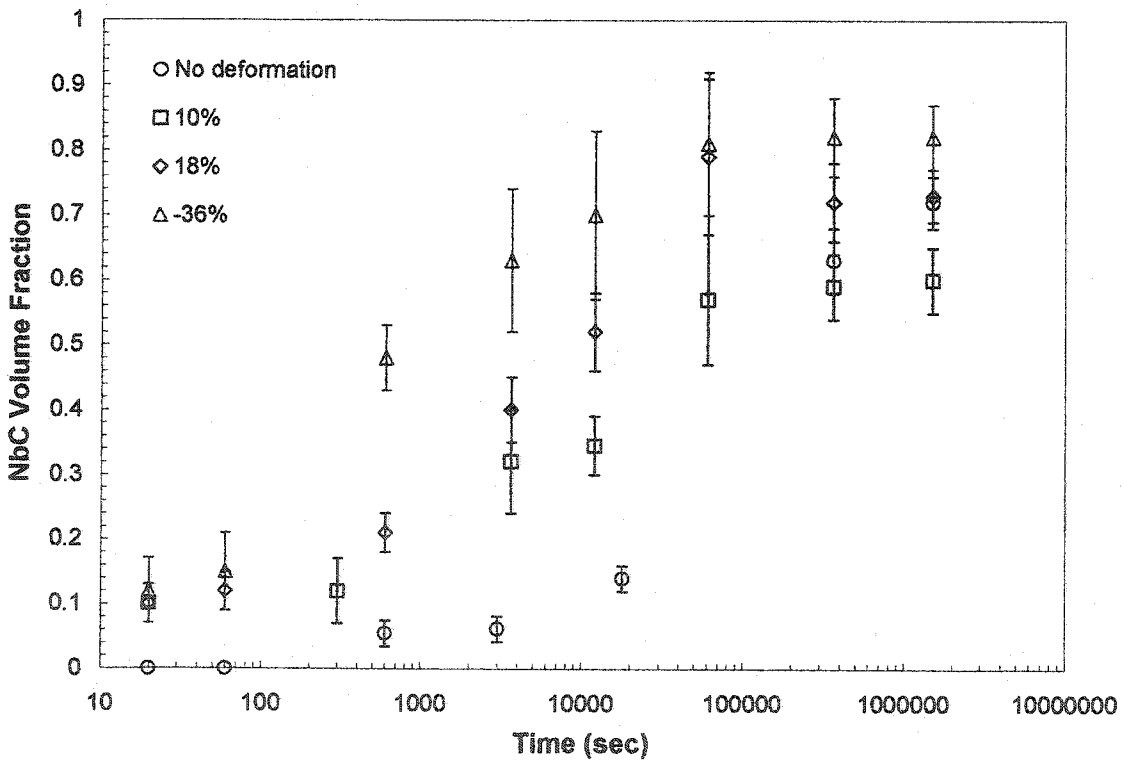

Figure (3.12): *Effect of deformation on the evolution of the precipitate volume fraction in alloy M at 700°C.*

The average size of the NbC precipitates was estimated using the approach described in section (3.3.1.2). The results are plotted in figure (3.13). To a first approximation, the precipitates appear to be 'growing' at the same rate in all four samples. This is particularly true at the early stages of the annealing treatment. This implies that Nb is diffusing over short distances in order to arrive to the precipitates. If this was not the case, smaller particles would be expected in the highly deformed samples which contain a greater number of precipitates. In microalloyed steels, deformation results in a significant refinement of the particle size [108]. This implies that in microalloyed steels Nb has to diffuse over long distances, which is consistent with the concentration of Nb being very low in these alloys.

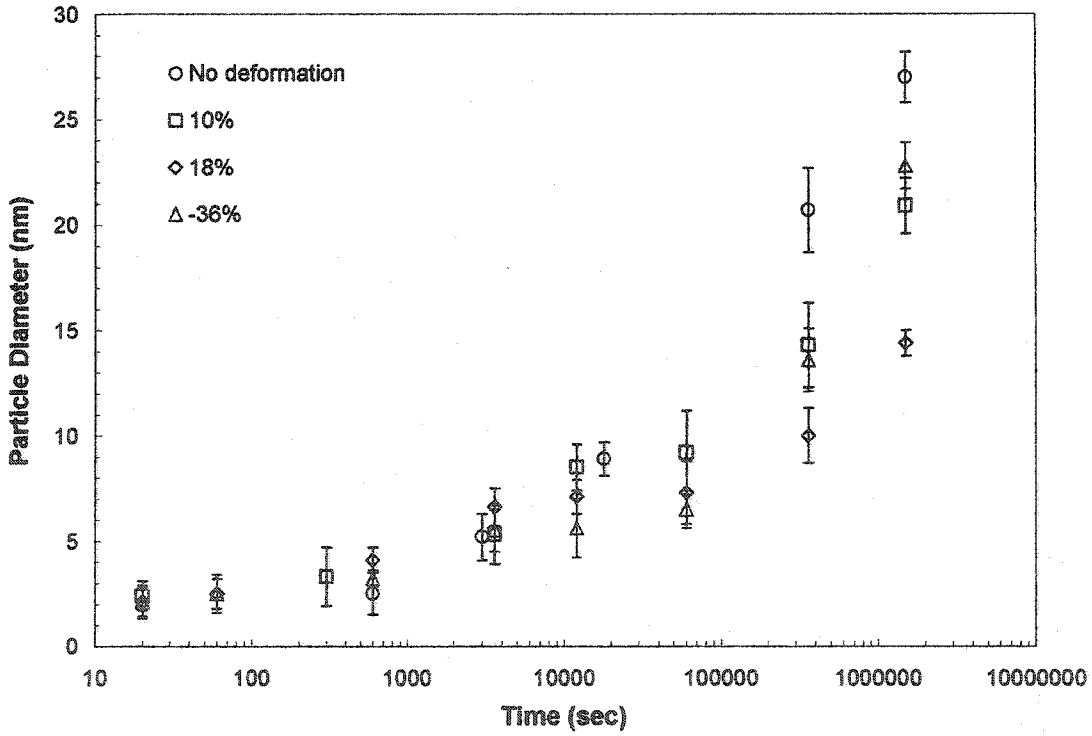

Figure (3.13): *Effect of deformation on the evolution of particle diameter in alloy M at 700°C.*

The number of precipitate particles was estimated from the intercept of the Guinier plot. The results are shown in figure (3.14). It is clear from the figure that nucleation takes place very quickly in the deformed samples. For the times investigated here, nucleation is already complete. This observation is in agreement with our model which predicts that nucleation is complete within a fraction of a second, in most cases. In contrast, nucleation is very sluggish in the undeformed sample. The results on number density and particle size, suggest that the enhancement of precipitation kinetics by deformation is largely due to an increase in the number of available nucleation sites (dislocations). This result is widely accepted in the literature [9].

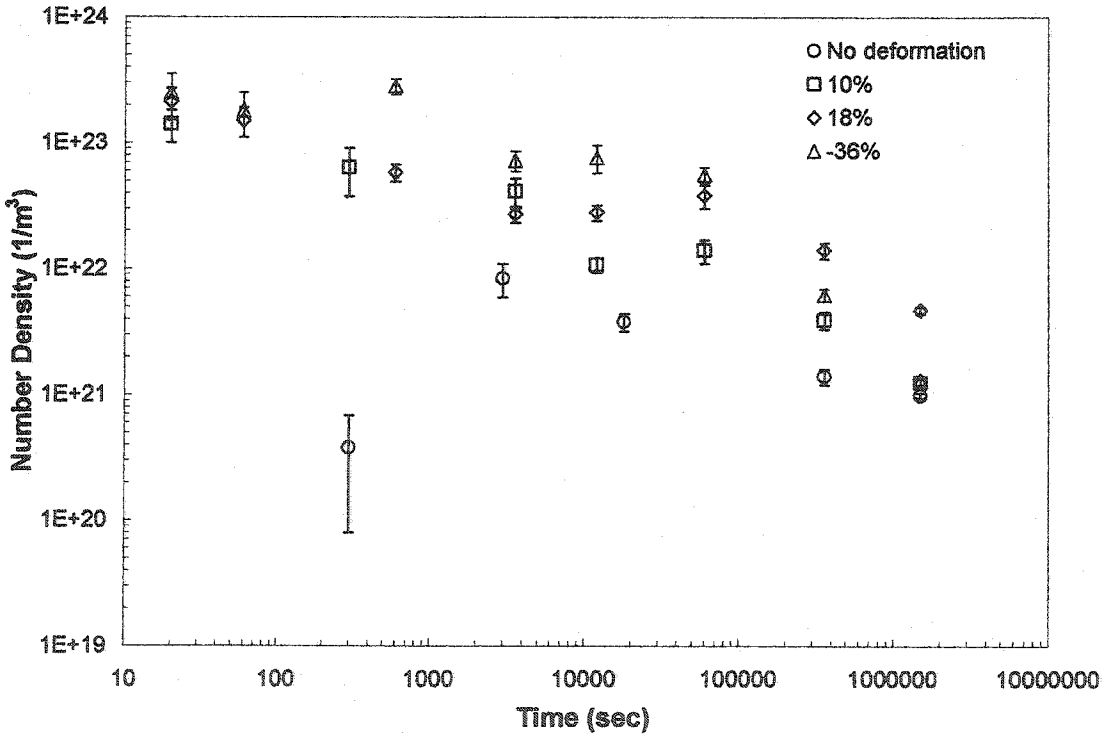

Figure (3.14): *Effect of deformation on the precipitate number density in alloy M at 700°C.*

The present neutron scattering work is complemented by extensive TEM measurements on extraction replicas. The evolution of the particle-size distribution of the undeformed sample has already been discussed in section (3.3.2.3). In addition, extraction replicas of the 10% and 18% samples were prepared for an annealing time of 12000 seconds. The average particle-size as measured from the extraction replicas was 6.9 nm in the 10% sample and 7.3 nm in the 18% sample. These values compare favourably with the neutron scattering estimates of 8.5 and 7.1 nm.

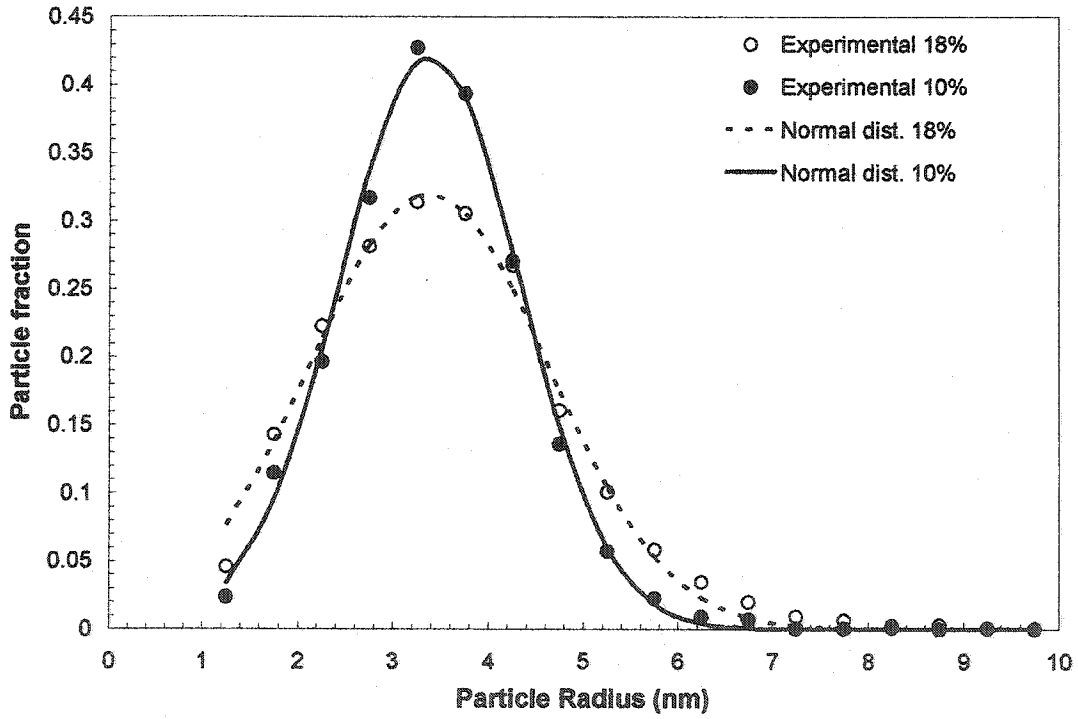

Figure (3.15): *Particle size distributions for alloy M, deformed by 10 and 18% , annealed for 200 minutes at 700°C.*

The particle-size distributions for the 10 and 18% samples are shown in figure (3.15). Both are accurately described by a Gaussian function. The standard deviation is $r/2.5$ in the case of the 10% sample and $r/2$ in the case of the 18% sample. This result is credible

because each distribution involved ~ 10,000 particles. We believe that the observed broadening of the size-distribution is due to the greater complexity of the deformed structure of the 18% sample. More intersections of dislocations are formed in the 18% sample. It is expected that the nuclei formed on these sites will have initial shapes and sizes that differ from those of the nuclei formed on straight segments of dislocations. In addition, the two types of nuclei may, initially, grow at different rates. It is argued that these initial variations persist, resulting in a broader distribution in the 18% sample.

3.4 Double-Deformation Experiments:

Double deformation tests of the type described in section (1.2), were used to study the softening kinetics of the model alloys at 700, 800, 875 and 945°C. We used tensile samples with a diameter of 4 mm and a gauge length of 16 mm. The samples were deformed at room temperature to a true flow-stress of 350 MPa. In this way, we are able to ensure that (to a first approximation) the various samples have the same initial dislocation density. Following the annealing treatment, the yield-stress was re-measured and the softening fraction was estimated using the *1% total-strain* method. In section (3.4.1) some of the most important experimental details are discussed. The effects of Nb and C (in solution) on the flow stress are discussed in section (3.4.2). A summary of the observed softening kinetics is presented in section (3.4.3).

3.4.1 Experimental Details:

The initial decarburisation and homogenization treatments (section 3.1.2) resulted in very large grain sizes in the range of 0.5 - 2 mm. This would leave 10 to 50 grains within the cross-section of the tensile samples used here. Strong single-crystal effects are then expected to appear on the stress-strain curve. To deal with this problem, it was necessary to grain-refine the model alloys. This was achieved by cold-rolling and annealing the samples twice to induce recrystallization. Both deformations were of the order of 40%. An annealing temperature of 1250°C was used to ensure the complete dissolution of any precipitates formed on heating. The annealing times varied from a minimum of 2 minutes in the case of alloy O, to a maximum of 6 minutes in the case of alloy M. These times were carefully chosen with two concerns in mind: First, the times should be long enough to ensure the dissolution of the precipitates formed during heating. Secondly, the times should be as short as possible in order to prevent excessive grain-growth. The final grain-sizes achieved in this way ranged from 100μm in the case of alloy M, to about 300μm in alloy O.

3.4.2 Effect of Nb and C on the Flow-Stress

Figure (3.16) is a typical example of the stress-strain curves obtained during the deformation of the model alloys. The yield stress is very low due to the relatively large grain-size and the total dissolution of the precipitates. Linear work-hardening is observed with an average work-hardening rate of ~G/150. This result is consistent with the low-

temperature deformation behaviour of FCC metals [149].

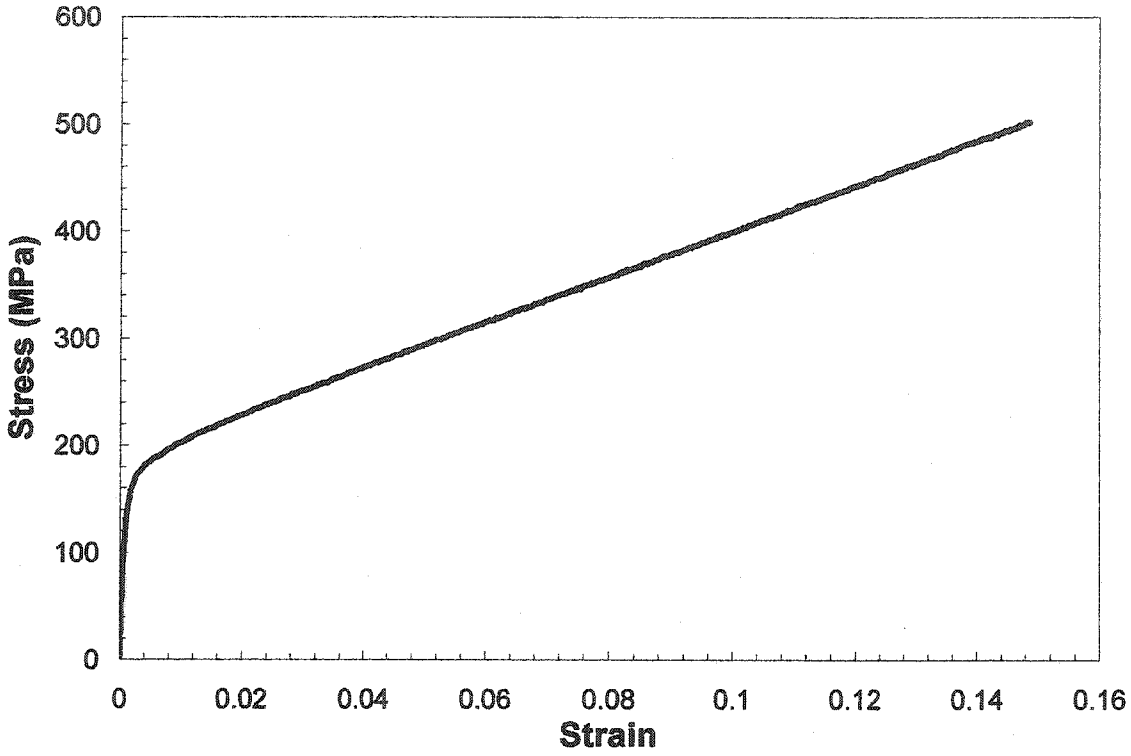

Figure (3.16): *Stress-strain curve of alloy M, deformed at room-temperature. Linear work-hardening is clearly seen.*

The composition dependence of the yield-stress and work-hardening rate were investigated in detail. In figure (3.17) we plotted the yield-stress as a function of the Nb and C concentrations. Each point represents the average yield-stress obtained from 5 to 10 samples. Theoretically [150], the critical resolved shear stress is expected to increase as $C^{1/2}$ or $C^{2/3}$. Given the large uncertainty of the experimental data, the two approaches are indistinguishable within the present composition range. For simplicity, we fitted the experimental data linearly to obtain:

$$\sigma_y = 140.2 + 47.4(at\%C + 0.95at\%Nb) \quad (3.5)$$

The observed dependence on the C and Nb concentration is in general agreement with experimental work on Stainless-steels [151].

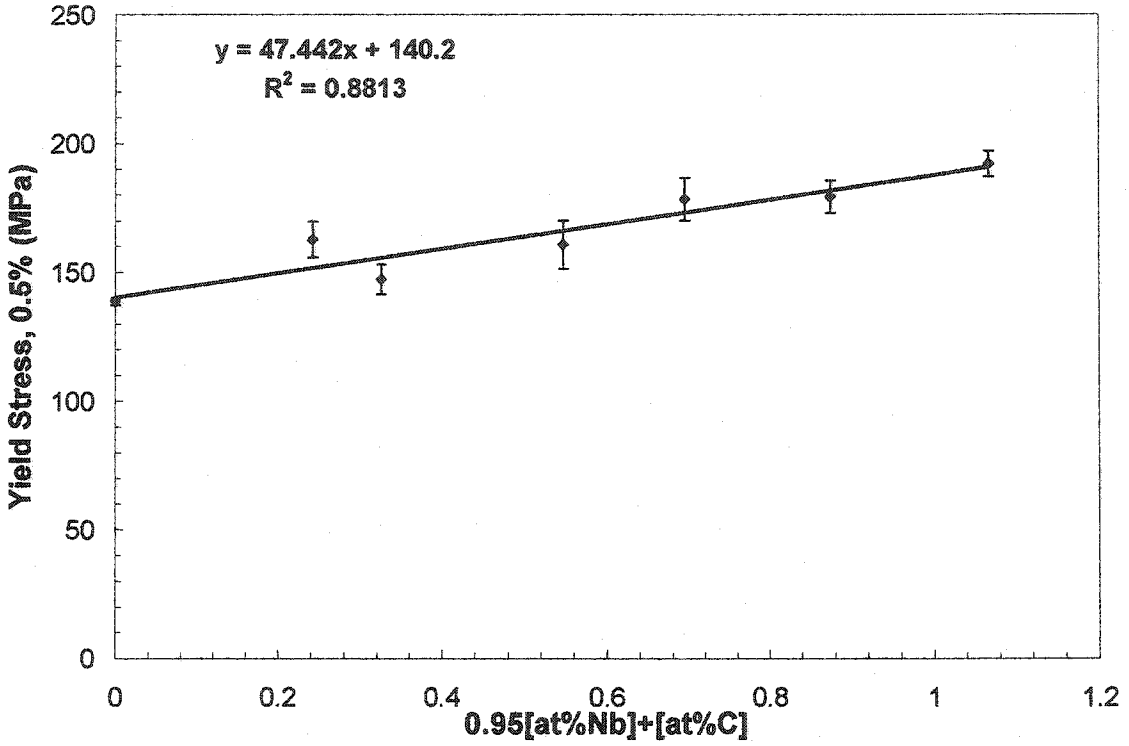

Figure (3.17): *Dependence of the yield-stress on the Nb and C concentrations.*

The composition dependence of the work-hardening rate is shown in figure (3.18). Once again, a linear concentration dependence was used to fit the data:

$$\theta = 1675.6 + 840.4(at\%C + 0.16at\%Nb) \quad (3.6)$$

The effect of C on the work-hardening rate is seen to be significantly greater than that of Nb. In contrast, the two elements had essentially the same effect on the yield-stress. The difference in behaviour might be related to the fact that C is much more mobile than Nb. As such, it is able to interact more strongly with the dislocations during work-hardening.

In conclusion, equations (3.5) and (3.6) may be combined to provide a complete description of the stress-strain curve as a function of the Nb and C contents. In chapter (4), this expression is used to estimate the decrease in solid-solution hardening as a result of precipitation.

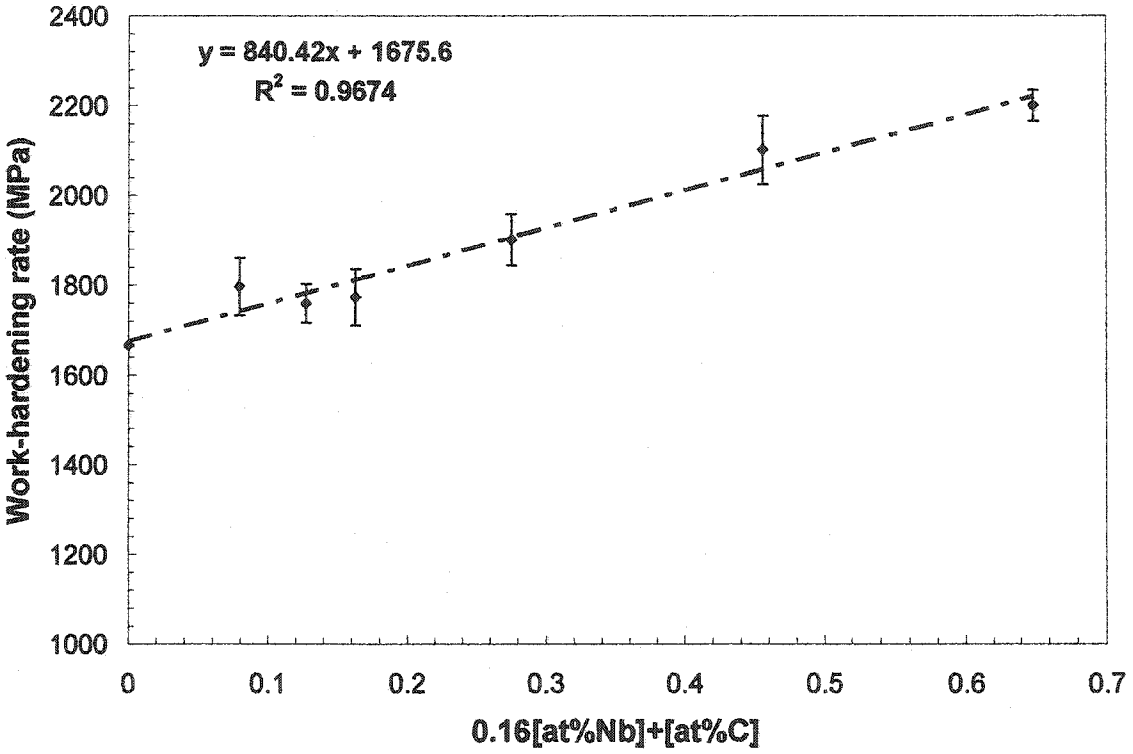

Figure (3.18): *Effect of niobium and carbon in solution, on the work-hardening rate.*

3.4.3 Softening Kinetics:

The interaction between precipitation and recovery was investigated using the double-deformation test. Figures (3.19)-(3.25) are the softening-curves of alloys O, M, M1, M2, M3, L and L1, respectively. The error bars were estimated based on the reproducibility

of the measurements as well as the uncertainty in the measured stresses. In most of the samples, the observed softening is due to recovery, with no contribution due to recrystallization. Partial recrystallization was observed in alloy L1 at 945°C and alloy O at all temperatures. The recrystallized fractions were evaluated quantitatively in a small number of samples. The numerical values are shown in a box next to the softening data (see figure 3.19 for example).

Detailed discussion of the softening data is deferred to chapter (4). For the time being, a number of observations are briefly reviewed:

- The temperature-dependence of the softening curves is consistent with increased particle pinning at lower temperatures. This is clearly seen in the alloys with the highest Nb and C contents. In alloy M, for example, a plateau or a hump is observed at all temperatures as a result of precipitation-hardening. The magnitude of the effect decreases with temperature as expected.
- Initial softening of the order of 10-20% takes place at all temperatures in all of the alloys. This is interesting in light of the fact that particle nucleation takes place very quickly as shown in section (3.4). This appears to support the argument that small precipitates (< 2 nm) are not very effective at pinning the dislocation structure.
- Recrystallization is very sluggish in alloy O, in spite of the fact that this alloy does not contain any Nb or C. Several factors could be responsible for this observation: The large grain-size (300μm) results in a small number of recrystallization nucleation-sites. Secondly, it appears that the applied *mode of deformation* was not

effective at creating the strain-heterogeneity which is needed for the nucleation of recrystallization. This is consistent with the fact that the applied deformation was uniaxial, small and totally inside stage II. The large grain-size is also important in this regard, because it results in fewer strain incompatibilities in the system.

- The softening data for alloy L at 945°C and alloy L1 at 875°C should be interpreted with caution. In both cases, the annealing temperature is about 30 degrees above the precipitate dissolution temperature. Ideally, the absence of precipitation should lead to a monotonously increasing fraction. This is not the case as seen in figures (3.24) and (3.25). This suggests that precipitates are formed in the above samples. We believe that the precipitates are formed during the heating up of the sample. The precipitates are not readily dissolved because the annealing temperature is only slightly above the dissolution temperature. For this reason, these two conditions will not be modelled in chapter (4).

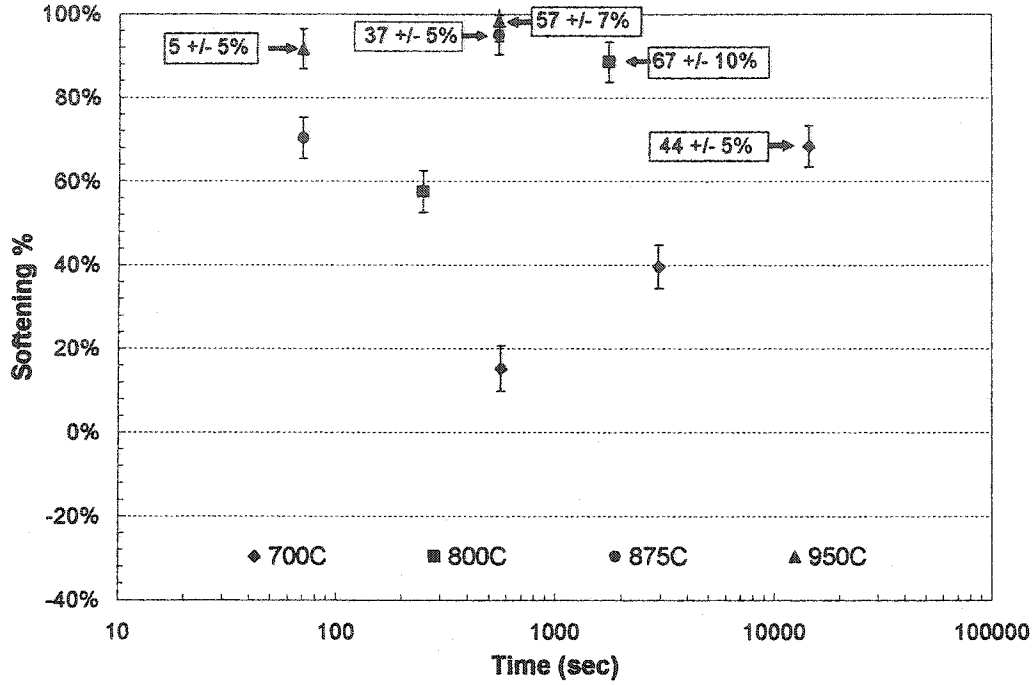

Figure (3.19): *Softening kinetics of alloy O. The optically measured values of the recrystallized fractions are shown inside the box.*

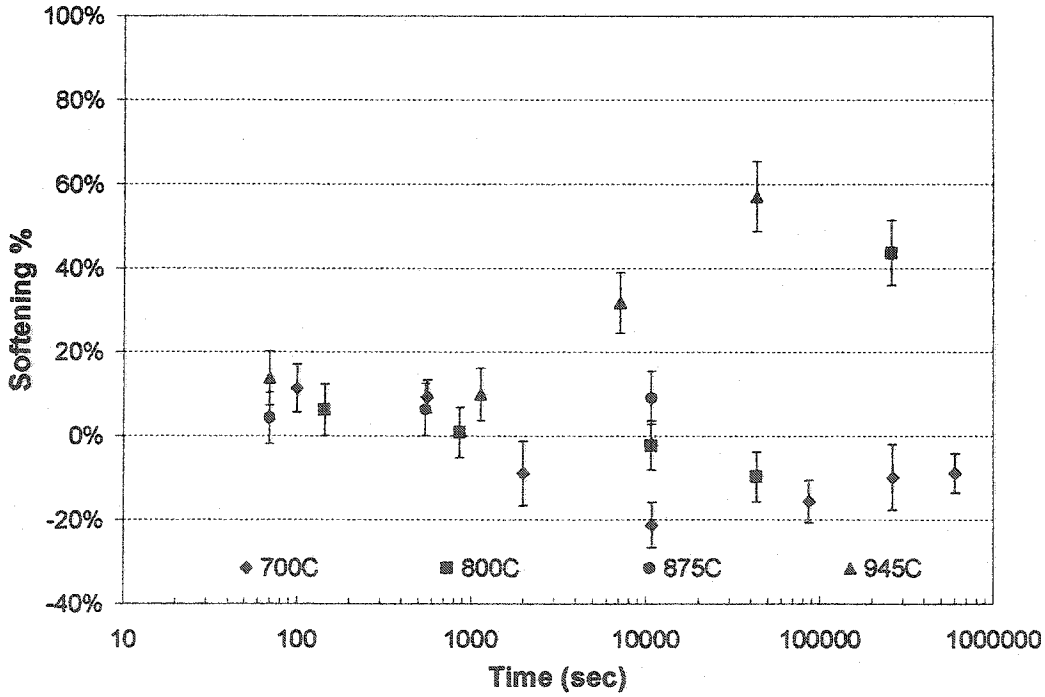

Figure (3.20): *Softening kinetics of alloy M.*

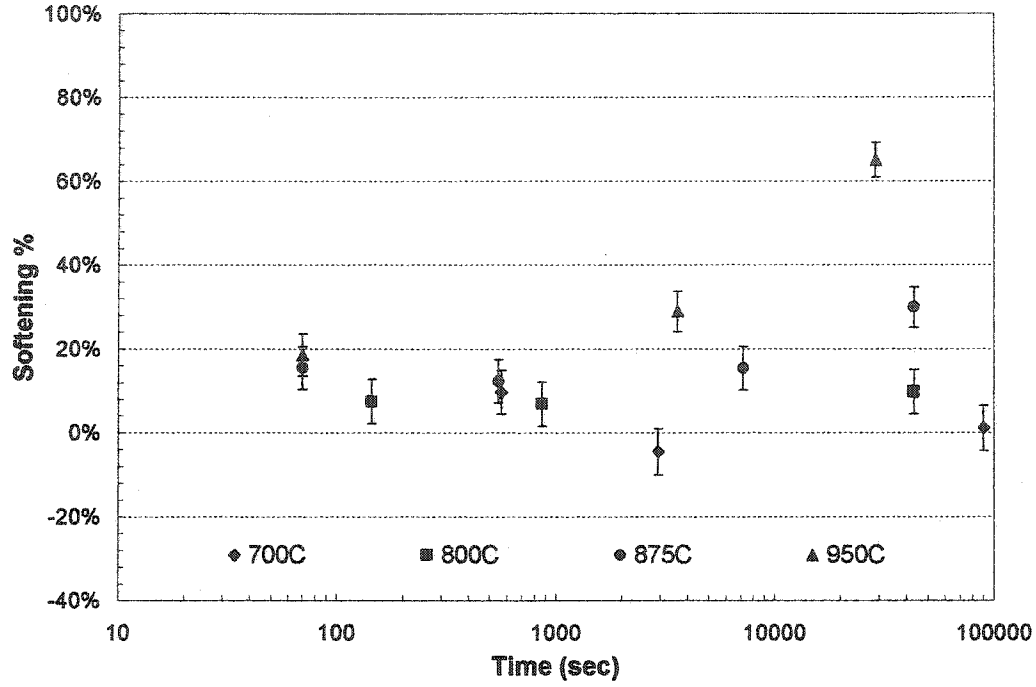

Figure (3.21): *Softening kinetics of alloy M1.*

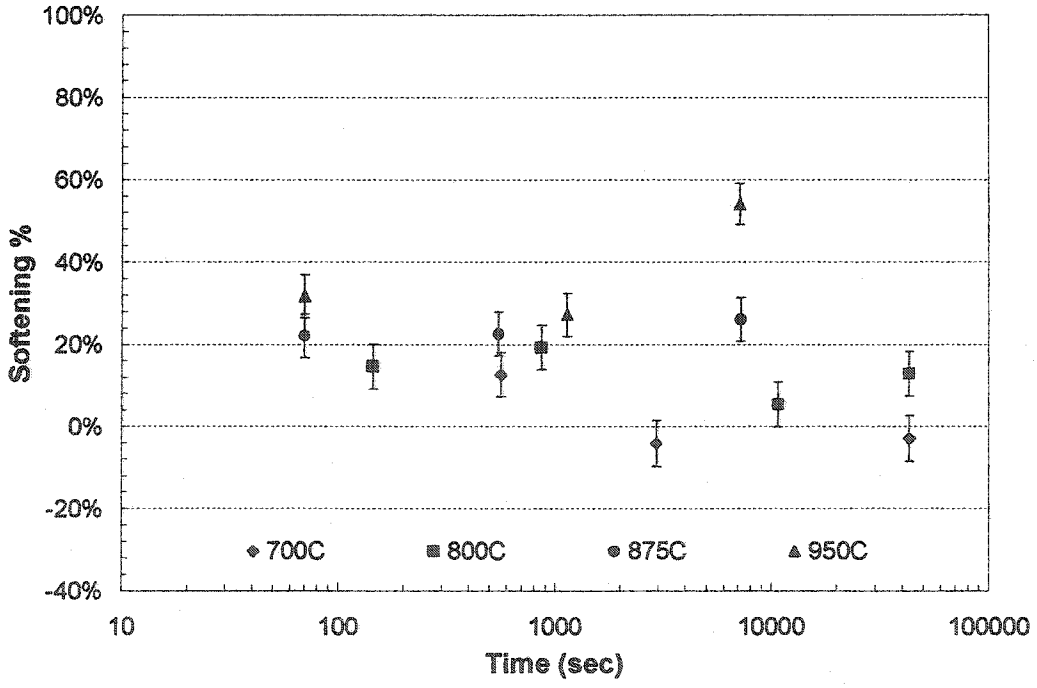

Figure (3.22): *Softening kinetics of alloy M2.*

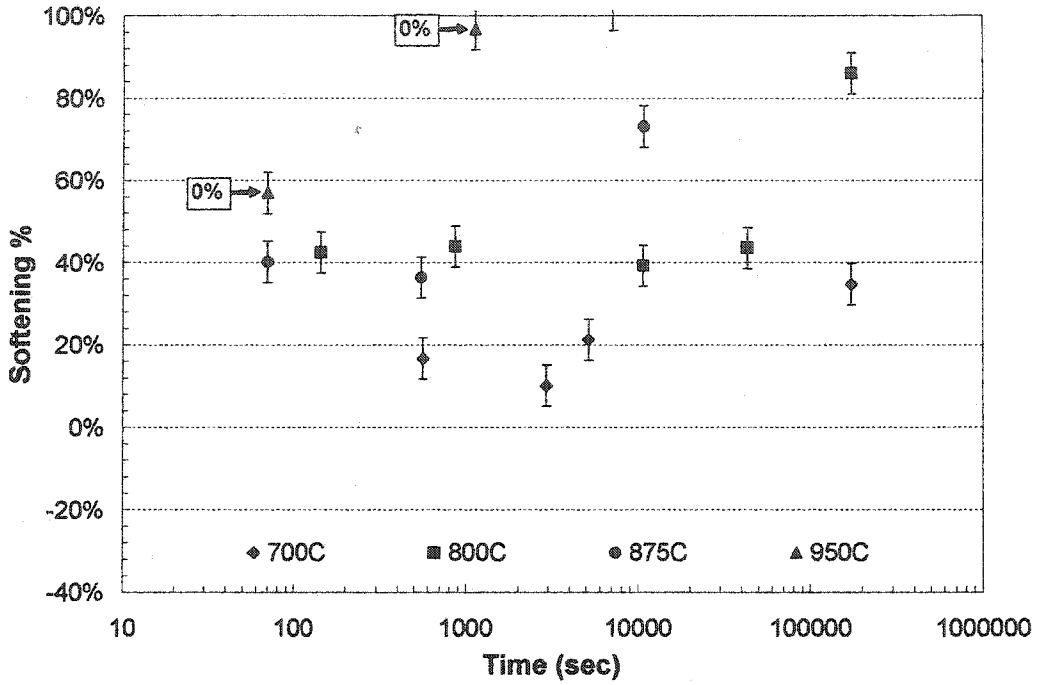

Figure (3.23): *Softening kinetics of alloy M3.*

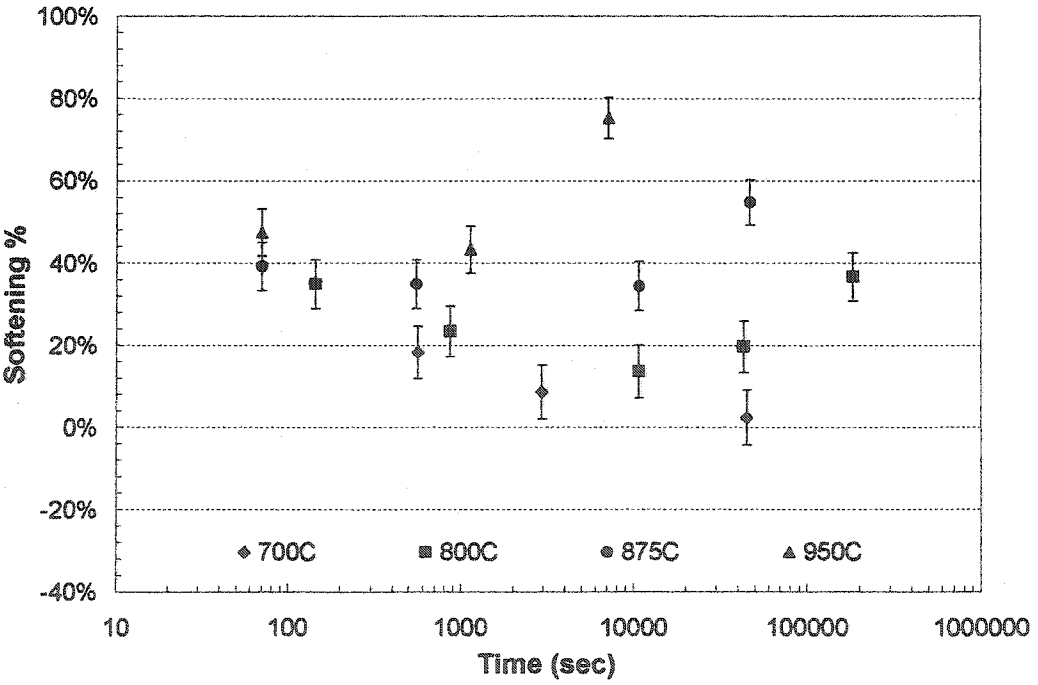

Figure (3.24): *Softening kinetics of alloy L.*

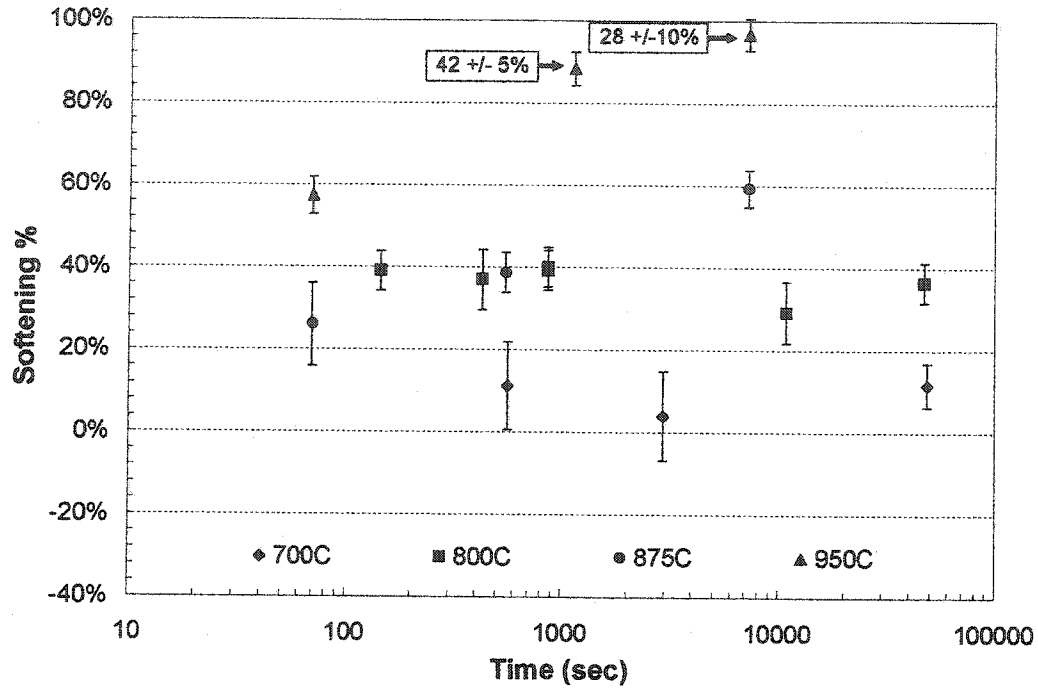

Figure (3.25): *Softening kinetics of alloy L1. The optically measured values of the recrystallized fraction are shown inside the box.*

Chapter 4:

Modelling and Discussion of Experimental Results

In this chapter the experimental results are analysed in terms of the physically-based model which was developed in chapter (2). This analysis serves two purposes: The experimental data allows us to identify the strengths and weaknesses of the proposed model. At the same time, the model provides a valuable insight into the process-interactions which lead to the observed softening-kinetics.

In section (4.1), the model is adapted to the *deform-and-anneal* treatments used in chapter (3). Special attention is given to the fact the yield-stress is measured at room-temperature. The modelling results are presented in three sections, (4.2)-(4.4). In the first section, we analyse the softening kinetics of alloy O, which is Nb- and C-free. The effect of *solute* Nb on the kinetics of recovery is discussed in section (4.3). For this purpose, we examine alloys L1 (0.33%Nb) and M3 (0.85%Nb) at 945°C, which is well above the precipitate dissolution temperature. The interaction between precipitation and recovery is discussed in section (4.4). Special attention is given to alloy M at 700°C. This conditions

was studied extensively using SANS, extraction replicas and double-deformation tests. As a result, detailed comparison with the model is possible.

A summary of the adjustable parameters used in the model is presented in section (4.5). The magnitude and meaning of these parameters are discussed in detail. This is followed by a discussion of the limitations of the model, section (4.6). A number of improvements are proposed in this section. These important improvements, however, come at the expense of simplicity.

4.1 Modification of the Model:

In chapter (2), we modelled the case in which deformation and annealing took place at the same temperature. The yield-stress was also measured at the annealing temperature. In contrast, the deform-and-anneal treatments of chapter (3), involved room-temperature deformation and high-temperature annealing. Following the completion of the heat-treatment, the yield-stress was measured at room-temperature. As a result, it is necessary to modify the model to reflect the method used in chapter (3).

Figure (4.1) is used to summarize the proposed modelling approach. The initial dislocation density is calculated from the flow-stress at room temperature. If heating from RT to the annealing temperature is instantaneous, then the dislocation density is unchanged

during heating. The initial flow-stress at the annealing temperature is related to the room-temperature value by a factor of μ_T/μ_{RT}. During annealing, the flow-stress and dislocation density decay as described in section (2.2). When the yield-stress is re-measured (at RT), the stress due to stored dislocations is estimated from the dislocation density at the end of annealing and using the RT value of the shear modulus. The room-temperature value of the modulus is also used for estimating the contribution due to precipitation-hardening.

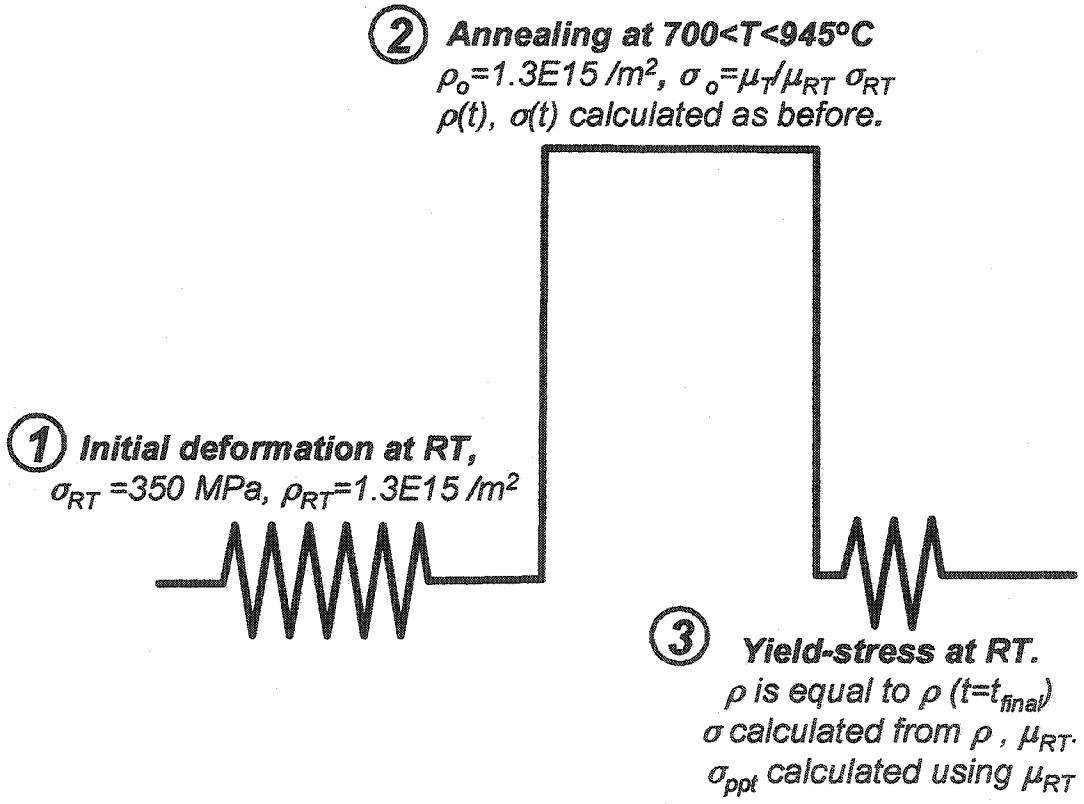

Figure (4.1): *The approach used to account for the fact that deformation, annealing and yield-stress measurements are carried out at different temperatures.*

4.2 Softening in the Absence of Nb and C.

Alloy O is a binary Ni-30%Fe alloy which does not contain any Nb or C. As a result, the effects of solute-drag and particle pinning are not relevant to the present discussion The microstructural evolution of alloy O is fully described by three parameters: i) the activation energy for recovery, U_a, ii) the activation volume, V_a, and iii) the number of recrystallization nuclei, N_{rex}. Once again, the activation energy is identified with that of bulk self-diffusion and the number of nuclei is calculated from equation (2.5), where k is an adjustable parameter. The values of the activation volume (V_a) and the nucleation constant (k) were adjusted to fit the experimental data (Table 4.1). The results are shown in figures (4.2)-(4.5), which correspond, respectively, to annealing at 700, 800, 875 and 945°C. In some figures, two recrystallization curves are shown. The solid curve is calculated based on the assumption that recrystallization can't proceed when the dislocation density is lower than 1×10^{13} /m^2. The dotted curve represents the case in which recrystallization is possible as long as $\rho>0$. Interestingly, recrystallization appears to come to a halt at 945°C as a result of rapid recovery. This point is discussed further in section (4.2.3). In the next two sections, the optimum values of the activation volume and the nucleation constant are discussed.

Temperature (°C)	Optimum value of V_a (b^3)	Optimum value of k
700	15	3×10^{-12}
800	20	1.5×10^{-10}
875	25	8×10^{-10}
945	30	8×10^{-9}

Table (4.1): *Values of the constants used to describe the softening behaviour of alloy O.*

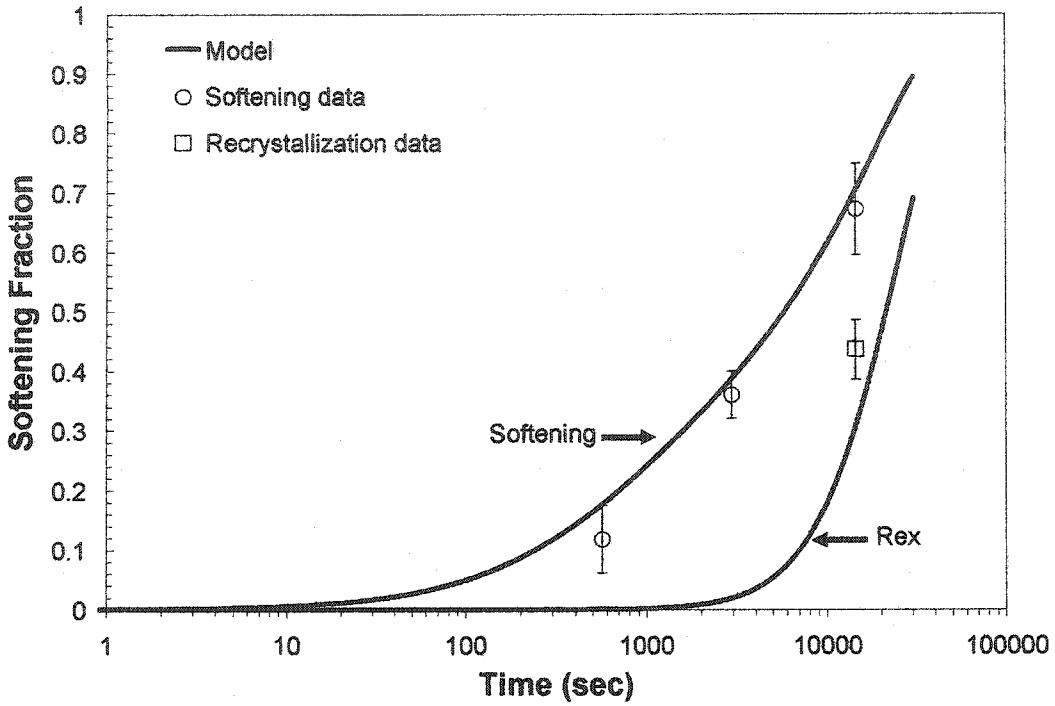

Figure (4.2): *Comparison of the predicted and measured softening and recrystallized fractions in alloy O at 700°C.*

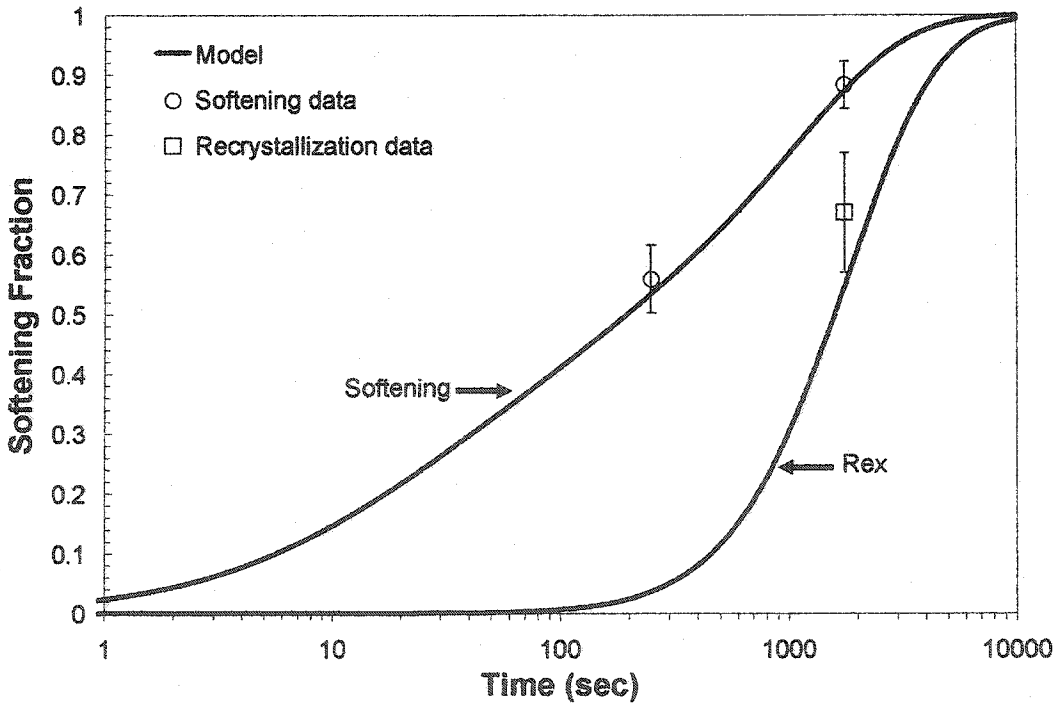

Figure (4.3): *Comparison of the predicted and measured softening and recrystallized fractions in alloy O at 800°C.*

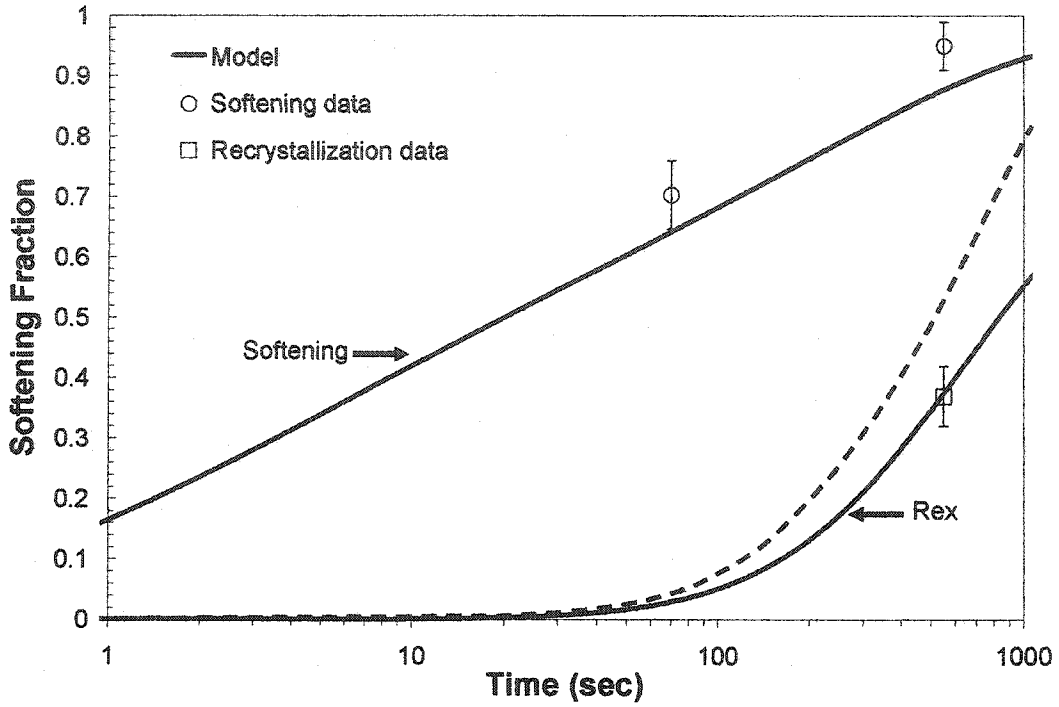

Figure (4.4): *Comparison of the predicted and measured softening and recrystallized fractions in alloy O at 875°C. Please refer to text for description of the dotted and solid curves.*

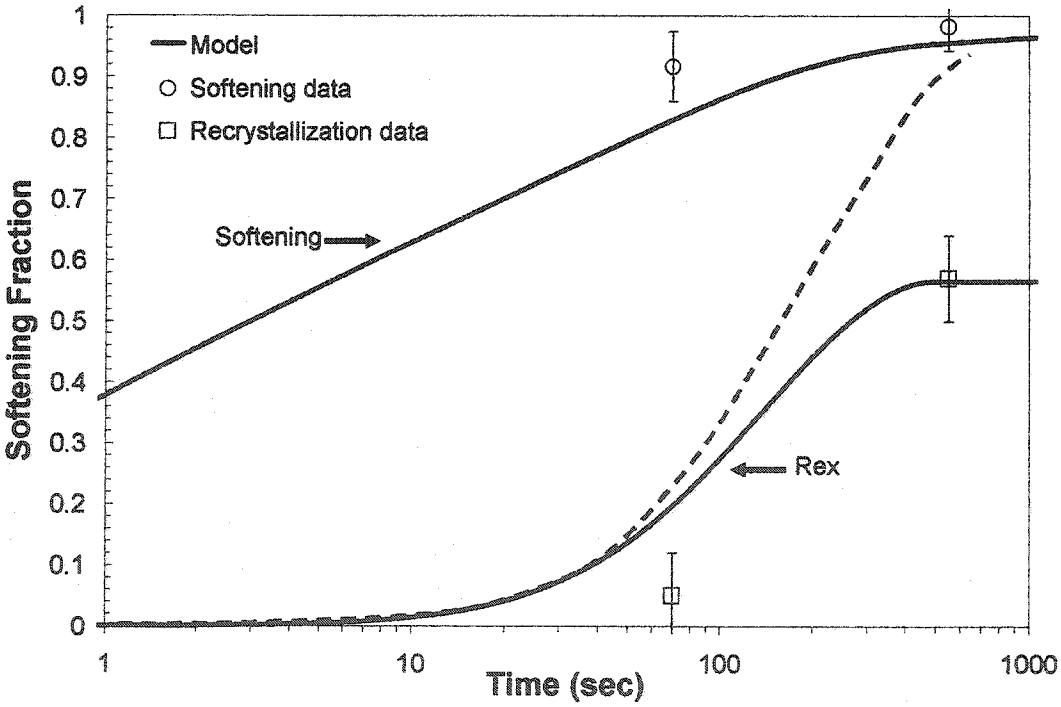

Figure (4.5): *Comparison of the predicted and measured softening and recrystallized fractions in alloy O at 945°C. Please refer to text for description of the dotted and solid curves.*

4.2.1 Optimum Value of the Activation-Volume (V_a):

Given the fact that very few data points are available at each temperature and given the large uncertainty associated with the measurements, the above values of the activation volume are viewed as crude estimates. In the absence of solute pinning, the activation volume is controlled by the spacing of jogs. Under these circumstances, equation (A2.1) simplifies to:

$$V \approx b^2 l = \frac{b^2 k_1}{\sqrt{\rho}} \qquad (4.1)$$

The activation volume is expected to increase gradually in the course of recovery. As a result, the values shown in table (4.1) should be interpreted as *average or effective* values of the activation volume. These average values increase with temperature because dislocations disappear more quickly at higher temperatures.

4.2.2 Optimum Number of Recrystallization Nuclei:

The number of recrystallization nuclei is calculated from equation (2.5). The constant, k, is an adjustable parameter that reflects the fact that only some of the potential nuclei are formed. In chapter (2), we pointed out that the value of k is expected to fall in the range of 5×10^{-2} - 5×10^{-5}. Attempts to model the recrystallization of alloy O using values within the above range resulted in complete recrystallization within 1-10 secs. Clearly, this is inconsistent with the experimental data which indicate that more than 1000 secs are

needed for complete recrystallization. It was necessary to use very small values of k in order to reproduce the experimental data. Unfortunately, these values are not physically meaningful as they imply that less than one recrystallized grain will form within the tensile samples used.

In chapter (3) we pointed out that the experimentally observed recrystallization kinetics are very sluggish because the applied deformation is small and uniform. Under these circumstances, the nucleation of recrystallization is difficult and the assumption of site-saturation is not applicable. In the present section, our interest in recrystallization is limited to the need to separate-out the contributions of recovery and recrystallization to the total softening. This purpose is served by the assumption of site-saturation and the values of k in table (4.1). As a result, these values are retained in spite of the fact that they are not physically meaningful.

4.2.3 Competition between Recovery and Recrystallization:

In figures (4.4) and (4.5), the model indicates that recrystallization would come to halt as a result of the depletion of dislocations by recovery. Unfortunately, additional samples of alloy O were not available to test the validity of this prediction. In the case of alloy L1 (see figure 4.6), recrystallization is experimentally observed to come to a halt when the sample is annealed for long times at 945°C. This result is equally likely in the case of alloy O at 875 and 945°C. In both cases, the softening fraction is in excess of 95%, while

the recrystallized fraction is less than 50%. Starting with the experimental softening and recrystallized fractions, one can calculate the dislocation density in the unrecrystallized grains. This leads to a dislocation density of 1×10^{13} /m^2 when alloy O is annealed for 10 minutes at 945°C. Clearly, this value is too small and recrystallization is expected to come to a halt.

The above situation is very uncommon. It is observed in the present experiments, because the nucleation of recrystallization is very sluggish. This is not expected to affect our results, however, because we are mainly concerned with the interaction between precipitation and recovery in the absence of recrystallization.

4.3 Softening with Nb and C in Solution:

The precipitate dissolution temperatures of alloys L1 and M3 are, respectively, 835 and 921°C. The effect of *solute* Nb on the softening kinetics is examined by comparing the softening kinetics of alloys O, L1 and M3 at 945°C. Once again, the experimental data is modelled by adjusting the values of the activation volume and the number of nuclei (Table 4.2). The results are presented in figures (4.6) and (4.7). The data points at the shortest times are believed to underestimate the actual softening fraction as a result of limited precipitation during heating.

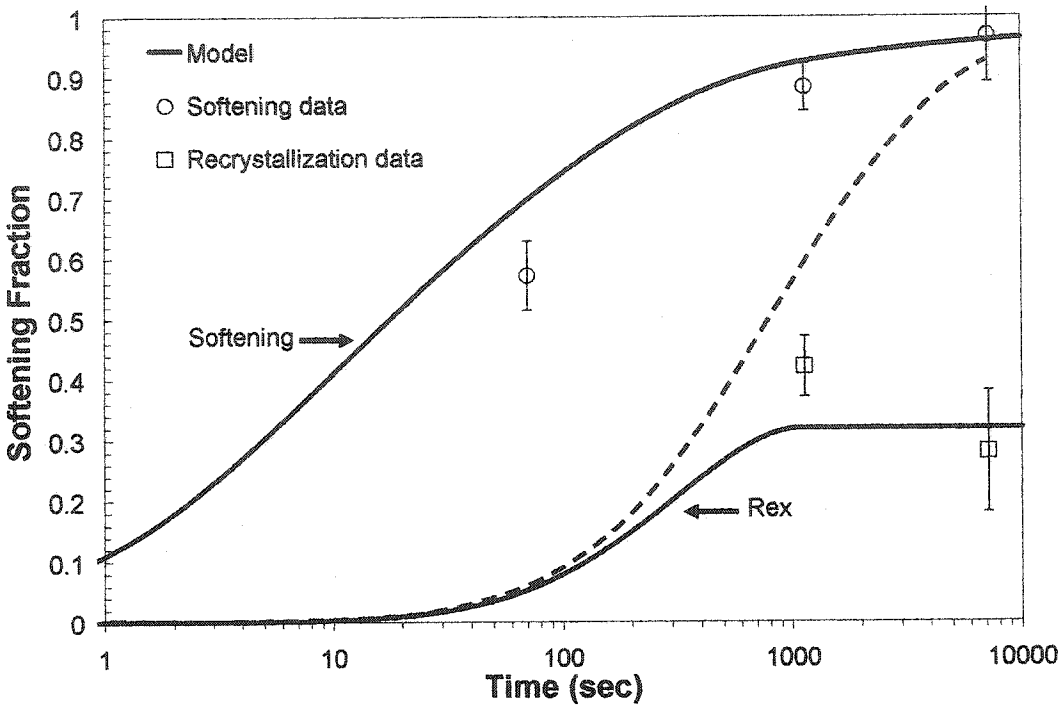

Figure (4.6): *Effect of solute-Nb on the kinetics of softening and recrystallization is examined using alloy L1 at 945°C. The dotted and solid curves are interpreted as in the previous section.*

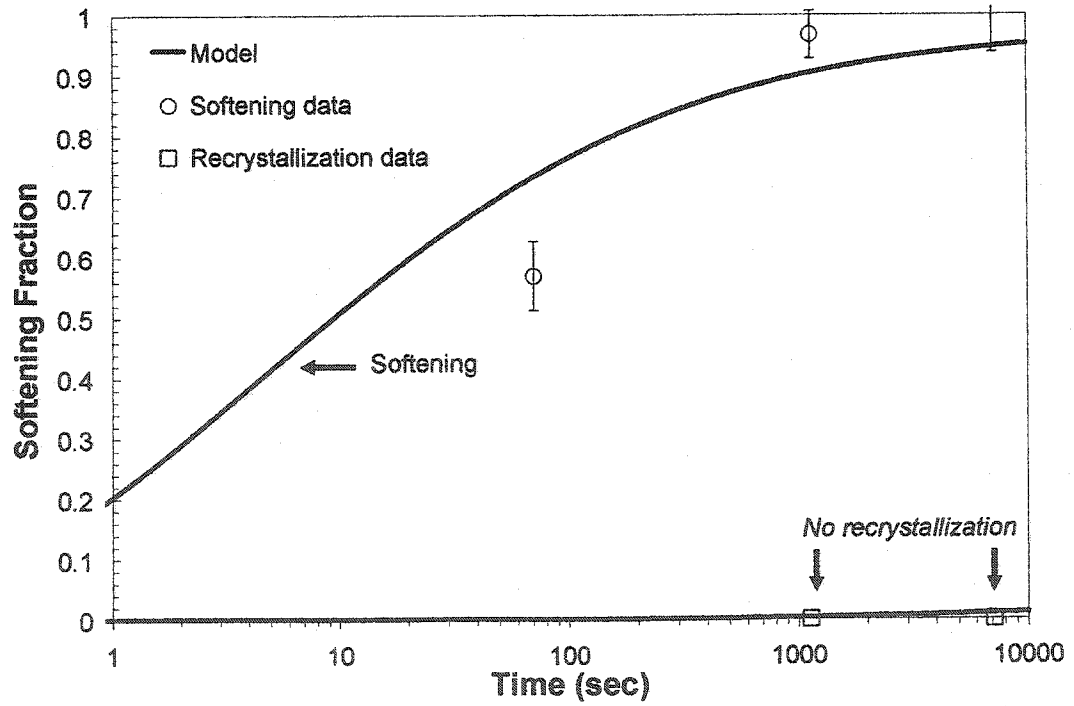

Figure (4.7): *Effect of solute-Nb on the kinetics of softening and recrystallization is examined using alloy M3 at 945°C.*

Alloy	Optimum value of V (b^3)	Optimum value of k
O (Nb and C-free)	30	8×10^{-9}
L1 (0.33%Nb, 0.009%C)	15*	2.2×10^{-4}
M3 (0.85%Nb, 0.009%C)	20*	3×10^{-5}

Table (4.2): *Values of the constants used to describe the softening behaviour of alloys O, L1 and M3 at 945°C. *The difference between the activation volumes of alloys L1 and M3 is not significant given the uncertainty of the measurements.*

The effect of *solute Nb on recovery* is discussed in terms of the activation volume. The addition of Nb is observed to lower the activation volume from $30b^3$ in alloy O, to ~ $15b^3$ in alloy L1. This behaviour is consistent with the predictions of the simple recovery model of Appendix (A2). Increasing the Nb content from 0.33% to 0.85% does not appear to result in any additional reduction in the activation volume. This result suggests that under most circumstances the depletion of Nb during precipitation will not significantly change the activation volume. It also implies that a single activation volume could be used for all of the compositions under investigation. For the rest of this work, an *average* activation volume of $20b^3$ is used. This value is assumed to be independent of composition and temperature.[a]

The effect of *solute Nb on recrystallization* is quantified by comparing the recrystallized fractions in alloys O, L1 and M3 after 1000 sec at 945°C. In the case of alloy O, the recrystallized fraction is ~60%. This is compared to 30% in alloy L1 and 0% in M3.

[a] We intended to study the temperature dependence of the activation volume of alloy L1. Unfortunately, the available data for alloy L1 at 875°C could not be modelled, perhaps as a result of precipitation during the heating-up step. See section (3.4).

The present result is not surprising considering the very high Nb concentrations in the model alloys. Consequently, recrystallization is not expected to interfere with our effort to study the interaction between precipitation and recovery. For all of the situations studied in the next section, it will be assumed that recrystallization does not take place.

4.4 Interaction between Precipitation and Recovery:

In total, 28 combinations of composition and temperature were considered in the present investigation. Seven of these conditions have already been analysed in sections (4.2) and (4.3). The remaining conditions are discussed in the present section. We start by examining precipitation in alloy M at 700°C. Extensive experimental data is available for this condition. In section (4.4.2), the analysis is extended to include the remaining alloys at 700°C. Softening at 800°C, is considered in section (4.4.3). Softening at 875°C and 945°C is discussed in section (4.4.4).

4.4.1 Alloy M at 700°C.

In this section, the outputs of the precipitation module are compared to the experimentally measured values of particle size, number and volume-fraction. The interaction between precipitation and recovery is analysed in terms of the measured

softening kinetics. Before proceeding, it is necessary to review the physical parameters that enter into the present model.

4.4.1.1 Physical Parameters:

The predictions of the model are dependent on the values of the physical parameters used. These values are summarised in table (4.3) below. Earlier expressions for the interphase energy, boundary mobility and the shear modulus are retained. The bulk diffusion coefficient of Nb in the model alloy was assumed to be equal to the coefficient for Nb diffusion in a Ni-1.2%Nb alloy [69]. This coefficient is smaller than the one used in chapter (2) by a factor of 1.5 to 3, depending on the temperature. A constant activation volume of $20b^3$ is used. A value of $15b^3$ or less might be more appropriate at 700°C. We verified that the effect of changing the activation volume is limited to reducing the height of the initial hump in the softening curve (see section (4.4.1.3)). A value of $20b^3$ is used throughout this work in order to minimize the number of adjustable parameters.

This leaves the model with three adjustable parameters: i) the precipitate nucleation constant (F), ii) the particle-strength constant, k_s, of equation (2.30) and iii) the recrystallization constant, k, of equation (2.5). The last of these is not relevant because recrystallization is not possible under the present conditions. As such, the experimental data is modelled with two adjustable parameters only.

Parameter	Value
Shear Modulus, μ	81×10^{9} [0.91-(T(K)-300)/1810] Pa [113]
Bulk diffusion coefficient of Nb, D_{bulk}	1.2×10^{-5} exp(-254000/RT) [152]
Interphase Energy, γ	$2.5\times10^{-5}(T_{sol}-T)1.5 + 0.375$
Activation volume, V,	$20b^3$
F, k_s, k	Adjustable parameters

Table (4.3): *Summary of the parameters that enter into the model.*

4.4.1.2 Precipitation Module:

In chapter (2), the effective diffusion coefficient was used to calculate the growth and coarsening rates. This quantity is a weighted average of the bulk and pipe diffusion coefficients. This approach, appears to grossly overestimate the growth and coarsening rates of alloy M at 700°C. The experimental data could not be fitted when the effective coefficient was used. In contrast, very good agreement between the model and experiment is obtained when the bulk diffusion coefficient is used. This could be interpreted in terms of the diffusion model shown in figure (4.8). Solute Nb arrives at the growing particle from the matrix and from dislocations. The two sources act in parallel and the total flux is given by:

$$J_{total} = \frac{A_p}{A_T} J_{pipe} + \left(1 - \frac{A_p}{A_T}\right) J_{bulk} \qquad (4.2)$$

where A_p and A_T are the areas of the dislocation pipe and the precipitate. The short-circuit flux is analysed in more detail in figure (4.8b). Each dislocation is assumed to collect Nb from the surrounding matrix and transfer it to the nearby NbC particles. The limiting step in this process depends on the spacing of the precipitates (l):

$$J_{pipe} = \min\left(\pi R_{core}^2 D_{pipe}, 2lR_{core} D_{bulk}\right) \tag{4.3}$$

When the precipitates are very far apart, *transfer <u>through</u> the pipe* is expected to limit the short-circuit contribution. In this case, equation (2.17) is immediately recovered:

$$J_{total} = -\left(\frac{\eta\pi R_{core}^2}{A_T}\right) D_{pipe} \nabla C - \left(1 - \frac{\eta\pi R_{core}^2}{A_T}\right) D_{bulk} \nabla C \tag{4.4}$$

$$D_{eff} = \rho\pi R_{core}^2 D_{pipe} + (1 - \rho\pi R_{core}^2) D_{bulk}$$

When the particles are very closely spaced, as in alloy M at 700°C, *transfer <u>to</u> the pipe* limits the short-circuit contribution. In this case, the overall process is controlled by volume diffusion.

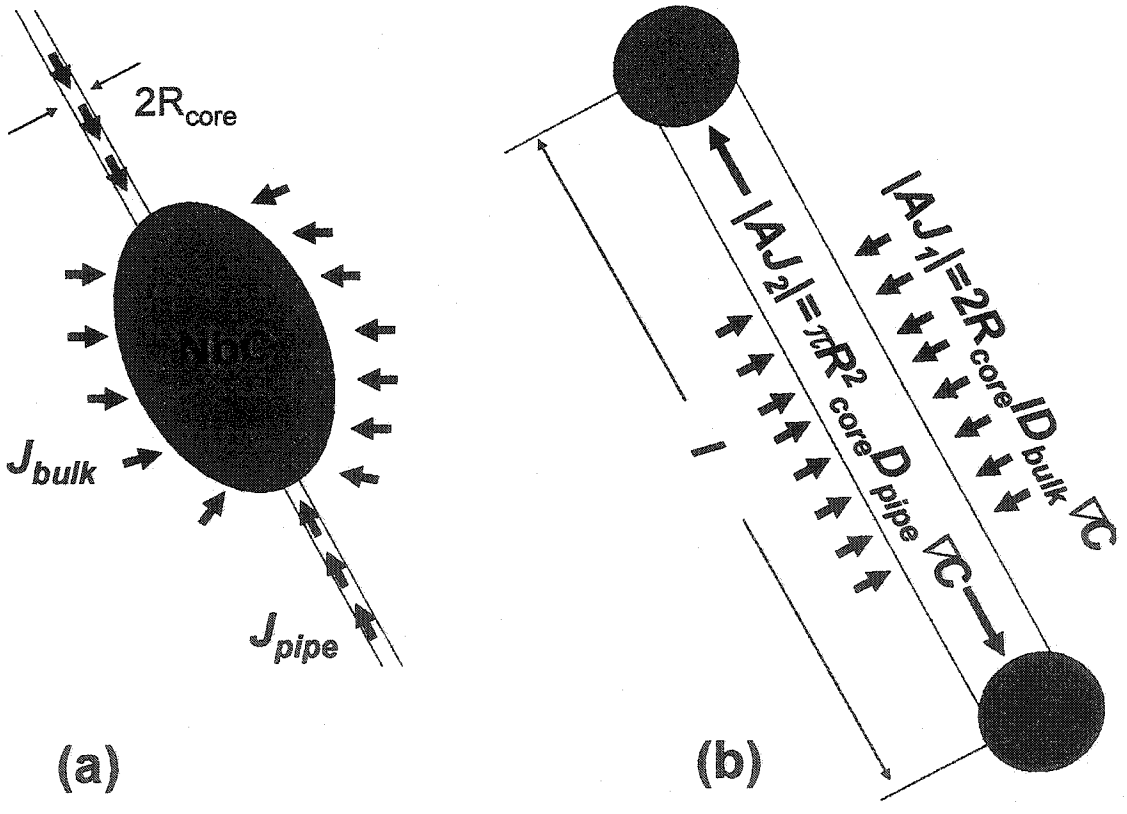

Figure (4.8): *The transport of Nb from the matrix to a growing NbC particle is shown in (a). Transport of Nb <u>to</u> and <u>through</u> the dislocation pipe is illustrated in (b).*

In conclusion, the bulk diffusion coefficient should be used when the particle spacing is very small. This is indeed the case for alloy M at 700°C, as shown in figure (3.10). In contrast, microalloyed steels contain fewer precipitates and the effective diffusion coefficient is more appropriate. A similar conclusion was reached in section (3.3.3) in connection with the effect of deformation on particle-size.

The experimental results on the precipitate number-density, size and volume fraction are modelled in figures (4.9)-(4.11), respectively. The modelling involved a single adjustable parameter, namely, the constant, F, which appears in the nucleation rate equation. A value of F=0.0075 is used in the above figures. Overall, excellent agreement is observed

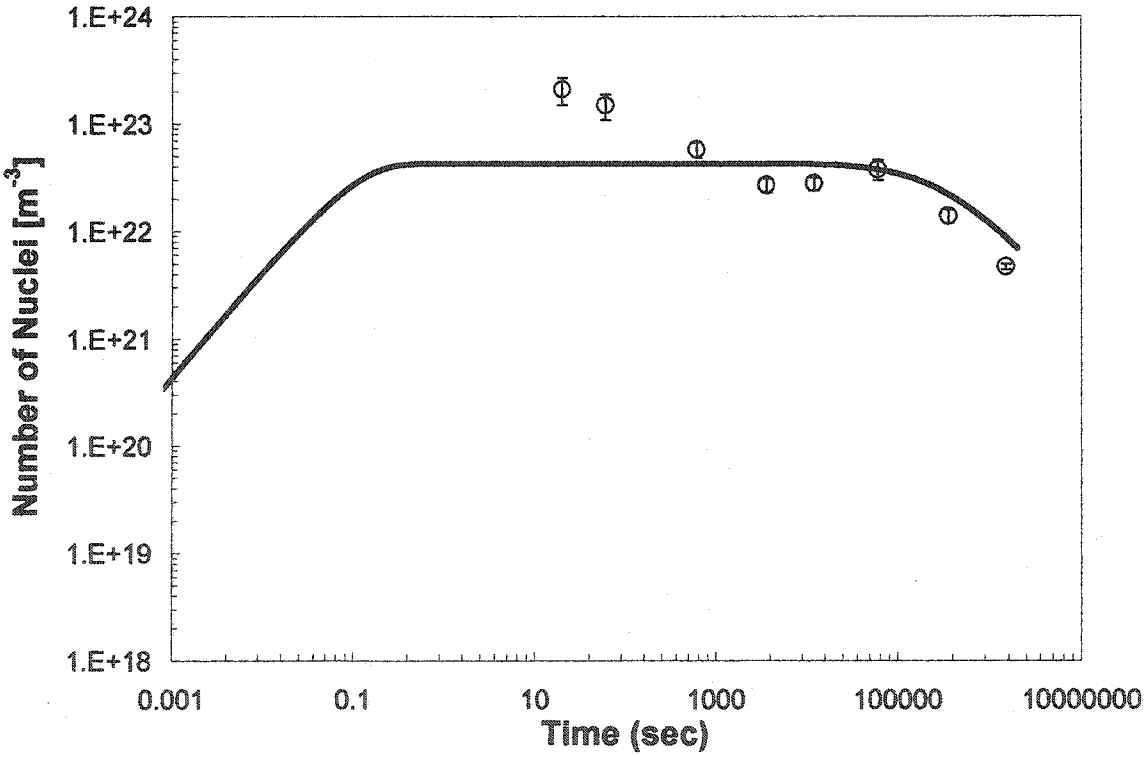

Figure (4.9): *Comparison of the predicted and measured particle number density in alloy M, deformed 18% at RT and annealed at 700°C.*

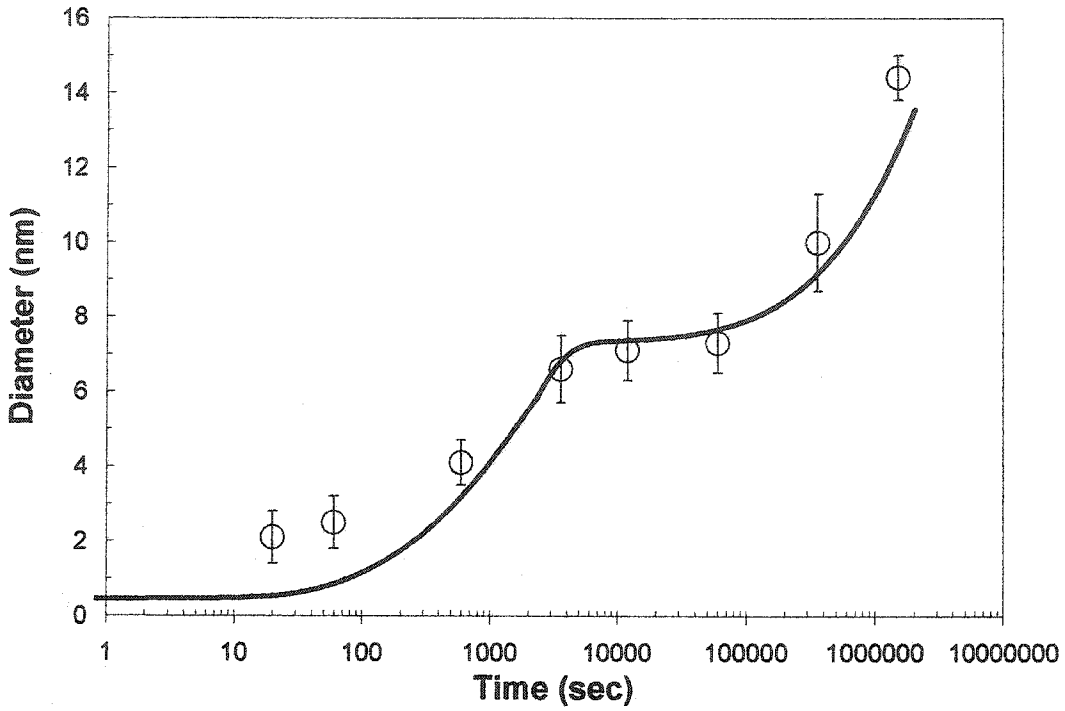

Figure (4.10): *Comparison of the predicted and measured particle size in alloy M, deformed 18% at RT and annealed at 700°C*

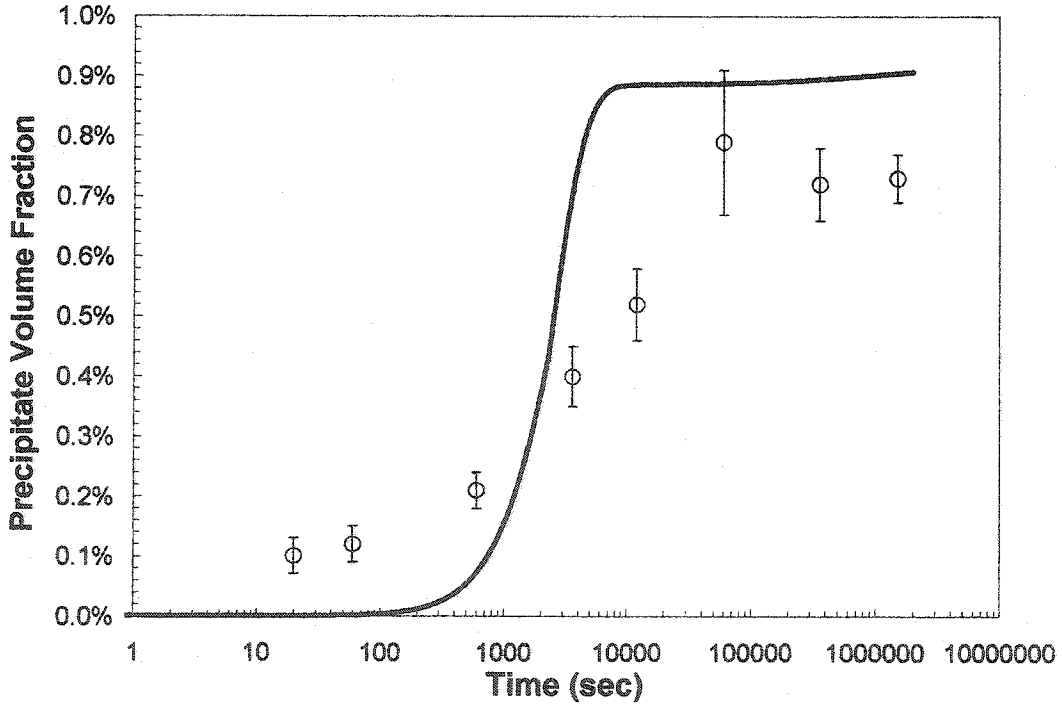

Figure (4.11): *Comparison of the predicted and measured precipitate volume fraction in alloy M, deformed 18% at RT and annealed at 700°C.*

between the experimental data and the model's prediction. In particular, the transition from growth to coarsening is well-described by the model. In all of the above figures, the points corresponding to t = 20, 60s appear to be in error. This is not surprising considering the weakness of the SANS signal at these early stages.

In figure (4.11), the predicted volume fraction appears to overestimate the measured fraction. This could be attributed to three reasons: Firstly, it may be that the thermodynamic model used overestimates the equilibrium volume fraction. Alternatively, it may be that limited decarburisation occurred in the course of the heat-treatment. A third possibility is that the difference is due to the long plate-like precipitates. Although these makeup less than 1% of the total number of precipitates, their volume fraction may be significant. The plate-like particles may not show up clearly within the experimentally measured range of scattering vector, because of their large size.

4.4.1.3 Interaction with Recovery:

A simple model for the interaction between precipitation and recovery was introduced in section (2.2). In this model, the process of particle-pinning was quantified by comparing the size of the dislocation mesh to the spacing of the precipitate particles. We also introduced a size-factor which accounts for the fact that very small particles (<2 nm) are unable to completely pin the dislocation network. In figure (4.12), the predictions of the model are compared to the available softening data of alloy M at 700°C. As expected, limited softening is observed at short-times because the precipitate particles are smaller than

2 nm. When the average particle size exceeds 2 nm, recovery is completely pinned. This continues to be the case, until coarsening is sufficiently advanced to make the particle spacing equal to the size of the dislocation network. From that point on, extended recovery is possible. In the above figure, the precipitation-hardening contribution was calculated from equation (2.30) with a particle-strength constant of $k_s = 0.05$ and a Taylor factor of 2.5. The standard deviation of the particle-size distribution was taken to be $r/2$ in agreement with the information from extraction replicas. The precipitation-hardening contribution dominates the softening curve for t > 1000s.

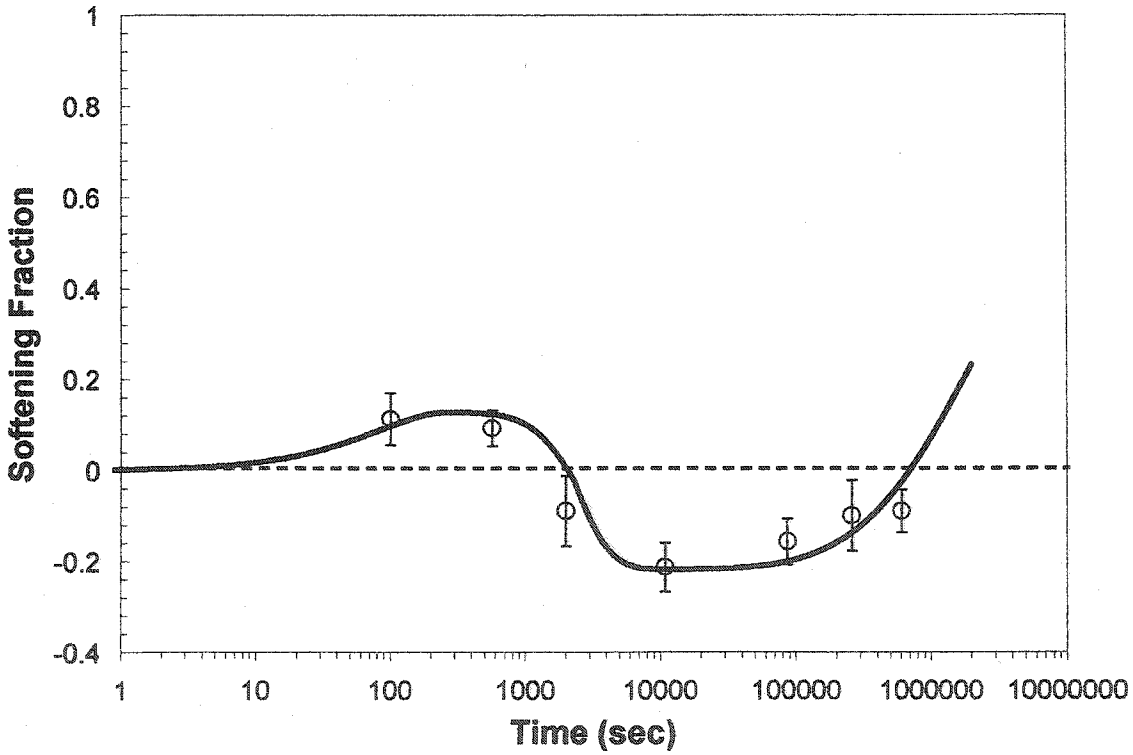

Figure (4.12): *Comparison of the predicted and measured softening fraction in alloy M, deformed 18% at RT and annealed at 700°C.*

The magnitude of the precipitation-hardening term is critical to the excellent agreement observed in figure (4.12). For this reason, it is necessary to discuss our choices for the particle-strength factor and the Taylor factor. The first quantity was used as a curve-fitting parameter. It leads to a transition from particle-cutting to particle bypass at a diameter of 8nm. This value is almost twice the theoretically predicted limit. Possible causes of this discrepancy are discussed in section (4.5). As for the Taylor factor, we found that a value of 3.1 overestimated the precipitation-hardening contribution. The current value of 2.5 is rationalized in terms of the texture of the tensile samples. In section (3.4.1), we pointed out that it was necessary to grain-refine the model alloys prior to the preparation of the tensile samples. To that end, the alloys were subjected to two cycles of cold-rolling (~35%) and high-temperature annealing to induce recrystallization. These conditions are known to lead to a strong cube texture ({001}<100>) in FCC materials of medium-high SFE [38, 152, 153]. The tensile samples were machined from the rolled sheets with the tensile axis parallel to the rolling direction. For this geometry, a Taylor factor of 2.49 is expected during tensile deformation.

It should be pointed out that we continued to use M = 3.1 for the purpose of calculating the dislocation density (Eq. 2.8). We felt that changing the Taylor factor from 3.1 to 2.5 was not necessary in this case, because the constant α_T is known only to within a factor of 2.

4.4.2 Other Alloys at 700°C.

The predictions of the model were shown to be in excellent agreement with the experimental data for alloy M at 700°C. Only one curve-fitting parameter (F) is needed to fit the precipitation data. A second parameter (k_s) was used to capture the effect of particle-size on precipitation hardening. In this section, the above analysis is extended to the remaining model alloys at 700°C. We continued to use $F = 0.0075$ and $k_s = 0.050$. These values are used to demonstrate the merit and robustness of the model. Improved fits could be obtained by changing the above values.

The predicted softening-fractions for alloys M1, M2, M3, L and L1 are shown in figures (4.13)-(4.17). In each case, the calculations were carried out using an activation volume of $15b^3$ (dotted curve) and $20b^3$ (solid curve). Satisfactory agreement between the predicted and the measured fractions is observed for alloys M1, M2 and L. In all three cases, an activation volume of $15b^3$ results in a better fit of the experimental data.

In contrast, the model fails to capture the behaviour of alloys M3 and L1. Two problems are identified: Firstly, the model overestimates the softening-fraction as seen in figures (4.15) and (4.17). Secondly, unreasonable values of particle-size and number density are predicted. For example, the model predicts a number density of $4\times10^{22}/m^3$ and a particle size of 3.5 nm in alloy M3 after 10,000 sec at 700°C. These values are compared to $4\times10^{22}/m^3$ and 7.5 nm for alloy M under the same conditions. This trend is at odds with the

observations of section (3.2.2.3), which showed that at 800°C the particle-size in alloy M3 is larger than that in alloy M.

The model's predictions could be improved in the case of alloys M3 and L1 by using the effective Nb diffusion coefficient in place of the bulk coefficient. This is justified by the fact that the equilibrium volume fraction in these alloys is smaller than the volume fraction in alloy M by a factor of 10 or more. Reasonable values of particle size and number density are obtained in this way. For example, the predicted particle size and number density in alloy M3 become 10 nm and $3\times10^{21}/m^3$, respectively. The above change did not, however, improve the agreement between the predicted and measured softening fractions. This is a limitation of the model which will be discussed in section (4.6).

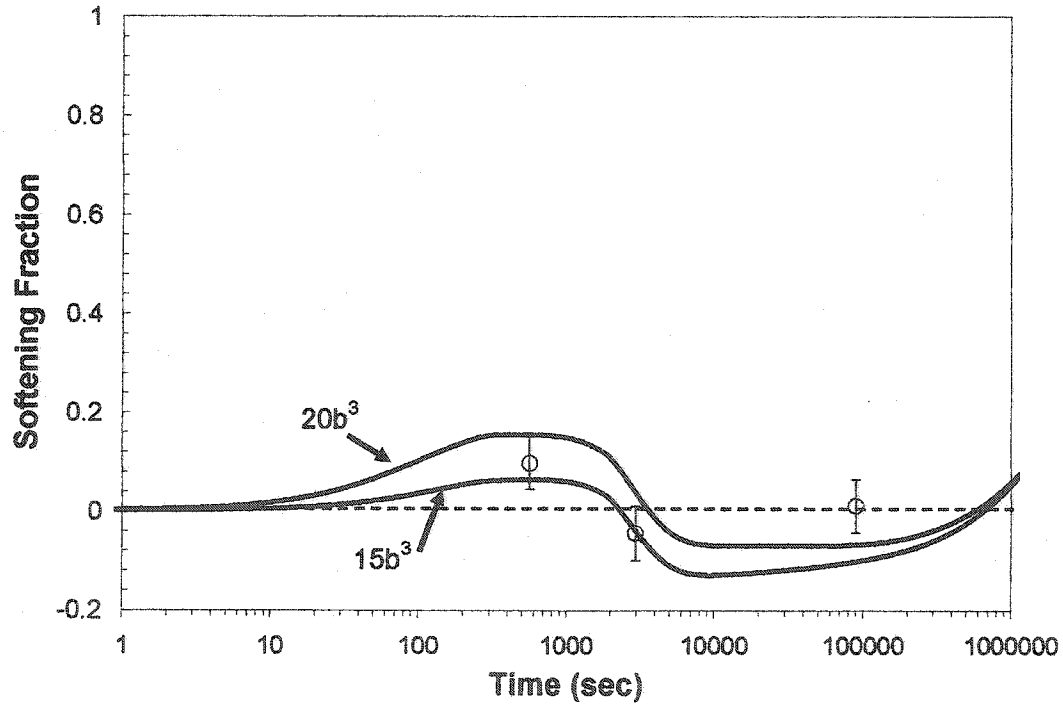

Figure (4.13): *Comparison of the predicted and measured softening fractions in alloy M1, deformed to a flow stress of 350 MPa and annealed at 700°C*

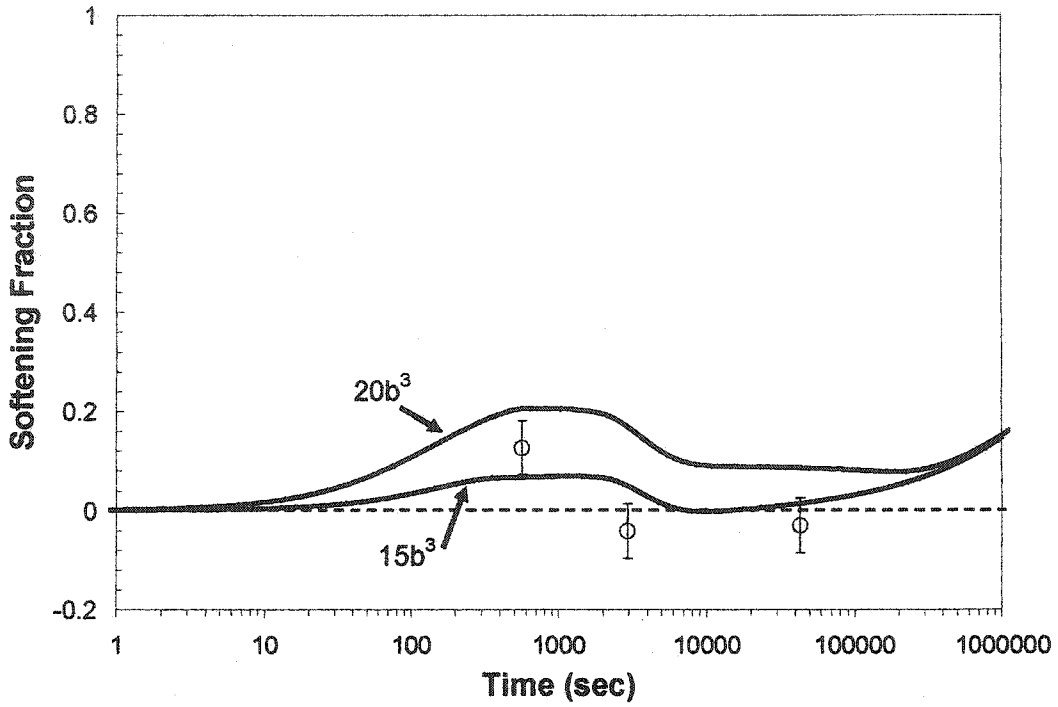

Figure (4.14): *Comparison of the predicted and measured softening fractions in alloy M2, deformed to a flow stress of 350 MPa and annealed at 700°C.*

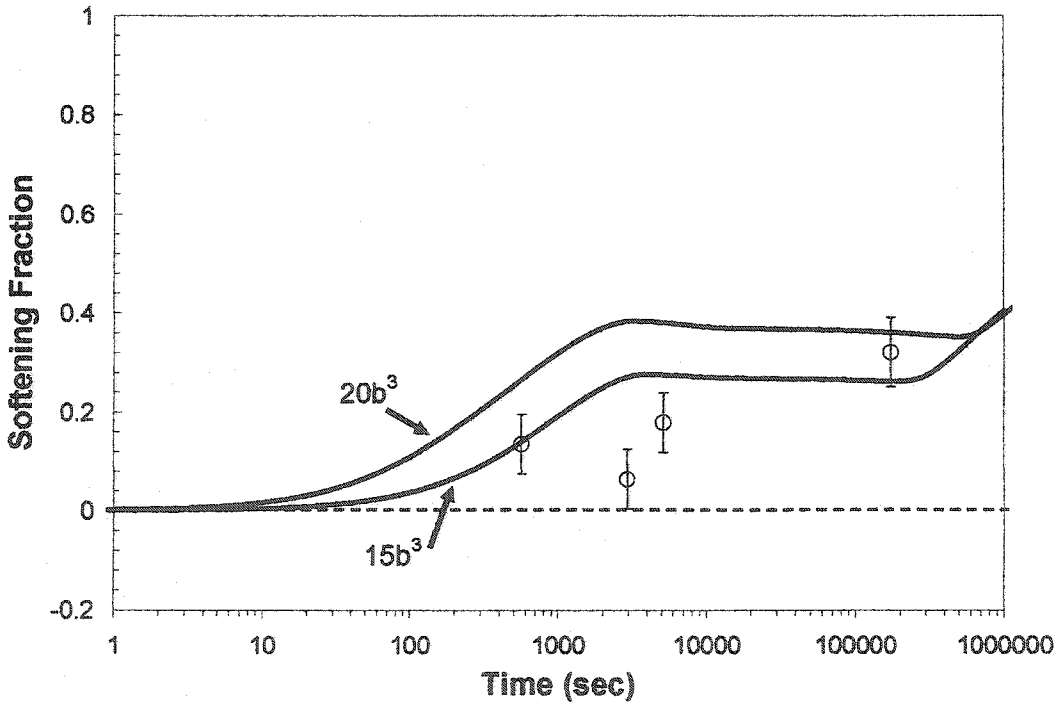

Figure (4.15): *Comparison of the predicted and measured softening fractions in alloy M3, deformed to a flow stress of 350 MPa and annealed at 700°C.*

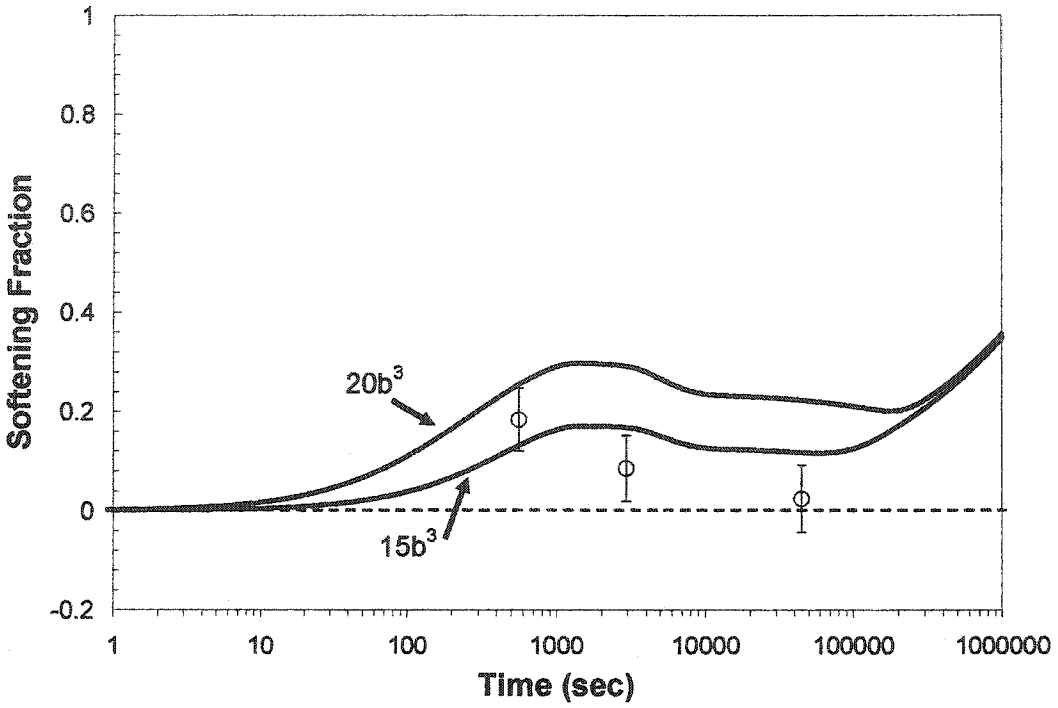

Figure (4.16): *Comparison of the predicted and measured softening fractions in alloy L, deformed to a flow stress of 350MPa and annealed at 700°C.*

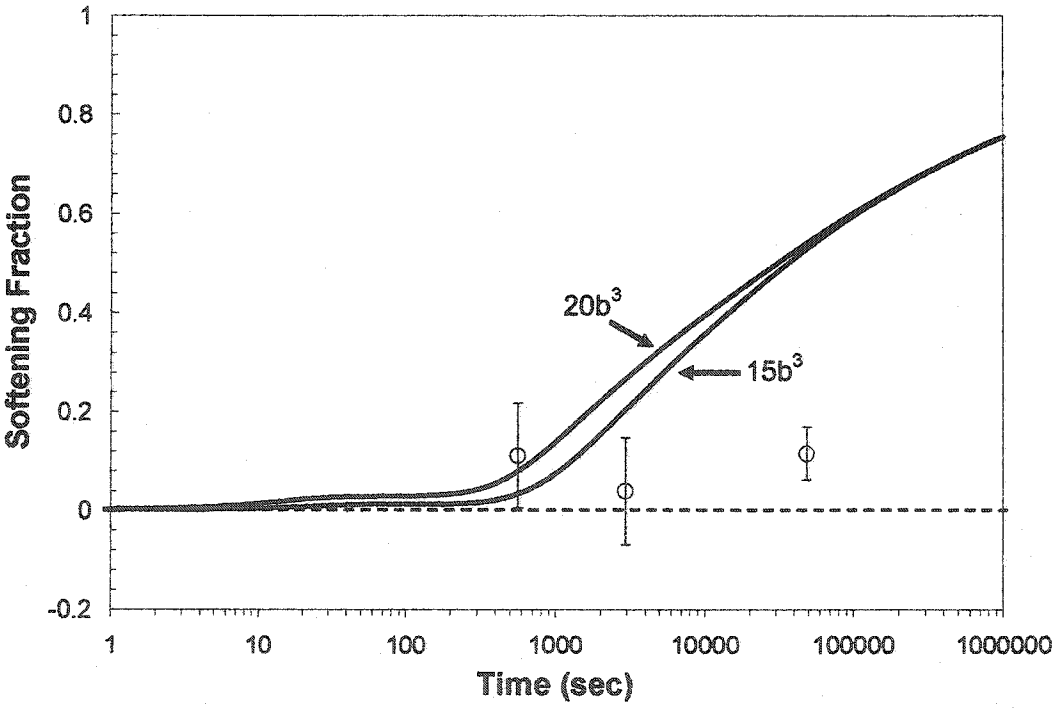

Figure (4.17): *Comparison of the predicted and measured softening fractions in alloy L1, deformed to a flow stress of 350 MPa and annealed at 700°C.*

4.4.3 Annealing at 800°C

In this section, the microstructural evolution of the model alloys at 800°C is considered. The available experimental data consists of i) the average particle-size after 12 hrs of annealing (3.2.2.3) and ii) the softening-fraction measurements (3.4.3). We fitted the experimental data using an activation volume of $20b^3$. The adjustable-parameters, F and k_s, were set equal to 0.0075 and 0.042, respectively. The bulk diffusion coefficient of Nb was used, except in the case of alloy M3, where we used the effective diffusion coefficient. Finally, precipitation in alloy L1 could not be modelled because the predicted size of the critical nucleus was excessively large (~1.7 nm). A similar situation was encountered in chapter (2). We'll revisit this issue in section (4.6).

The predicted and experimentally measured particle sizes are compared in Table (4.4). Reasonable agreement is obtained between the measured and predicted values. In addition, the effect of supersaturation on particle size is correctly captured by the model. This result deserves further attention: In the above calculations, the same value of the nucleation constant, F, was used for all five alloys. In addition, the same initial dislocation density was used in all cases. Therefore, all of the alloys had the same number of *potential* nucleation sites. The *actual* number of nucleation sites was calculated by the model and is listed in table (4.4). As expected the actual number of nuclei decreases with decreasing supersaturation. This is an important result, because it demonstrates the model's ability to describe the effect of supersaturation on the nucleation and growth-rates. At a practical

level this result shows that one could safely overestimate the value of F. In most cases, the model would still be able to predict the right number of particles. This result is very convenient when one is dealing with a new alloy or a new set of conditions for which an initial value of F is not known.

	Particle Size		Number Density
	Measured (nm)	**Predicted (nm)**	**Predicted ($1/m^3$)**
M	9 ± 3	12	8.5×10^{21}
M1	7 ± 3	11	8.3×10^{21}
M2	5 ± 3	9	7.5×10^{21}
M3	23 ± 8	23	9.5×10^{19}
L	10 ± 4	10	2.6×10^{21}
L1	15 ± 7	*could not be modelled*	

Table (4.4): *Comparison of the predicted and measured particle-sizes following an annealing treatment of 12hrs at 800°C. The predicted number density is also included.*

The softening data for alloys M, M1, M2, M3 and L is modelled in figures (4.18)-(4.22). Two curves are shown on each diagram. For the time being, we are concerned with the dark-curves which are calculated using the standard methods of chapter (2). The calculated curves are in reasonable agreement with the experimental data for alloys M, M1, M2 and L. Poor results are observed, once again, for alloy M3.

In all cases, the model appears to overestimate the softening fraction at the longest times. This is attributed to the manner in which the contributions of precipitation and

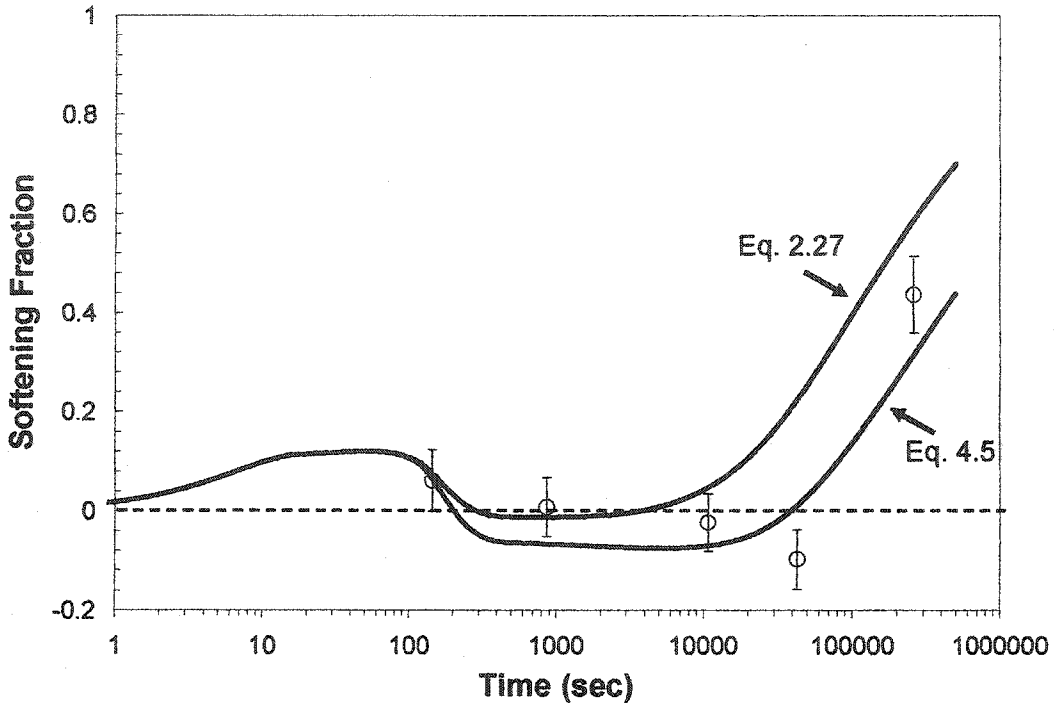

Figure (4.18): *Comparison of the predicted and measured softening fractions in alloy M, deformed to a flow stress of 350 MPa and annealed at 800°C. See text for details.*

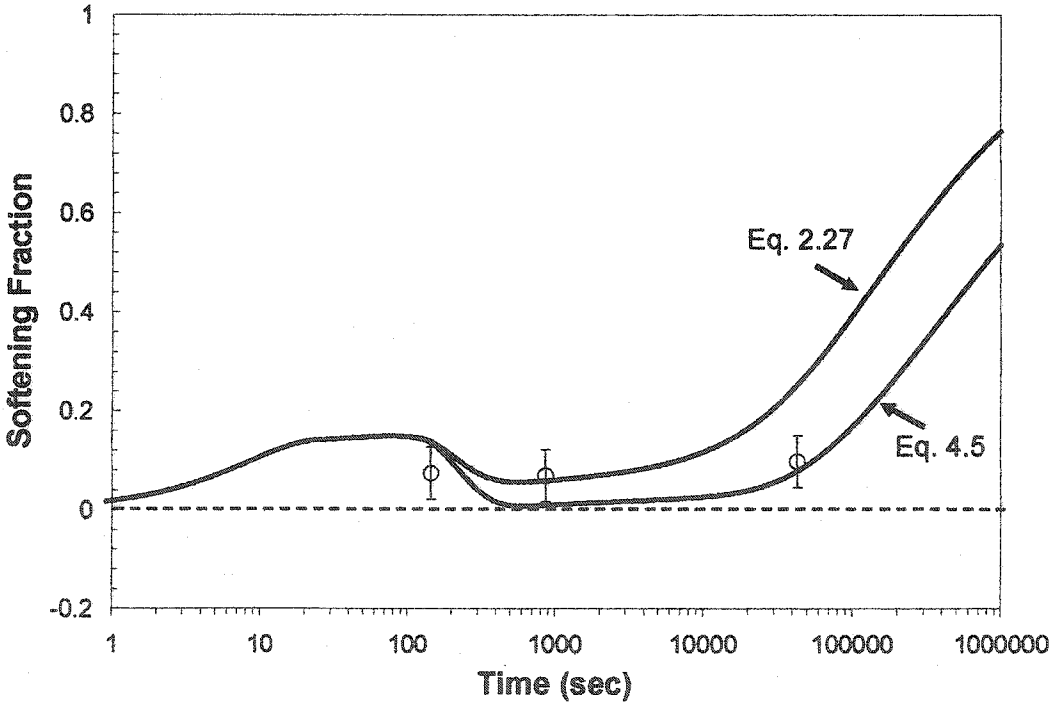

Figure (4.19): *Comparison of the predicted and measured softening fractions in alloy M1, deformed to a flow stress of 350 MPa and annealed at 800°C. See text for details.*

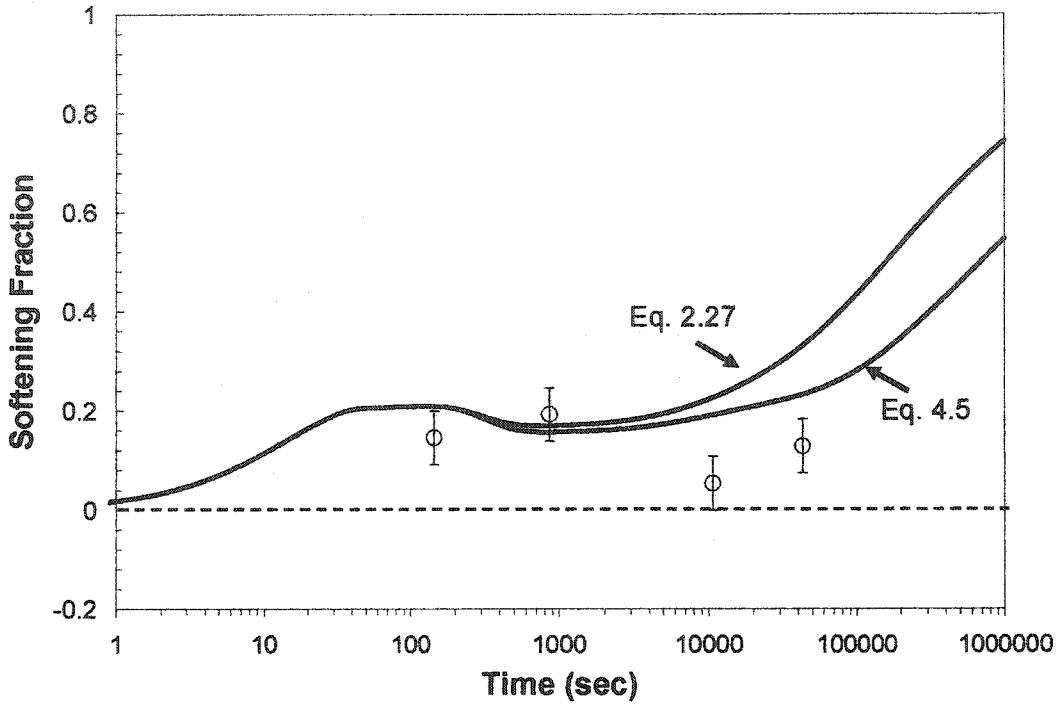

Figure (4.20): *Comparison of the predicted and measured softening fractions in alloy M2, deformed to a flow stress of 350 MPa and annealed at 800°C. See text for details.*

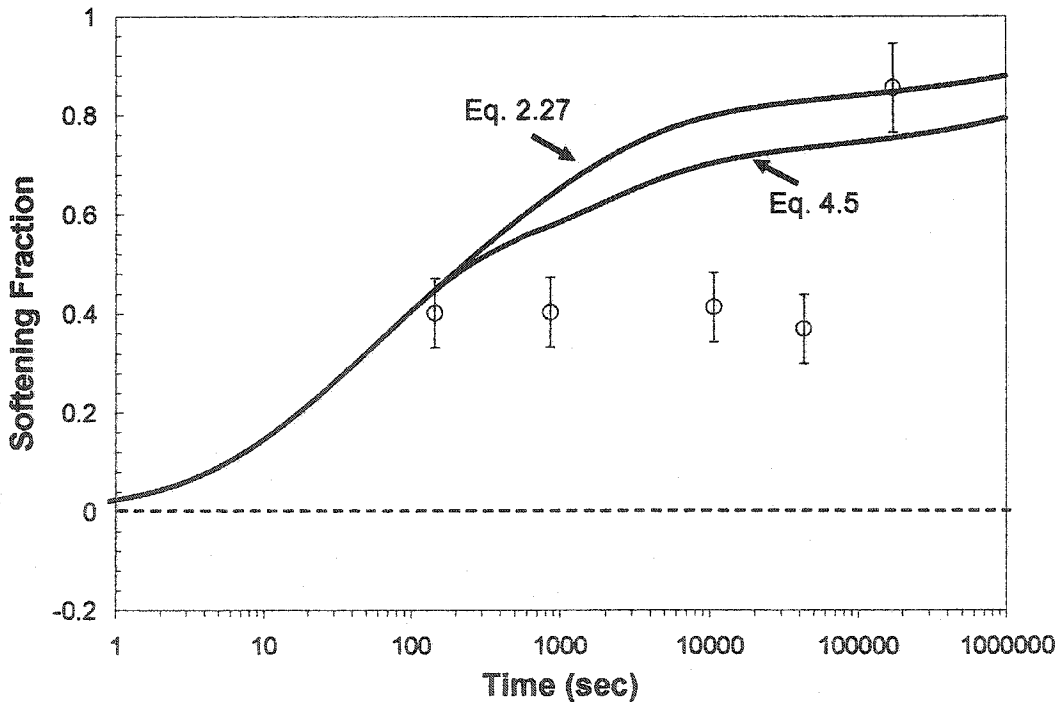

Figure (4.21): *Comparison of the predicted and measured softening fractions in alloy M3, deformed to a flow stress of 350 MPa and annealed at 800°C. See text for details.*

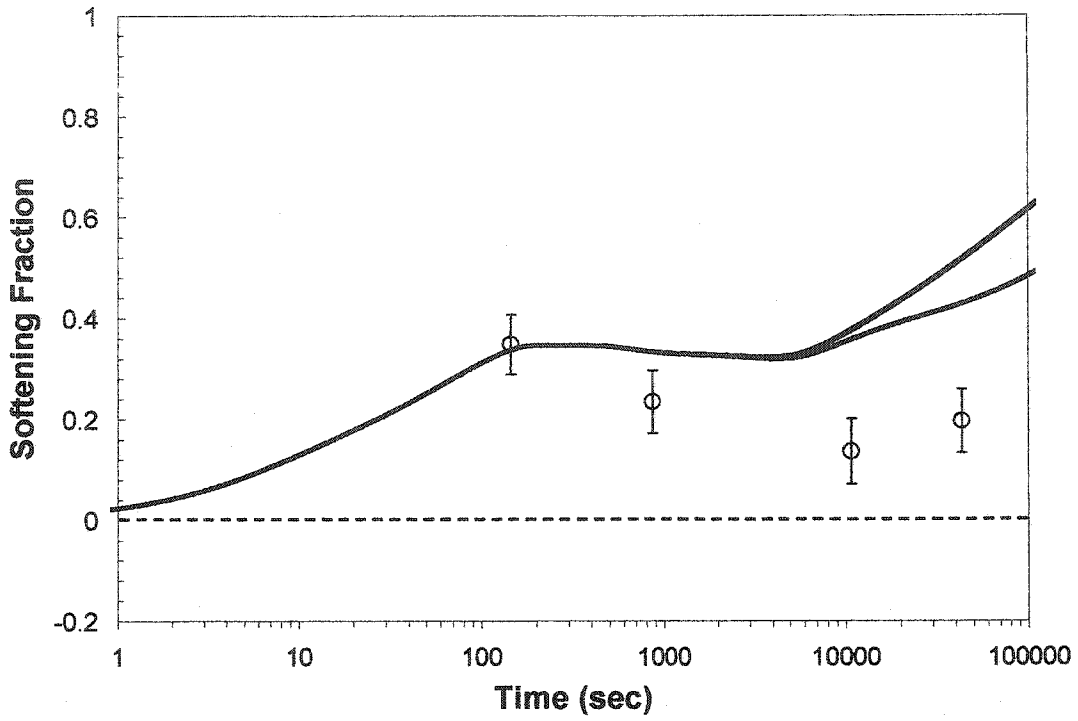

Figure (4.22): *Comparison of the predicted and measured softening fractions in alloy L, deformed to a flow stress of 350 MPa and annealed at 800°C. See text for details.*

dislocation hardening are added. In equations (2.27) and (2.28) the two contributions are added quadratically. According to Embury [154], this approach is justified in the case of particle-shearing. When precipitation-hardening is controlled by the Orowan mechanism, linear addition of the two contributions is more appropriate. In order to incorporate this description into the present model, equations (2.27) and (2.28) are re-written in the form:

$$\sigma = \left(\sigma_{matrix}^{m+1} + \sigma_{ppt}^{m+1}\right)^{1/(m+1)} \tag{4.5}$$

where m is the fraction of particles being sheared. Once again, a normal particle-size distribution is assumed and the standard-deviation is taken to be $r/2$. When the precipitate particles are very small, m is equal 1 and equations (2.27) and (2.28) are recovered. The value of m will decrease gradually as the average particle-size increases. When the average

radius is equal to r_c (cutting-to-bypass transition) the value of m is equal to ½ . As the particles continue to grow, the value of m will approach zero leading to linear addition. The results of this treatment are shown by the gray-curves in figures (4.18)-(4.22). Significant improvement is achieved at long times and the new results are very satisfactory.

4.4.4 Annealing at 875 and 945°C

The available data on the microstructural evolution of the alloys at 875 and 945°C is limited to the softening fraction measurements. Table (4.5) summarizes the conditions which are discussed in this section. It should be noted that alloys L1 and M3 at 945°C have already been discussed in section (4.3). Four other conditions could not be modelled because the predicted size of the critical nucleus was excessively large (>1 nm).

Alloy [dissolution T °C]		875 °C	945 °C
M	[1198]	Figure (4.23)	Figure (4.24)
M1	[1143]	Figure (4.25)	Figure (4.26)
M2	[1066]	Figure (4.27)	*could not be modelled*
M3	[921]	*could not be modelled*	Modelled in section (4.3)
L	[957]	*could not be modelled*	*could not be modelled*
L1	[835]	See section (4.3)	Modelled in section (4.3)

Table(4.5): *Summary of the conditions that are discussed in this section.*

Once again, the activation volume was set equal to $20b^3$. The nucleation constant and the particle-strength constant were set equal to 0.0075 and 0.040, respectively. The bulk diffusion coefficient was used in all of the five cases considered below. The predicted softening-curves are shown in figures (4.23)-(4.27). Once again two curves are plotted for each condition. The dark-curve corresponds to addition method of chapter (2), while the gray curve is calculated using the method of section (4.4.3). The latter approach, leads to very reasonable agreement between the experimental and the predicted curves.

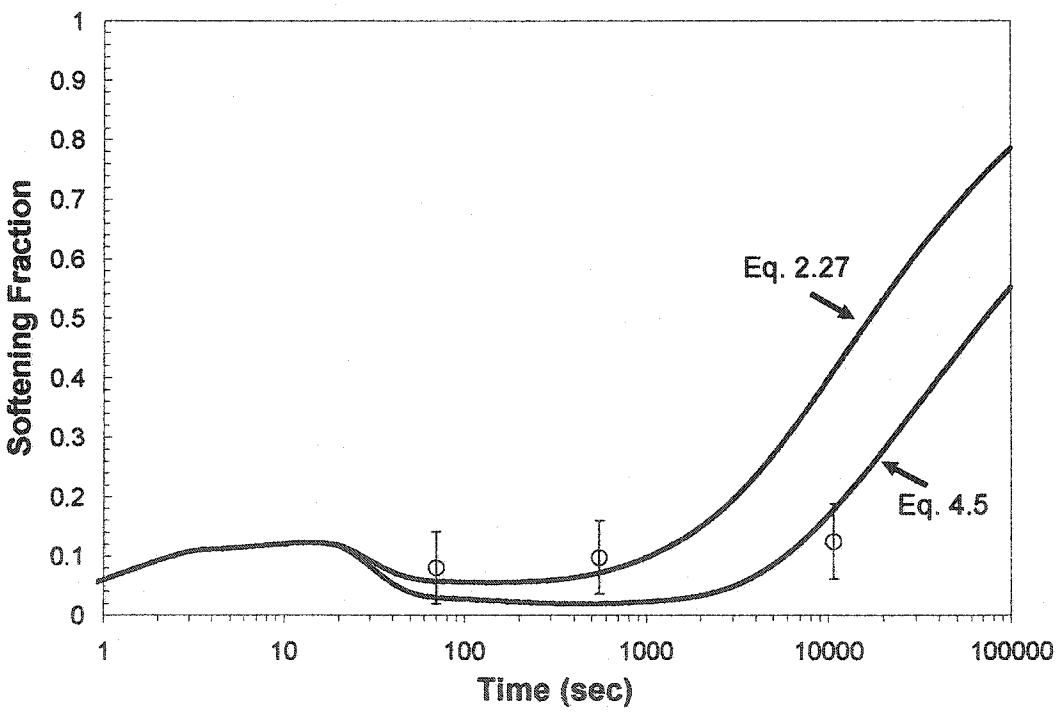

Figure (4.23): *Comparison of the predicted and measured softening fractions in alloy M, deformed to a flow stress of 350 MPa and annealed at 875°C. See text for details.*

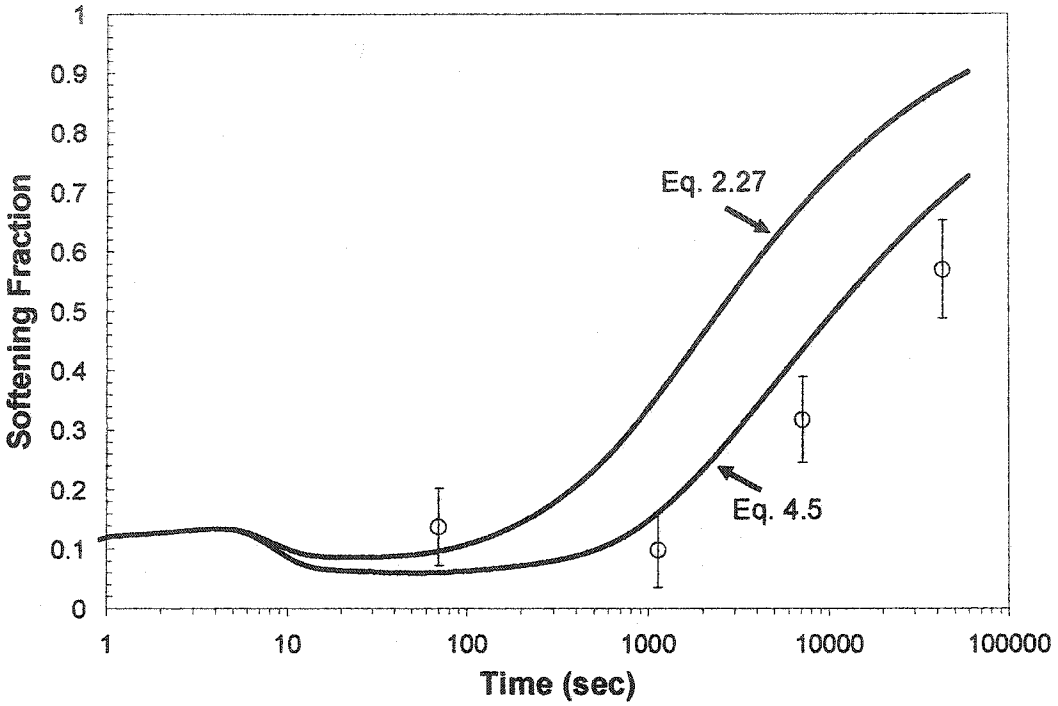

Figure (4.24): *Comparison of the predicted and measured softening fractions in alloy M, deformed to a flow stress of 350 MPa and annealed at 945°C. See text for details.*

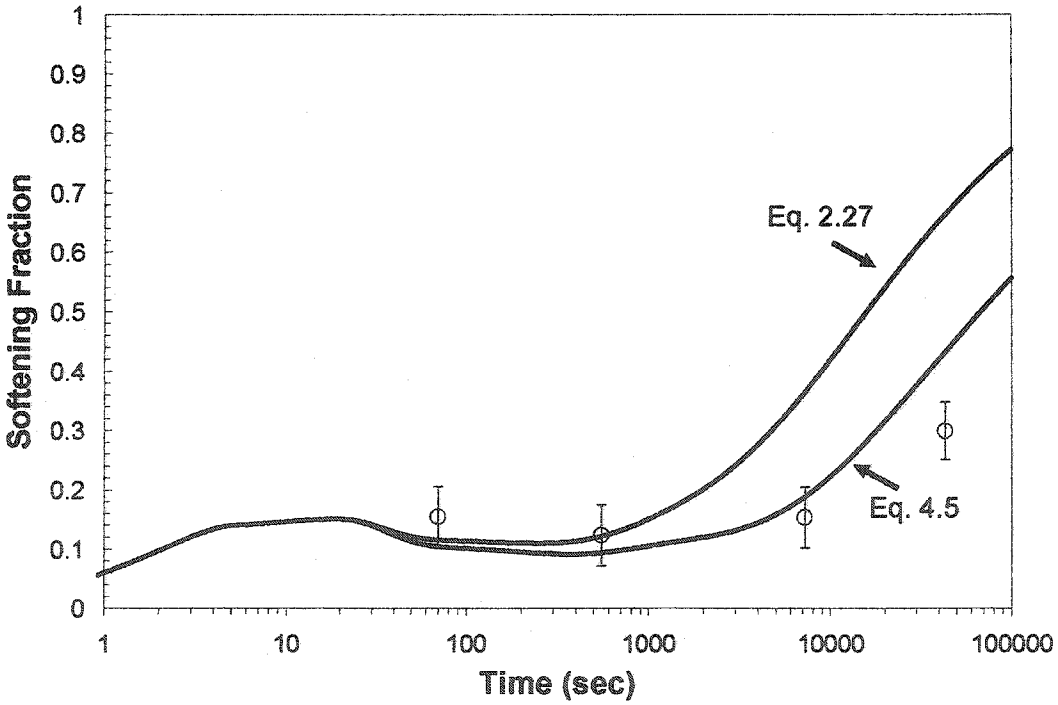

Figure (4.25): *Comparison of the predicted and measured softening fractions in alloy M1, deformed to a flow stress of 350 MPa and annealed at 875°C. See text for details.*

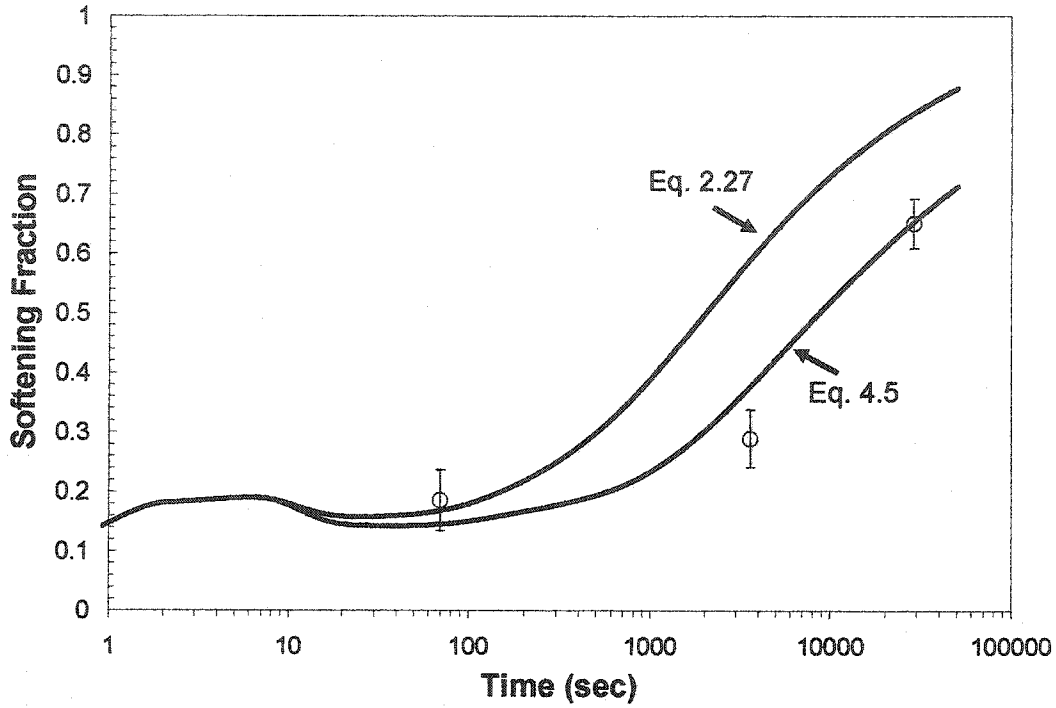

Figure (4.26): *Comparison of the predicted and measured softening fractions in alloy M1, deformed to a flow stress of 350 MPa and annealed at 945°C. See text for details.*

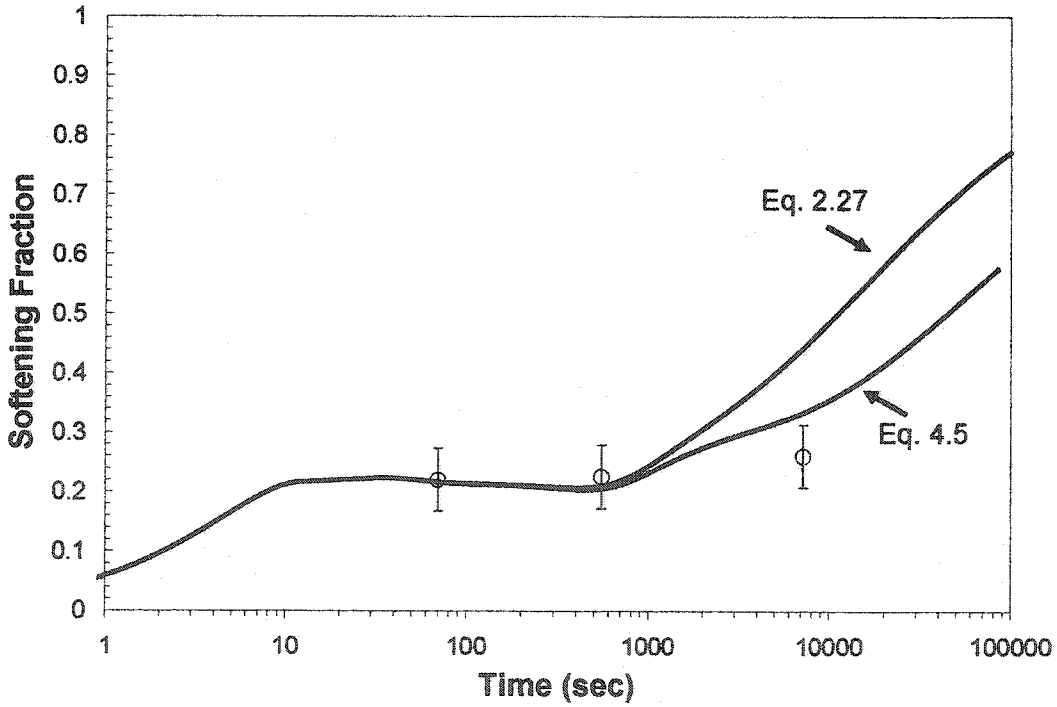

Figure (4.27): *Comparison of the predicted and measured softening fractions in alloy M2, deformed to a flow stress of 350 MPa and annealed at 875°C. See text for details.*

4.5 Adjustable Parameters:

The model contains a number of adjustable and unknown parameters. Every effort has been made to identify these parameters in a consistent manner. In sections (4.2) and (4.3), the activation volume was back-calculated from the available experimental data in the absence of precipitation. Our analysis indicated that the activation volume is a weak function of the Nb concentration. A constant activation volume of $20b^3$ was used for all of the cases considered in section (4.4).

In the process of modelling the interaction between precipitation and recovery two adjustable-parameters were used: The precipitation nucleation constant, F, was adjusted to fit the SANS data on alloy M at 700°C. A value of 0.0075 was obtain in this way. This value was retained throughout this investigation. The other adjustable-parameter is the particle-strength constant, k_s, which appears in equation (2.30). This parameter was assumed to be independent of composition and weakly dependant on temperature. The values of k_s ranged from 0.050 at 700°C to 0.040 at 945°C. Table (4.6) provides a summary of the values of the adjustable and unknown parameters used in the model. The merit of the model is evident from the fact that 14 different combinations of temperature and composition were accurately fitted by varying, essentially, one parameter!

Parameter	Range of Values Used	Comments
Activation volume, V_a	20 b^3	Determined from the softening data of alloys M1 and L3 in the absence of precipitation.
Nucleation Constant, F	0.0075	Determined from the SANS data on alloy M at 700°C.
Particle-Strength, k_s	0.05 - 0.04 (function of T only)	Adjusted to best-fit the experimental data at a given temperature.

Table (4.6): *Summary of the quantities used to model the interaction between precipitation and recovery in section (4.4).*

The main criticism of the above treatment is related to the magnitude of the particle-strength constant, k_s. It was pointed out earlier that k_s is related to the particle size at which particle-bypass becomes preferable to particle-cutting:

$$r_c = \frac{0.8b}{k_s} \tag{4.6}$$

The above values of 0.05 - 0.04 lead to transition radii in the range of 4- 5 nm. A simple estimate of the theoretical transition radius could be obtained by equating the line-tension of the Orowan loop to the theoretical strength of the carbide particle:

$$\frac{\mu_\gamma b}{2r_c} = \frac{\mu_{NbC}}{30} \qquad r_c = 15\frac{\mu_\gamma}{\mu_{NbC}} b \sim 7.5b \sim 1.9\text{nm} \tag{4.7}$$

Thus, the values of r_c which are used in the model are approximately twice the theoretical values. Furthermore, our r_c values appear to have the wrong dependence on temperature; Based on equation (4.7) the value of r_c should decrease with temperature because the temperature dependence of μ_γ is stronger than that of μ_{NbC}.

The above discrepancy could be explained in two ways. Firstly, it may be that the carbide particles are imperfect, in which case they could yield at a stress which is lower than the theoretical strength. The imperfection could be due to the fact that the precipitate is nucleated on a dislocation. It could also be due to the imperfect stoichiometry of the precipitate. Admittedly, these arguments are very speculative and no TEM observations are available to support the idea that NbC particles as large as 10 nm could be cut by dislocations. An alternative explanation of the discrepancy is that dislocations are able to bypass particles by climbing locally over them. This effect would lower the Orowan stress by a factor of $1/\sqrt{2}$ [89]. This effect is not captured in the model. Instead, the model compensates for the above effect by delaying the transition from particle-cutting to particle-bypass. Clearly, additional work is still needed in this area.

4.6 Limitations and Future Work:

The purpose of this section is to identify the limitations of the proposed model (4.6.1) and the experimental procedure (4.6.2). In addition, possible future work is discussed in section (4.6.3).

4.6.1 Limitations of the Model:

We presented a physically-based model that provides an excellent description of the processes of precipitation and recovery as well as their interactions at low temperatures. At high-temperatures, the model suffers from two limitations: The first of these is related to the nucleation of precipitation close to the precipitate dissolution temperature. In general, we find that excessively large nuclei are predicted by the model when the annealing temperature is less than 100°C below the solubility limit. This results in a very small nucleation rate and precipitate number density. The second limitation, is related to the interaction between precipitation and recovery. The model underestimates the effect of precipitation on recovery at high-temperatures. This problem is encountered even when the first problem is not present. This difficulty is believed to result from the fact that well-developed substructures are formed when the sample is annealed at high temperatures. This leads to a non-uniform distribution of precipitates and increased pinning at the sub-boundaries and cell walls. The same limitations were encountered in chapter (2) when we modelled the hot-deformation of microalloyed steels. The reader is referred to section (2.7) for additional details.

4.6.2 Limitations of the Experimental Procedure:

The present experimental procedure provides a convenient method of studying the interactions of recovery and precipitation. Some of the limitations of the present method are discussed briefly:

4.6.2.1 Alloy Composition:

Alloy design was a key aspect of our experimental approach. A series of model alloys were designed to resemble microalloyed steels. However, important differences exist between the model alloys and microalloyed steels. The most important of these is the Nb content. The model alloys contain ~ 10 times the amount of Nb in a typical microalloyed steels. This had four undesired consequences:

a) It made recrystallization practically impossible at temperatures below ~ 1000°C. As a result, the model alloys could not be used to study the interaction of recrystallization with recovery and precipitation.

b) In section (3.3) we pointed out that deformation of the model alloys did not significantly change in the average particle-size. In contrast, the deformation of microalloyed steels is known to result in a significant refinement of the precipitate particle size. The difference in behaviour was attributed to the fact that Nb is abundantly available in the model alloys. As such, the precipitates do not compete for the available Nb at short -times and the particle size is not affected by the presence of more particles in the deformed sample.

c) The particle number density in the model alloys is approximately an order of magnitude larger than the number density in microalloyed steels. As a result, strong-pinning conditions are frequently encountered in the model alloys. In addition, the large number of particles causes the precipitation kinetics to be controlled by bulk diffusion as described in section (4.4.1). In contrast, both pipe and bulk diffusion are believed to contribute to the growth kinetics in microalloyed steels.

d) The niobium to carbon ratio in the model alloys was in the range of 1-10. In contrast, the niobium to carbon ratio in microalloyed steels is usually in the range of 0.05 - 0.2. It is not clear if this difference would affect the precipitation behaviour.

4.6.2.2 Deform-and-Anneal Treatment:

The deform-and-anneal approach of section (3.1) is very attractive because of its simplicity. One should keep in mind, however, that the dynamic effects which take place during high-temperature deformation are not captured by the present approach. Another concern is the possibility of precipitation when the sample is being heated from room-temperature to the annealing temperature. This effect is particularly important when the alloy is being annealed above the nose of the precipitation C-curve. One could envisage a situation in which precipitation during heating allows the system to overcome the sluggish nucleation kinetics encountered at high temperatures. An effect of this type appears to have occurred when alloy L1 was heated to 800°C. Figure (3.25) shows strong pinning in this alloy in spite of the fact that it is being annealed within 35°C of the precipitate dissolution temperature.

4.6.2.3 Double-deformation Method:

The double-deformation test provides an accurate method of monitoring the softening kinetics. However, a very large number of samples is needed for this method and this limits the number of data points. For example, in sections (4.2) and (4.3), the activation volumes could not be determined accurately due to the lack of experimental points.

4.6.3 Future Work:

At present, the applicability of the model is limited to the case in which the deformed structure is made up of randomly distributed dislocations. The model is inadequate at high temperatures, where well-developed dislocation substructures are formed. In order to model the high-temperature case, it is necessary to study the deformed structure as well as the distribution of the precipitates formed on this structure. The model alloys offer a unique opportunity for studies of this type. The information gained from these studies could then be used to construct a new model that takes into account the dislocation density and the subgrain/cell size. Special consideration should be given to the interaction of recovery and precipitation in the case of precipitation on the cell and subgrain boundaries

Experimentally, a number of improvements could be made. For example, the activation volume for recovery could be determined accurately using the technique of stress-relaxation. The effects of Nb, C and temperature on the activation volume could be studied efficiently in this way. Additional experimental work could also be carried out to take advantage of the austenitic structure of the model alloy. For example, atom-probe measurements could be used to study the segregation of Nb and C to grain-boundaries and sub-boundaries in austenite. An investigation of this type would provide valuable information on the forces that hamper the nucleation of recrystallization.

Summary

The deformation of supersaturated microalloyed austenite sets the stage for the simultaneous processes of recovery, recrystallization and strain-induced precipitation. The evolution of the microstructure is controlled by the manner in which the above processes interact. In this work, we presented a novel physically-based model for the microstructural evolution of microalloyed steels. The model has a number of important distinguishing features:

- For the first time, the processes of recovery, recrystallization and precipitation as well as their interactions are considered, explicitly, within a single model.

- The effect of precipitation on recovery is considered quantitatively in terms of the pinned-fraction of the dislocation network. This novel treatment allowed us to clarify a number of important experimental observations, including the appearance of plateaus on the softening-fraction and stress-relaxation diagrams.

- The effects of precipitation and solute-drag on the onset and progress of recrystallization are captured quantitatively in the model.

The model was applied successfully to a wide range of Nb-microalloyed steels. All of the experimentally observed features were captured by the model. In particular, the occurrence of single and double softening-plateaus was predicted and rationalized using the model. In addition, the model was successfully used to quantify the contributions of precipitation and solute-drag to the retardation of recrystallization.

The most significant result of the model is that the interaction between precipitation and recovery dominates the microstructural evolution of microalloyed steels at low (finishing) temperatures. This interaction was experimentally investigated using a series of model austenitic alloys. The alloys were designed to have the same stacking fault energy as the austenite phase in C-Mn steels. This important feature distinguishes the present work from previous work in the area.

Precipitation in the model alloys was studied extensively, using the techniques of small-angle neutron scattering and transmission electron microscopy. The experimental data on the evolution of particle size, number density and volume fraction was accurately described by the model. In addition, deform-and-anneal experiments were carried out to study the interactions between precipitation and recovery. Overall, excellent agreement was observed between the calculated and experimentally measured softening fractions at low-temperatures. Less satisfactory results were obtained at high-temperatures. This was attributed to fact that the model does not take into account the well-developed cell and boundary structures that form at high-temperatures. In practical terms, this means that the

model is most applicable to the industrial process of finish rolling which is carried out at (relatively) low temperatures.

Bibliography

1. T. Gladman, The Physical Metallurgy of Microalloyed Steels, The Institute of Metals, (1997).

2. R.C. Sharma, V. K. Lakshmanan and J. S. Kirkaldy, *Metallurgical Transactions A*, **15A**, (1984): 545.

3. S. Zajac and B. Jansson, *Metallurgical and Materials Transactions B*, **29B**, (1998): 163.

4. W. Huang, *Zeitschrift fur Metallkunde*, **81**, (1990): 397.

5. E. J. Palmiere, C. I. Garcia and A. J. DeArdo, *Metallurgical and Materials Transactions*, **25A**, (1994): 277.

6. V. K. Lakshmanan and J. S. Kirkaldy, *Metallurgical Transactions A*, **15A**, (1984): 541.

7. W. Kesternich, Materials Research Society Symposium Proceedings, **62**, Materials Research Society, (1986): 229.

8. V. Thillou et al, *Materials Science Forum*, **284-286**, (1998): 311.

9. B. Dutta and C. M. Sellars, *Materials Science and Technology*, **3**, (1987): 197.

10. A. R. Jones, P. R. Howell and B. Ralph, *Journal of Materials Science*, **11**, (1976): 1593.

11. A. R. Jones, P. R. Howell and B. Ralph, *Journal of Materials Science*, **11**, (1976): 1600.

12. W. J. Liu and J. J. Jonas, *Metallurgical Transactions A*, **20A**, (1989): 689.

13. S. H. Park, S. Yue and J. J. Jonas, *Metallurgical Transactions A*, **23A**, (1992): 1641.

14. B. Dutta, E. Valdes and C. M. Sellars, *Acta Metallurgica et Materialia*, **40**, (1992): 653.

15. S. Yamamoto, C. Ouchi and T. Osuka, in Thermomechanical Processing of Microalloyed Austenite, ed. A. J. DeArdo, G. A. Ratz and P. J. Wray, The Metallurgical Society of AIME, (1982): 613.

16. W. J. Liu, *Metallurgical and Materials Transactions A*, **26A**, (1995): 1641.

17. M. Militzer, W. P. Sun and J. J. Jonas, *Acta Metallurgica et Materialia.*, **42**, (1994): 133.

18. M. Militzer and D. Meade, in J. J. Jonas Symposium on Thermomechanical Processing of Steel, ed. S. Yue and E. Es-sadiqi, Canadian Institute of Mining, Metallurgy and Petroleum, (2000): 453.

19. N. Fujita and H. K. D. H. Bhadeshia, *Materials Science and Technology*, **17**, (2001): 403.

20. B. Dutta, E. J. Palmiere and C. M. Sellars, *Acta Materialia*, **49**, (2001): 785.

21. T. Furuhara, N. Sugita and T. Maki, in Interface Science and Materials Interconnections (Proceedings of the 8th International conference on Intragranular and Interphase Boundaries in Materials), Japan Institute of Metals, (1996): 363.

22. J. M. Silcock, *Journal of the Iron and Steel Institute*, **201**, (1963): 409.

23. Y. Ohmori, *Transactions of the Iron and Steel Institute of Japan*, **15**, (1975): 194.

24. A. T. Davenport, L. C. Brossard and R. E. Miner, *JOM*, (1975): 21.

25. M. Sundararaman and P. Mukhopadhyay, *High Temperature Materials and Processes*, **11**, No. 1-4, (1993): 352.

26. N. Sugita, Master's Thesis, Kyoto University, (1996).

27. W. J. Liu and J. J. Jonas, *Materials Science and Technology*, **5**, (1989): 8.

28. U. Wolf, S. M. Foiles and H. F. Fischmiester, *Acta Metallurgica et Materialia*, **39**, (1991): 373.

29. P. Gumbsch, *Zeitschrift fur Metallkunde*, **83**, (1992): 500.

30. Z.-G. Yang and M. Enomoto, in Proceedings of the International Conference on Solid-Solid Phase Transformations '99, ed. M. Koiwa, K. Otsuka and T. Miyazaki, The Japan Institute of Metals, (1999): 599.

31. Z.-G. Yang and M. Enomoto, *Acta Materialia.*, **47**, (1999): 4515.

32. Z.-G. Yang and M. Enomoto, *Metallurgical and Materials Transactions A.*, **32A**, (2001): 267.

33. S. Suzuki, G. C. Weatherly and D. C. Houghton, *Acta Metallurgica*, **35**, (1987): 341.

34. M. Prikryl et al, *Metallurgical and Materials Transactions A*, **27A**, (1996): 1149.

35. H. Zou and J. S. Kirkaldy, *Canadian Metallurgical Quarterly*, **28**, 171, 1989.

36. G. M. Michal and I. E. Locci, *Scripta Metallurgica*, **22**, (1988): 1801.

37. J. W. Cahn and J. E. Hilliard, *The Journal of Chemical Physics*, **28**, (1958): 258.

38. F. J. Humphreys and M. Hatherly, Recrystallization and Related Annealing Phenomena, Pergomon Press, (1996).

39. P. L. Orsetti Rossi and C. M. Sellars, *Acta Materialia* , **45**, (1997): 137.

40. S. S. Hansen, J. B. Vander Sands and M. Cohen, *Metallurgical Transactions A*, **11A**, (1980): 387.

41. J. S. Perttula and L. P. Karjalainen, *Materials Science and Technology*, **14**, (1998): 626.

42. A. I. Fernandez, B. Lopez and J. M. Rodriguez-Ibabe, *Scripta Materialia*, **40**, (1999): 543.

43. O. Kwon and A. J. DeArdo, *Acta Metallurgica et Materialia*, **38**, (1990): 41.

44. G. Li et al, *ISIJ International*, **36**, (1996): 1479.

45. A. Laasraoui and J. J. Jonas, *Metallurgical Transactions A*, **22A**, (1991): 151.

46. K. B. Kang et al, *Scripta Materialia*, **36**, (1997): 1303.

47. T. Furu, K. Marthinsen and E. Nes, *Materials Science and Technology*, **6**, (1990): 1094.

48. R. A. Vandermeer, in Recrystallization and Grain Growth: Proceedings of the First Joint International Conference, ed. G. Gottstein and D. A. Molodov, Springer, (2001): 645.

49. J. W. Cahn, in Materials Research Society Symposium Proceedings, **398**, Materials Research Society, (1996): 425.

50. K. Lücke, G. Masing and P. Nölting, *Zeitschrift fur Metallkunde*, **47**, (1956): 64.

51. K. T. Aust and J. W. Rutter, *Transactions of the Metallurgical Society of AIME*, **215**, Feb., (1959): 119.

52. J. W. Cahn, *Acta Metallurgica*, **10**, (1962): 789.

53. K. Lücke and H. P. Stüwe, *Acta Metallurgica*, **19**, (1971): 1087.

54. M. Hillert and B. Sundman, *Acta Metallurgica*, **24**, (1976): 731.

55. M. J. Luton, R. Dorvel and R. A. Petkovic, *Metallurgical Transactions A*, **11A**, (1980): 411.

56. J. J. Jonas and I. Weiss, *Metal Science*, **13**, (1979): 238.

57. J. J. Jonas and M. G. Akben, *Metals Forum*, **4**, (1981): 92.

58. H. L. Andrade, M. G. Akben and J. J. Jonas, *Metallurgical Transactions A*, **14A**, (1983): 1967.

59. E. A. Simielli, S. Yue and J. J. Jonas, *Metallurgical Transactions A*, **23A**, (1992): 597.

60. E. Nes, *Acta Metallurgica et Materialia*, **43**, (1995): 2189.

61. N. Maruyama, R. Uemori and M. Sugiyama, *Materials Science and Engineering A*, **250**, (1998): 2.

62. W. J. Liu and J. J. Jonas, *Metallurgical Transactions A*, **19A**, (1988): 1415.

63. J. M. Silveira e Silva and R. Barbosa, *Scripta Metallurgica et Materialia*, **29**, (1993): 881.

64. F. G. Arieta and C. M. Sellars, *Scripta Metallurgica et Materialia*, **30**, (1994): 707.

65. J. M. Silveira e Silva, W. Dahl and R. Barbosa, in Recrystallization and Grain Growth: Proceedings of the First Joint International Conference, ed. G. Gottstein and D. A. Molodov Springer, (2001): 1167.

66. M. Verdier, Y. Brechet and P. Guyot, *Acta Materialia*, **47**, (1999): 127.

67. R. Monzen, J. Asaoka and M. Iguchi, *Scripta Materialia*, **38**, (1998): 1577.

68. J. Fridberg, L. Torndahl and M. Hillert, *Jernkontorets Annalers*, **153**, (1969): 263.

69. C. J. Smithells, *Smithells Metals Reference Book*, 6th edition, Butterworths, (1979).

70. A. R. Jones and B. Ralph, *Acta Metallurgica*, **23**, (1975): 355.

71. W. Kesternich and D. Meertens, *Acta Metallurgica*, **34**, (1986): 1071.

72. A. R. Jones and B. Ralph, *Acta Metallurgica*, **25**, (1977): 939.

73. C. S. Smith, *Transactions of the American Institute of Mining Engineers*, **175**, (1948): 15.

74. M. F. Ashby, J. Harper and J. Lewis, *Transactions of the Metallurgical Society of A.I.M.E.*, **245**, (1969): 413.

75. R. D. Doherty, *Metal Science*, **16**, (1982): 1.

76. W-B. Li and K. E. Easterling, *Acta Metallurgica et Materialia*, **38**, (1990): 1045.

77. E. Nes, N. Ryum and O. Hunderi, *Acta Metallurgica*, **33**, (1985): 11.

78. P. M. Hazzledine, *Czechoslovak Journal of Physics*, **38**, (1988): 431.

79. P. M. Hazzledine, P. B. Hirsch and N. Louat, in Recrystallization and Grain Growth of Multi-Phase and Particle Containing Materials, ed. N. Hansen, A. R. Jones and T. Leffers, Riso National Laboratory, (1980): 159.

80. K. J. Lee, *Scripta Materialia*, **40**, (1999): 837.

81. S. F. Medina et al, *ISIJ International*, **39**, (1999): 913.

82. D. Q. Bai et al, *Metallurgical Transactions A*, **24A**, (1993): 2151.

83. D. Weygand, Y. Brechet and J. Lepinoux, *Acta Materialia*, **47**, (1999): 961.

84. O. Kwon, A. J. DeArdo, *Acta Metallurgica et Materialia*, **39**, (1991): 529.

85. A. J. DeArdo, C. I Garcia and E. J. Palmiere, ASM Handbook, **4**, ASM International, (1992): 237.

86. S. Almaguer, C. M. Sellars and W. M. Rainforth, in Recrystallization and Grain Growth: Proceedings of the First Joint International Conference, ed. G. Gottstein and D. A. Molodov, Springer, (2001): 831.

87. W. M. Rainforth et al, *Acta Materialia*, **50**, (2002): 735.

88. C. J. Tweed, B. Ralph and N. Hansen, *Acta Metallurgica*, **32**, (1984): 1407.

89. L. M. Brown and R. K. Ham, in Strengthening Methods in Crystals, ed. A. Kelly and R. B. Nicholson, Applied Science Publishers, (1971): 12.

90. V. Gerold, in Dislocations in Solids, **4**, ed. F. R. N. Nabarro, North-Holland Publishing Co., (1979): 219.

91. R. B. Scarlin and J. W. Edington, *Metal Science Journal*, **7**, (1973): 208.

92. R. B. Nicholson, Effect of Second Phase Particles on the Mechanical Properties of Steel, Iron and Steel Institute, (1971): 1.

93. J. M. Silcock, *Scripta Metallurgica*, **10**, (1976): 367.

94. R. A. Vandermeer and B. B. Rath, *Metallurgical Transactions A*, **20A**, (1989): 391.

95. P. L. Orsetti Rossi and C. M. Sellars, *Materials Science and Technology*, **15**, (1999): 185.

96. H. P. Stuwe, A. F. Padilha, F. Siciliano Jr., *Materials Science and Engineering A*, **333**, (2002): 361.

97. N. Maruyama, G. D. W. Smith and A. Cerezo, *Materials Science and Engineering A*, submitted (2002).

98. D. Turnbull, *Transactions of the American Institute of Mining Engineers*, **191**, (1951): 661.

99. A. Yoshie et al, *ISIJ International*, **32**, (1992): 395.

100. J. E. Bailey and P. B. Hirsch, *Proceedings of the Royal Society*, **A267**, (1962): 11.

101. J. G. Speer and S. S. Hansen, *Metallurgical Transactions A*, **20A**, (1989): 25.

102. O. Kwon and A. J. DeArdo, *Acta Metallurgica et Materialia*, **39**, (1991): 529.

103. G. Saada, *Acta Metallurgica*, **8**, (1960): 841.

104. A. Deschamps and Y. Brechet, *Acta Materialia*, **47**, (1999): 293.

105. K. C. Russell, *Advances in Colloid and Interface Science*, **13**, (1980): 205.

106. J. W. Cahn, *Acta Metallurgica*, **5**, (1957): 169.

107. R. Gomez-Ramirez and G. M. Pound, *Metallurgical Transactions*, **4**, (1973): 1563.

108. S. Okaguchi and T. Hashimoto, *ISIJ International*, **32**, (1992): 283.

109. K. Narita, *Transactions of the Iron and Steel Institute of Japan*, **15**, (1975): 145.

110. I. M. Lifshitz and V. V. Slyozov, *Physics and Chemistry of Solids*, **19**, (1961): 35.

111. C. Wagner, *Zeitschrift fur Elektrochemie*, **65**, (1961): 581.

112. J. W. Martin, R. D. Doherty and B. Cantor, Stability of Microstructure in Metallic Systems, 2nd edition, Cambridge University Press, (1997).

113. H. J. Frost and M. F. Ashby, Deformation Mechanism Maps, Pergmon Press, (1982).

114. J. Geise and C. Herzig, *Zeitschrift Metallikde.*, **76**, (1985): 622.

115. I. Kaur, W. Gust and L. Kozma, Handbook of Grain and Interphase Boundary Diffusion Data, **1**, Ziegler Press, (1982).

116. M. Suehiro, Z. K. Liu and J. Agren, *Acta Metarialia*, **44**, (1996): 4241.

117. P. Dumoulin and M. Guttmann, *Materials Science and Engineering*, **42**, (1980): 249.

118. D. Alaoua et al, *Materials Science Forum*, **126-128**, (1993): 185.

119. M. Enomoto, N. Nojiri and Y. Sato, *Materials Transactions JIM*, **35**, (1994): 859.

120. M. Menyhard, M. Yan and V. Vitek, *Acta Metallurgica et Materialia*, **42**, (1994): 2783.

121. A. Yoshie et al, *ISIJ International*, **36**, (1996): 467.

122. Gomez et al, in Recrystallization and Grain Growth: Proceedings of the First Joint International Conference, Ed. G. Gottstein and D. A. Molodov, Springer, (2001): 831.

123. M. G. Burke et al, *Materials Science and Technology*, **4**, (1988): 113.

124. S. F. Medina and A. Quispe, *Materials Science and Technology*, **16**, (2000): 635.

125. A. Quispe et al, Recrystallization and Grain Growth: Proceedings of the First Joint International Conference, Ed. G. Gottstein and D. A. Molodov, Springer, (2001): 1155.

126. N. Maruyama and G. D. W. Smith, *Materials Science and Engineering A*, **327**, (2002): 34.

127. T. B. Massalski, Binary alloy phase diagrams, **1**, American Society of Metals, (1986).

128. T. Wada et al, *Metallurgical Transactions*, **2**, (1971): 2199.

129. R. M. Poths, R. L. Higginson and E. J. Palmiere, Recrystallization and Grain Growth: Proceedings of the First Joint International Conference, Ed. G. Gottstein and D. A. Molodov, Springer, (2001): 785.

130. P. J. Hurley et al, *Materials Science Forum*, **284-286**, (1998):159.

131. P. J. Hurley, P. D. Hodgson and B. C. Muddle, *Scripta Materialia*, **45**, (2001): 25.

132. Y. Adachi, T. Tomida and S. Hinotani, *ISIJ International*, **40**, (2000): S194.

133. W. Charnock and J. Nutting, *Metal Science Journal*, **1**, (1967): 78.

134. W. Charnock and J. Nutting, *Metal Science Journal*, **1**, (1967): 123.

135. P. S. Kotval, *Transactions of the Metallurgical Society of AIME*, **242**, (1968): 1651.

136. M. Ueki, S. Horie and T. Nakamura, *Materials Science and Technology*, **3**, (1987): 329.

137. ThermoCalc and Fe-data are available from, *Thermo-Calc Software*, Stockholm Technology Park, Björnnäsvägen 21, SE-113 47 Stockholm, SWEDEN

138. J. M. Silcock and W. J. Tunstall, *Philosophical Magazine*, **10**, (1964): 361.

139. J. M. Silcock and A. W. Denham, in The Mechanism of Phase Transformation in Crystalline Solids, Institute of Metals, (1969): 59.

140. V. M. Adeyev and Yu. N. Petrov, *Physics of Metals and Metallography*, **48**, (1981): 128.

141. L. G. Martinez, K. Imakuma and A. F. Padilha, *Steel Research*, **62**, (1992): 221.

142. B. E. P. Beeston and L. K. France, *Journal of the Institute of Metals*, **96**, (1968): 105.

143. R. B. Scarlin and J. W. Edington, *Journal of Materials Science*, **9**, (1974): 1590.

144. Q. Z. Chen, C. N. Jones and D. M. Knowles, *Scripta Materialia*, **47**, (2002): 669.

145. A. Guinier, X-Ray Diffraction in Crystals, Imperfect Crystals and Amorphous Bodies, W. H. Freeman & Co., (1963).

146. G. Kostroz, in Physical Metallurgy, 3rd edition, ed. R. W. Cahn and P. Haansen, Elsevier Science Publishers, (1983): 793.

147. G. Kostroz, *Treatise on Materials Science and Technology*, **15**, (1979): 227.

148. G. E. Bacon, Neutron Diffraction, 3rd edition, Clarendon Press, (1971).

149. E. Nes, *Progress in Materials Science*, **41**, (1998): 129.

150. P. Haasen, in Dislocations in Solids, **4**, ed. F. R. N. Nabarro, North-Holland Publishing Co., (1979): 153.

151. J. Eliasson and R. Sandstrom, *Steel Research*, **71**, (2000): 249.

152. R. K. Ray and J. J. Jonas, *International Material Reviews*, **35**, (1990): 1.

153. T. Sato et al, *ISIJ International*, **38**, (1998): 640.

154. Private Communication from J. D. Embury: Department of Materials Science and Engineering, McMaster University.

Appendix (A1): Methods of Estimating the Recrystallized Fraction from Restoration Experiments.

A number of methods have been developed to estimate the recrytallized fraction from softening data. These methods are most applicable when recrystallization and recovery are the only processes taking place. Under these circumstances, it is argued that the values of σ_P, σ_W and σ_R can be chosen careful to exclude the effect of recovery. Six of these methods are described below:

i) *0.2% off-set*: This is the oldest method. The flow stresses of the completely and partially recrystallized materials are identified as the 0.2% yield stress of the first and second flow curves, respectively. The flow stress of the work-hardened material is identified as the maximum stress of the first curve. It is now accepted that this method does very little to exclude the effect of recovery [41-43].

ii) *20% softening:* This method was introduced to improve the accuracy of the 0.2% off-set method. The argument is that about 20% of the observed softening is due to recovery. Therefore, $R_{20\%} = (R_{0.2\%\ \text{off-set}} - 0.2) / 0.8$ [42, 44]. This method is questionable because it does not account for the fact that the recovery contribution will change with composition and temperature [42].

iii) *2% off-set:* This is an improvement on the 0.2% off-set method. In this case a 2% off-set is used to determine the flow stresses of the partially and completely

recrystallized materials. Several authors claimed that this approach provides a reasonable estimate of the recrystallized fraction [42, 44].

iv) *5% total-strain:* In this method the flow stresses of the partially and completely recrystallized materials are identified using a 5% strain. The value of σ_W is estimated from the extrapolation of the first curve when the strain is 5% relative to the origin of the second curve [42]. Several authors [41, 42] argued that this method is effective at excluding the effect of recovery.

v) *Back extrapolation:* This method is closely related to the 0.2% off-set method. In fact, the values of σ_W and σ_R are the same as those of the 0.2% off-set method. The value of σ_P is obtained by shifting the first deformation curve so that its work-hardening region coincides with the work-hardening region of the second curve. The intersection between the unloading line and the shifted curve represents σ_P. Comparison with metallographic data suggests that this method consistently overestimates the recrystallized fraction [42].

vi) *Mean stress:* In this case σ_R and σ_P are replaced by the mean flow stresses. These are obtained by integrating the first and second curves, respectively, and dividing by the pass strain. The mean flow stress of the work-hardened material is calculated from the flow curve of a hypothetical second hit that corresponds to no softening [45]. This method appears to provide a good estimate of the recrystallized volume fraction [42, 45].

The accuracy of these methods was examined by a number of authors [42, 43]. It

appears that the 2% off-set, the 5% total strain and the mean stress methods are the most promising. The results of theses methods are within ±5-10% of those obtained from optical measurements, *provided that recrystallization and recovery are the only processes taking place.*

Appendix (A2): Simple Model for the Effect of Solute Concentration on the Activation Volume of Recovery.

The activation volume in equation (1.9) was defined as $b\,a^*\,l$, where l is the obstacle spacing. The effective obstacle spacing will include contributions from both solute-atoms and forest-type jogs. For simplicity, the two contributions are added in parallel, leading to an equation of the form:

$$\frac{1}{l} = \frac{1}{l_{jogs}} + \frac{1}{l_{solute}} = \frac{\sqrt{\rho}}{k_1} + \frac{C^n}{k_2} \qquad \text{(A2.1)}$$

This approach provides for a smooth transition from glide control to solute-drag control as the solute concentration increases.

Interestingly, equations (1.9) and (A2.1) do not contain any solute-specific information. As a result, the dependence of recovery on the type of solute is not captured. In order to deal with this criticism, the concentration is replaced by $C_o \exp(E_b/RT)$. Here, C_o is the bulk concentration of solute, while $C_o \exp(E_b/RT)$ is the concentration of solute at the dislocation (due to segregation). In the new equation, the effectiveness of a given solute depends on the value of the solute-dislocation binding energy, E_b. In addition, the effectiveness of a given solute increases with decreasing temperatures in agreement with the observations of Yamamoto et al [15].

The results of this simple model are plotted in figure (A2.1). Clearly the experimental trends are all captured by this simple model. In our calculations, we used the typical values of k_1 =1, n = ⅔ and $Q = Q_{self}$ = 286 kJ/mole. The binding energies of Nb, Ti and V were assumed to be 0.20, 0.15 and 0.05 eV, respectively. Finally, the constant, k_2, was used as an adjustable parameter.

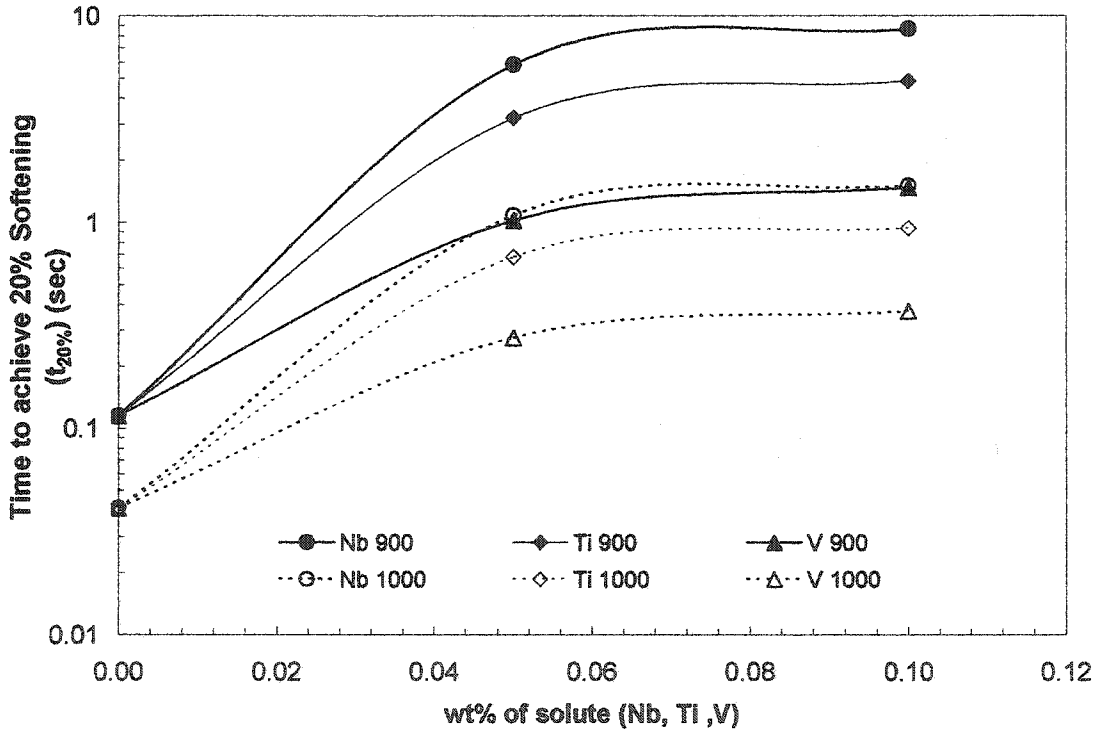

Figure (A2.1): *Predicted effects of Nb, Ti and V on the time needed for 20% softening. Compare with the experimental data of figure (1.1).*

Appendix (A3): Computational Issues Relating to the Precipitation Model

In section (2.3), the problem of heterogenous nucleation on dislocations was simplified by assuming that the nucleus is spherical. This assumption is inherently flawed because it leads to an initial *radius of curvature* which is smaller than the homogenous nucleation radius. Consequently, negative growth-rates are obtained when the standard Gibbs-Thompson equation is used to calculate the growth-rate for $r < r$(homogenous). To deal with this difficulty, the Nb concentration in equilibrium with a particle of radius r was calculated from a modified version of the Gibbs-Thompson equation. Thus, C_{Nb}^{r} was calculated by solving for the Nb concentration in the equation:

$$\frac{d\Delta G}{dr} = 0 \qquad \text{(A3.1)}$$

where ΔG is given by equation (2.15). In this way, the growth rate, $dr/dt|_{\text{growth}}$ is guaranteed to go to zero for the initial (heterogenous) nucleation radius. It should be emphasized that this approach has no physical basis. It is purely a mathematical manipulation that allows us to use equation (2.15) without running into negative growth rates for $r < r$(homogenous). The concentrations obtained from Eq. (A3.1) differ from the values of the Gibbs-Thompson equation at short times only. At long times, the Gibbs-Thompson Equation is recovered.

Appendix (A4): Estimation of the Binding Energy of Nb to Grain-Boundaries.

Atomistic simulations suggest that the binding energy varies depending of the type of grain boundary. In fact, within the same grain boundary, there exists a range of sites with varying segregation/ binding energies. The energies measured experimentally, represent the average binding energy for a given boundary or for the random group of boundaries that was sampled [120]. Both theory and experiment suggest that E_b varies with composition. In general, the binding energy decreases as the solute concentration increases [116, 120].

The values listed in table (A4.1) are typical of a large misfitting solute in an FCC matrix. Most are of the order of 0.20-0.25 eV. Only the data of Suehiro et al [116] takes into account the effect of composition on the binding energy. For the purpose of the present model, a constant binding energy of 0.25 eV appears reasonable.

E_b (eV)	Source/ Comments
The following data is for Nb in low carbon steels.	
0.38	Maruyama et al [97]/ AP-FIM data on GB segregation in α-iron at 800°C. (0.087%Nb)
0.24	Suehiro et al[116]/ from a model of the γ ⇨ α transformation. (0.250%Nb & 0.23% Mn)
0.29	Suehiro et al [116] for a more typical composition. (0.041% Nb & 1.23% Mn)
The following data is for Ti in low carbon steels.	
0.22	Dumoulin et al [117] /Based on measurements in a binary Fe-Ti system. (in α-iron)
0.20	Alaoua et al [118] /Based on surface measurements in an alloy containing P and S. (in α-iron)
The following data is for V in low carbon steels.	
0.20	M. Enomoto et al [119]/ experimental measurements on former austenite boundaries. (0.87%V).
The following data is for Ag in Cu. (Ag has 15% size mismatch in Cu just like NbC in Fe).	
0.17	Menyhard et al[120]/ atomistic simulations and experimental measurements. (310)/[100] Σ5 boundary. (0.6 at% Ag)
0.20	Menyhard et al/ [120] same as above. (0.3 at% Ag)

Table (A4.1): *A List of the available estimates of the binding energy between Nb and austenitic grain boundaries.*

A5: Full Text of: ***H. S. Zurob, Y. Brechet and G. Purdy, Acta Materialia, 49, (2001): 4183-4190***

Pergamon

Acta mater. 49 (2001) 4183–4190

Acta MATERIALIA

www.elsevier.com/locate/actamat

A MODEL FOR THE COMPETITION OF PRECIPITATION AND RECRYSTALLIZATION IN DEFORMED AUSTENITE

H. S. ZUROB[1], Y. BRECHET[2] and G. PURDY[1]†

[1]McMaster University, Department of Materials Science and Engineering, Hamilton, Ontario, Canada and
[2]Domaine Universitaire de Grenoble, LTPCM/ENSEEG, St. Martin d'Hères Cedex, France

(Received 13 October 2000; received in revised form 5 August 2001; accepted 8 August 2001)

Abstract—The hot-deformation of a microalloyed steel sets the stage for the processes of static-recrystallization and strain-induced precipitation. A physically-based model was developed to describe the interaction of these two processes. The precipitates were assumed to form, exclusively, on dislocations. Dynamic effects as well as static recovery were ignored. Given the alloy composition, deformation temperature and dislocation density, the model is able to predict the recrystallized fraction as a function of time. The model may be used to construct recrystallization–time–temperature (RTT) maps as well as deformation–temperature (DT) maps. The predictions of the model are in excellent qualitative agreement with experimental observations. © *2001 Published by Elsevier Science Ltd on behalf of Acta Materialia Inc.*

Keywords: Microalloying; Recrystallization; Precipitation; Modelling

1. INTRODUCTION

The interaction between precipitation and recrystallization is a complex process; it has profound implications for the control of microstructure and structure-dependent properties of alloys. This is particularly true for the case of microalloyed steels, which depend critically for many of their properties on the control of ferrite grain size (which is dependent in turn on the grain size of the precursor austenite).

High-strength low-alloy steels are produced by cycles of controlled thermal and mechanical processing. Microalloying elements such as niobium have been used extensively in the development of fine ferrite grain sizes. Niobium in solution is believed to play a role in the retardation of austenite recrystallization after deformation, through a process of solute drag [1–7]. However, because of its strong affinity for the interstitial solutes, carbon and nitrogen, niobium can also retard the recrystallization process by precipitating in combination with them to form dispersed pinning particles [8–10].

The response of microalloyed steels to thermomechanical processing has been the subject of a great deal of experimental work. Over the years, advanced databases and powerful empirical relations have been developed to relate the extent of recrystallization to the deformation temperature, the amount of deformation and the chemistry of the material [11–14]. The present work was undertaken with the object of developing and exploring a physically-based model of the interaction of microalloying elements with the recrystallization process. In a later section, the model will be compared with experiment and with empirical expressions. Our ultimate goal is a convergence between the two approaches, and a deeper understanding of the factors that determine the final structure of deformed and recrystallized austenite. The more limited objective of the present work is a fundamentally based treatment of the static recrystallization of austenite, supersaturated with respect to the precipitation of NbC.

2. A SIMPLE MODEL FOR THE EFFECT OF MICROALLOYING ON THE RECRYSTALLIZATION KINETICS

The hot-deformation of austenite sets the stage for two competing processes, namely, static recrystallization and strain-induced precipitation. The interaction of the two phenomena is complicated by the presence of alloying elements in solution. These solutes change the collective behaviour of dislocations (mainly through their influence on the dynamic recovery kinetics): for the same strains and strain rates, the alloys might have both a different stored dislocation density and a different subgrain structure. Since subgrains play an important role in the nucleation

† To whom all correspondence should be addressed. fax:

1359-6454/01/$20.00 © 2001 Published by Elsevier Science Ltd on behalf of Acta Materialia Inc.
PII: S1359-6454(01)00315-9

step, this will likely influence both the nucleation and the growth kinetics of the recrystallized grain. In the following, we will bypass this difficulty by assuming site saturation for the nucleation of new grains at the pre-existing grain boundaries, and by considering the stored energy (assumed for the sake of simplicity to be proportional to the dislocation density) as a control variable. The effect of solute elements on both the subgrain structure and on dislocation storage will not be treated. We will focus on the effect the solute element exerts on the mobility of grain boundaries.

Assuming site saturation (N sites per unit volume) and a linear relation between the velocity, v, and the stored energy due to dislocations, G_r, leads to a Johnson–Mehl–Avrami law of the form:

$$X_{ext} = N\left(\int_0^t M(t)G_r\,dt\right)^3 \qquad (2.1)$$

Here, X_{ext} is the extended recrystallized volume fraction and $M(t)$ is the grain boundary mobility as a function of time. In the present approach, we neglect static recovery during annealing so that the driving force remains constant. The estimation of the driving force for recrystallization is done using the simplest possible approach; if ρ is the stored dislocation density, the stored energy is assumed to be:

$$G_r = \tfrac{1}{2}\rho\mu b^2 \qquad (2.2)$$

Here, μ and b are the shear modulus and the magnitude of the Burgers vector, respectively. An alternative estimate could be based on an analysis of the subgrain structure. Both the subgrain size and the subgrain misorientation are dependent on the stored dislocation density. This method of estimation would, however, require extra information on the evolution of subgrain misorientation. At the level of sophistication of the present model, it is sufficient to capture the fact that stored energy (G_r) increases with ρ. This approach leads to a driving force of 1 MPa for a dislocation density of 4×10^{14} m^{-2}.

We now need to consider the effect of precipitation on the recrystallization kinetics. Strictly speaking, the Zener pressure is a threshold force for the motion of grain boundaries. The grain boundary is stationary in the case where the driving force (here the stored dislocation energy) is lower than the pinning force. When the driving force exceeds the pinning force the kinetics is identical to that obtained by a driving force which is diminished by the pinning force (P). Making this simple assumption leads to the grain boundary velocity being:

$$v = M(\tfrac{1}{2}\rho\mu b^2 - P(t)) \qquad (2.3)$$

This approach has been used in the past [15, 16]. Recently [17], Vertex simulations of grain growth confirmed the accuracy of equation (2.3).

The pinning of grain boundaries by particles has been investigated in many ways since the seminal suggestion of Zener to Smith [18]. The effects of particle shape, spatial distributions, and the statistics originating from the finite flexibility of the grain boundary have all been investigated, either analytically, or through computer simulation. At the level of approximation of the present paper, these refinements are simply unnecessary. Therefore, the simple Zener formula is used:

$$P = \frac{3\gamma_{gb}F_v}{2r} \qquad (2.4)$$

where γ_{gb}, F_v, and r represent the grain boundary energy (taken as 0.75 J/m^2), the precipitate volume fraction and the average precipitate radius, respectively. This simple formula captures the essential physics of the problem: an increase of the volume fraction of precipitates increases the total pinning force, while coarsening at a constant volume fraction decreases the pinning force. The extended recrystallized volume fraction is therefore given by:

$$X_{ext} = N\left(\int_0^t M(t)\left[\frac{1}{2}\rho\mu b^2 - \frac{3}{2}\frac{\gamma_{gb}F_v}{r}\right]dt\right)^3 \qquad (2.5)$$

Assuming a random spatial distribution of nuclei, the actual recrystallized volume fraction (X) is given by:

$$X = 1 - \exp(-X_{ext}) \qquad (2.6)$$

In order to predict the recrystallized fraction, accurate estimates of the mobility, $M(t)$, the Zener pressure, $P(t)$, and the number of recrystallization nuclei, N, are needed. These quantities are discussed next.

2.1. *Solute drag: M(t)*

The effect of solute elements on the mobility has been treated extensively by Cahn [19]. The drag effect reduces the mobility in a non-linear manner depending on the velocity. We have simplified the present approach by taking a mobility, which is constant with velocity and proportional to the solute content (either the fast branch or the slow branch of Cahn's solution). For a low driving force, Cahn's solution simplifies to:

$$M(t) = \left(\frac{1}{M_{Pure}} + \alpha C_{Nb}\right)^{-1} \qquad (2.7a)$$

where,

$$\alpha = \frac{\delta N_v (kT)^2}{E_b D}\left(\sinh\left(\frac{E_b}{kT}\right) - \frac{E_b}{kT}\right) \qquad (2.7b)$$

In equation (2.7a), M_{pure} and C_{Nb} refer, respectively, to the intrinsic grain boundary mobility and the concentration of Nb in solution. Referring to equation (2.7b), δ is the width of the grain boundary, N_v is the number of atoms per unit volume and E_b is the solute-boundary binding energy. In the same equation, D is the average value of the diffusion coefficient in the vicinity of the grain boundary. We have equated D to the bulk diffusion coefficient, based on APFIM results of Smith and Maruyama [20], which show a very wide segregation profile near the boundary.

The estimation of a standard mobility, even in a pure material, is a difficult problem. We are also interested in the mobility as a function of both the temperature and the solute content. The classical estimate by Turnbull [21], is clearly an upper bound because it neglects all possible attachment kinetics. A rough order of magnitude estimate of a real mobility in a pure metal is 1/10 of the Turnbull estimate.

$$M_{Pure} = \frac{1}{10}\frac{\delta D_{gb} V_m}{b^2 RT} \qquad (2.8)$$

Here, D_{gb} is the grain boundary self-diffusion coefficient, V_m is the molar volume of austenite and b is Burgers' vector. This assumption leads to an activation energy for grain boundary motion of the same magnitude as the energy for grain boundary diffusion.

The segregation energy of Nb to grain boundaries (E_b) is not accurately known. A value of 19.3 kJ/mol is our best estimate based on the data in the literature [20, 22–26]. Knowing, M_{pure}, E_b and D, equations (2.7) and (2.8) can be used to calculate the mobility for any given temperature and Nb content.

2.2. Zener pinning, P(t)

We are concerned here with the effect of precipitation occurring during the recrystallization treatment. The classical effect of particle-stimulated nucleation as studied by Humphreys [27] and stemming from the presence of high dislocation densities around undeformable particles is of a different nature. We consider that the material is in the solution treated condition. It is then deformed at a temperature below the solvus. This sets the stage for both recrystallization and strain-induced precipitation. In the alloys being considered the precipitates are nucleated heterogeneously due to the large volume difference between the precipitates and the matrix. This leaves the grain boundaries and dislocations as the only important nucleation sites. Recrystallization affects precipitation by changing the dislocation density. The effect of precipitation on recrystallization is more complex. On the one hand the progress of precipitation will lower the solute content (and thus increase grain boundary mobility through a decrease of the solute drag effect). On the other hand the precipitates will provide a pinning force opposing the motion of the grain boundaries. In what follows we will propose a simple model for describing these interactions.

2.2.1. Precipitation on dislocations. As a first approximation we assumed that precipitation takes place exclusively on dislocations. The omission of grain boundary precipitates is reasonable because these account for less than 1% of the total [8]. Two questions must be addressed regarding precipitation on dislocations: (a) During the heat treatment, how much solute is effectively accessible for precipitation along the dislocations? (b) What effect will the amount of accessible solute have on the precipitation kinetics? The first question is related to the diffusion of solute atoms toward dislocations. A rough first estimate is that the solute available should be in a cylinder of radius $(Dt)^{1/2}$. Then the fraction of solute available for precipitation is of the order of $\rho\pi Dt$. For the situation considered in the present paper, and thanks to the especially large diffusion coefficient for niobium in austenite, the diffusion process is rapid enough so that all the solute in solution is effectively available for precipitation on dislocations. With lower dislocation densities, or at lower temperatures, that would not necessarily be the case. In the presence of solute/dislocation interaction, Cottrell–Bilby kinetics [28] would certainly be more appropriate. The amount of solute available would then scale as $t^{2/3}$ rather than t. However, in order to be consistent with such a description, a coupled equation between the solute arriving on dislocations and the precipitation kinetics would be needed. In our model, we assumed that the rate of nucleation limits the precipitate volume fraction under all conditions. A more rigorous treatment does not appear to be justified knowing the precision of the available data for the thermodynamics and diffusion quantities.

2.2.2. Nucleation. For the sake of simplicity, precipitation along dislocations is assumed to take place in two steps. In the first step, one assumes a constant nucleation rate with constant precipitate size. This corresponds to a constant influx of solute toward dislocations. The nucleation rate is given by the classical theory of nucleation:

$$J = Z\beta^* \psi \exp\left(\frac{-\Delta G_n}{kT}\right) \qquad (2.9)$$

Here, Z is the Zeldovich non-equilibrium factor, β^* is the rate at which the atoms are being added to the critical nucleus, ψ is the number of nucleation sites per unit volume and ΔG_n is the energy of formation of the nucleus. Following Russell [29], the product

$Z\beta^*$ was approximated as $D_{pipe}C_{Nb}/a^2$, where D_{pipe} is the diffusion coefficient along dislocations and a is the jump distance which is approximately equal to the lattice constant. The density of nucleation sites was approximated as $F\rho/r_n$, where F is an adjustable factor smaller than unity. The critical energy, G_n, and radius, r_n, were estimated using the following energy balance [30, 31]:

$$\Delta G = V\Delta G_V + A\gamma - \frac{\mu b^2 r \ln(r/b)}{2\pi(1-\nu)} - \mu b^2 r/5 \tag{2.10}$$

Here, V and A are, respectively, the volume and area of the nucleus. In the same equation, γ is the interphase energy (taken as 0.75 J/m^2) and ν is Poisson's ratio.

This nucleation model differs from the ones used by Dutta *et al.* [8] and Liu *et al.* [9] in two ways: First the model contains only one adjustable parameter, F. Secondly, the nucleation sites are assumed to be enriched in Nb by a factor of $\exp(E_b/kT)$.

2.2.3. Coarsening. Once all the available solute has precipitated, one enters a coarsening regime, with a constant precipitate volume fraction. The transport of solute is assumed to take place by pipe diffusion. The coarsening kinetics are then described by [32]:

$$r^5 - r_o^5 = (1.0338)^5\left(\frac{3}{4}\right)^4\left(\frac{5}{6}\frac{\gamma C_o D_{pipe} r_p^2 N V_p^2 \eta}{RT}\right)(t - t_o) \tag{2.11}$$

In this equation, r_p is the radius of the dislocation pipe ($\sim b/2$), V_p is the molar volume of the precipitate, C_o is the equilibrium concentration of solute and N is the number of dislocations intersecting the precipitate particle. The constants, r_o and t_o represent the particle radius and the time at the onset of coarsening. Finally, the parameter, η, is given by: $4F_v^{0.5}/e^{4F_v}\Gamma(0.5, 4F_v)$, where Γ is the gamma function.

At this stage it is useful to summarize the assumptions of our two-stage model of precipitation. During the first stage, i.e. nucleation, the precipitate volume fraction increases linearly with time and the precipitate radius remains constant. In the second stage, the volume fraction is constant while the average radius increases with $t^{1/5}$. Temperature influences the kinetics both through the thermodynamics (by changing the driving force) and through transport (diffusion coefficient). The dislocation density enters the kinetics via the number of nucleation sites. It is also possible to envisage a situation where the dislocation density affects the kinetics by influencing the amount of solute available. This second possibility will not be considered.

Figure 1(a) is an illustration of the time-dependence of the Zener force resulting from the evolution of precipitation. The time evolution of the Zener drag is a function of both the temperature [Fig. 1(b)] and the initial dislocation density [Fig. 1(c)]. The temperature dependence is due to changes in the thermodynamic driving force and the diffusion coefficient with temperature. Dislocation density affects the Zener drag through the number of nucleation sites.

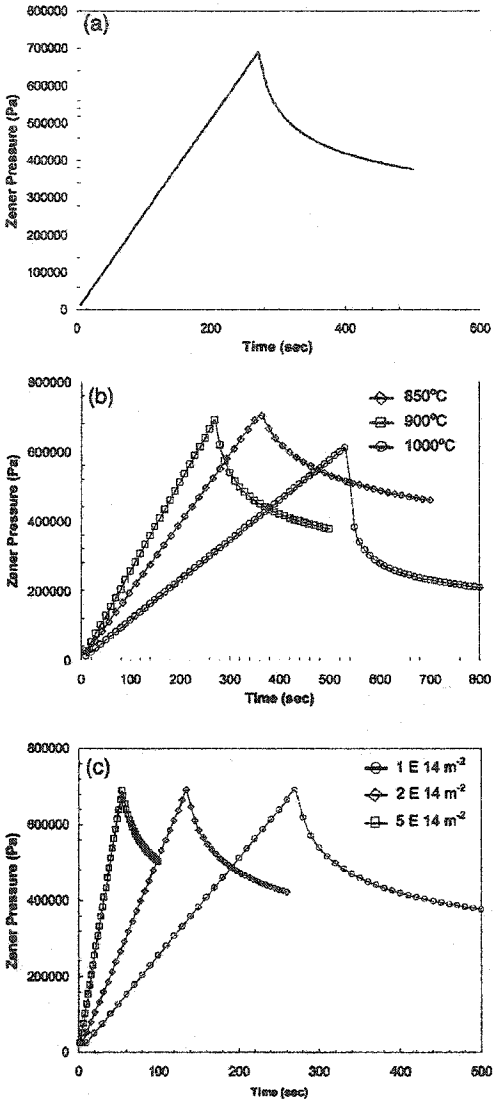

Fig. 1. (a) The evolution of the Zener pressure is described in two stages. During the first, the Zener pressure increases linearly as the precipitate volume fraction increases. During the second stage, the Zener pressure drops as the precipitates coarsen at constant volume fraction. (b) Changing the temperature will change the peak Zener pressure and the time at which this peak occurs. (c) The dislocation density only affects the time needed to achieve the peak stress. [The results are for a steel containing 0.06% Nb and 0.10% C. The nose of the precipitation curve is at 925°C.]

2.3. *Nucleation of recrystallization, N*

Nucleation is assumed to occur from the beginning of annealing, at a number of sites proportional to the grain boundary area per unit volume S_v (which is approximately equal to $3/D$ where D is the initial grain size). If A is the area occupied on the grain boundary by each nucleus, one will have:

$$N = \frac{kS_v}{A} \tag{2.12}$$

where k is a geometric factor. The size of the nuclei (A) depends on the driving force. Classical nucleation theory predicts that A is proportional to $1/G^2$. The same dependence is predicted by the Bailey–Hirsch theory [33]. Using this approach, a nucleus size of 3 μm is expected for a dislocation density of 4×10^{14} m^{-2}.

3. RESULTS

3.1. *The effect of temperature*

The results of our modelling are shown in Fig. 2(a). At high temperature, the recrystallization kinetics is so rapid that precipitation (which has a relatively low driving force) will not interfere. As the temperature decreases, precipitation occurs simultaneously with recrystallization. This leads to a Zener force, which may eventually stop recrystallization. Coarsening then takes place, leading to a reduction of the Zener force. Eventually, the Zener force is sufficiently decreased that recrystallization can proceed. This is the origin of the plateau, which is sometimes observed on the X–t curves at lower temperatures. In the present model, recrystallization would always start again, provided that coarsening is sufficiently advanced. However, it is then likely that recovery, which has been neglected thus far will decrease the driving force for recrystallization so that the plateau can last indefinitely. The inclusion of recovery would then lead to a final recrystallized fraction lower than 1, as is often observed in industrial alloys after hot rolling.

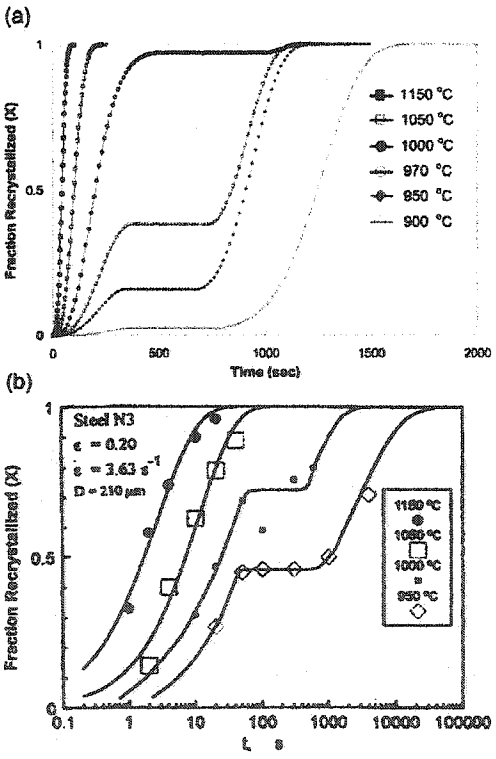

Fig. 2. (a) The model is applied to a steel containing 0.024% Nb, 0.21% C and 0.0058% N. (b) The same steel was studied experimentally by Medina *et al.* [34]. To be able to produce comparable results the dislocation density had to be estimated. This was done using the flow stress relations developed by Medina and colleagues [35–37].

The results of Fig. 2(a) should be compared to the experimental results of Medina *et al.* [34] [Fig. 2(b)]. In order to reproduce the experimental conditions, the dislocation density was estimated using the flow stress relations developed by Medina and colleagues [35–37]. The solubility of the carbonitride was calculated using the method described by Gladman [38] and utilizing the data of Narita [39]. Finally, the precipitate nucleation constant (F) was estimated using the data of Le Bon *et al.* [40]. This led to a nucleation rate (at 900°C) of 6×10^6/s/m of dislocation. It is clear from the diagrams that the present model captures the main features of the experimental data.

3.2. *Effect of Nb content*

The model that we have presented here allows the description of the effect of temperature and stored energy on the recrystallization kinetics. All the parameters used have a physical meaning and all can be estimated from experimental data. In this section the effect of composition is considered. We will not pursue a systematic investigation of the temperature, composition and strain path dependence. We will simply illustrate the expected effect of changing the Nb content on the kinetics.

Figure 3 shows the effect of Nb content on the overall kinetics. The complex behaviour results from the trade-off between solute drag and precipitate pinning. Increasing the Nb content shifts the nose of the precipitation C-curve to shorter times and higher temperatures. In addition, the higher Nb content reduces the mobility. At Nb contents of 0.06% or more, precipitation is advanced enough to halt recrystallization.

As mentioned earlier, our present model does not take into account the solute effect on the dislocation storage kinetics. These interactions should be included in order for our description of the composition dependence to be self-consistent. The control parameters of the model would then become the strain and strain rate rather than the dislocation density.

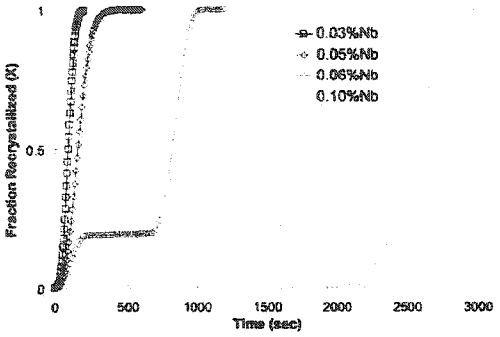

Fig. 3. Changes of the Nb content will dramatically change the recrystallization kinetics. The results shown were calculated for steels containing 0.10% C and at a temperature of 1000°C. These results are interpreted in terms of the interplay of the Zener pressure and mobility (solute drag).

3.3. Recrystallization maps

Traditionally, the transformation kinetics are represented in a so-called Transformation Temperature Time (TTT) diagram. In the microalloying literature the recrystallization and precipitation kinetics are plotted on the same diagram. Such a diagram is traditionally referred to as a Recystallization–Precipitation–Time–Temperature (RPTT) map. The model was used to construct such a diagram for an alloy containing 0.10% Nb and 0.10% C (Fig. 4). As expected, solute drag is the dominant retarding force at high temperatures. As precipitation progresses, the Zener pinning increases and the solute drag contribution decreases.

RPTT maps are very useful for understanding the kinetics of recrystallization. Temperature–deformation (TD) maps provide more direct information for analysing the effect of interpass annealing. These diagrams give the dislocation density (deformation) needed to achieve a certain percentage of recrystallization at a given temperature and within a given time interval. Two such maps are shown in Fig. 5. The effect of precipitation on the kinetics of the first alloy (0.03% Nb) is barely visible. In the second alloy (0.06% Nb) precipitation effectively stops the progress of recrystallization for temperatures between 950–1000°C.

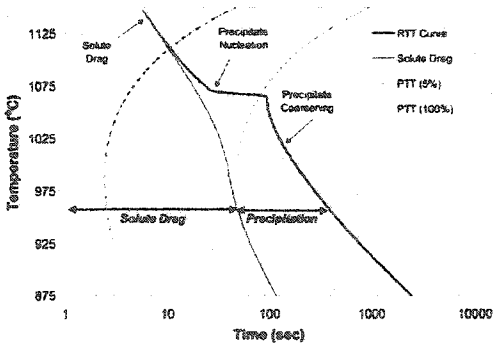

Fig. 4. The RPTT map for an alloy with 0.10% Nb and 0.10% C. The recrystallization curve shown is for 50% recrystallization and $\rho = 2\times10^{14}/m^2$.

4. COMPARISON WITH EMPIRICAL FORMULAE

Numerous empirical and semi-empirical relations have been developed to describe the kinetics of recrystallization in microalloyed steels. The equations are generally represented in the form:

$$X = 1-\exp\left(-0.693\left(\frac{t}{t_{0.5}}\right)^{n}\right)$$

where,

$$t_{0.5} = AD_o^m\varepsilon^{-p}Z^{-q}\exp\left(\frac{Q}{RT}\right)$$

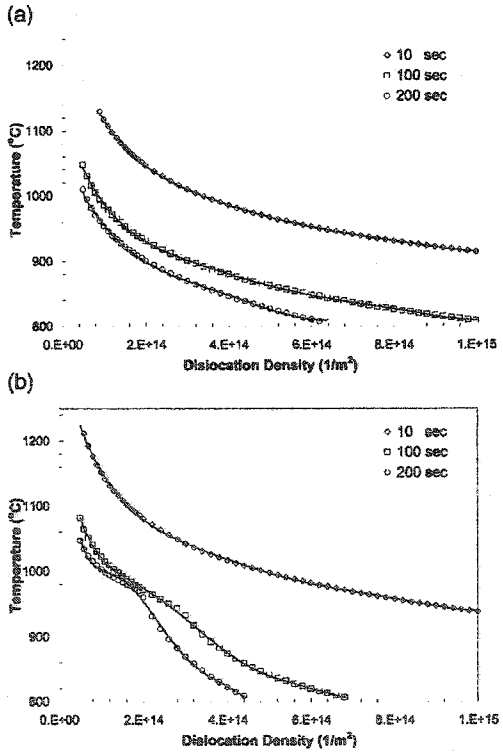

Fig. 5. Temperature–deformation maps provide a practical way of summarizing data on recrystallization. Two such maps were computed: (a) TD map for an alloy containing 0.03% Nb and 0.10% C, (b) TD map for an alloy contain 0.06% Nb and 0.10% C. In both cases the curves shown correspond to recrystallized volume fractions of 50%.

In this equation, Z is the Zener–Holloman parameter, ϵ is the applied strain and Q is the activation energy for static recrystallization. The parameters n, A, m, p, q and Q are determined experimentally. Significant variations exist between the parameters determined by different authors. Typically, n and m are between 1 and 2, p is believed to lie between 2 and 4, q is probably between 3/8 and 0 while Q is in the range of 300–350 kJ/mol [41, 42].

In order to assess the accuracy of our model we will compare it with the empirical expressions. We start by comparing the Avrami exponent. Our model is based on the assumption of site saturation. As a result, an exponent of 3 is expected. However, as the Zener term grows the net driving force changes with time. This variation leads to an exponent, which is itself a function of time. In all cases, the exponent is initially 3. As recrystallization progresses the exponent decreases reaching values of less than one in some cases. The Avrami exponents that appear in the empirical formulae are certainly within the range of exponents predicted by the model. As for the activation energy of recrystallization, our model predicts a value of 253 kJ/mol. This value is reasonable in light of the difficulties associated with defining the activation energy of recrystallization. Finally, the values of m, p, and q can not be estimated because our model uses the dislocation density, rather than ε and $\dot{\varepsilon}$, as an input parameter.

The above comparison demonstrates that our simple model captures the main features of the empirical relations. It is thus a reasonable starting point for a physically based approach to the recrystallization kinetics.

5. CONCLUSIONS

This paper proposes a simple approach to the modelling of static recrystallization in competition with precipitation. As it stands, the model is able to incorporate solute drag effects, as well as the Zener pinning caused by strain-induced precipitation. We have shown that this simple approach, with physically identifiable parameters, is able to describe the recrystallization kinetics. The comparison with empirical formulae, which are known to describe correctly a wide range of experimental data, is encouraging as far as the general applicability of the model is concerned. In its present formulation, the control parameters of the model are the initial state of the alloy (composition and stored energy) as well as the process parameters of the recrystallization treatment. A next step in process modelling would relate the rolling parameters (strain, temperature and strain rates) to the stored energy. This step could be achieved by using internal variables for the plastic behaviour in the absence of precipitation. Other improvements relate to recovery. In its present state, the model does not include the effect of recovery on the stored energy. Under the hypothesis of nucleation site-saturation for the recrystallization, one would expect that the main effect of recovery should be to diminish the driving force for recrystallization, and that effect can be straightforwardly included in the present framework. Finally, the physical basis of the model allows one naturally to treat without further assumptions cases of non-isothermal recrystallization for continuously decreasing temperature ramps (which excludes reversion problems), provided that the nucleation hypothesis (site saturation) remains valid.

Acknowledgements—This work is supported by the Natural Sciences and Engineering Research Council of Canada (NSERC).

REFERENCES

1. Cordea, J. N. and Hook, R. E., *Metal Transactions*, 1970, **1**, 111.
2. Kozasu, I., Shimisu, T. and Kubota, *Transactions of the Iron and Steel Institute of Japan*, 1971, **11**, 367.
3. Gladman, T., McIvor, I. D. and Pickering, F. B., *Journal of the Iron and Steel Institute*, 1971, **209**, 308.
4. Suehiro, M., *ISIJ International*, 1998, **38**(6), 547.
5. Bai, D. Q., Yue, S., Sun, W. P. and Jonas, J. J., *Metallurgical Transactions A*, 1993, **24A**, 2151.
6. Maruyama, N., Uemori, R. and Sugiyama, M., *Materials Science and Engineering A*, 1998, **A250**, 2.
7. Yamamoto, S., Ouchi, C. and Osuka, T., in *Thermomechanical Processing of Microalloyed Steels*, ed. A. J. DeArdo, G. A. Ratz and P. J. Wray. The Metallurgical Society of AIME, Warrendale, PA, 1982, p. 613.
8. Dutta, B. and Sellars, C. M., *Materials Science and Technology*, 1987, **3**, 197.
9. Liu, W. J. and Jonas, J. J., *Metallurgical Transactions A*, 1989, **20A**, 689.
10. Liu, W. J., *Metallurgical and Materials Transactions A*, 1995, **26A**, 1641.
11. Sellars, C. M., in *Proceedings of the International Conference on Hot Working and Forming Processes*, ed. C. M. Sellars and G. J. Davies. The Met. Society, New York, 1980, p. 1.
12. Hodgson, P. D. and Gibbs, R. K., *ISIJ International*, 1992, **32**, 1329.
13. Medina, S. F. and Mancilla, J. E., *ISIJ International*, 1993, **33**, 1257.
14. Laasraoui, A. and Jonas, J. J., *Metallurgical Transactions A*, 1991, **22A**, 151.
15. Furu, T., Marthinsen, K. and Nes, E., *Materials Science and Technology*, 1990, **6**, 1093.
16. Lee, K. J., *Scripta Materialia*, 1999, **40**(7), 837.
17. Weygand, D., Brechet, Y. and Lepinoux, J., *Acta Materialia*, 1999, **47**(3), 961.
18. Smith, C. S., *Transactions of the American Institute of Mining Engineers*, 1948, **175**, 15.
19. Cahn, J. W., *Acta Metallurgica*, 1962, **10**, 789.
20. Smith, G. and Maruyama, N., Private communication, 2000.
21. Turnbull, D., *Transactions of the American Institute of Mining Engineers*, 1951, **191**, 661.
22. Hansen, S. S., Vander Sande, J. B. and Cohen, M., *Metallurgical Transactions A*, 1980, **11A**, 387.
23. Suehiro, M., Liu, Z. K. and Agren, J., *Acta Metallurgica et Materialia*, 1996, **44**(10), 4241.
24. Alaoua, D., Larere, A., Lartigue, S. and Priester, L., *Materials Science Forum*, 1992, **126-128**, 185.
25. Enomoto, M., Nojiri, N. and Sato, Y., *Materials Transactions JIM*, 1994, **35**(12), 859.
26. Menyhard, M., Yan, M. and Vitek, V., *Acta Metallurgica et Materialia*, 1994, **42**(8), 2783.

27. Humphreys, F. J. and Hatherly, M., *Recrystallization and Related Annealing Phenomena*. Pergamon Press, Oxford, 1996.
28. Cottrell, A. H. and Bilby, B. A., *The Proceedings of the Physical Society: Section A*, 1949, **62**(Feb.), 49.
29. Russell, K. C., *Advances in Colloid and Interface Science*, 1980, **13**, 205.
30. Gomez-Ramirez, R. and Pound, G. M., *Metallurgical Transactions*, 1973, **4**, 1563.
31. Okaguchi, S. and Hashimoto, T., *ISIJ International*, 1992, **32**(3), 283.
32. Ardell, A. J., *Acta Metallurgica*, 1972, **20**, 601.
33. Bailey, J. E. and Hirsch, P. B., *Proceedings of the Royal Society*, 1962, **A267**, 11.
34. Medina, S. F., Quispe, A., Valles, P. and Banos, J. L., *ISIJ International*, 1999, **39**(9), 913.
35. Medina, S. F. and Hernandez, C. A., *Acta Materialia*, 1996, **44**(1), 137.
36. Medina, S. F. and Hernandez, C. A., *Acta Materialia*, 1996, **44**(1), 149.
37. Medina, S. F., Hernandez, C. A. and Ruiz, J., *Acta Materialia*, 1996, **44**(1), 155.
38. Gladman, T., *The Physical Metallurgy of Microalloyed Steels*. The Institute of Materials, 1997, p. 108.
39. Narita, K., *Transactions of the Iron and Steel Institute of Japan*, 1975, **15**, 145.
40. Le Bon, A., Rofes-Vernis, J. and Rossard, C., *Metal Science*, 1975, **9**, 36.
41. Devadas, C., Samarasekera, I. V. and Hawbolt, E. B., *Metallurgical Transactions A*, 1991, **22A**, 335.
42. Li, G., Maccagno, M., Bai, D. Q. and Jonas, J. J., *ISIJ International*, 1996, **36**(12), 1479.

A6: Full text of: ***H. S. Zurob, C. R. Hutchinson, Y. Brechet, G. Purdy, Acta Materialia, (2002): 3075-3092.***

Pergamon

Acta Materialia 50 (2002) 3075–3092

Acta MATERIALIA

www.actamat-journals.com

Modeling recrystallization of microalloyed austenite: effect of coupling recovery, precipitation and recrystallization

H.S. Zurob [a], C.R. Hutchinson [b,*], Y. Brechet [b], G. Purdy [a]

[a] *McMaster University, Department of Materials Science and Engineering, Hamilton, Ontario, Canada*
[b] *Laboratoire de Thermodynamique et Physico-Chimie Métallurgiques, Domaine Universitaire, St. Martin d'Hères 38402, Cedex, France*

Received 3 January 2002; received in revised form 20 February 2002; accepted 3 March 2002

Abstract

In this contribution, existing models for precipitation, recovery and recrystallization have been coupled, with their interdependencies explained, to describe the microstructural evolution in a supersaturated alloy after hot deformation. Microalloyed austenite has been used as an example system and the time evolution of the precipitate diameter and the recrystallization and softening fractions are compared with the available experimental data. The model predictions are in excellent quantitative agreement with the experimental observations. Particular attention is paid to the occurrence of 'plateaus' or 'humps' in the softening and recrystallization fraction plots. In both cases, the incorporation of recovery is an essential ingredient for a quantitative description of the microstructural evolution in the hot-worked structure.

Keywords: Microalloying; Recrystallization; Recovery; Precipitation; Modeling

1. Introduction

The development of thermomechanical process modeling for the optimization of industrial alloy properties has been a constant trend during the last two decades [1–8]. The ultimate goal of this modeling process is to relate the process parameters to the final properties of the material through a quantitative description of the microstructural evolution. Such an approach builds on the knowledge and modeling of basic physical metallurgy problems such as solidification, precipitation, dislocation storage by work hardening, recovery, recrystallization and grain-growth. But the various elementary descriptions must be *coupled* in order to describe realistically the complex behavior of industrial alloys. The present paper is to be put into this perspective. We focus our attention on the effects of recovery and precipitation on the evolution of the recrystallized and softening fractions.

The deformation of metals and alloys increases the internal energy of the material through the storage of dislocations. Following deformation, the system reduces its energy by lowering its dislocation content. Depending on the conditions of predeformation and heat-treatment, this approach to thermodynamic equilibrium may occur in one of two ways: The system may undergo a process of

* Corresponding author. Fax: 00-33-4-76-82-66-63..
E-mail address: hutch@ltpcm.inpg.fr (C.R. Hutchinson).

1359-6454/02/$22.00
PII: S1359-6454(02)00097-6

Nomenclature

a	Lattice parameter of austenite
A	Area of the precipitate nucleus [eq. (12)].
A_c	Area of a critical recrystallization nucleus
b	Magnitude of the Burgers vector
C_{Nb}	Instantaneous concentration of Nb in solution (expressed as atom fraction)
C_{Nb}^{Eq}	Equilibrium concentration of Nb in solution
$C_{Nb}^{Eq}\exp(R/R_o)$	Matrix-Nb concentration in equilibrium with a particle of radius R
C_{Nb}^{P}	Concentration of Nb in the precipitate
D_{bulk}	Dulk Nb diffusion coefficient in austenite
D_{eff}	A weighted average of the bulk and pipe diffusion coefficients of Nb in austenite
d_p	Spacing of the precipitate particles on dislocations
D_{gb}	Grain boundary self-diffusion coefficient of austenite
D_{pipe}	Nb diffusion coefficient through dislocations in austenite
D_R	Diameter of the recrystallized austenite grains
D_γ	Austenite grain diameter in micrometers
$dR/dt_{coarsening}$	The rate of change of precipitate size due to pure coarsening [33]
dR/dt_{growth}	The rate of change of precipitate size due to pure growth [33]
E	Young's modulus
E_b	Binding energy of Nb to grain boundaries
F	Adjustable factor in eq. (11) ($N_{total} = F\Delta/b$)
F_c	Coarsening function. F_c is equal to 0 during pure growth and 1 during pure coarsening [33]
$F_v(t)$	Precipitate volume fraction
$G(t)$	Net driving force for recrystallization
G_v	Chemical driving force for precipitation
k_B	Boltzman's constant
k	Adjustable parameter in eq. (7)
M	Taylor factor
$M(t)$	Grain-boundary mobility in the presence of solute
M_{pure}	Grain-boundary mobility of pure material
$N(t)$, N	Number of precipitate particles
$N_c(t)$	Number of dislocation nodes
N_{rex}	Number of recrystallization nuclei
N_{total}	Peak number of precipitates
N_v	Number of atoms per unit volume
R_g	Gas constant
$R(t)$,R	Precipitate radius
R_{core}	Radius of dislocation core
R_n	Radius of the critical precipitate nucleus
S_v	The surface area per unit volume of an austenite grain
T	Temperature
T_{sol}	Temperature at which precipitates are completely dissolved
t	Time
U_a	Activation enthalpy of the operating recovery process

V	Volume of the precipitate nucleus [eq. (12)]
V_a	Activation volume of the operating recovery process
ν	Poisson's ratio
ν_d	Debye frequency
V_m	Molar volume of austenite
X	Recrystallized fraction
X_{ext}	Extended recrystallized fraction
Z	Zeldovich non-equilibrium factor
α	Interaction parameter in Cahn's solute-drag model [eq. (5)]
α_r	Constant to the order of 0.15 [eq. (9)]
α_n	Constant on the order of 1.05 (Fig. 2)
$\beta*$	The rate at which atoms are being added to the critical precipitate nucleus
γ	Interphase energy
γ_{gb}	Grain-boundary energy
δ	Grain-boundary thickness
ΔG_n	Activation energy for precipitation
γ	Applied strain
$\dot{\varepsilon}$	Strain rate
μ	Shear modulus
$\Delta(t)$, Δ	Dislocation density
σ	Total stress
$\sigma_{Non\ Rex}$	Flow stress of the unrecrystallized material
σ_{ppt}	Precipitation-hardening contribution
σ_{Rex}	Flow stress of the recrystallized material
σ_y	Yield stress

continuous rearrangement and annihilation of dislocation; one then speaks of 'recovery'. Alternatively, the system may lower its energy through the discontinuous nucleation of new grains, free of dislocations, growing into a matrix which is heavily loaded with structural defects. This process is referred to as 'recrystallization'. Since the conditions for recovery are less stringent than those for recrystallization, and the consequence of this process is less spectacular, the two phenomena are traditionally considered separately. However, recovery certainly occurs at the high temperatures where recrystallization occurs, and in principle, recovery decreases the driving force for recrystallization. It is therefore a priori unjustified to decouple the two phenomena: the coupling should be investigated if for no other reason than to evaluate those situations in which it may be important.

Traditionally, materials are classified according to their dominant hardening mechanisms. Hardening by 'precipitation' and hardening by 'deformation and dislocation storage' are two classical methods widely used both in ferrous and non-ferrous metallurgy. Traditionally, there has been a tendency to decouple these two phenomena. This is justified only if the two mechanisms operate at markedly different ranges of temperature. More generally, however, the precipitation kinetics and the precipitate morphology are known to be influenced by the presence of structural defects such as dislocations, subgrain boundaries and grain-boundaries. At the same time, the migration of boundaries and dislocations is known to be influenced by the presence of precipitates via a collective pinning phenomenon. When precipitation occurs in the same range of temperature as recrystallization, the coupling between these phenomena cannot be a priori neglected.

The previous statements are methodological. They are relevant to any alloy system in which pre-

cipitation, recovery and recrystallization are possible in the same temperature range. In a previous paper [9], we investigated the *qualitative* consequences of the coupling between precipitation and recrystallization in microalloyed austenite whose recrystallization kinetics showed some peculiarities such as a stasis plateau or an incomplete recrystallization. There now exists a need for a *quantitative* evaluation. We have chosen to focus again on the example of the recrystallization of microalloyed austenite, for which both microstructural and hardness data over a wide range of experimental conditions are available. The aim of the present paper is to model the evolution of the grain structure, the dislocation density, the precipitation characteristics and their consequence on the mechanical properties (hardness in the present case) of the alloy. Throughout the model, we have tried to use the smallest possible number of adjustable parameters. In all cases, the parameters used have a clear physical meaning and the order of magnitude of these parameters is known. The method and the model proposed here are expected to be adaptable to other systems for which the parameter identification will have to be carried out[1].

The paper is structured in the following way: in Section 2 we propose a detailed overview of the interactions between the various elementary phenomena listed above: precipitation, recovery and recrystallization. In Section 3 we present the model as a general formulation potentially applicable to a wide class of materials. In Section 4, we indicate how the identification of the parameters of a specific alloy is performed, leading to the quantitative comparison with experimental data presented in Section 5. The discussion and perspectives for this work are presented in Section 6.

2. Overview of the interactions between recovery, recrystallization and precipitation

The hot-deformation of alloys (such as microalloyed austenite) is often followed by the simultaneous processes of recovery, recrystallization and (at low temperatures) strain-induced precipitation. The purpose of this contribution is to identify the key process-interactions that need be considered when modeling the microstructural evolution of supersaturated austenite after hot-deformation.

Consider first the recrystallization–precipitation interaction. In microalloyed steels, recrystallization and precipitation may interact in at least three distinct ways [9]:

- Strain-induced heterogeneous precipitation often occurs on dislocations in the matrix. A decrease in the dislocation density through recrystallization reduces the number of precipitate nucleation sites available and can thus retard the onset of precipitation.
- A precipitate dispersion can provide a pinning (Zener) force [10] that could slow down or even halt the progress of the recrystallization front [3,5,9].
- The mobility of grain-boundaries is known to be strongly affected by the solute content of the matrix [11]. The progress of precipitation, which reduces the matrix solute content, also affects the mobility of grain boundaries and can influence the progress of recrystallization.

Let us now consider the recrystallization–recovery interactions. The driving force for both recovery and recrystallization is the stored energy of deformation. The progress of recovery will therefore reduce the driving force available for the *migration* of recrystallization boundaries and should slow down the recrystallization process. However, it is thought that under suitable conditions, for instance in very pure metals, recovery may facilitate the *nucleation* of recrystallization by cleaning-up the subgrain microstructure [12]. In the present treatment, it is assumed that recrystallization is site-saturated, which is legitimate for many industrial alloys. Recrystallization and recovery are therefore viewed as competing processes.

The potential interactions between recovery and precipitation are similar to those between recrystallization and precipitation: the presence of precipitates reduces the mobility of structural defects

[1] Researchers at the Delft University of Technology have independently developed a similar model to describe the microstructural evolution of deformed Al-alloys (S. van der Zwaag, private communication).

and the presence of structural defects may enhance precipitation. At least three distinct interactions can be identified:

- Recovery may delay the progress of precipitation by lowering the number of available nucleation sites.
- The precipitation of fine particles can pin segments of the dislocation network and therefore retard recovery [13].
- Microalloying elements in solution are thought to retard the progress of recovery through solute-drag effects on dislocation mobility. The activation enthalpy and activation volume for recovery are both influenced by the presence of the microalloying elements in solution [14].

Most of the microalloying literature is centered on the Zener interaction between recrystallization and precipitation [3,5,6,9,15,16] and the role of large particles in the particle-stimulated nucleation (PSN) of recrystallization (e.g. [12]). The role of concurrent recovery in microstructural evolution after hot rolling is frequently overlooked. Kang et al. [17] provide an example of the magnitude of the potential role of recovery. These investigators showed that in a Nb-microalloyed steel deformed at 950°C to a strain of 0.3 at a strain rate of 10/s, the material softened by ~25% within 10 s, yet metallographic examination revealed no evidence of recrystallization. Presumably, this softening is the result of recovery processes. The present work demonstrates that the incorporation of recovery is a key ingredient for a quantitative description of the microstructural evolution in the hot-worked alloys.

Each of the previous phenomena has been investigated in the literature. In each case, we have chosen the simplest model which would allow us to account quantitatively for the coupling effects.

3. Model

Some of the elementary blocks of the present modeling exercise have been developed in previous publications. We give here the main features of these models, referring to the original papers for technical details. We have emphasized here the necessary adaptations of the original models and the specificities which allow us to consider the coupling effects.

3.1. Recrystallization

The present description of the progress of recrystallization is based on the recent treatment by Zurob et al. [9]. Assuming site-saturation (N_{rex} sites per unit volume) and a linear relation between the velocity, $\bar{v}$, and the stored energy due to dislocations, $G(t)$, leads to a Johnson–Mehl–Avrami law of the form:

$$X_{ext} = N_{rex}\left(\int_0^t M(t)G(t)\mathrm{d}t\right)^3 \quad (1)$$

where X_{ext} is the extended recrystallized volume fraction and $M(t)$ is the grain-boundary mobility. In the case of a random distribution of recrystallization nuclei, X_{ext} is related to the recrystallized fraction in the following way:

$$X = 1-\exp(-X_{ext}). \quad (2)$$

The recrystallized volume fraction depends on: (a) the net driving force for recrystallization, $G(t)$; (b) the mobility of grain boundaries $M(t)$; and (c) the number of recrystallization nuclei, N_{rex}. The driving force for recrystallization, $G(t)$, and the grain boundary mobility, $M(t)$ are time dependent and depend critically upon the time evolution of the simultaneous recovery and precipitation processes.

3.1.1. The driving force for recrystallization, $G(t)$

The driving force for recrystallization is the stored energy of deformation, often expressed as $\frac{1}{2}\rho\mu b^2$ where ρ is the dislocation density, μ, the shear modulus of the matrix and b the burgers vector. A number of authors [18,19] have shown that the effect of concurrent precipitation on the driving force for recrystallization may be expressed as a stored energy modified by a retarding Zener drag term, eq. (3). In this treatment, it is assumed that these are the only contributions to the driving force for recrystallization. Under conditions of an evolv-

ing precipitate distribution and a dislocation density subject to recovery processes, a time dependent net driving force is observed:

$$G(t) = \frac{1}{2}\rho(t)\mu b^2 - \frac{3\gamma_{gb}F_v(t)}{R(t)}. \quad (3)$$

The Zener pressure exerted by the precipitates is described by the second term in eq. (3). γ_{gb}, $F_v(t)$ and $R(t)$ denote the austenite grain boundary energy, precipitate volume fraction and the mean precipitate radius, respectively. The description of the Zener pressure resulting from a precipitate distribution is found to vary from $3\gamma_{gb}F_v(t)/2R(t)$ [12,20–22] to an upper limit equal to twice this value when the precipitate interphase energy exhibits a strong dependence on orientation [20,23]. Preferred orientation relationships exist for the precipitation of Nb(C,N) in austenite [23–25] and it is assumed that the interphase energy is a strong function of orientation. By utilizing this upper limit for the Zener pressure, we hope to more convincingly demonstrate that in many cases, the Zener force is of insufficient magnitude to halt recrystallization in the absence of recovery processes.

3.1.2. Grain boundary mobility

The effect of solute elements on the mobility of grain boundaries has been treated by Cahn [26]. The drag effect reduces the mobility in a non-linear manner depending on the velocity. A simplified mobility which is constant with velocity and proportional to the solute content is used in this treatment. For low driving forces, Cahn's solution simplifies to

$$M(t) = \left(\frac{1}{M_{Pure}} + \alpha C_{Nb}\right)^{-1} \quad (4)$$

where

$$\alpha = \frac{\delta N_v (k_B T)^2}{E_b D}\left(\sinh\left(\frac{E_b}{k_B T}\right) - \frac{E_b}{k_B T}\right) \quad (5)$$

where M_{pure} and C_{Nb}, refer to the intrinsic grain boundary mobility and the concentration of Nb in solution, δ is the grain boundary width (~1 nm), N_v is the number of atoms per unit volume, E_b is the solute-boundary binding energy and D is the average value of the diffusion coefficient in the vicinity of the grain boundary. We have equated D to the bulk diffusion coefficient, based on the APFIM results of Maruyama and Smith [27], which show a very wide segregation profile near the boundary.

An order of magnitude estimate of the intrinsic mobility in a pure metal is 1/10 of the Turnbull estimate [28]. The Turnbull estimate is considered to be an upper limit because it neglects all possible attachment kinetics:

$$M_{Pure} = \frac{1}{10}\frac{\delta D_{gb} V_m}{b^2 R_g T}. \quad (6)$$

In this equation, D_{gb} is the grain boundary self-diffusion coefficient and V_m is the molar volume of austenite.

3.1.3. Recrystallization nucleation sites

The nucleation of recrystallization is assumed to occur at the onset of annealing, at a number of sites proportional to the grain boundary area per unit volume S_v. If A_c is the area occupied on the grain boundary by each nucleus, the number of recrystallization nuclei per unit volume can be expressed as:

$$N_{rex} = \frac{kS_v}{A_c} \quad (7)$$

where k is a geometric factor. The area of the nucleus, A_c, depends on the driving force. The Bailey–Hirsch theory [29] for recrystallization nucleation predicts that A_c is proportional to $1/G^2$. Using this approach, a nucleus size of 3 μm is expected for a dislocation density of 4×10^{14} m^{-2}.

3.2. Recovery

It is assumed that the flow stress of the precipitate-free austenite, σ, is related to the total dislocation density, ρ, and the yield stress of the precipitate-free fully-recrystallized state, σ_y, by the forest-type hardening relation [30]:

$$\sigma = \sigma_y + M\alpha_r \mu b\sqrt{\rho} \quad (8)$$

where M is the Taylor factor (~3.1 for FCC) and α_r is a constant of the order of 0.15.

The recovery kinetics of the dislocation contri-

bution to the hardening, $\sigma-\sigma_y$, is described using the approach proposed by Verdier et al. [31]. The basic physical idea of this approach dates back to Friedel [32] who considered recovery as a relaxation process of the internal stresses, the rate of which is a function of the plastic strain-rate ($\dot{\varepsilon}_p$) induced by these internal stresses. The improvements proposed by Verdier et al. [31] allow for a better understanding of the activation parameters through a more detailed description of $\dot{\varepsilon}_p$ involving the dislocation density ($\sim(\sigma-\sigma_y)^2$) and the dislocation velocity (varying as sinh function of the effective stress). The rate of change of internal stress due to the dislocations is then expressed as [31]:

$$\frac{d(\sigma-\sigma_y)}{dt} = -\frac{64(\sigma-\sigma_y)^2 v_d}{9M^3\alpha_r^2 E}\exp\left(-\frac{U_a}{k_B T}\right)\sinh\left(\frac{(\sigma-\sigma_y)V_a}{k_B T}\right) \quad (9)$$

where U_a and V_a are the activation energy and activation volume of the recovery process and are assumed to be independent of temperature and composition. The constants, v_d and E are the Debye frequency and Young's modulus.

The simplest possible approach has been used to capture the effect of precipitation on the kinetics of recovery. The presence of precipitates limits the motion of dislocation segments necessary for recovery to occur. For the sake of simplicity, it is assumed that precipitation 'pins' the dislocation nodes and such segments are unavailable to recover until they are 'unpinned' during the coarsening of the precipitate distribution. A recovery pinning term has been incorporated into eq. (10) to capture this effect:

$$\frac{d(\sigma-\sigma_y)}{dt} = \left[-\frac{64(\sigma-\sigma_y)^2 v_d}{9M^3\alpha_r^2 E}\exp\left(-\frac{U_a}{k_B T}\right)\sinh\left(\frac{(\sigma-\sigma_y)V_a}{k_B T}\right)\right]\left(1-\frac{N(t)}{N_c(t)}\right) \quad N<N_c$$

$$\frac{d(\sigma-\sigma_y)}{dt} = 0 \quad N\geq N_c \quad (10)$$

where, $N(t)$ is the number of precipitate particles and $N_c(t)$ is the total number of dislocation nodes, approximated as $0.5\rho(t)^{1.5}$. When the number of precipitate particles exceeds the total number of dislocation nodes, $N>N_c$, recovery is completely halted. Fig. 1(a) is an example of the predicted stress-relaxation in a Nb microalloyed steel at 950°C in the presence of concurrent precipitation using the recovery model discussed above [eq. (10)]. Fig. 1(b) is the experimental stress-relaxation data of Liu and Jonas [13] for a Ti-microal-

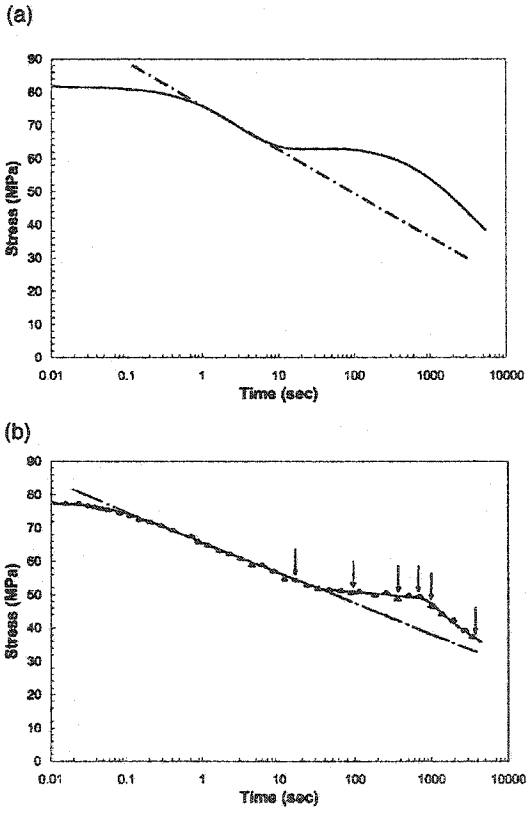

Fig. 1. (a) Model predictions [eq. (10)] of stress relaxation due to recovery processes in the presence of concurrent precipitation in a microalloyed steel containing 0.024%Nb and 0.21%C at 950°C. (b) Experimental stress relaxation data measured at 900°C by Liu and Jonas [13] in a microalloyed steel containing 0.25% Ti and 0.05% C. The plateau caused by the onset of precipitation is indicated by the arrows. The similarity between the two figures is interpreted as a validation of the general form of the recovery–precipitation interaction described in eq. (10).

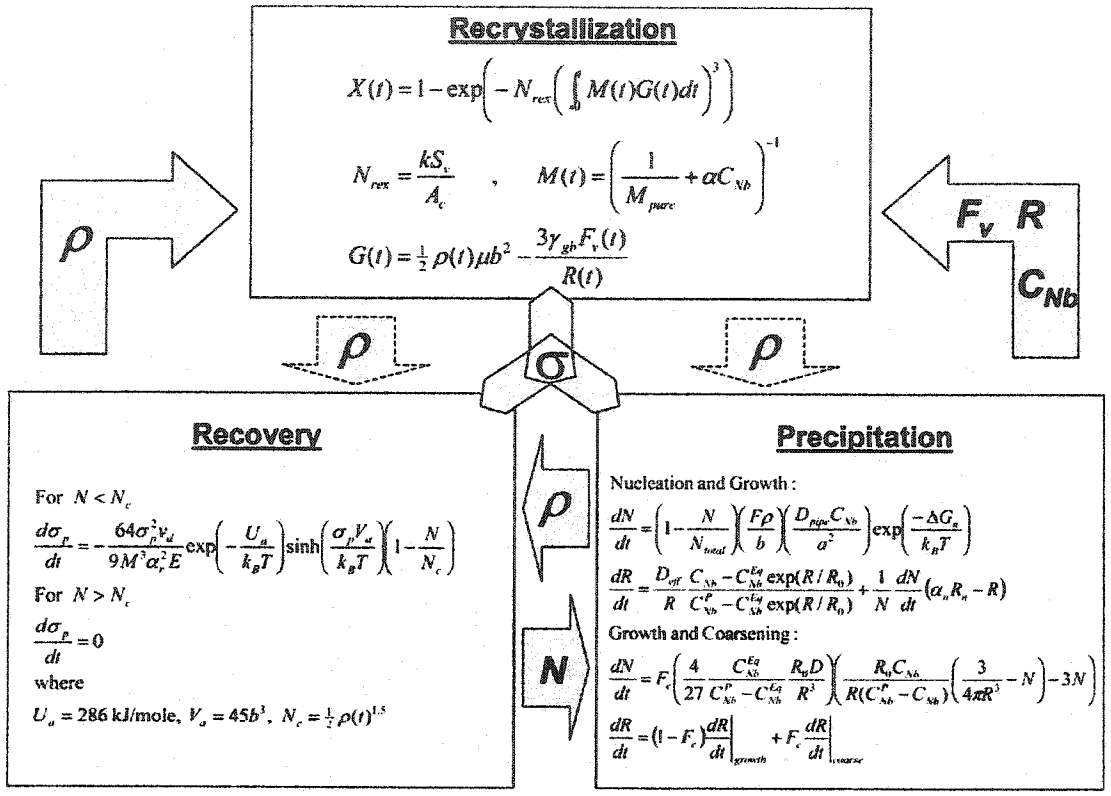

Fig. 2. Summary of the recovery, recrystallization and precipitation modules used in the present model. The variables that provide the coupling between each of the modules are highlighted to emphasis the interdependency of each of these processes. The dotted arrows refer to interactions that were not considered in the present model. Additional details on the recrystallization, recovery and precipitation models are found in references [9,31,33].

loyed steel that also exhibits concurrent recovery and precipitation processes. The model predictions in Fig. 1(a) are able to well reproduce the general form of the stress relaxation curve in the presence of precipitation, Fig. 1(b). This is interpreted as a validation of the general form of eq. (10).

3.3. Precipitation model

The precipitation of Nb(C,N) in austenite has been described using the recent approach of Deschamps and Brechet [33]. Precipitation is assumed to occur in two stages. The first stage treats nucleation and growth as concurrent processes and the second treats growth and coarsening. The mean precipitate radius and the number density of precipitates are monitored. This approach has recently been applied to the precipitation of NbC in austenite [34] and appears to result in reasonable agreement with the experimental data.

3.3.1. Nucleation

Nucleation is assumed to occur exclusively on dislocations. Dutta and Sellars [3] have demonstrated that this is indeed a reasonable assumption. The steady-state nucleation rate is given by:

$$\frac{dN}{dt} = \left(1-\frac{N}{N_{total}}\right)Z\beta^* N_{total}\exp\left(\frac{-\Delta G_n}{k_B T}\right) \qquad (11)$$

where Z is the Zeldovich non-equilibrium factor,

β^* is the rate at which atoms are added to the critical nucleus, N_{total} is the number of nucleation sites and ΔG_n is the activation barrier for the nucleation process. An Avrami-type term $(1-N/N_{total})$ has been added to the classical nucleation equation to account for the progressive consumption of available nucleation sites [35]. Following Russell [36], the product $Z\beta^*$ was approximated as $D_{pipe} C_{Nb}/a^2$, where D_{pipe} is the solute diffusion coefficient along dislocations and a is the jump distance which is approximately equal to the lattice constant. The density of nucleation sites was approximated as $F\rho/b$, where F is an adjustable factor smaller than unity. The critical energy, ΔG_n, and radius, R_n, were estimated using the following energy balance [9,37,38]:

$$\Delta G = V\Delta G_V + A\gamma - \frac{\mu b^2 R \ln(R/b)}{2\pi(1-\nu)} - \mu b^2 R/5 \quad (12)$$

where, V and A are the volume and area of the nucleus, G_V is the free energy change attending nucleation, γ is the interphase energy and ν is Poisson's ratio. The chemical driving force, G_V, and the composition of the carbonitride, were estimated using the method described by Gladman [39] and the solubility constants of Narita [40].

3.3.2. Growth and coarsening

An effective diffusion coefficient, D_{eff}, expressed as a weighted mean of the bulk diffusion, D_{bulk}, and pipe diffusion, D_{pipe}, coefficients is used in the description of the precipitate evolution [34]

$$D_{eff} = D_{pipe}\pi R_{core}^2 \rho + D_{bulk}(1-\pi R_{core}^2 \rho) \quad (13)$$

where R_{core} is the radius of the dislocation core, taken to be equal to the burgers vector, b.

A summary of the model is shown in Fig. 2 with those terms that provide the coupling between concurrent recovery, recrystallization and precipitation highlighted to emphasize the interdependency of these processes.

4. Model parameters

Whereas the previous derivations are expected to reflect a general approach, independent of material system, the requirement to reach a quantitative description forces the specialization to a specific system (for which the thermodynamic and diffusion data are well known). The simplifying assumptions are listed below, together with the methodology used to identify the physical parameters of the problem, for a given alloy. Microalloyed austenitic steel is chosen here as a model system to test the model.

4.1. Simplifying assumptions

Several simplifying assumptions have been made concerning the interactions between recovery, recrystallization and precipitation.

- It is assumed that the progress of recrystallization does not influence the precipitation processes. This includes the reduction in the number of potential precipitation nucleation sites due to recrystallization and any differences in the evolution of precipitate size and number density that may exist between the recrystallized and unrecrystallized regions in a partially recrystallized sample. In doing so, we assume that precipitation occurs mainly on dislocations in the unrecrystallized regions, and that it is not perturbed by the migration of the recrystallization front.
- The nucleation of recrystallization is assumed to be site-saturated. The possible role of recovery in facilitating the nucleation of recrystallization is not considered. This hypothesis seems reasonable for industrial alloys for which the recrystallization sites are mainly related to structural heterogeneities. It would not be acceptable for very pure materials where the recovery of the dislocation subgrains control not only the stored energy, but also the new grain mobility.
- A constant activation enthalpy, U_a, and volume, V_a, for recovery is assumed in the present treatment. The effect of a varying matrix solute content (arising from the progress of precipitation) on the activation energy and volume of recovery are not considered. This assumption is made for the sake of simplicity and amounts to the consideration of the activation enthalpy and activation volume as average quantities having a

slow and small variation with the solute content. Strong effects are expected for low solute concentrations where the relative variation of V becomes important.

4.2. Parameter identification

Most of the physical quantities that enter into the present model are known with a reasonable degree of accuracy and are listed in Table 1. Three parameters require discussion: the interphase energy, γ, and the recovery activation enthalpy, U_a and volume, V_a.

Estimates of the austenite-MC interphase energy vary from ~0.3 to more than 1.5 J/m^2 [24,39,44–47]. In addition, the interphase energy is expected to exhibit both a temperature and a composition dependence [24]. In order to arrive at a reasonable expression for the interphase energy, the C-curves for carbide precipitation in three different steels were examined [3,15,17,48]. The C-curve behavior of these steels is satisfactorily reproduced using an interfacial energy of the following form:

$$\gamma = 1.1024 \times 10^{-3}(T_{sol} - 0.519T) - 0.3964 \quad (14)$$

where γ and T are expressed in units of J/m^2 and K, respectively. The composition dependence of the interfacial energy enters through T_{sol} which is the temperature at which the precipitate is completely dissolved. The temperature dependence is of the order of 0.5 mJ/K, in general agreement with the measured temperature dependence of grain-boundary energies in metals [49]. The interphase energy is then ~1.1 J/m^2 at 0 K which is in reasonable agreement with the atomistic modeling of Yang and Enomoto [24]. At hot-working temperatures γ varies between 0.35 and 0.60 J/m^2. To be consistent, the grain-boundary energy, γ_{gb}, is also expressed as a function of temperature, thus:

$$\gamma_{gb} = 1.3115 - 0.0005T. \quad (15)$$

As before, the boundary energy is expressed in units of J/m^2, while the temperature is expressed in K. This expression, leads to the reasonable values of 0.5–0.75 J/m^2 within the hot-working regime.

The activation energy for the recovery process is expected to lie between 0.6 and $1Q_{diff}$, where Q_{diff} is the activation energy for self-diffusion or solute-diffusion (depending on the rate controlling process) [50]. The activation energy for the self-diffusion of Fe in austenite is ~286 kJ/mol [51] while that of Nb diffusion in austenite is 266 kJ/mol [41]. Therefore, a compositionally independent activation enthalpy, U_a, of 286 kJ/mol was chosen. An average activation volume of $45b^3$ was then obtained by fitting the stress-relaxation data of Arieta and Sellars [14] and Silveira e Silve *et al.* [52] to eq. (9) with, U_a=286 kJ/mol, M=3.1 and ν_d=2×10^{12} s^{-1}.

5. Comparison with experimental data

There exists in the literature some confusion regarding the experimental recrystallization data in the presence of concurrent precipitation and recovery. If recrystallization is the only operative mechanism, it is legitimate to consider a simple measurement such as hardness as a good quantitative indicator of the recrystallized volume fraction. If simultaneous recovery is occurring, the unrecrystallized regions soften at the same time as the recrystallized regions grow: the overall hard-

Table 1
Model input parameters

Parameter	Value
Bulk diffusion coefficient of Nb in austenite, D_{bulk}	$0.83\times10^{-4}\exp(-266500/RT)$ m^2/s[41]
Pipe diffusion coefficient of Nb in austenite, D_{pipe}	$4\times10^{-4}\exp(-172500/RT)$ m^2/s; an average value based on [42].
Nb-grain boundary binding energy, E_b	25 kJ/mol; estimate based on [9] and [27].
Shear modulus, μ	81×10^9 [0.91–(T(K)−300)/1810] Pa [43]

ness evolution is a convoluted combination of these two phenomena. If, in addition, precipitation occurs, it may contribute to the hardness evolution through the decrease of solid solution hardening as well as precipitation hardening. In our comparison with experimental data, care has been taken to distinguish carefully between hardness evolution and recrystallization kinetics.

5.1. Available experimental data

5.1.1. Softening fraction plots

The overwhelming majority of experimental information concerning the time evolution of the interaction of recovery, recrystallization and precipitation is in the form of fractional softening plots evaluated from double-deformation experiments. In these experiments the amount of recrystallization is indirectly estimated from the fractional softening measured from an interrupted mechanical test (compression, tension or torsion). These methods have been reviewed and critically evaluated by a number of authors [53–55]. The observed fractional softening is a convolution of recovery, recrystallization and (where applicable) precipitation contributions. A variety of data-manipulation techniques have been proposed to separate the contributions of recovery and recrystallization, usually through a subtraction of a portion of the stress which is attributed to recovery [53]. Rarely is the contribution of precipitation considered and in some cases it is assumed that the softening fraction is approximately equal to the recrystallized fraction [e.g. 15].

5.1.2. Experimental data for the microstructure evolution

The progress of the static recrystallization of austenite can be directly measured from metallographic examination. Despite this, very limited metallographically determined recrystallized-fraction data is available in the literature. In some cases, complexities in observing the quenched austenite may arise and this may partially explain the paucity of metallographically measured static recrystallization data in the microalloyed steel literature [53]. Concerning the evolution of the precipitate distribution, only in rare cases is a direct measure of the precipitate diameter evolution obtained by transmission electron microscopy (TEM).

5.2. Comparison of model predictions with experimental data

The present description of the interaction between recovery, recrystallization and precipitation has been tested by application to four Nb-steels [15,17,56]. The compositions of these steels are listed in Table 2. To the authors' knowledge the data compiled by Kang et al. [17] represents the most complete and useful set for an analysis of the interaction of recovery, recrystallization, and precipitation in a microalloyed steel. These investigators measured the precipitate particle diameter (TEM), the softening fraction (double-deformation) and the recrystallized fraction (optical metallography) as a function of time for several temperatures in a given Nb microalloyed steel (N1, Table 2). The works of Gomez et al. [56] (N2, Table 2) and Medina et al. [15] (N3 and N4, Table 2) report only softening fraction curves evaluated through double-deformation tests.

The experimental data of Kang et al. [17] is examined first. Samples of the microalloyed steel (N1) examined by Kang et al. were solution treated at 1200°C for 10 min to dissolve all of the carbides. A compression to a fixed true strain of 0.30 was applied at the deformation temperature using a hot rolling simulator. The sample was held at the temperature for varying times, between 0.1 and 10 000 s before applying a second deformation in the order of 1–8%. The double-compression test provided data on the softening fraction as a function of time. Selected samples were quenched immediately following the annealing treatment so that the recrystallized fraction and the precipitation evolution could be measured by optical metallography and TEM, respectively.

The nucleation parameter, F [eq. (11)], was estimated from knowledge of the equilibrium precipitate volume fraction and the precipitate diameter at the onset of coarsening, measured from the 'knee' in Kang et al.'s plots of particle-size evolution. At 850°C, F was found to be 2.07×10^{-3}. The predicted evolution of particle-diameter in the pres-

Table 2
Alloy compositions (wt%) used to test the validity of the model

Alloy [Ref.]	C	Si	Mn	P	S	Nb	Al	N
N1 [17]	0.076	0.06	1.34	0.0058	0.0026	0.030	–	0.0061
N2 [56]	0.20	0.20	1.0	0.024	0.013	0.007	0.006	0.0056
N3 [15]	0.21	0.18	1.08	0.023	0.014	0.024	0.007	0.0058
N4 [15]	0.21	0.19	1.14	0.023	0.015	0.058	0.008	0.0061

ence of concurrent recovery and recrystallization is in excellent agreement with the measured particle diameters as shown in Fig. 3(a).

The geometric parameter, k [eq. (7)], was chosen to optimize the agreement between the predicted and experimentally observed recrystallized fractions. The softening fraction data has been modeled using the 5% offset method [53]. This method is very similar to the method used by Kang et al. [17] to evaluate the experimental softening fractions. The flow stress of a partially recrystallized sample is evaluated assuming a simple rule of mixtures of the recrystallized, σ_{Rex}, and unrecrystallized, $\sigma_{Non\text{-}Rex}$, fractions.

$$\sigma = \sigma_{Rex}X + \sigma_{Non\text{-}Rex}(1-X) \tag{16}$$

The flow stress of the recrystallized material, σ_{Rex}, contains a contribution from precipitation, σ_{ppt}, and a contribution from the dislocation free matrix, $\sigma_{Rex\text{-}Matrix}$, including the contribution of solid-solution hardening [eq. (17)].

$$\sigma_{Rex} = \sqrt{\sigma^2_{Rex\text{-}Matrix} + \sigma^2_{ppt}} \tag{17}$$

The flow stress of the unrecrystallized material, $\sigma_{Non\text{-}Rex}$, contains contributions from precipitation, σ_{ppt}, and the work-hardened matrix, $\sigma_{NonRex\text{-}Matrix}$, including the contribution of solid-solution strengthening:

$$\sigma_{Non\text{-}Rex} = \sqrt{\sigma^2_{NonRex\text{-}Matrix} + \sigma^2_{ppt}}. \tag{18}$$

Details of the evaluation σ_{ppt}, $\sigma_{Rex\text{-}Matrix}$ and $\sigma_{Non\text{-}Rex\text{-}Matrix}$ are contained in the Appendix.

The predicted softening and recrystallization fractions are plotted along with the experimental data in Fig. 3(b). The agreement between model and experiment is excellent for both softening and recrystallization. It is especially interesting to note that the 'hump' in the experimental softening curve between 1 and 100 s is very well reproduced by the model.

The same procedure was applied to the available experimental data at 900°C. The predicted time

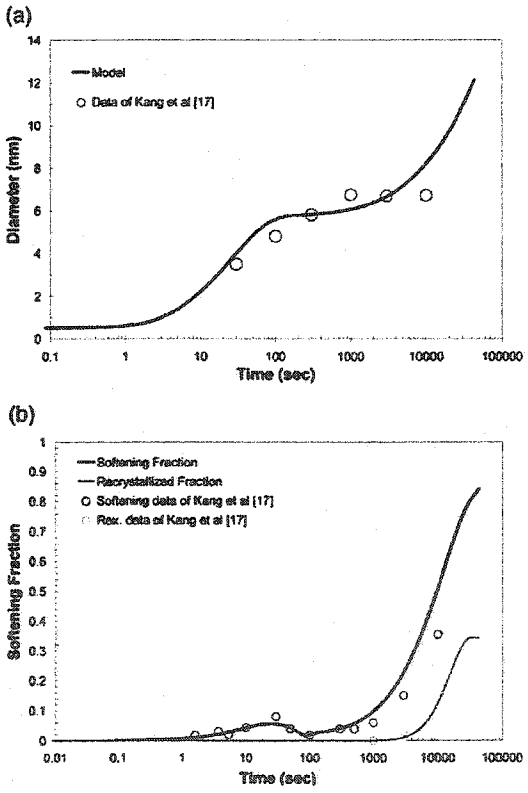

Fig. 3. (a) Predicted and experimentally measured particle size evolution in steel N1 at 850°C (strain=0.3, strain rate=10 s^{-1}). (b) Predicted and experimentally measured softening and recrystallized fractions for alloy N1 at 850°C.

evolution of the particle diameter is again in excellent agreement with the experimental observation, Fig. 4(a). The softening and recrystallization fractions show reasonable agreement with experiment, Fig. 4(b). In this case, the predicted softening fraction is generally larger than the experimentally measured fraction. This indicates that our simple descriptions of recovery and precipitation hardening do not accurately capture the temperature-dependence of these processes.

The model has also been applied to the experimental data of Gomez et al. [56] (Alloy N2) and Medina et al. [15] (Alloys N3 and N4) to illustrate its applicability to a range of microalloyed Nb

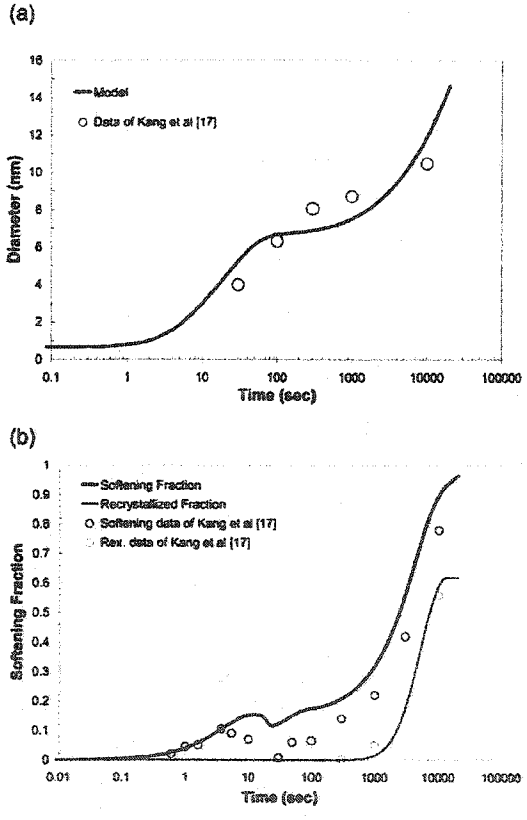

Fig. 4. (a) Predicted and experimentally measured particle size evolution in steel N1 at 900°C (strain=0.3, strain rate=10 s^{-1}). (b) Predicted and experimentally measured softening and recrystallized fractions for alloy N1 at 900°C.

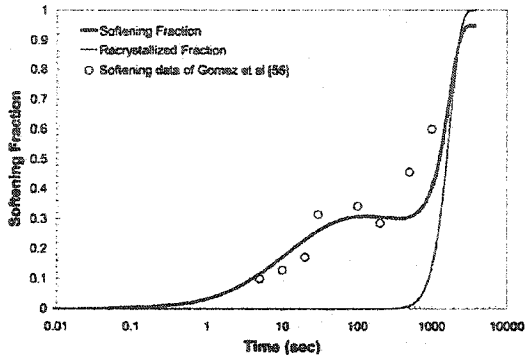

Fig. 5. Predicted and experimentally measured softening fractions for steel N2 at 850°C. The predicted recrystallized fraction is also shown (strain=0.35, strain rate=3.63 s^{-1}).

steels. The predicted and experimentally observed softening fractions for the three alloys N2, N3 and N4 are plotted in Figs. 5–7. In each case, F and k were chosen to give the best fit with the experimental data. The predictions of the model are in excellent agreement with the experimental data.

5.3. Magnitude of the constants F and k

We have presented a simple physically-based model for the interaction between precipitation, recovery and recrystallization in microalloyed austenite. The model contains two physically-based adjustable-parameters. The first parameter, F, is

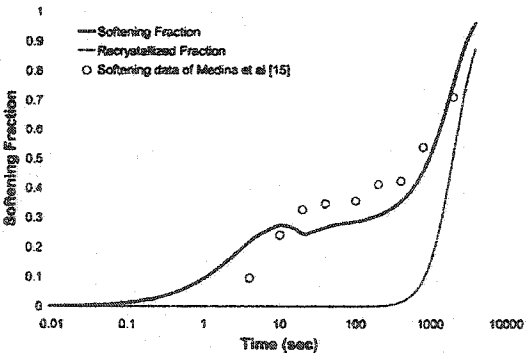

Fig. 6. Predicted and experimentally measured softening fractions for steel N3 at 950°C. The predicted recrystallized fraction is also shown (strain=0.35, strain rate=3.63 s^{-1}).

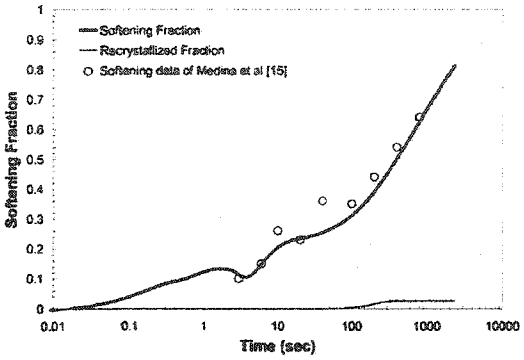

Fig. 7. Predicted and experimentally measured softening fractions for steel N4 at 1000°C. The predicted recrystallized fraction is also shown (strain=0.35, strain rate=3.63 s^{-1}).

related to the average particle-spacing on the dislocation line:

$$d_p = \frac{b}{F} \tag{19}$$

In the present model, the optimum value of F varied between ~1×10^{-3} and 3×10^{-3}. This leads to the very reasonable particle spacing of 100–200 nm. The second adjustable parameter is the geometric factor, k, which appears in eq. (7). The value of k is directly related to the recrystallized austenite grain-size. If we assume that the recrystallized grains are spherical with an average diameter D_R, then:

$$\frac{kS_v}{A_c} = \left(\frac{4}{3}\pi\left(\frac{D_R}{2}\right)^3\right)^{-1}. \tag{20}$$

The value of k is then expected to lie between 5×10^{-2} and 5×10^{-5} depending on the initial grain-size and the applied deformation. The optimum k values obtained in the present investigation were in the order of 10^{-6} to 10^{-7}. These values are clearly outside the expected range. We believe that this is due to the omission of the threshold force needed to initiate recrystallization. It is known that a minimum deformation of ~ 5–10% is needed to initiate the process of recrystallization [12]. If this force is incorporated into eq. (3), we arrive at the more reasonable values of 10^{-3}~10^{-4}. For simplicity, however, we will continue to use eq. (3) without the incorporation of the threshold force.

6. Discussion and conclusions

The occurrence of plateaus in the softening-fraction vs time curve is well-documented in the literature [e.g. 15, 56]. From the present analysis, it is clear that one must consider carefully the different meanings of a plateau in the recrystallization curve and a plateau in the softening curve.

6.1. Recrystallization fraction plateaus

A plateau in the time evolution of the true recrystallized fraction arises when the Zener pinning pressure exceeds the stored energy driving the migration of the recrystallization front, i.e. the net driving force acting on the recrystallization interface falls to zero, eq. (3). The beginning of a plateau in recrystallization can be seen in the predicted plots for Alloy N1 at 850°C [Fig. 3(b)] and 900°C [Fig. 4(b)]. Fig. 8 is a plot of the time evolution of the driving force and the Zener pressure for alloy N1 at 850°C. It is clear that the stored energy greatly outweighs the Zener pressure for much of the investigated time range. The Zener pressure only begins to outweigh the stored energy at very long times [~30 000 s, corresponding with the onset of the recrystallization plateau in Fig. 3(b)] and only after the stored energy has been substantially diminished through recovery processes.

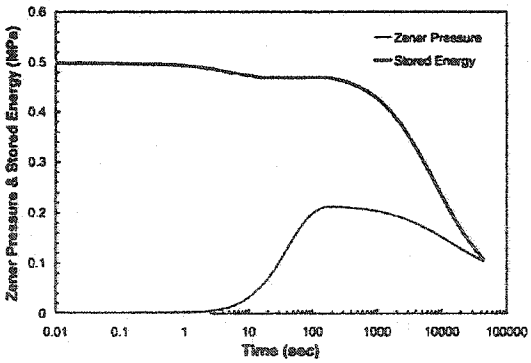

Fig. 8. Plot of the time evolution of the stored energy and the Zener pressure for steel N1 at 850°C. In general, the Zener pressure is of insufficient magnitude to outweigh the driving force for recrystallization except at long times when recovery processes have substantially reduced the stored energy.

Recovery appears to be a key ingredient for the understanding of the plateau in the recrystallization fraction.

6.2. Softening fraction plateaus

Plateaus in the softening fraction curves, which are reported frequently in the experimental literature, arise as a result of the convolution of several softening and hardening phenomena. During annealing, recovery and recrystallization processes soften the material but precipitation processes harden the material. The softening fraction curve is a manifestation of the time evolution of the net effect of these contributions.

Consider, for example, the softening curve for steel N1 at 850°C in Fig. 3(b). The curve exhibits a 'hump' or 'plateau' between 1 and 100 s after which the softening fraction curve steadily rises. The hump is due to the interaction between recovery processes and precipitation and is not a consequence of recrystallization. The experimental recrystallization data of Kang et al. [17] clearly shows that the onset of recrystallization does not occur for 2000 s in this alloy. Examination of the time evolution of the stored energy in Fig. 8 aids in an explanation. The stored energy plot in Fig. 8 falls from a value of ~0.5 to ~0.46 MPa in the first 10 s after which a plateau in the stored energy is observed. The decrease in stored energy is a consequence of the decrease in dislocation density due to recovery processes and the plateau in stored energy arises from the inhibition of recovery processes through precipitation pinning. The plateaus observed in the stress relaxation data in Fig. 1 are of exactly the same origin. Coarsening of the precipitate distribution 'unpins' the dislocation network and allows for recovery processes to resume and consequently the stored energy begins to decrease again. At early times, the morphology of the softening curve depends on the time evolution and the relative magnitudes of the softening due to recovery and the hardening due to precipitation. During the period where recovery is inhibited, precipitation hardening is the dominant contribution and hardens the material giving rise to a hump in the softening curve instead of a plateau. Even if the stored energy falls substantially, to the point where it is outweighed by the Zener force, and a plateau is observed in the recrystallization curve, this will not manifest itself as a plateau in the softening curve, because of the continuing contribution of recovery to the overall softening, e.g. Figs 3(b), 4(b) and 7. Interpretation of the experimentally observed softening curves must be made carefully with a consideration of the relative magnitudes of all the operative contributions to hardening.

From the previous discussion, it is clear that conjugate plots of the time evolution of the Zener pressure and stored energy, including recovery contributions, would be an efficient tool for predicting the occurrence of a plateau in the recrystallized fraction curve. Consider for instance, Alloy N4. This alloy contains a reasonably high Nb concentration and gives rise to a substantial volume fraction of Nb(C,N) precipitation. The time evolution of the driving force for recrystallization and the Zener pressure resulting from precipitation is shown in Fig. 9. In this case the stored energy driving recrystallization falls below the Zener pressure after only ~400 s of annealing, corresponding with the onset of the plateau in the recrystallized fraction plot in Fig. 7.

One further point is worth making concerning the plots of driving force in Figs 8 and 9. In both cases, the rate of decrease of stored energy driving

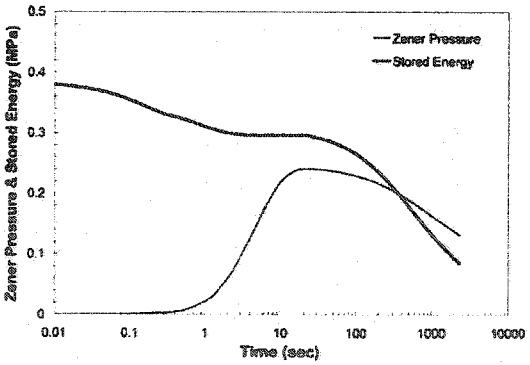

Fig. 9. Plot of the time evolution of the stored energy and the Zener pressure for steel N4 at 1000°C. In this case, the combination of recovery processes and a large Zener pressure gives rise to a situation where the retarding Zener pressure outweighs the driving force for recrystallization at reasonably early times.

recrystallization is greater than the rate of decrease of the Zener pressure due to coarsening in the time regime where these pressures are of the same magnitude. The plateaus observed in the recrystallization plots will therefore appear as 'indefinite' plateaus and the recrystallized fraction will not again begin to rise, as is observed for the plateaus in the softening fraction plots.

Considering its inherent simplicity, this model provides a satisfactory description of the precipitation kinetics as well as the recrystallization and softening kinetics, capturing the essential coupling between each of these processes. However, there is clearly some further work required to fully complete the program proposed in the Introduction.

- The temperature-dependence of recovery is imperfectly captured by the model.
- The possibility of dynamic precipitation accompanying predeformation is not considered.
- The possible influence of dislocation structure (beyond the single parameter of dislocation density, ρ) on the precipitation kinetics has not been addressed.

A further area for development of the present model is to include more explicitly the compositional influence, not only on the thermodynamics of precipitation but also on the recovery and recrystallization kinetics.

These limitations are not insurmountable and further work is in progress including more detailed analysis of recrystallization processes.

Acknowledgements

CRH gratefully acknowledges the financial support of IRSID. The financial support of the NSERC (Canada) in the form of a research grant to GRP and a graduate scholarship to HSZ is gratefully acknowledged. In addition, the authors acknowledge many useful and stimulating discussions with Drs D Quidort, P. Maugis and J. D. Embury.

Appendix. Evaluation of the softening fraction

Several methods have been developed to evaluate the softening fraction from a double-deformation test. These methods have been reviewed and critically evaluated by a number of authors [53–55]. The softening fraction is typically evaluated as:

$$S = \frac{\sigma_1 - \sigma_3}{\sigma_1 - \sigma_2} \tag{A1}$$

where σ_1, σ_2 and σ_3 are, respectively, the flow stresses of the work hardened, partially softened and completely softened material. The various methods of calculating the softening fraction (S) differ in the details of the evaluation of σ_1, σ_2 and σ_3. The 5% offset method [53–55] has been used in the present contribution.. In this method, σ_1 is the flow stress evaluated by extrapolating the initial loading curve by a strain of 5%. The stress in the recrystallized material, σ_3, is taken to coincide with the (first) loading stress at a strain of 5%. Finally, σ_2 is the flow stress on reloading (after annealing) evaluated at a strain of 5%.

The empirical flow stress relation of Yoshie et al. [57] for microalloyed Nb steels has been used for evaluation of σ_1, σ_2 and σ_3. The values of σ_1, and σ_3 are evaluated directly from eq. (A2) assuming that no dynamic processes (recrystallization or precipitation) occur during loading:

$$\sigma = 22.7\varepsilon^{0.223}\dot{\varepsilon}^{0.048}D_\gamma^{-0.07}\exp\left(\frac{2880}{T}\right)\exp(166C_{Nb}). \tag{A2}$$

The calculation of σ_2 is complex as it includes contributions from precipitation-hardening, recrystallization and work-hardening. Each of these contributions is discussed below.

Recrystallization contribution

The 5% flow stress evaluated on reloading after annealing has been estimated using a simple rule of mixtures of the recrystallized and unrecrystallized fractions:

$$\sigma_2 = \sigma_{Rex}X + \sigma_{Non\text{-}Rex}(1-X) \tag{A3}$$

where X is the recrystallized volume fraction, and σ_{Rex} and $\sigma_{Non\text{-}Rex}$ are the 5% flow stresses of the recrystallized and unrecrystallized portions of the material.

There are two contributions to σ_{Rex}, the contribution from precipitation hardening and the contribution from the dislocation free matrix. The two contributions are added in a non-linear manner:

$$\sigma_{Rex} = \sqrt{\sigma^2_{Rex\text{-}Matrix} + \sigma^2_{ppt}} \quad (A4)$$

$\sigma_{Rex\text{-}Matrix}$ is the 5% flow stress evaluated upon reloading using eq. (A2), with the current Nb content of the matrix. The precipitate contribution is discussed below.

Precipitation contribution

The contribution of precipitation hardening to the 5% flow stress is evaluated using a simple shearing/bypassing model of dislocation–precipitation interaction. The contribution when particle shearing is the dominant mechanism of hardening is evaluated from [33]:

$$\sigma_{ppt} = \sqrt{\frac{3}{4\pi\beta}}\frac{k^{3/2}M\mu}{\sqrt{b}}(f_v R)^{1/2}, \beta = 0.5, k = 0.06 \quad (A5)$$

where k is the shearing constant, M is the Taylor factor, μ is the shear modulus, b is the burgers vector, f_V is the volume fraction of precipitates and R the radius of precipitates. Scarlin and Edington [58] have shown that in the VC-austenite system, particle shearing is the dominant dislocation/precipitate interaction when the precipitate diameter is less than ~4 nm. At larger particle sizes, particle by-pass is the dominant precipitate–dislocation interaction [59]:

$$\sigma_{ppt} = \frac{2\mu b}{R\sqrt{\pi/F_v}}. \quad (A6)$$

Recovery and work-hardening

The contribution to the 5% flow stress upon reloading from the non-recrystallized portion of the sample is also a non-linear sum of two contributions:

$$\sigma_{Non\text{-}Rex} = \sqrt{\sigma^2_{UnRex\text{-}Matrix} + \sigma^2_{ppt}} \quad (A7)$$

where $\sigma_{UnRex\text{-}Matrix}$ is the contribution from the matrix including dislocation strengthening. The relaxation of internal stress due to recovery processes is monitored at all times. For simplicity, we assume that during recovery, the stress relaxation retraces the initial loading curve. At each point in time a strain, $\varepsilon(t)$, can be identified that is consistent with the current value of the flow stress, $\sigma(t)$. The value of $\sigma_{UnRex\text{-}Matrix}$ is then calculated from eq. (A2) by extrapolating this strain by 5%.

References

[1] Sellars CM. In: Sellars CM, Davies GJ, editors. Hot working and forming processes. The Metals Society; 1980. p. 3.
[2] Andrade HL, Akben MG, Jonas JJ. Metallurgical Transactions A 1983;14:1967.
[3] Dutta B, Sellars CM. Materials Science and Engineering 1988;3:197.
[4] Sellars CM. Materials Science and Technology 1990;6:1072.
[5] Bai DQ, Yue S, Sun WP, Jonas JJ. Metallurgical Transactions A 1993;24A:2151.
[6] Hodgson PD. Materials Forum 1993;17:403.
[7] Fernandez I, Uranga P, Lopez B, Rodriguez-Ibabe JM. ISIJ International 2000;40:838.
[8] Cho SH, Kang KB, Jonas JJ. ISIJ International 2001;41:63.
[9] Zurob HS, Brechet Y, Purdy G. Acta Materialia 2001;49:4183.
[10] Smith CS. Transactions of the American Institute of Min Engineers 1948;175(15):15.
[11] Rutter JW, Aust KT. Transactions of the Metallurgical Society of AIME 1960;218:682.
[12] Humphreys FJ, Hatherly M. Recrystallization and related annealing phenomena. Oxford: Pergamon Press, 1996.
[13] Liu J, Jonas JJ. Metallurgical Transactions A 1988;19A:1415.
[14] Arieta FG, Sellars CM. Scripta Metallurgica et Materialia 1994;30:707.
[15] Medina SF, Quispe A, Valles P, Banos JL. ISIJ 1999;39:913.
[16] Lee KJ. Scripta Materialia 1999;40:837.
[17] Kang KB, Kwon O, Lee WB, Park CG. Scripta Materialia 1197;36:1303.
[18] Weygand D, Brechet Y, Lepinoux J. Acta Materialia 1999;47(3):961.
[19] Furu T, Marthinsen K, Nes E. Materials Science and Technology 1960;6:1093.

[20] Ashby MF, Harper J, Lewis J. Transactions of AIME 1969;245:413.
[21] Nes E, Ryum N, Hunderi O. Acta Metallurgica 1985;33:11.
[22] Hazzledine PM. Czech Journal of Physics 1988;B38:431.
[23] Doherty RD. Metal Science 1982;16:1.
[24] Yang ZG, Enomoto M. Metallurgical and Materials Transactions A 2001;32:267.
[25] Jones AR, Ralph B. Acta Metallurgica 1975;23:355.
[26] Cahn JW. Acta Metallurgica 1962;10:789.
[27] Maruyama N, Smith G. Private communication, 2000.
[28] Turnbull D. Transactions of the American Institute of Mining Engineers 1951;191:661.
[29] Bailey JE, Hirsch PB. Proceedings of the Royal Society 1962;A267:11.
[30] Saada G. Acta Metallurgica 1960;8:841.
[31] Verdier M, Brechet Y, Guyot P. Acta Materialia 1999;47:127.
[32] Friedel J. Dislocations. Oxford: Pergamon Press, 1964.
[33] Deschamps A, Brechet Y. Acta Materialia 1999;47:293.
[34] Dutta B, Palmiere EJ, Sellars CM. Acta Materialia 2001;49:785.
[35] Fujita N, Bhadeshia HKDH. Materials Science and Technology 2001;17:403.
[36] Russell KC. Advances in Colloid and Interface Science 1980;13:205.
[37] Gomez-Ramirez R, Pound GM. Metallurgical Transactions 1973;4:1563.
[38] Okaguchi S, Hashimoto T. ISIJ International 1992;32:283.
[39] Gladman T. The physical metallurgy of microalloyed steels. The Institute of Materials, 1997; p. 108.
[40] Narita K. Transactions of the Iron and Steel Institute of Japan 1975;15:145.
[41] Geise J, Herzig C. Z Metallikde 1985;76:622.
[42] Kaur I, Gust W, Kozma L. Handbook of grain and interphase boundary diffusion data, vol. 1. Ziegler Press; 1982.
[43] Frost HJ, Ashby MF. Deformation-mechanism maps. Oxford: Pergamon Press, 1982.
[44] Dutta B, Valdes E, Sellars CM. Acta Metallurgica et Materialia 1992;40:653.
[45] Zou H, Kirkaldy JS. Canadian Metallurgical Quarterly 1989;28:171.
[46] Michal I GM, Locci E. Scripta Metallurgica 1988;22:1801.
[47] Yang Z-G, Enomoto M. Acta Materialia 1999;47:4515.
[48] Le Bon A, Rofes-Vernis J, Rossard C. Metal Science 1975;9:36.
[49] Martin JW, Doherty RD, Cantor B. Stability of microstructure in metallic systems, 2nd ed. Cambridge: Cambridge University Press, 1997.
[50] Nes E. Acta Metallurgica et Meterialia 1995;43:2189.
[51] Fridberg J, Torndahl L-E, Hillert M. Jernkont Ann 1969;153:263.
[52] Silveira e Silva JM, Dahl W, Barbosa R. In: Gottestein G, Molodov DA, editors. Berlin: Springer-Verlag; 2001. p. 116-7.
[53] Fernandez AI, Lopez B, Rodriguez-Ibabe JM. Scripta Materialia 1999;40:543.
[54] Li G, Maccagno TM, Bai DQ, Jonas JJ. ISIJ International 1996;36:1479.
[55] Perttula JS, Karjalainen LP. Materials Science and Technology 1998;14:626.
[56] Gomez M, Medina SF, Quispe A, Valles P. In: Gottestein G, Molodov DA, editors. Recrystallization and grain growth: Proceedings of the First Joint International Conference. Berlin: Springer-Verlag; 2001. p. 116-7.
[57] Yoshie A, Fujita T, Fujioka M, Okamoto K, Morikawa H. ISIJ International 1996;36:467.
[58] Scarlin RB, Edington JW. Metal Science Journal 1973;7:208.
[59] Brown LM, Ham RK. In: Kelly A, Nicholson RB, editors. Strengthening methods in crystals. Amsterdam: Elsevier; 1971.

A7: Full text of: *Y. J. Wang and H. S. Zurob, Applied Physics A, 74 [suppl.], (2002): S1213-1215*

The Precipitation of NbC on Dislocations in Austenite

Y. J. Wang*, H. S. Zurob
Department of Materials Science and Engineering, McMaster University,
1280 Main Street W, Hamilton, ON, Canada, L8S 4L7

Abstract. Small Angle Neutron Scattering (SANS) was used to study the kinetics of NbC precipitation in an austenitic alloy containing 69.2% Ni, 29.7%Fe, 0.851% Nb and 0.114% C (mass percent). The kinetics were measured at 700°C for a non-deformed sample as well as samples deformed by 10, 20 and 30%. The effect of deformation is to increase the rate of precipitation and to reduce the precipitate particle size. The use of SANS appears to provide reliable information on the precipitate volume fraction as well as the average particle size.

The precipitation of NbC in austenite is a key step in the production of microalloyed steels as well as several important grades of stainless steel [1,2]. The precipitates are most effective when present in the form of very fine dispersions (< 20 nm) [1-3]. Over the years, numerous investigations have been carried out in order to understand the precipitation process [4]. In most cases, the results were difficult to interpret due to the complex chemistry of the steel as well as the onset of other phase transformations. In addition, valuable information was lost because the traditional techniques of extraction replicas and TEM are unable to reliably measure particle sizes that are smaller than 3 nm in diameter.

In the present work, the technique of SANS was utilised to study the precipitation of NbC. This technique provides a reliable method for measuring the precipitate volume fraction as well as the average particle size. Every effort was made to ensure that the precipitation of NbC is the only process taking place. To that end a simple alloy was designed containing 69.2% Ni, 29.7%Fe, 0.851% Nb and 0.114% C (mass percent). Our thermodynamic computations indicate that the alloy exists as a single-phase solid solution above 1200°C. At lower temperatures (down to 500°C), NbC is expected to precipitate exclusively. The precipitates are believed to nucleate heterogeneously on dislocations and grain-boundaries [2, 4, 5]. An annealing temperature of 700°C was chosen in order to avoid the onset of recrystallization and to limit the extent of recovery. In this way, we are able to follow the progress of precipitation on a stable network of dislocations.

* Corresponding author.

1 Experimental

The alloy was prepared in a laboratory unit capable of producing 60-kg ingots. The material was hot rolled to produce 15-mm slabs. Four specimen were prepared from the above slabs. The specimen were sealed in quartz and solution treated at 1225°C for at least 20 hours. The solution treatment was terminated by quenching the samples in water. The solution-treatment resulted in a grain-size in excess of 500 μm. This large grain size is critical, because it leaves dislocations as the only significant precipitate nucleation sites.

Of the four samples, one was retained in the undeformed condition. Two other samples were deformed in tension to (engineering) strains of 10 and 20%. The remaining sample was rolled to a reduction of 30%. The samples were then cut into slices 1 to 2-mm thick. All four samples were annealed at 700°C for up to 100 hours. The annealing treatment was interrupted at various stages in order to perform the scattering measurements. It is worth pointing out that for the first 3600 seconds the samples were aged in a salt-bath. Further ageing was carried out in a conventional furnace and under vacuum.

The neutron scattering measurements were carried out using the conventional small-angle neutron scattering facility (SANS-2) at GKSS. The neutron wavelength was 0.53 nm. A 2-dimensional detector was positioned at distances between 1 and 20 m from the sample. This provided a scattering vector (q) interval ranging from 0.02 nm^{-1} to 2.5 nm^{-1}. Because of the ferromagnetic nature of the alloy, a horizontal magnetic field was applied perpendicular to the incoming neutron beam in order to fully align the magnetic moment of the sample. We determined that an applied field of 2

Tesla is sufficient to achieve full alignment under the present conditions. The application of the magnetic field meant that only nuclear scattering occurred in the horizontal plane, while both nuclear and magnetic scattering occurred in the vertical plane. We are thus able to isolate the nuclear scattering component.

We also investigated the effect of sample orientation on the scattering measurements. To than end, some of the samples were measured twice, once with the deformation direction parallel to the magnetic field and once with the deformation direction perpendicular to the field. The scattering spectra were identical in both cases.

Finally, selected aging conditions were also examined using the techniques of extraction replicas and thin-foil electron microscopy. These measurements were used to complement and verify the present SANS work.

2 Results and discussion

Scanning transmission electron microscopy (STEM) confirmed that NbC is the only precipitate formed under the present annealing conditions. In addition, we used TEM to confirm that the precipitates are formed primarily on dislocations.

The scattering data were processed using the standard methods described in [6, 7]. For each sample, the differential scattering cross-section was extracted from the measured horizontal scattering intensity. Figure (1) is a plot of the difference between the differential scattering cross-sections in the solution-treated and annealed states vs. the scattering vector. The evolution of the curve is attributed to the progress of NbC precipitation. The precipitate volume fraction (f) was estimated using the fact that $f(1-f)$, is proportional to the integrated intensity. This quantity was calculated from the data presented in figure (1) with the assumption of a q^{-4} extrapolation for q values outside the range measured here. This extrapolation would of course lead to a high uncertainty at the shortest aging times. The time-evolution of the precipitate fraction is shown in Figure (2). We chose to plot $\ln(\ln(1/(1-f)))$ vs. $\ln(t)$ in order to fit the form of the Avrami equation ($f = 1-\exp(-Bt^n)$)

The deformed samples appear to have the same Avrami exponent n of 0.3. The kinetic factor (B), on the other hand, is a strong strong function of the applied strain. This seems to support the hypothesis that deformation enhances the kinetics of precipitation mainly by increasing the number of nucleation sites [4]. It is difficult to estimate the Avrami exponent of the undeformed sample. It appears, however, that the exponent is larger than that of deformed samples.

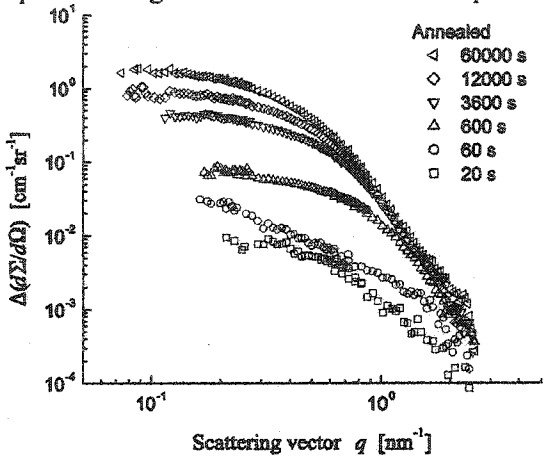

Fig 1. The difference between the differential scattering cross sections of the homogenized and annealed states of the 20% deformed sample.

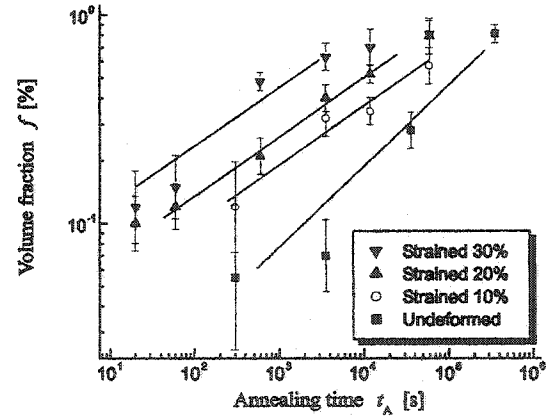

Fig. 2. Avrami plot of the evolution of precipitate volume fraction as a function of time. The y-axis is $\ln(\ln(1/(1-f)))$ while the x-axis is $\ln(t)$.

The average size of the NbC precipitates was estimated using the Guinier plot. Figure (3) is a plot of the average particle size as a function of time. The figure carries two important results: Firstly, the particle diameter appears to increase as $t^{1/5}$. This dependence is attributed to the processes of nucleation and growth. This

interpretation is supported by the fact that the y-intercepts in Figure (1) are larger for longer times. The y-intercept is known to be proportional to the precipitates' number-density. Secondly, for a given annealing time, the average particle size of the deformed samples is smaller than that of the undeformed sample.

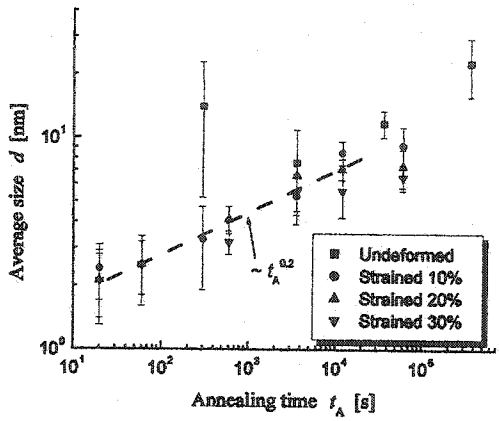

Fig3. The evolution of the average particle size as a function of time.

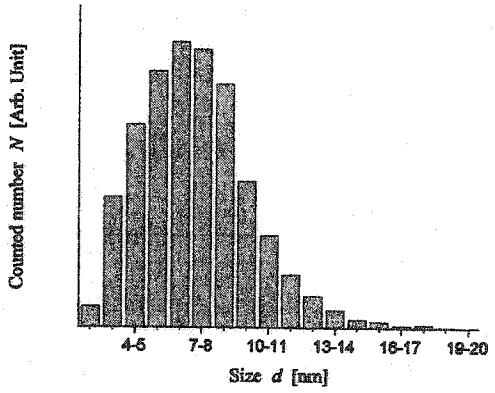

Fig. 4. The precipitate size distribution in the sample deformed by 20% and aged for 12000 s at 700°C.

Figure (4) is the particle size distribution obtained from measurements on extraction replicas of the 20% sample following an annealing time of 12000 seconds. The average size obtained in this way is 7.3 nm, which is in excellent agreement with that obtained using the technique of SANS (7 nm). The agreement confirms the accuracy of the SANS approach, which may now be applied with confidence to those cases (short times) where the technique of extraction replicas is less accurate.

In summary, SANS was shown to be an accurate technique for studying the precipitation of NbC in austenite. The data presented here confirm several important results: 1) Deformation dramatically enhances the kinetics of precipitation by increasing the number of available nucleation sites. 2) Under the present experimental conditions which do not permit recrystallization, and for a given annealing time, the average particle size in the deformed samples is smaller than that in the undeformed sample.

Acknowledgements. The alloys were prepared at IRSID in collaboration with Dr. D. Quidort. The financial support of NSERC and GKSS is gratefully acknowledged. We are also thankful to Dr. G. R. Purdy for supporting this work.

References:

[1] A. J. DeArdo, C. I. Garcia, E. J. Palmiere, *ASM Handbook,* Vol. 4, (ASM International, Metals Park 1992) 273

[2] W. Kesternich, D. Meertens, *Acta metall.* **34**, 1071 (1986).

[3] B. Dutta, C. M. Sellars, *Mat. Sci. and Tech.* **2**, 146 (1986).

[4] B. Dutta, C. M. Sellars, *Mat. Sci. and Tech.* **3**, 197 (1987).

[5] W. J. Liu, *Metall. and Mater. Trans.A*, **26A**, 1641 (1994).

[6] G. E. Bacon, *Neutron Diffraction*, 3rd edition (Clarendon Press, Oxford 1971)

[7] G. Kostorz, Ed., *A Treatise on Materials Science and Technology*, Vol. 15 (Academic Press, New York 1979)